UNIVERSITY of CALIFORNIA
SANTA CRUZ

PROPERTIES OF THE HADRONIC FINAL STATE IN DIFFRACTIVE DEEP INELASTIC SCATTERING TAGGED WITH THE LEADING PROTON SPECTROMETER OF ZEUS

A dissertation submitted in partial satisfaction of the
requirements for the degree of

DOCTOR OF PHILOSOPHY

in

PHYSICS

by

Riko Wichmann

December 1999

The dissertation of Riko Wichmann is approved:

Professor Abraham Seiden, Chair

Professor Hartmut F.-W. Sadrozinski

Professor Howard E. Haber

Dean of Graduate Studies

Copyright © by
Riko Wichmann
1999

Contents

List of Figures vi

List of Tables ix

Acknowledgements xi

1 Introduction 1

2 Theoretical Approaches to Diffractive DIS 3
- 2.1 Basics of QCD . . . 3
  - 2.1.1 Fragmentation and Confinement . . . 5
- 2.2 Deep Inelastic Scattering . . . 6
  - 2.2.1 Kinematic Variables . . . 7
  - 2.2.2 Parton Model . . . 8
  - 2.2.3 Evolution Equation . . . 9
- 2.3 Diffraction . . . 12
- 2.4 The Exchange Picture . . . 13
  - 2.4.1 Regge Phenomenology . . . 13
  - 2.4.2 Partonic Pomeron . . . 15
- 2.5 QCD Pomeron - Photon Dissociation . . . 15

3 The ZEUS Detector at HERA 17
- 3.1 The HERA Electron-Proton Collider . . . 17
- 3.2 The ZEUS Detector . . . 19
- 3.3 The Central Tracking Detector (CTD) . . . 23
- 3.4 The Uranium Calorimeter (UCAL) . . . 24
- 3.5 The Small Angle Rear Tracking Detector (SRTD) . . . 26
- 3.6 The ZEUS Trigger and Data Acquisition System . . . 26

4 The Leading Proton Spectrometer (LPS) 29
4.1 LPS Hardware . . . 29
4.1.1 Spectrometer Components . . . 29
4.1.2 The Silicon-Microstrip Detectors . . . 31
4.1.3 The Front-End Electronics . . . 33
4.2 LPS operation . . . 36
4.3 LPS Reconstruction . . . 39
4.3.1 Coordinate Reconstruction . . . 39
4.4 Track Fitting . . . 40
4.5 Alignment - A brief overview . . . 42
4.5.1 Alignment Procedure . . . 42
4.5.2 Status of the Alignment for 1997 Data . . . 45

5 Monte Carlo Simulation 47
5.1 Monte Carlo Generators . . . 48
5.1.1 Introduction . . . 48
5.1.2 RAPGAP with H1 fit . . . 50
5.1.3 RAPGAP with Bartels-Lotter-Wüsthoff $q\bar{q}$ . . . 53
5.1.4 RAPGAP with Bartels-Wüsthoff $q\bar{q}g$ . . . 54
5.1.5 The Saturation Model - SATRAP . . . 55
5.1.6 RIDI . . . 57
5.1.7 Beam Halo Background . . . 59
5.2 ZEUS Monte Carlo Simulation . . . 60
5.3 LPS Standalone Simulation with MOLPS . . . 60
5.4 Comparison Data with Monte Carlo . . . 62
5.4.1 RAPGAP Reweighting . . . 64

6 Reconstruction of Diffractive Kinematic Variables 76
6.1 Electron Identification . . . 76
6.1.1 Electron Finding with SINISTRA . . . 76
6.1.2 Electron Position Reconstruction . . . 77
6.2 Final State Particle Reconstruction with ZUFOs . . . 78
6.3 DIS Kinematic Variables . . . 80
6.3.1 Electron Method . . . 81
6.3.2 Jacquet-Blondel Method . . . 82
6.3.3 Double Angle Method . . . 83
6.4 Reconstruction of the Invariant Mass M_X . . . 85
6.5 Event Selection . . . 87
6.6 Kinematic Phase Space of the Analysis . . . 89
6.7 Systematic Checks . . . 90
6.7.1 Hadronic Systematic Checks . . . 90

6.7.2 Electron Systematic Checks . . . 92
6.7.3 Systematic Checks on the LPS . . . 92
6.7.4 Monte Carlo Systematic Checks . . . 93
6.8 Correction . . . 94

7 The Diffractive Hadronic Final State 95
7.1 Reference Frame and Boost Method . . . 96
7.2 Global Event Shape Variables . . . 98
7.2.1 Definition of Thrust and Sphericity . . . 99
7.2.2 Thrust and Sphericity Distributions . . . 105
7.2.3 Average Thrust and Sphericity . . . 113
7.2.4 Summary of the Thrust and Sphericity Measurement . . . 116
7.3 Transverse Momenta . . . 120
7.3.1 Definition of $p^2_{t,in}$, $p^2_{t,out}$ and $p^2_{t,thrust}$ . . . 120
7.3.2 Study of the Thrust Angle Θ_{thrust} . . . 122
7.3.3 Average Transverse Momenta . . . 132
7.3.4 Summary of the Transverse Momenta Measurement . . . 135
7.4 Inclusive Distributions . . . 137
7.4.1 Energy Flow . . . 140
7.4.2 Transverse Energy Flow . . . 143
7.4.3 Summary of the Energy Flow Measurement . . . 147

8 Summary and Conclusion 149

A 152
A.1 Tables for $\frac{1}{N}\frac{dN}{dT}$ . . . 152
A.2 Tables for $\frac{1}{N}\frac{dN}{dS}$ . . . 155
A.3 Tables of $<T>$ and $<S>$ . . . 158
A.4 Tables of $<p^2_{T,in}>$ and $<p^2_{T,out}>$ . . . 159
A.5 Tables of Energy Flow . . . 160
A.6 Tables of Transverse Energy Flow . . . 163

Bibliography 166

List of Figures

2.1 Sketch of the Beginning of a Fragmentation Process 5
2.2 Sketch of Hadronization 6
2.3 Neutral and Charged Current DIS Event 7
2.4 Measurement of the Proton Structure Function F_2 11
2.5 Feynman Diagram of a Diffractive Event 13
2.6 Total Photoproduction Cross Section 14
2.7 Feynman Diagrams of Diffractive Photon Dissociation 16

3.1 HERA Collider 18
3.2 Integrated Luminosity Delivered by HERA 1992 to 1997 20
3.3 Cross Sectional View of the ZEUS Detector (x=0 plane) 21
3.4 Cross Sectional View of the ZEUS Detector (z=0 plane) 22
3.5 Cross Sectional View of the ZEUS Calorimeter along the Beam Direction 25
3.6 Schematic Diagram of the ZEUS Trigger and DAQ System 28

4.1 Layout of the LPS 30
4.2 Sketch of the HERA Proton Beam Optics 31
4.3 Functional Principle of a Silicon Microstrip Detector 32
4.4 Schematic Illustration of the Binary Readout System of the LPS . . . 33
4.5 Layout of an LPS Hybrid 34
4.6 Simplified Schematic of one Channel of the TEKZ Chip 35
4.7 Simplified Schematic of the DTSC 36
4.8 Schematic of the LPS Readout System 37
4.9 Illustration of the LPS Insertion Procedure 38
4.10 Correlation Lines in Stations S5 and S6 41
4.11 Comparison of LPS Alignment 1995 and 1997 46

5.1 Feynman Diagrams Contributing to an ep DIS Process 48
5.2 Light Quark and Gluon Distributions of the RAPGAP H1fits 51
5.3 Feynman Diagrams Implemented in RAPGAP for a Resolved $\mathbb{P}$ . . . 52
5.4 Diagrams for Diffractive Photon Dissociation 54

5.5 Diagram of the Basic Saturation Model Process 55
5.6 Comparison of the BEKW Fit and $F_2^{D(2)}$ Data 57
5.7 Diagrams Implemented in RIDI 58
5.8 MC Comparison of LPS p_x and p_y 63
5.9 Mismatch between DATA and RAPGAP for Diffractive DIS Variables 65
5.10 Comparison between DATA and Corrected RAPGAP 66
5.11 Comparison between DATA and Reweighted RAPGAP 67
5.12 Data RAPGAP Comparison for Kinematic Variables 68
5.13 Data RAPGAP Comparison for Kinematic Variables 69
5.14 Data RAPGAP Comparison for Kinematic Variables 70
5.15 Data RAPGAP Comparison for LPS Variables 71
5.16 Data RAPGAP Comparison of the Hadronic Final State 73
5.17 M_X Distribution in Data and RAPGAP 75

6.1 Electron Position Reconstruction in Data and MC 78
6.2 Schematic Representation of ZUFOs 79
6.3 ZUFO Distributions of Energy and Momentum 81
6.4 Schematic of an ep DIS Process 82
6.5 Reconstruction of Q^2, y, and x with Electron, DA, and JB Method . 84
6.6 Resolution and Calibration of M_X 86
6.7 Sketch of the H1-shaped Box Cut 89
6.8 Fractional Energy Deposit in the FCAL Inner Ring 91

7.1 Diffractive Event in Center-of-Mass Frame 96
7.2 $\mathbb{P}$ Momentum Reconstruction for Boost 98
7.3 Resolution of T and S 101
7.4 Reconstruction Quality of T and S 102
7.5 Comparison Data T and S with RAPGAP 103
7.6 Systematic Uncertainties on $\langle T \rangle$ and $\langle S \rangle$ 104
7.7 Corrected T Distributions with e^+e^-, RAPGAP 106
7.8 Corrected T Distributions with RIDI, $q\bar{q}$, $q\bar{q}g$ 107
7.9 Corrected T Distributions with SATRAP,RAPGAP *H1fit1* 109
7.10 Corrected S Distributions with e^+e^-, RAPGAP 110
7.11 Corrected S Distributions with RIDI, $q\bar{q}$, $q\bar{q}g$ 111
7.12 Corrected S Distributions with SATRAP, RAPGAP *H1fit1* 112
7.13 $\langle T \rangle$, $\langle S \rangle$ with e^+e^-, H1 thrust measurement, RAPGAP *H1fit2* and *H1fit1*, SATRAP 115
7.14 $\langle T \rangle$, $\langle S \rangle$ with RIDI, $q\bar{q}$, $q\bar{q}g$ 117
7.15 $\langle T \rangle$ and $\langle S \rangle$ in two Bins of Q^2 118
7.16 $\langle T \rangle$ and $\langle S \rangle$ in two Bins of $x_{\mathbb{P}}$ 119
7.17 Definition of the Event Plane 120

7.18 Resolution of Transverse Momenta 121
7.19 Reconstruction and Reproduction of Transverse Momenta 123
7.20 Systematic Uncertainties of $<p^2_{T,in}>$ and $<p^2_{T,out}>$ 124
7.21 Reconstructed Distributions of Θ_{thrust} 126
7.22 Reconstructed Distributions of Θ_{thrust} Scaled in RAPGAP 127
7.23 Comparison Scaled Θ_{thrust} in RAPGAP with SATRAP, $q\bar{q}$, $q\bar{q}g$ 128
7.24 Contributions of SATRAP $q\bar{q}$ and $q\bar{q}g$ to Θ_{thrust} 129
7.25 Contributions of RAPGAP $q\bar{q}$ and BGF to Θ_{thrust} 131
7.26 $<p^2_{T,in}>$, $<p^2_{T,out}>$ with JETSET, RAGAP *H1fit2* and *H1fit1*, SATRAP 133
7.27 $<p^2_{T,in}>$, $<p^2_{T,out}>$ with RIDI, $q\bar{q}$, $q\bar{q}g$ 134
7.28 Ratio of $<p^2_{T,in}>$ and $<p^2_{T,out}>$ Compared to JETSET 135
7.29 Reconstruction Quality of the (Transverse) Energy Flow 138
7.30 Data RAPGAP Comparison for (Transverse) Energy Flow 139
7.31 Energy Flow with H1, RAPGAP, JETSET 141
7.32 Energy Flow with RIDI, $q\bar{q}$, $q\bar{q}g$ 142
7.33 Energy Flow with SATRAP, RAPGAP *H1fit1* 144
7.34 Transverse Energy Flow with RAPGAP, JETSET 145
7.35 Transverse Energy Flow with RIDI, $q\bar{q}$, $q\bar{q}g$ 146
7.36 Transverse Energy Flow with SATRAP, RAPGAP *H1fit1* 148

List of Tables

2.1 Properties of the Six Quarks 4

3.1 HERA Design Parameters and Actual Performance in 1997 19

4.1 Quality Codes for LPS Coordinates 40

5.1 Reweighting of RAPGAP BGF Events 74

6.1 Backsplash Codes 80

7.1 Thrust and Sphericity Illustration 100
7.2 Fraction of $q\bar{q}g$ in RIDI 114

8.1 Summary of Final Results with MC Models 150

A.1 Table of $\frac{1}{N}\frac{dN}{dT}$ for $4.0 < M_X < 7.5$ GeV 152
A.2 Table of $\frac{1}{N}\frac{dN}{dT}$ for $7.5 < M_X < 16$ GeV 153
A.3 Table of $\frac{1}{N}\frac{dN}{dT}$ for $16 < M_X < 35$ GeV 154
A.4 Table of $\frac{1}{N}\frac{dN}{dS}$ for $4.0 < M_X < 7.5$ GeV 155
A.5 Table of $\frac{1}{N}\frac{dN}{dS}$ for $7.5 < M_X < 16$ GeV 156
A.6 Table of $\frac{1}{N}\frac{dN}{dS}$ for $16 < M_X < 35$ GeV 157
A.7 Table of $<T>$ versus M_X 158
A.8 Table of $<S>$ versus M_X 158
A.9 Table of $<p^2_{T,in}>$ versus M_X 159
A.10 Table of $<p^2_{T,out}>$ versus M_X 159
A.11 Table of $\frac{1}{N}\frac{dE}{d\eta}$ for $4.0 < M_X < 7.5$ GeV 160
A.12 Table of $\frac{1}{N}\frac{dE}{d\eta}$ for $7.5 < M_X < 16$ GeV 161
A.13 Table of $\frac{1}{N}\frac{dE}{d\eta}$ for $16 < M_X < 35$ GeV 162
A.14 Table of $\frac{1}{N}\frac{dE_T}{d\eta}$ for $4.0 < M_X < 7.5$ GeV 163
A.15 Table of $\frac{1}{N}\frac{dE_T}{d\eta}$ for $7.5 < M_X < 16$ GeV 164
A.16 Table of $\frac{1}{N}\frac{dE_T}{d\eta}$ for $16 < M_X < 35$ GeV 165

Abstract

Properties of the Hadronic Final State in Diffractive Deep Inelastic Scattering tagged with the Leading Proton Spectrometer of ZEUS

by

Riko Wichmann

One of the exciting results discovered at the ep collider HERA at DESY, Hamburg, is the occurrence of diffractive Deep Inelastic Scattering (DIS) events observed previously in hadron-hadron collisions. The ZEUS detector is equipped with the Leading Proton Spectrometer (LPS), which, for a restricted parameter set, allows to measure all products of the reaction $ep \to epX$, including the final state proton, which otherwise would escape through the forward beam pipe. The nature of the diffractive exchange is studied in terms of the properties of the hadronic final state X characterized by the global event shape variables thrust and sphericity, and by the dynamic quantities of transverse momenta in and out of the event plane as a function of the energy scale (M_X) of the final state. Inclusive distributions of energy and transverse energy flow are presented as a function of pseudo-rapidity. These variables are sensitive to the parton level mechanism responsible for the diffractive exchange. The measurement of the hadronic final state is compared to results from e^+e^- annihilation and to predictions of various Monte Carlo models, which describe diffraction by the exchange of a hadronic object (Pomeron) and by photon dissociation into quarks and gluons, respectively. The hadronic final state exhibits a dominantly two-jet structure. This structure is also predicted by Monte Carlo models, which include gluons in the final state. The overall best description of the diffractive hadronic final state is given by models, which implement a QCD-based photon dissociative approach. The analysis is based on the 1997 data set and is restricted to the region of $4 < M_X < 35$ GeV, $4 < Q^2 < 150$ GeV^2, $0.0003 < x_{_{IP}} < 0.03$ and $0.03 < y < 0.7$.

Acknowledgements

This is the right time and place to thank everybody, who gave me help and support on my way, which led me to where I stand now. First of all, I'm very grateful for the financial and moral support I have received from my family, especially from my Mom, over the many years of my education. Her encouragement and believe in my hopes and plans made the completion of my studies and my PhD possible.

Many thanks go to the Santa Cruz Institute for Particle Physics at the University of California at Santa Cruz and the wonderful people I had the honor to work with: Abe Seiden and Hartmut Sadrozinski, who gave me advise, encouragement, and the freedom to pursue my analysis following my own course; Jeff Rahn, who gave me a head start at DESY with his insight and computer code; Dave C. Williams, who was an invaluable source for me of knowledge and advise at DESY; Georgia Hamel, Nora Rogers, Ariane Frey, Bill Rowe, and Alec Webster, who created a working environment at SCIPP, which I cannot imagine to be more pleasant; and everybody else at SCIPP: it was my pleasure to work with you. However, my very special thanks go to Teela Pulliam and Wilko Kröger, and to Sumita Jagger and Tim Dubbs, who not only became some of my best friends, but also gave me a place to stay for many weeks, when I came back from Hamburg and didn't have a place on my own.

While working at DESY, I worked with many wonderful people of the LPS group, which made running a difficult detector an (almost) joyful experience: Michele Arneodo, Roberto Cirio, Marco Costa, Vincenzo Monaco, Antonio Pellegrino, Marta Ruspa, Roberto Sacchi, Ada Solano, and Amedeo Staiano. The diffractive group created the working environment for my physics efforts with thanks to Halina Abramowicz, Laura Iannotti, Henri Kowalski, Peter Markun, Krzysztof Piotrzkowski, Jim Whitmore, Yuji Yamazaki, and, from H1, Hannes Jung.

Last but not least, my loving thanks go to Katarzyna Klimek, who gave me courage, when mine faded, and comfort, when everything including the DESY computers seem to be working against me.

THANK YOU ALL!
You are truly the best ! :)

Chapter 1

Introduction

One of the questions scientists have tried to answer for almost a century now, and are still working on in experiments, which grow bigger and bigger, employing state of the art technology and hundreds of physicists and engineers, is concerned with the structure of matter and the forces which keep it together. Results from these experiments and their interpretation are not only interesting to the community known as "particle" or "high-energy physicists," but has a growing influence on Cosmology and Astrophysics to help explain the history, development, and future of the universe.

An old, but still up-to-date and irreplaceable method to investigate this question is to scatter point-like projectiles off a target. Measuring the resulting energy or angular distributions of the scattering products gave insight into the structure of matter and resulted in a theory which can explain a wide range of phenomena from a few fundamental principles. This theory is known as the *Standard Model of Particle Physics*.

Rutherford [1] was the first one who conducted the now classical experiment of scattering α-particles off a gold foil, interpreting his measurement in such a way, that the mass of an atom is concentrated in a nucleus. Point-like particle of spin-$\frac{1}{2}$ (electrons) were then used and the formula found by Rutherford was modified by Mott [2]. Since then, electrons (or in general leptons) are probably the most extensively used probe to study the constituents and forces of matter.

Scattering experiments with electrons led to the discovery of the proton structure [3], the excitation of nuclei to resonances, and ultimately to an estimate of the size of the proton [4]. To classify the observed baryonic states in these experiments, symmetries were proposed, which ultimately let to the formulation of the quark parton model (QPM) and its extension toward Quantum Chromodynamics (QCD), which is the quantized field theory of the strong interaction responsible for the formation of hadrons. Chapter 2 gives a brief introduction to QCD, with an emphasize on the physics involved in the analysis presented in this thesis.

Even though QCD has been an outstanding success (together with the theory of electroweak interactions) in describing many of the features and phenomena of current high-energy physics, there are regions of particle physics where perturbative QCD is no longer applicable and phenomenological models and approaches have to be employed to explain them. Diffractive ep scattering is one of these fields, which is the domain presented in the analysis of this thesis. Diffractive physics is often viewed in the context of a transition between so called "soft" physics, which is not described by perturbative QCD because the coupling constant is too large, and "hard" physics, where perturbative methods are applicable. An introduction is given in Chapter 2.

The method used in this analysis is to study the final state, which is produced by the diffractive ep scattering process, to gain some insight into the underlying exchange and its soft or perturbative nature. The events studied were recorded with the ZEUS experiment at the HERA accelerator (Chapter 3) using a special detector component, the Leading Proton Spectrometer (Chapter 4), to select the diffractive events. Monte Carlo models (Chapter 5) are used to make predictions about the applicability of various theoretical scenarios. The kinematics of the events and the method of reconstructing the necessary variables are described in Chapter 6, followed by a discussion of the properties of the hadronic final state in Chapter 7. Concluding remarks on the analysis are given in Chapter 8.

Chapter 2

Theoretical Approaches to Diffractive DIS

2.1 Basics of QCD

Quantum Chromodynamics (QCD) is the quantized field theory developed to describe the interaction of hadrons governed by the strong force [5] [6]. The fundamental constituents are quarks and gluons. Table 2.1 gives a summary of the properties of the six known quarks. The idea of quarks arose from observations in the spectra of low-mass meson and baryons, which manifested the need of an SU(3) symmetry (of flavor). The observed baryons are interpreted as three-quark states. To account for the observed spin states of the baryons, their quark constituents were forced to have half-integer spin. However, spin-$\frac{3}{2}$ baryons are then symmetric states of space, spin, and flavor (SU(3)) degree of freedom, therefore violating the Pauli Exclusion Principle, which states that two fermions cannot occupy the same state; their wavefunctions need to be totally antisymmetric. To resolve this problem, a new quantum number was introduced: the color degree of freedom [7]. Each quark carries a color index a of three possible values (usually called *red, green,* and *blue* for $a = 1, 2, 3$). Since the introduction of the color degree of freedom would lead to a proliferation of states, a color-singlet hypothesis was imposed, stating that only color-neutral states (of color *white*) can exist in nature. Color-singlet states are formed by a state of a quark and anti-quark carrying a color and its anti-color. These states are called *mesons*. A three-quark state is color neutral if all three (anti-) colors are present. Color-singlet three-quark states form the *baryons*. The quarks which form these color-singlet states are called *valence quarks*.

The carriers of the color interaction, which always have a combination of color and anti-color (such as $r\bar{b}, g\bar{r}$ ...), are eight differently colored gauge bosons, called *gluons*. Since the gluons carry the color charge, they can couple to each other, which makes

Quark	Charge	Mass	Isospin
u	$+\frac{2}{3}$	~ 4 MeV	$+\frac{1}{2}$
d	$-\frac{1}{3}$	~ 7 MeV	$-\frac{1}{2}$
c	$+\frac{2}{3}$	~ 1.5 GeV	0
s	$-\frac{1}{3}$	~ 150 MeV	0
t	$+\frac{2}{3}$	~ 175 GeV	0
b	$-\frac{1}{3}$	~ 5 GeV	0

Table 2.1: The properties of the six quarks.

QCD a non-abelian gauge theory. This self-coupling of the gauge bosons is the main difference with respect to Quantum Electrodynamics (QED), where the photon does not carry the charge of the theory and therefore does not interact with itself. In QED, the coupling constant α increases slightly with Q^2 [14], while the strong coupling constant α_S is large at small Q^2 (large distances) but decreases as Q^2 increases (small distances). The running of α_S, i.e., its dependence on the energy, makes the theory asymptotically free and perturbative methods can be applied at high enough energies to calculate observable quantities in perturbative QCD (pQCD). However, typically a non-perturbative or *soft* component from phenomenological models is added to the pQCD calculations if low energy interactions are involved.

The dependence of the strong coupling constant α_S on the scale μ is given by the renormalization group equation

$$\mu \frac{\partial \alpha_S}{\partial \mu} = \beta(\alpha_S). \tag{2.1}$$

The β function has a perturbative expansion [8, 9, 10]

$$\beta(\alpha_S) = -b_0 {\alpha_S}^2 (1 + b_1 \alpha_S + O({\alpha_S}^2)) \tag{2.2}$$

where

$$\begin{aligned} b_0 &= \frac{33 - 2n_f}{12\pi} \\ b_1 &= \frac{153 - 19n_f}{2\pi(33 - 2n_f)} \end{aligned} \tag{2.3}$$

and n_f is the number of active light flavors, i.e., their mass is smaller than the scale. Perturbative QCD does not give an absolute value of the coupling constant, but just determines how α_S varies as a function of scale μ. Introducing the Λ parameter, which indicates the order of magnitude of the scale at which α_S becomes strong, the leading order expression for α_S is:

$$\alpha_S(\mu) = \frac{1}{b_0 \ln(\mu/\Lambda^2)}. \tag{2.4}$$

Although the value of Λ depends on the precise definition, it is in the neighborhood of 200 MeV.

QCD requires a modification of the quark parton model (QPM), which will be introduced in Section 2.2.2. Since quarks interact through gluons, they can radiate gluons, which in turn can split again in quark anti-quark ($q\bar{q}$) pairs (*sea quarks*) or gluons (QCD Compton process).

2.1.1 Fragmentation and Confinement

The scale dependence of α_S and its increase with decreasing energy results in the characteristics of hadrons referred to as confinement and fragmentation [11] [12]. At scales comparable to the mass of light hadrons ($\mu \simeq 1$ GeV^2) the coupling α_S becomes large, forcing a quark to always stay with an anti-quark or with two other quarks to form color-neutral states. These color-neutral states can be viewed as independent particles, since the strong interaction between them vanishes at large distances. Therefore, quarks can never be observed as free particles, a fact which is called *confinement*.

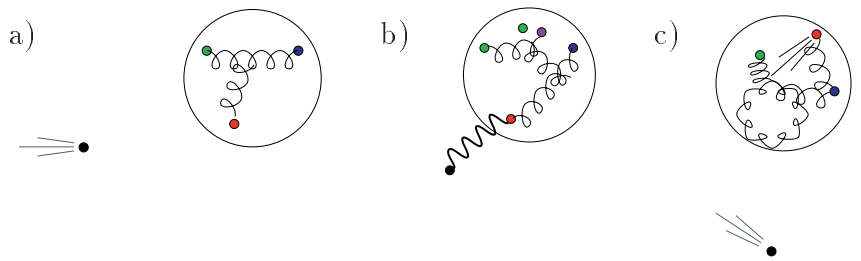

Figure 2.1: Sketch of the initiation of the fragmentation process in an ep scattering process. The electron transfers a large amount of momentum to a quark within proton.

To illustrate the concept of *fragmentation*, which is closely related to the confinement of quarks in hadrons, an ep scattering event can be viewed as sketched in Figures 2.1 and 2.2. A highly energetic electron approaches the proton in Figure 2.1a. The electron can couple to a quark within the proton (2.1b) via the exchange of a photon, which transfers a considerable amount of momentum to the struck quark. Both the electron and the quark recoil from the scattering. The electron, which does not participate in the strong interaction, now leaves (2.1c). The quark also eventually leaves the hadron (2.2a), but its energy is converted into a gluon field which connects it to the hadron, forming a color string. After the string has absorbed enough energy from the escaping quark, its gluon field fluctuates into $q\bar{q}$ pairs which form color neutral states (2.2b). These states are then observed as free hadrons in the final state.

In e^+e^- annihilation, a $q\bar{q}$ pair is formed. A gluon field forms between the two quarks as they travel in opposite directions, which breaks up into hadrons in a similar way as described for the ep scattering event.

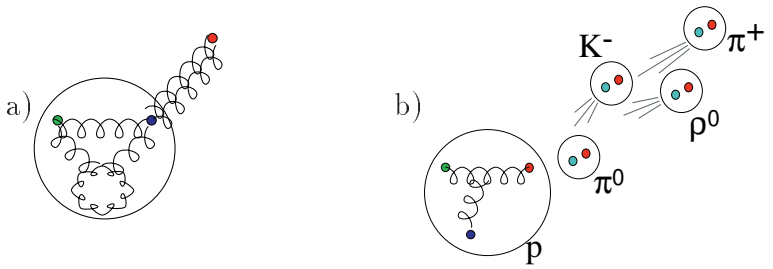

Figure 2.2: The struck quark hit in Figure 2.1 recoils out of the proton and hadronizes into free particles.

The fragmentation process happens at scales where the strong coupling between quarks and gluons is large. Therefore, it cannot be calculated in perturbation theory. Only phenomenological models are available, employing parameterizations of the process based mainly on observations in e^+e^- annihilation.

2.2 Deep Inelastic Scattering

The scattering of high-energy leptons (electrons e, muons μ, or neutrinos ν) off protons usually results in an inelastic scattering process, in which the proton disintegrates and a large number of hadronic particles form the resulting final state. The structure of the proton [13] and the measurement of its structure function interpreted in terms of the momentum distribution of its constituents is one of the famous results of deep inelastic scattering (DIS) experiments.

There are two fundamental classes of deep inelastic scattering of an electron e (or any other lepton) off a proton P (Figure 2.3):

$$e^{\pm} + P \to e^{\pm} X \quad \text{and} \quad e^{\pm} + P \to \overset{(-)}{\nu} X \tag{2.5}$$

where X represents the hadronic final state originating from the disintegration of the proton. The four-momenta of the initial and final lepton are $k = (E; \mathbf{k})$ and $k' = (E'; \mathbf{k}')$, respectively, and the one of the proton $p = (E_p; \mathbf{p})$ and of the photon $q = (E_\gamma; \mathbf{q})$.

If the charge of the lepton is conserved (Figure 2.3, left), the intermediate vector boson is neutral (either a γ or Z°) and the process is therefore referred to as neutral current (NC) DIS. On the right hand side of Figure 2.3, the lepton converts into a

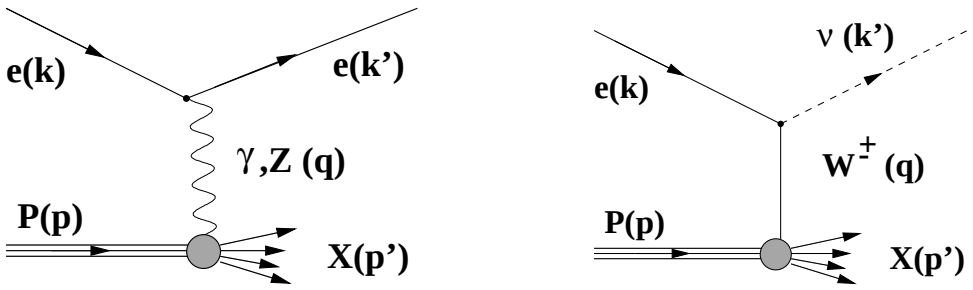

Figure 2.3: Diagram of a neutral (left) and charged current (right) deep inelastic scattering event.

ν exchanging a charged vector boson (W^+ or W^-) and the process is called charged current DIS.

Since the momentum exchanged at the lepton vertex is small in the analysis presented in this thesis, and the masses of the $W^{\pm}$ and Z° are large (80.2 GeV and 91.4 GeV, respectively), their exchange is suppressed compared to the photon exchange by a factor of $\frac{Q^4}{(Q^2+M^2_{Z,W})^2}$. The processes considered in the following will therefore be dominated by photons. Ignoring weak effects, the interaction is independent of whether electrons or positrons are considered. For this reason, only the terms "photon" and "electron" will be used for the remainder of the discussion.

2.2.1 Kinematic Variables

The processes depicted in Figure 2.3 at a given center-of-mass energy $\sqrt{s}$ can be described by any two of the following three Lorentz-invariant variables:

$$Q^2 = -q^2 = -(k-k')^2 \tag{2.6}$$

$$x = \frac{Q^2}{2p\cdot q} \tag{2.7}$$

$$y = \frac{p\cdot q}{p\cdot k}. \tag{2.8}$$

Q^2 is the negative square of the momentum transfer at the electron vertex and gives the virtuality of the exchanged photon. Q^2 sets the scale for the interaction between the γ^* and the constituents of the proton. In the rest frame of the proton, y corresponds to the fractional energy transfer from the electron to the proton. The variable x (often called "Bjorken"-x) is a measure of the fraction of the proton momentum carried by the struck quark.

If $Q^2 \gg M^2$, with M being the mass of the proton, the wavelength of the virtual

photon is given by

$$\lambda = \frac{h}{q} = \frac{hc}{\sqrt{\nu^2 + Q^2}} \simeq \frac{2Mx}{Q^2} \tag{2.9}$$

with $\nu = \frac{q \cdot p}{M}$ being the photon energy in the proton rest frame. For a given x, the wavelength is proportional to the inverse of Q^2. Increasing Q^2 probes therefore smaller and smaller distances of the proton structure. Throughout the rest of this thesis, natural units will be used: $\hbar = c = 1$.

2.2.2 Parton Model

In the approximation of single boson exchange, the cross section of lepton-hadron scattering can be factorized considering the interaction at the lepton vertex and at the hadron vertex separately. The emission of the virtual photon can be calculated exactly from QED, while the hadronic interaction is parameterized in terms of structure functions describing how the target is "seen" by the virtual photon. Neglecting the proton mass, the cross section can then be written as [14]

$$\begin{aligned} \frac{d\sigma(e^{\pm}p \to e^{\pm}X)}{dx\,dQ^2} &= \frac{4\pi\alpha^2}{x\,Q^4}\left[\left(1 - y + \frac{y^2}{2}\right) F_2(x,Q^2) - \frac{y^2}{2} F_L(x,Q^2)\right. \\ &\quad \left. \mp \left(y - \frac{y^2}{2}\right) x F_3(x,Q^2)\right] \end{aligned} \tag{2.10}$$

where F_i denotes the structure functions. F_L is related to the coupling of longitudinally polarized photons to the quarks alone, while F_2 has contributions from transverse as well as longitudinally polarized photons. For both these structure functions parity is conserved. F_3 results from the weak interaction and therefore violates parity.

Using leptons as probes of the proton structure function, only the electrically charged constituents of the proton are picked out. The Quark Parton Model (QPM) gives a description of how the partons form hadrons and therefore the proton. According to the parton model of Feynman [6], the hadrons, like the proton, consist of free spin-$\frac{1}{2}$ point-like constituents, called partons. The cross section of inelastic ep scattering is then given by the sum of quasi-elastic electron-quark scattering cross sections

$$\frac{d\sigma}{dQ^2} = \frac{4\pi\alpha^2 e_i^2}{xQ^4}(1 - y + \frac{y^2}{2}). \tag{2.11}$$

The cross section in ep scattering can then be obtained by summing over all quarks of type i weighted by the probability of finding the quark i carrying a fraction x of the proton momentum:

$$\frac{d\sigma}{dx} = \sum_i e_i^2 f_i(x) \frac{d\sigma}{dQ^2} \tag{2.12}$$

with e_i being the charge of the quark q_i. The parton densities $f_i(x)$ are related to the structure function 2.10 of the proton by

$$F_2(x) = \sum_i e_i^2 f_i(x) \qquad \text{and} \qquad F_L = 0. \tag{2.13}$$

In the high-energy limit, where $Q^2, \nu \to \infty$, the structure functions obey a scaling law [15] and depend only on the dimensionless variable x.

Bjorken scaling implies that the virtual photon scatters off *point-like* constituents, because otherwise the dimensionless structure functions would depend on the ratio Q/Q_0, with $1/Q_0$ being some length scale characterizing the size of the constituents.

The partons were identified as the quarks proposed by Gell-Mann [16] and Zweig [17] earlier. The postulated number of three valence quarks in the proton (uud) and the neutron (ddu) was confirmed using the Gross-Llewellyn-Smith sum rule [18].

This naive parton model was modified by QCD. Quarks not only interact through gluons, but can also radiate them in a QCD Compton process. Radiated gluons in turn can split into $q\bar{q}$ pairs (*sea quarks*). The gluon radiation gives transverse momentum to the quark in the infinite momentum frame, in which the proton is moving very fast. In the naive QPM, the transverse momentum of the quarks is 0 and helicity conservation requires that the quarks can couple only to transverse polarized photons. In QCD, they can also couple to longitudinally polarized photons causing F_L to be non-zero. The parton densities $f_i(x)$ become a function of Q^2 and give the probability of finding the parton i carrying a momentum fraction x, when probed with a photon of virtuality Q^2:

$$f_i(x) \to f_i(x, Q^2). \tag{2.14}$$

Also, the structure function depends on Q^2 and therefore breaks the scaling law of the naive parton model.

A first indication of the existence of gluons was found when the momentum sum of all charged constituents of the proton was measured to be $\simeq 0.5$ [19], implying that part of the proton momentum is carried by neutral constituents. If the proton consisted only of charged quarks, the sum of the momenta would be:

$$\int_0^1 x \sum_i f_i(x) = 1. \tag{2.15}$$

Direct evidence of the existence of the gluon was found at DESY when three-jet events were observed in e^+e^- annihilation [20].

2.2.3 Evolution Equation

Due to non-perturbative contributions, the structure functions cannot be calculated from QCD. However, the evolution of the structure functions with Q^2 is

dominantly a perturbative effect and predictions of the Q^2 evolution can therefore be based on QCD calculations and provide an excellent test of QCD. The Q^2 evolution of the quark $q_i(x)$ and gluon $g(x)$ distributions in pQCD is governed by the Dokshitzer-Gribov-Lipatov-Altarelli-Parisi (DGLAP) equation [21] [22], which in leading order is given by:

$$\begin{aligned}
\frac{dq_i(x,Q^2)}{d\ln Q^2} &= \frac{\alpha_S(Q^2)}{2\pi}\int_x^1 \frac{dy}{y}\left[P_{qq}\left(\frac{x}{y}\right)q_i(y,Q^2) + P_{qg}\left(\frac{x}{y}\right)g(y,Q^2)\right] \\
\frac{dg(x,Q^2)}{d\ln Q^2} &= \frac{\alpha_S(Q^2)}{2\pi}\int_x^1 \frac{dy}{y}\left[\sum_j P_{gq}\left(\frac{x}{y}\right)q_j(y,Q^2) + P_{gg}\left(\frac{x}{y}\right)g(y,Q^2)\right] \quad (2.16)
\end{aligned}$$

At high enough Q^2, partons can split to form additional partons or additional partons can be created by radiation. The rate at which these additional partons are created is described by the *parton splitting functions* P_{ij}. They represent the probability of a parton j emitting a parton i with momentum fraction z of the parent parton when the scale changes by $d\log Q^2$. The splitting functions cover four cases: a quark emits a gluon (P_{qg}) or a quark (P_{qq}) and a gluon emits a gluon (P_{gg}) or a quark (P_{gq}). These splitting functions can be calculated in pQCD and are given to first order by:

$$\begin{aligned}
P_{qq}(z) &= \frac{4}{3}\frac{1+z^2}{1-z} && (2.17)\\
P_{qg}(z) &= \frac{1}{2}\left[z^2+(1-z)^2\right] && (2.18)\\
P_{gq}(z) &= \frac{4}{3}\frac{1+(1-z)^2}{z} && (2.19)\\
P_{gg}(z) &= 6\left[\frac{z}{1-z}+\frac{1-z}{z}+z(1-z)\right]. && (2.20)
\end{aligned}$$

If the parton distribution function $f_i(x,Q_0^2)$ is measured over a range from x up to 1 at a fixed scale Q_0^2, then f_i can be predicted for any $Q^2 > Q_0^2$ within this range of x. With only the evolution of the parton densities accessible via pQCD but not the densities themselves, they need to be measured and parameterized to describe the data. Many parameterization are available [23] [24] [25].

Figure 2.4 shows how well the DGLAP equation describes the evolution of the structure functions (their slope) measured at HERA [26] [27] [28] and fixed-target experiments.

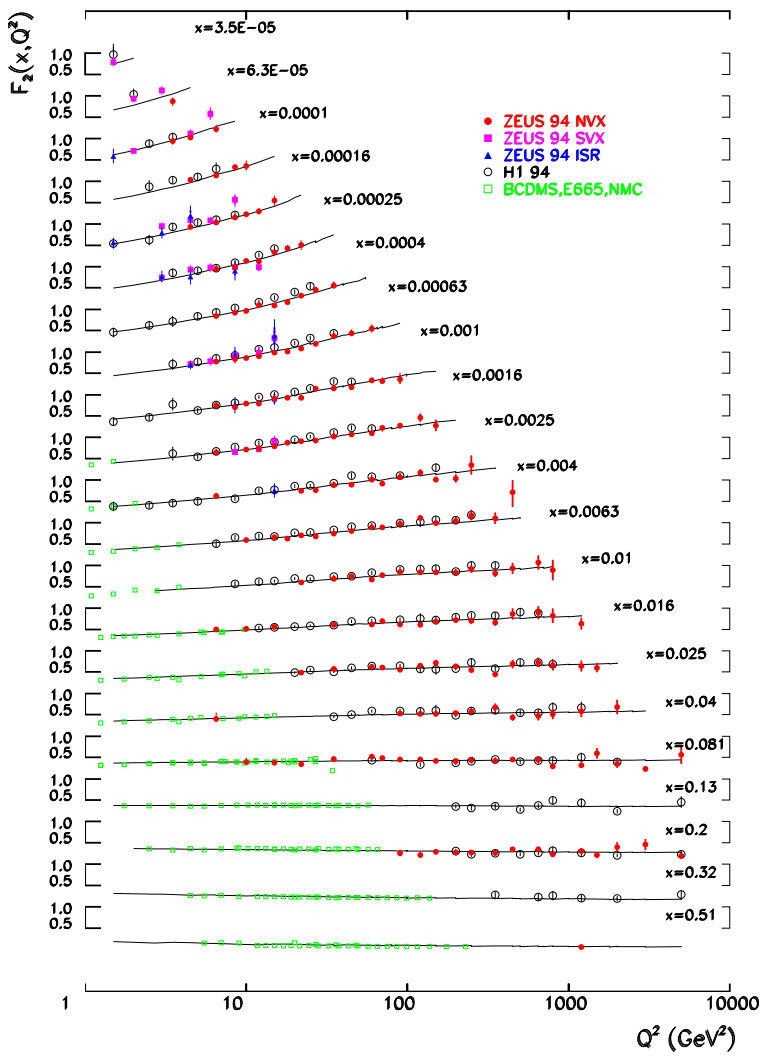

Figure 2.4: Measurements of the proton structure function F_2 as a function of Q^2 from ZEUS, H1, and fixed-target experiments. The predictions from the DGLAP evolution equations (equation 2.16) (line) is in excellent agreement with the data.

2.3 Diffraction

A special class of events has been recorded in $p\bar{p} \to pX$ scattering, in which the proton is detected at large values of rapidity[1] and a gap in rapidity between the final proton and the final state X is observed [29] [30] [31] [32] [33] [34]. The process was viewed in analogy to optical diffraction in the sense, that the proton diffracts around the black sphere of the $\bar{p}$ breaking it up. The outgoing proton is scattered at small angles and retains most of its initial energy. An equivalent class of events was observed in DIS at HERA [35] [36].

Diffractive events are usually selected in two ways: select events with a rapidity gap between the beam pipe (where the proton is normally lost) and the first hadronic activity, or record the diffractively scattered proton in a specially designed detector like the ZEUS Leading Proton Spectrometer (Chapter 4). In addition, the M_X distribution can be used to separate the diffractive part from the DIS peak [37].

Diffraction is most commonly ascribed to a colorless exchange between the virtual photon and the proton. The exchanged "object" is called a *Pomeron* ($\mathbb{P}$). Figure 2.5 illustrates a diffractive event.

In addition to the variables defined in Section 2.2.1, the following quantities are useful when describing diffractive events:

$$x_L = \frac{E'_p}{E_p} \tag{2.21}$$

$$x_{I\!P} = \frac{M_X^2 + Q^2 - t}{Q^2 + W^2 + m_p^2} \simeq 1 - x_L \tag{2.22}$$

$$\beta = \frac{x}{x_{I\!P}} \simeq \frac{Q^2}{Q^2 + M_X^2}. \tag{2.23}$$

Here, M_X defines the invariant mass of the hadronic system X and t is the momentum transfer at the proton vertex and is typically small. W denotes the total energy of the γ^*-proton system. In the picture of diffraction mediated by the exchange of a $\mathbb{P}$, $x_{I\!P}$ gives the fraction of the proton momentum carried by the $\mathbb{P}$. If the $\mathbb{P}$ is viewed as a hadronic object with a partonic substructure, the variable β is equivalent to x in the proton case and gives the momentum fraction of the $\mathbb{P}$ carried by the struck quark in the diffractive scattering process. The cross section for diffractive scattering can then be written in terms of a diffractive structure function $F_2^{D(4)}$:

$$\frac{d^4\sigma}{d\beta dQ^2 dx_{I\!P} dt} = \frac{2\pi\alpha^2}{\beta Q^2}\left(1 + (1-y)^2\right) F_2^{D(4)}(\beta, Q^2, x_{I\!P}, t), \tag{2.24}$$

neglecting the longitudinal and parity violating contributions.

[1] The rapidity y is defined by $y = \frac{1}{2} ln(\frac{E+p_z}{E-p_z})$.

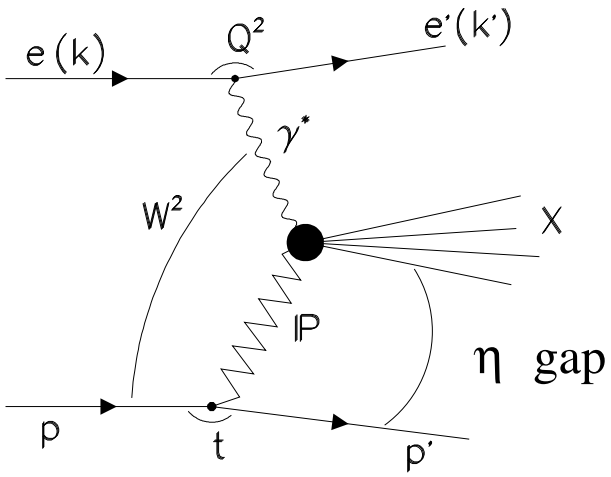

Figure 2.5: Feynman diagram of a diffractive event modeled by IP exchange.

So far, there is no model, which describes all aspects of diffractive DIS correctly. The difficulty arises from the fact that diffractive type of reactions combine soft physics, which are mainly described by phenomenological models, and hard physics, which can be calculated by perturbative QCD. In view of that, there are two main categories of models available, which are widely used today to compare measurements in diffractive physics with model predictions. In the following section, these main model types used to describe diffractive DIS are outlined.

2.4 The Exchange Picture

2.4.1 Regge Phenomenology

With pQCD failing to describe the soft effects in deep inelastic scattering correctly, Regge theory [38] [39] was used to make predictions about the hadron-hadron scattering cross section and about leading particle production as a function of total center-of-mass energy $\sqrt{s}$.

In the low-energy regime of $\sqrt{s} \lesssim 1$ GeV, the process $A\bar{C} \to \bar{B}D$ is dominated by the production of resonances. In Regge phenomenology, this type of reaction can be described by the exchange of the resonances as the fundamental particles of the field theory. One of the important features of these resonances, which are inherent to Regge theory, is the linear relation between the spin J and the square of the mass m. The correlation is described by the Regge trajectory:

$$\alpha(t) = \alpha(0) + \alpha' \cdot t \tag{2.25}$$

with $\alpha = J$ and $t = m^2$. $\alpha(0)$ is known as the *intercept* of the trajectory. According

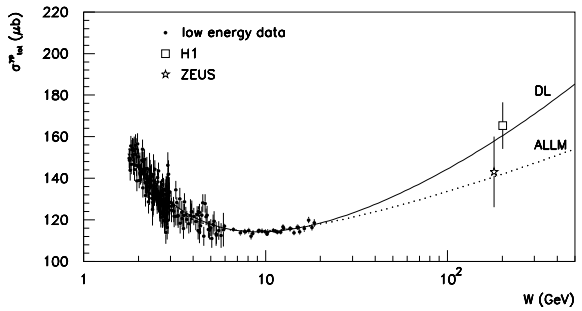

Figure 2.6: Total photoproduction cross section as a function of the center-of-mass energy W of the γp system. The lines correspond to Regge fits with $\alpha_{\mathbb{P}}(0) = 1.0808$ (solid) [40] and $\alpha_{\mathbb{P}}(0) = 1.045$ (dotted) [42]. The data are taken from [43] [44] [45].

to Regge theory, the behavior of the elastic hadron scattering amplitude is controlled by a sequence of Regge trajectories corresponding to an exchange of families of particles with different spin. The contribution of all particle trajectories to the considered process should be summed.

Using crossing symmetry, Regge phenomenology was successful in describing the crossed reaction $AB \to CD$. The square of the center-of-mass energy s, which describes the mass of the exchanged particle, is replaced by $t = (p_A - p_B)^2$, which is normally negative. Therefore, the exchanged particles are off-shell and the associated resonances cannot be observed directly in this channel. In the asymptotic limit of $s \to \infty$, the cross section behavior follows:

$$\frac{d\sigma}{dt} \propto \beta(t) \cdot s^{2(\alpha(t)-1)} \tag{2.26}$$

where β depends also on the colliding particles.

The elastic hadronic and quasielastic photoproduction cross section were found to fall initially with increasing center-of-mass energy, but then levels off and shows a slight rise (see Figure 2.6). The initial fall can be described by a Reggeon ($\mathbb{R}$) trajectory with intercept $\alpha_{\mathbb{R}}(0) = 0.55$ and slope $\alpha'_{\mathbb{R}} \simeq 1$ GeV^{-2}, while the rise can be fit by a Pomeron ($\mathbb{P}$) trajectory with $\alpha_{\mathbb{P}}(0) = 1.08$ and $\alpha'_{\mathbb{P}} \simeq 0.25$ GeV^{-2} [40]. The growth of the cross section was first predicted by Pomeranchuk [41], after whom the trajectory was named. The $\mathbb{R}$ trajectory corresponds to the exchange of mesons like the ρ, ω, a_2, or f_2. The $\mathbb{P}$ trajectory corresponds to the exchange of vacuum quantum numbers and is expected to dominate the elastic and diffractive cross section at high energies.

2.4.2 Partonic Pomeron

The Regge model of diffractive scattering can be extended to the case, where the $\mathbb{P}$ has a partonic substructure. The process then factorizes into a part which describes the emission of a $\mathbb{P}$ from the proton and a part which models its interaction with the virtual photon (or anti-proton in hadron-hadron collision). After the $\mathbb{P}$ is emitted, it should behave just like any other hadron, having a structure function and parton densities analogous to the proton. A possible partonic structure of the $\mathbb{P}$ was first identified by Ingelman and Schlein [46].

The diffractive structure function $F_2^{D(4)}$ (Equation 2.24) then factorizes into the flux $f_{p,\mathbb{P}}$ of Pomerons out of the proton and the structure function $F_2^{\mathbb{P}}$ of the $\mathbb{P}$:

$$F_2^{D(4)}(\beta, Q^2; x_{_{IP}}, t) = f_{p,\mathbb{P}}(x_{_{IP}}, t)\, F_2^{\mathbb{P}}(\beta, Q^2). \tag{2.27}$$

Given factorization at the proton vertex, the $\mathbb{P}$ flux $f_{p,\mathbb{P}}$ is assumed to be universal and can be extracted from hadron-hadron scattering data. Its functional form contains the $\mathbb{P}$ trajectory encountered in Section 2.4.1. The intercept was found to vary slightly with Q^2 [47], and therefore indicates that the simple factorization of Equation 2.27 is broken.

The structure function $F_2^{\mathbb{P}}$ of the $\mathbb{P}$ can be interpreted in terms of quark and gluon distributions analogous to the proton structure function of Equation 2.10. An important feature of this kind of $\mathbb{P}$ model is that after the scattering, a remnant of the $\mathbb{P}$ should remain. However, such a remnant has not be observed so far. With increasing $x_{_{IP}}$, contributions from $\mathbb{R}$ exchange might become important. They can be included in the diffractive structure function by adding a $\mathbb{R}$ term with flux factor and $\mathbb{R}$ structure function to Equation 2.27.

For a more detailed discussion of the partonic $\mathbb{P}$, see Section 5.1.2, where this type of model is discussed in the context of the RAPGAP MC generator.

2.5 QCD Pomeron - Photon Dissociation

The deep inelastic scattering process can be visualized in the rest frame of the proton as the fluctuation of the virtual photon into a $q\bar{q}$ pair, which interacts with the proton [49] [50]. The final state in diffractive DIS in this view is very simple and just contains a $q\bar{q}$ pair and the diffractively scattered proton (Figure 2.7a).

One of the quarks will have a large longitudinal momentum, so that an aligned jet configuration can be expected, which is well understood in QCD [51] [52] [53]. The quarks interact with the proton by the color singlet exchange of a gluonic system.

Nikolaev and Zakharov [54] showed that the β distribution of the aligned quark model can be derived from pQCD for the exchange of two gluons to be

$$F_{q\bar{q}}^T \propto \beta(1-\beta) \tag{2.28}$$

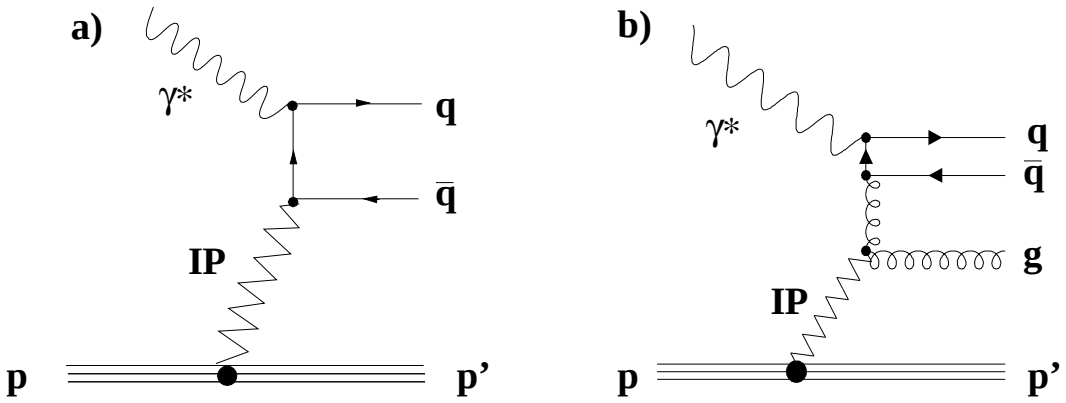

Figure 2.7: Feynman diagrams for the fluctuation of the virtual photon into a) $q\bar{q}$ pair and b) subsequent gluon radiation into $q\bar{q}g$. Both are coupled to the scattered proton by two-gluon exchange indicated as a $\mathbb{P}$ exchange.

(first derived by Donnachie-Landshoff [40]) while the production of a $q\bar{q}g$ final state (Figure 2.7b) from longitudinal polarized photons was found to be of leading twist with a β dependence of

$$F^L_{q\bar{q}g} \propto (1-\beta)^\gamma \tag{2.29}$$

with $\gamma = 2$. Finally, the contribution of $q\bar{q}$ pairs from longitudinal photons is of higher twist and the β dependence is [55]:

$$F^L_{q\bar{q}} \propto \beta^3(1-\beta)^2. \tag{2.30}$$

In [55], the exponent γ of Equation 2.29 was determined to be $\gamma = 3$. The exponent $\gamma = 2$ was determined in [54] from the approximate behavior of the structure function at small β, while the asymptotic behavior for $\beta \to 1$ was used in [55] (after integration over the momentum fraction carried by the gluon) and gives the large value of $\gamma = 3$.

In all models based on pQCD, the dependence on $x_{I\!P}$ is given by the square of the gluon density of the proton.

Several models are based on this frame work and are discussed in detail in Sections 5.1.3 through 5.1.6.

Chapter 3

The ZEUS Detector at HERA

3.1 The HERA Electron-Proton Collider

The Hadron Elektron Ring Anlage (HERA) [59] in Hamburg, Germany, is a lepton proton collider designed to collide protons with an energy of 820 GeV with electrons or positrons with an energy of 30 GeV, yielding a center-of-mass energy of $\sqrt{s} = 314$ GeV. Two separate storage rings for electrons[1] and protons are placed in a 6.34 km long tunnel 10 to 25 meters under ground. The beams are brought into collision at zero degree crossing angle at four interaction points. The two main experiments, H1 and ZEUS, are located in the north and south hall, respectively. The remaining two halls are used by experiments which use the electron beam (HERMES) or the proton beam (HERA-B) only. HERMES is designed to study the spin structure of the nucleons using the scattering of longitudinally polarized photons off polarized gas targets. HERA-B is designed to investigate CP violation in the $B^0\bar{B}^0$ system, using a wire target to produce B-mesons in the proton beam halo.

Figure 3.1 shows a schematic layout of the HERA accelerator complex.

Hydrogen ions serve as the proton source. The protons are accelerated up to 50 MeV in a linear accelerator. These protons are then injected in the DESY III accelerator ring, which is filled with up to eleven proton bunches. The bunches in DESY III already have the same bunch spacing as HERA, namely 96 ns, and are accelerated up to 7.5 GeV. Then, the protons are transferred to PETRA (Positron-Electron Tandem Ring Anlage), where seventy bunches are accumulated and accelerated up to 40 GeV, and then transferred to HERA. This is done until HERA is filled with up to 210 proton bunches. In HERA, the protons are accelerated up to their final energy[2] of 820 GeV with a beam life time of several days.

[1] Both electrons and positrons can be and were used in the HERA ring. In the following, "electron" is used as a generic name for the colliding beam lepton.

[2] In the 1998/99 running period, the proton energy in HERA was increased to 920 GeV.

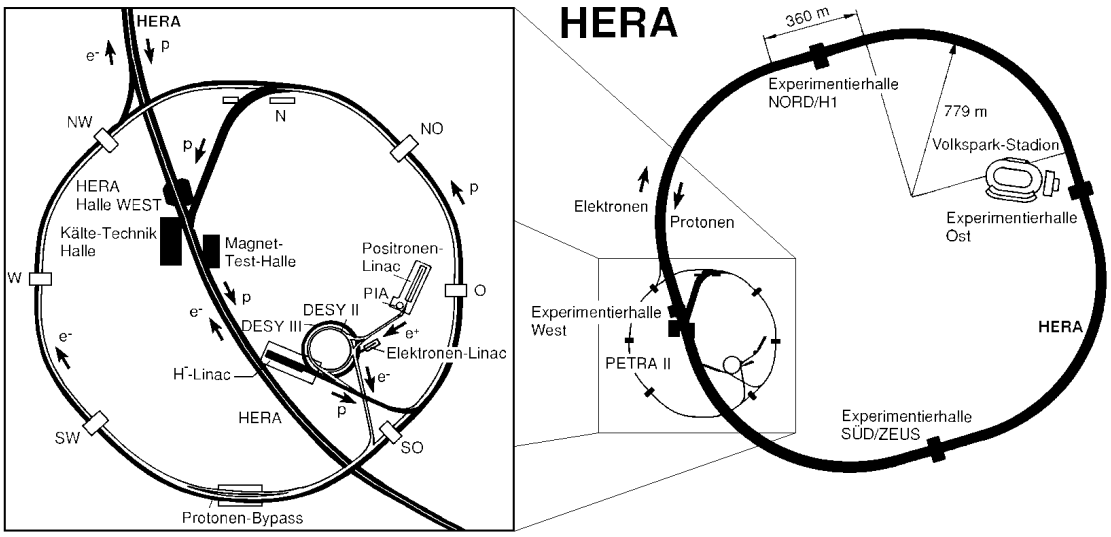

Figure 3.1: HERA collider with the four experimental halls and the preaccelerator system.

Electrons are injected into the LINAC I and then passed onto LINAC II, where they are accelerated to 220 MeV and 450 MeV, respectively. In the next step, the positron intensity accumulator (PIA) is filled with a single bunch with an electron current up to 60 mA. The bunch is then transferred to DESY II and accelerated up to 7.5 GeV. When passing the bunch to PETRA II, it is stretched, so that seventy bunches with 96 ns spacing are obtained. After accelerating the electrons to 14 GeV, they are transferred to HERA. HERA is filled with up to 210 bunches and the electrons are accelerated to 27.5 GeV with a life time of about 8 hours (for positrons). Under standard operation, HERA is not filled with all bunches. Satellite bunches (unpaired bunches) can be used to estimate beam related background rates. Empty bunches allow an estimation of background rates due to cosmic rays. In the 1997 data taking period, HERA operated with an average of 176 ep bunches, 20 electron, and 5 proton bunches.

Some HERA design parameters [60] and the machine performance during the 1997 data taking period are summarized in Table 3.1.

HERA was commissioned in 1991 and first ep interactions were observed and recorded in H1 and ZEUS during spring 1992. Since these first collisions in 1992, the integrated luminosity delivered by HERA has been continuously increased as can be seen in Figure 3.2. In 1997, HERA delivered 36.4 pb^{-1} of which ZEUS gated 27.7 pb^{-1} with all main components in good condition. The analysis presented in

HERA parameters	Design values		1997	
	e^-	p	e^+	p
Energy (GeV)	30	820	27.5	820
Instantaneous luminosity ($cm^{-2}s^{-1}$)	$1.7 \cdot 10^{31}$		$1.1 \cdot 10^{31}$	
Specific luminosity ($cm^{-2}s^{-1}(mA)^{-2}$)	$3.9 \cdot 10^{29}$		$6.0 \cdot 10^{29}$	
Integrated luminosity (pb^{-1})	30		36.35	
Magnetic field (T)	0.165	4.65	-	
Current(mA)	58	163	30	75
Number of bunches	210		176+20	176+5
Beam σ_x (mm) at IP	0.30	0.27	0.27	0.18
Beam σ_y (mm) at IP	0.06	0.09	0.06	0.06
Beam σ_z (cm) at IP	0.8	11	0.8	11

Table 3.1: HERA design parameters and actual performance in 1997. The luminosity values are typical values (specific) and typical peak values (instantaneous) towards the end of the running period.

the thesis is based on this data set.

3.2 The ZEUS Detector

The ZEUS collaboration includes more than 450 physicists and an equal number of technicians from 51 institutes in 11 countries.

The ZEUS detector [61] covers almost the full solid angle (except for the beam holes) and is designed to study numerous aspects of lepton-hadron scattering, including the structure of the proton, photon, and Pomeron; the photoproduction of vector mesons and jets; the production of leading protons and neutrons; and more exotic phenomena like contact interactions and excited fermions to list an excerpt of the research topics currently under way in the ZEUS collaboration. The design incorporates the large forward-backward asymmetry of the ep final state resulting from the large difference in energy of the incoming proton and lepton giving a center-of-mass system, which moves in the direction of the proton beam relative to the lab frame. Since the construction and installation of the detector in the HERA south hall (see Figure 3.1) was finished at the beginning of 1992, several detector upgrades and additions have taken place to enlarge the physics scope of the experiment.

The ZEUS coordinate system is a right-handed orthogonal system with its origin (X = Y = Z = 0) at the nominal interaction point (IP). The Z-axis is given by the proton beam direction, the X-axis is pointing towards the center of the HERA ring,

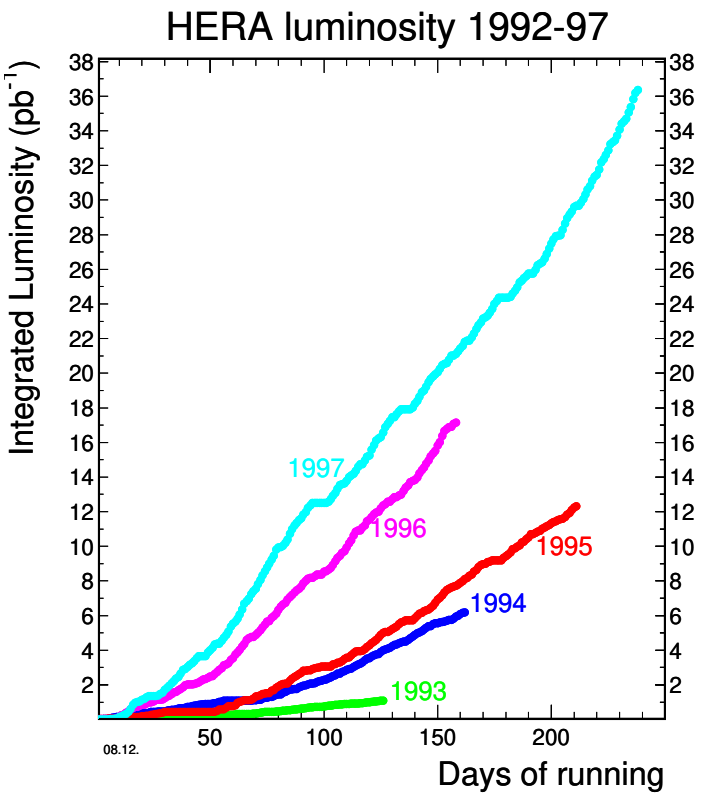

Figure 3.2: Integrated luminosity delivered by HERA during the data taking periods 1992 to 1997.

and the Y-axis is pointing upwards. This means that the polar angle (measured with respect to the positive Z-axis) of the proton and electron is 0° and 180°, respectively, and the azimuthal angle is measured with respect to the X-axis.

However, in this thesis, the "nominal proton beam" reference frame is usually used as a ZEUS coordinate system. In this frame, the design location of the proton beam defines the Z-axis. The difference between the standard ZEUS coordinate system and the nominal proton beam frame are negligible within the region of the central detector. But far away from the IP, the two coordinate systems are quite different, since the ZEUS Z-axis does not follow the bends of the proton beam due to the beam line optics.

Figures 3.3 and 3.4 show a cross sectional view of the layout of the ZEUS detector along and perpendicular to the beam direction.

The remaining part of this section will give a brief overview about the major detector components. A more complete description can be found in [61]. The parts

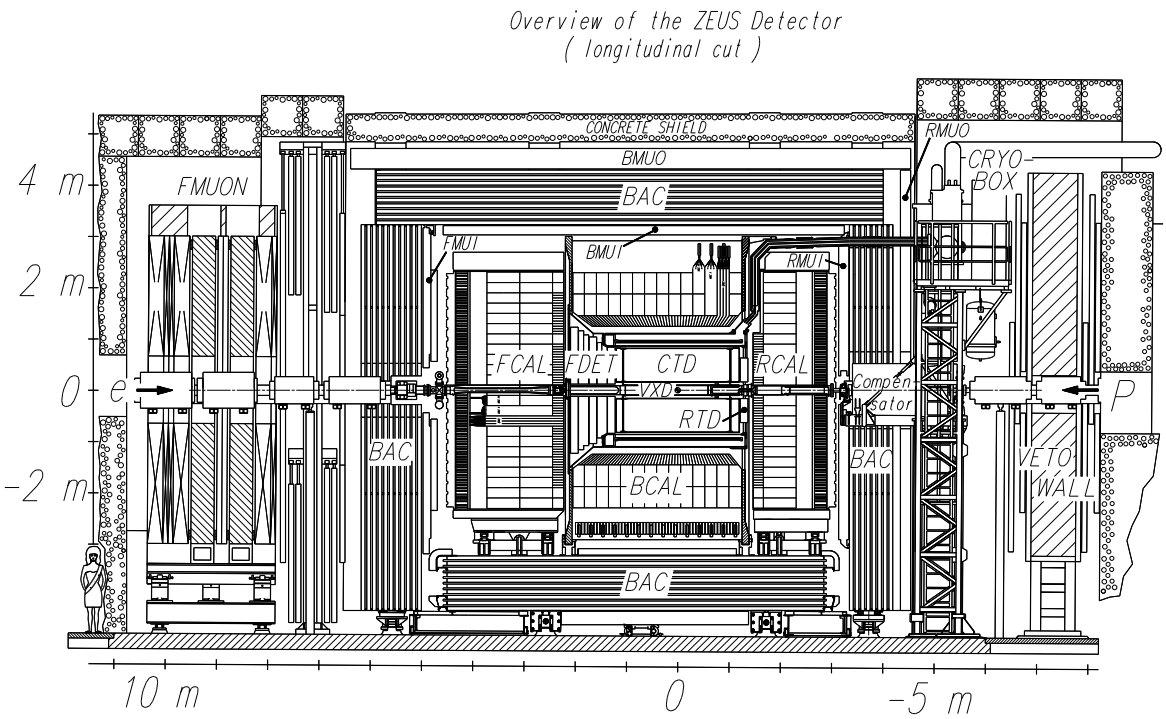

Figure 3.3: Cross sectional view of the ZEUS detector along the beam direction (x=0 plane) showing most of the central components.

of the detector which play a key role for this analysis will be presented in more detail in the following sections.

Two approaches are generally used in high-energy physics to detect particles in the final state: tracking detectors to determine the momentum and direction of charged particles from their path in a magnetic field and calorimeters to measure the energy of charged and neutral particles by stopping them and measuring the energy deposited in the calorimeter material. The ZEUS tracking system consists of the Central Tracking Detector (CTD) in the center of the main detector surrounding the interaction point. Additional tracking information and particle identification in the forward and rear direction is given by the Forward and Rear Tracking Detectors (FTD and RTD). The FTD has three sets of planar drift chambers with Transition Radiation Detectors (TRD) in between. The RTD consists of one planar chamber with three layers. The whole tracking system is enclosed by a superconducting

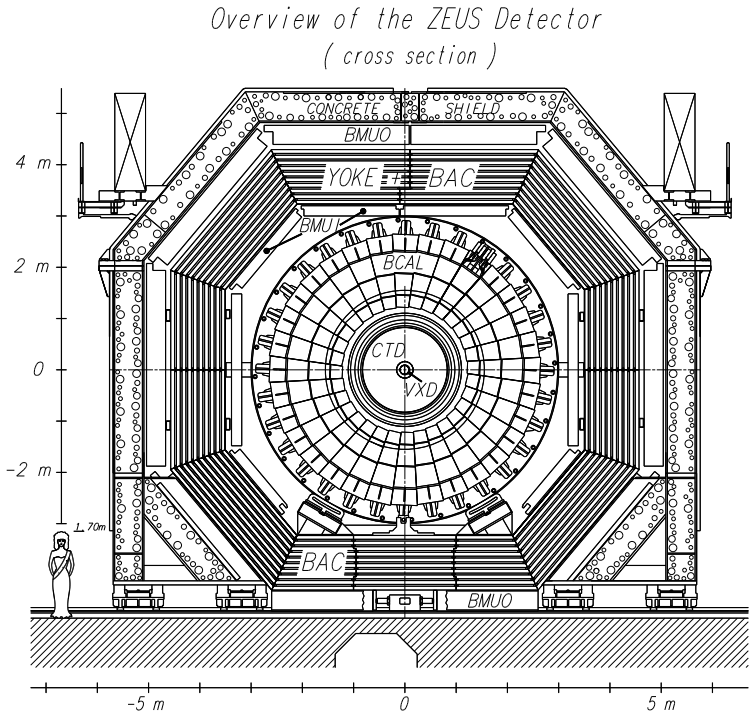

Figure 3.4: Cross sectional view of the ZEUS detector perpendicular to the beam direction showing most of the central components.

solenoid which provides an axial magnetic field of 1.43 T. The Vertex Detector (VXD) still shown in Figures 3.3 and 3.4 was removed in the winter shutdown 1995/96.

The tracking system is surrounded by a high resolution Uranium Calorimeter (UCAL), which is divided in three sections: the Forward Calorimeter (FCAL), the Rear Calorimeter (RCAL), and Barrel Calorimeter (BCAL) enclosing the central region. The Small Angle Rear Tracking Detector (SRTD) is mounted behind the RTD on the face of the RCAL covering an area of $68 \times 68\,\mathrm{cm}^2$ around the rear beam-pipe hole. In front of the RCAL and FCAL, Rear and Forward Presampler detectors (RPRES and FPRES) are installed, consisting of a single layer of scintillator plates. The main calorimeter UCAL is enclosed by muon identification chambers (FMUI,

BMUI, and RMUI) on the inner side of an iron yoke, which provides the return path for the magnetic field. The yoke also serves as an absorber for the Backing Calorimeter (BAC), which measures the energy leakage from late showering particles. Outside the yoke, the outer muon chambers (FMUON, BMUON, and RMUON) are installed within a toroidal magnetic field of 1.7 T.

Just behind the RCAL module, a small sampling calorimeter is installed near the beam pipe to explore the low Q^2 region. This Beam Pipe Calorimeter (BPC) is accompanied by a small Beam Pipe Tracker (BPT). An iron-scintillator Vetowall is located at $Z = -7.3$ m behind the main detector to reject beam related background. Further down the electron beam direction (negative Z-axis), three lead-scintillator electromagnetic calorimeters are located at $Z = -34$ m, $Z = -44$ m, and $Z = -107$ m to measure electrons from bremsstrahlung, photoproduction events, and photons from bremsstrahlung events used to determine the luminosity at ZEUS.

In the forward direction, the Proton Remnant Tagger (PRT), a lead-scintillator counter is installed at $Z = 5.1$ m around the beam pipe to obtain information about the hadronic final state in the range of pseudorapidity[3] $4.3 < \eta < 5.8$, for example a dissociating proton. Between about 20 m to 90 m in positive Z-direction the 6 stations of silicon microstrip detectors of the Leading Proton Spectrometer (LPS) are located to measure the very forward scattered, outgoing proton with small transverse momentum transfer (< 1 GeV). The Forward Neutron Calorimeter (FNC) is a lead-scintillator sandwich situated at $Z = 105$ m.

The short time spacing of the ep bunches at HERA of 96 ns results in a nominal beam crossing rate of about 10 MHz. To reduce the rate of detected events to the level of a few Hz at which the data can be written to tape, ZEUS uses a three-level trigger system.

3.3 The Central Tracking Detector (CTD)

The Central Tracking Detector (CTD) [62] measures with high precision the direction and momentum of charged particles and gives additional information for particle identification via the mean energy loss dE/dx of charged particles within the gas chamber volume of the CTD.

The CTD is a cylindrical drift chamber consisting of 72 layers organized in 9 superlayers. Its active volume has a length of 205 cm, with an inner radius of 18.2 cm and an outer radius of 79.4 cm. This gives a coverage of the polar angle of $15° < \theta < 164°$ (corresponding to $2.04 > \eta > -1.96$ in pseudorapidity) and a full coverage of the azimuthal angle. The chamber is filled with a mixture of argon, CO_2 and ethane. The superlayers alternate between those which have the wires orientated

[3]The pseudorapitidy is defined as $\eta = -ln(\tan\frac{\theta}{2})$ with θ being the polar angle associated with the hadronic final state.

parallel to the beam axis (axial superlayers carrying odd numbers) and those which have a 5° angle with the beam axis (stereo layers carrying even numbers) allowing the determination of the Z-position of the hit. The three inner axial superlayers are also instrumented with a Z-by-timing system to allow the measurement of the Z position from the time difference in the arrival time on both ends of the chamber. The spatial resolution of the CTD is about 230 μm in r-ϕ, corresponding to a momentum resolution of

$$\frac{\sigma(p)}{p} = 0.005 \cdot p \oplus 0.0016 \tag{3.1}$$

(p in GeV) for long tracks. The interaction vertex is measured on an event-by-event basis with a typical resolution along and transverse to the beam axis of 0.4 and 0.1 cm, respectively.

3.4 The Uranium Calorimeter (UCAL)

The ZEUS calorimeter (Figure 3.5) is subdivided into three parts: BCAL [63], FCAL, and RCAL [64]. The Barrel Calorimeter (BCAL) covers the polar angle θ from 36.7° to 129.1° (corresponding to $1.1 > \eta > -0.74$); the Forward Calorimeter (FCAL), the polar angle between 2.2° and 39.9° (corresponding to $4.0 > \eta > 1.0$); and the Rear Calorimeter (RCAL), the polar angle from 128.1° to 176.5° (corresponding to $-0.72 > \eta > -3.49$).

The UCAL is a sampling calorimeter consisting of alternating layers of 3.3 mm thick depleted uranium[4] as an absorber and 2.6 mm thick plastic scintillator plates[5]. The thickness of these materials was chosen so that the calorimeter provides compensation, i.e., the response of the calorimeter to electrons (e) and hadrons (h) of equal energies is the same ($e/h = 1.00 \pm 0.02$). This is important for the energy resolution of hadronic energy, since hadronic showers have a statistically fluctuating electromagnetic component. Under test beam conditions, the resolution of the calorimeter was measured to be

$$\frac{\sigma(E)}{E} = \frac{0.35}{\sqrt{E}} \tag{3.2}$$

for hadrons and

$$\frac{\sigma(E)}{E} = \frac{0.18}{\sqrt{E}} \tag{3.3}$$

for electrons with an energy of E in GeV.

The three sections of the calorimeter are divided into modules, which are orientated perpendicular to the beam axis in the BCAL and longitudinal to the beam

[4] An alloy of 98.4% U^{238}, 1.4% Nb, and $\leq$ 0.2% U^{235}.

[5] SCSN-38

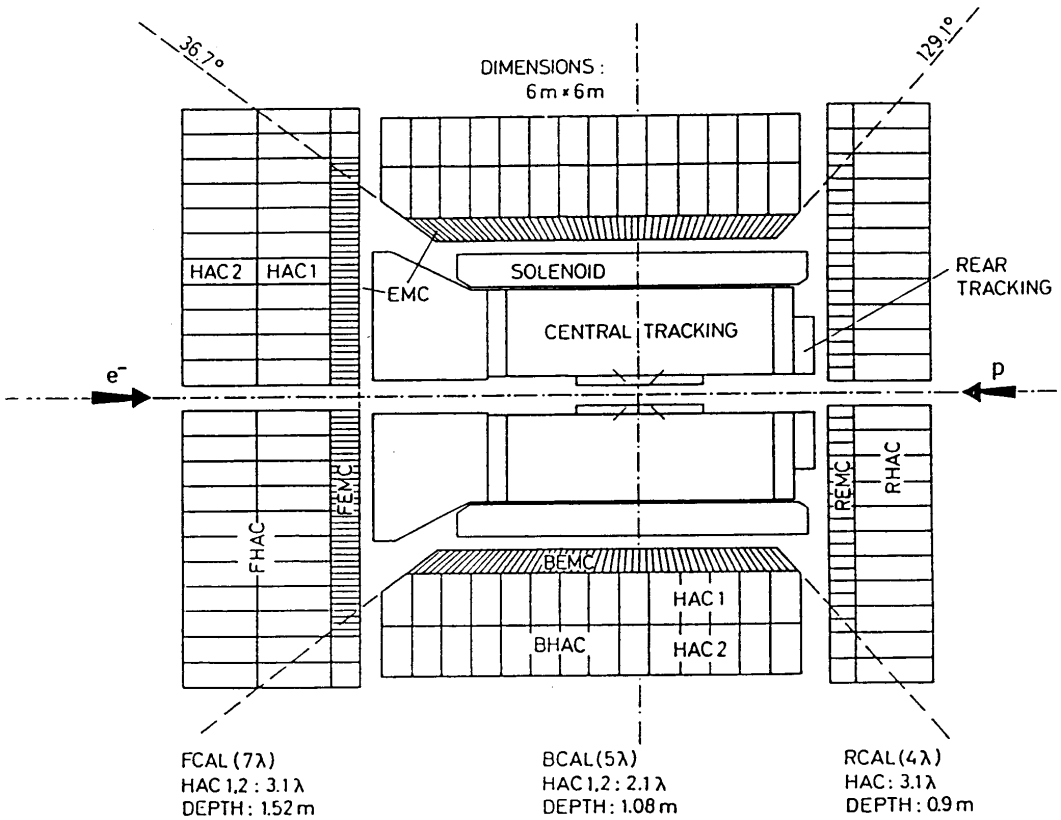

Figure 3.5: Cross sectional view of the ZEUS calorimeter along the beam direction.

axis for FCAL and RCAL. Each module is subdivided into towers of dimensions 20×20 cm^2. Each tower in turn has a longitudinal structure of one electromagnetic section (EMC) and two (one in RCAL) hadronic sections (HAC1, HAC2). Every EMC section consists of four 5×20 cm^2 cells (two 10×20 cm^2 in RCAL). Each cell of the calorimeter is read out on two sides by wavelength shifters, which are coupled to photomultiplier tubes (PMT). The energy corresponds to the sum of both PMTs and is therefore independent of the impact point of the particle in the cell. However, a comparison of both PMTs allows to determine a position reconstruction within a cell. The longitudinal depth of the UCAL is chosen, so that 90% of all recorded jets lose a minimum of 95% of their energy in the UCAL. Besides the energy measurement, the UCAL also gives very precise timing information with a resolution for a single cell of better than

$$\sigma(t) = \frac{1.5}{\sqrt{E}} \oplus 0.5\,\mathrm{ns} \tag{3.4}$$

for energy deposits over 3 GeV.

The large forward-backward asymmetry of the ep final state due to the different

energies of the incoming electron and proton is reflected in the forward-backward asymmetry of the calorimeter. The FCAL has a depth of 7 absorption lengths λ, while for the RCAL, 4λ are sufficient.

The natural radioactivity of U^{238} provides a stable reference signal for a channel-by-channel calibration of the calorimeter. The precision of this calibration is good to 1%.

3.5 The Small Angle Rear Tracking Detector (SRTD)

The Small Angle Rear Tracking Detector (SRTD) [65] is a scintillator strip detector located at $Z = -148$ cm on the face of the RCAL covering 68×68 cm^2 around the rear beam hole. The SRTD consists of two planes of orthogonally placed (x, y) strips with a 1 cm pitch. Each plane is subdivided into four quadrants. The strips provide a position and pulse height measurement for charged particles via an optical fiber photomultiplier readout.

The SRTD supplies additional tracking (to the CTD) to measure the scattered electron near the rear beam pipe more precise than with the RCAL alone. Also, the SRTD is used to correct for energy losses due to inactive material (mostly cables and tracking detector end-plates) in this detector region. Electrons preshower in these materials and the energy deposit of the preshowers in the SRTD can be used to correct for these energy losses. The SRTD serves as a presampler in this case.

3.6 The ZEUS Trigger and Data Acquisition System

The short bunch crossing time in HERA of 96 ns, which corresponds to a rate of about 10 MHz, requires an advanced trigger and data acquisition system. Out of a total interaction rate of about $10 - 100$ kHz, which is dominated by interactions of the proton with residual beam gas, the true ep interaction rate is only a few 10 Hz. Other sources for background are electron beam gas interactions and cosmic ray events. The ZEUS three-level trigger system [66], which is sketched in Figure 3.6, selects physics events efficiently and reduces the total rate of accepted events to a few Hz, which can then be handled by the data acquisition system.

Each detector component has its own First Level Trigger (FLT), which is implemented as a hardware trigger and is designed to reduce the event rate to below 1 kHz. The data are stored in a pipeline and the FLT makes its decision within 2 μs after the bunch crossing. The information is then passed to the Global First Level

Trigger (GFLT), which issues a global trigger decision based on logical combination of the component's trigger input. The decision by the GFLT of whether an event is accepted or rejected is returned to the component within 4.4 μs. The GFLT is designed to reduce the trigger rate below 1 kHz.

If an event is accepted by the GFLT, the data are transferred to the Second Level Trigger (SLT). The SLT is designed to reduce the input rate to below 100 Hz. Each component has its own SLT, which is software based and runs on a network of transputers. The decisions of the local SLTs are passed to the Global Second Level Trigger (GSLT) [67] and are combined to issue a final decision.

If an event is accepted by the GSLT, the data from each component are sent to the Eventbuilder, which produces an event structure to combine all data in one data set. The data from the Eventbuilder are then accessible to the Third Level Trigger (TLT) software. The TLT finally reduces the input rate to a few Hz of ep physics events. Events which are accepted by the TLT are written to tape.

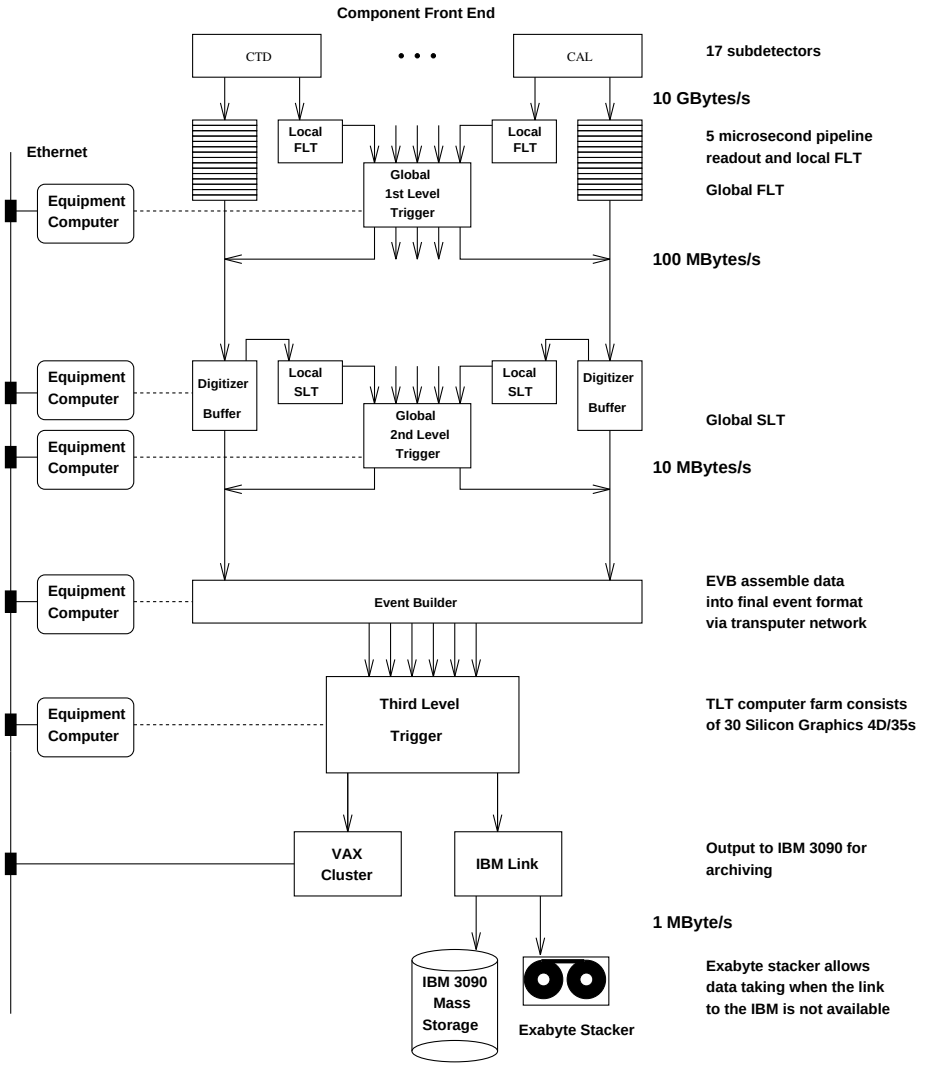

Figure 3.6: Schematic diagram of the ZEUS trigger and data acquisition system.

Chapter 4

The Leading Proton Spectrometer (LPS)

The Leading Proton Spectrometer (LPS) is a single arm spectrometer positioned along the outgoing proton beam between $Z \simeq 20$ m and $Z \simeq 90$ m. It is designed to detect protons, which would otherwise escape through the beam pipe. To achieve this task, a spectrometer consisting of 6 stations of silicon-microstrip detectors was placed in the proton beam line using the beam optic magnets for particle deflection. In this chapter, the LPS hardware is described in detail as well as the LPS operation, which involves moving the detector stations out of the beam line during the refilling of HERA and luminosity tuning. To use the LPS data in a physics analysis, a careful alignment and reconstruction of the tracks is necessary which is reviewed at the end of this section.

4.1 LPS Hardware

4.1.1 Spectrometer Components

Figure 4.1 shows a compressed layout of the detector.

The beam line magnets serve as the optical elements with vertical and horizontal bends using mainly magnetic dipole fields plus focusing elements using quadrupole magnets. In the interaction region of ZEUS, the HERA accelerator uses a long, straight section for the beam line with normal conducting magnets. Outside that region, the proton and electron beams need to be separated and the protons elevated so that the proton and electron ring can be stacked through the HERA tunnel. The extraction and elevation is done with two strong bending magnets, which subdivide the six stations of the LPS into two independent spectrometers: S1 to S3, and S4 to S6, respectively. S1 to S3 take advantage of the horizontal electron separation

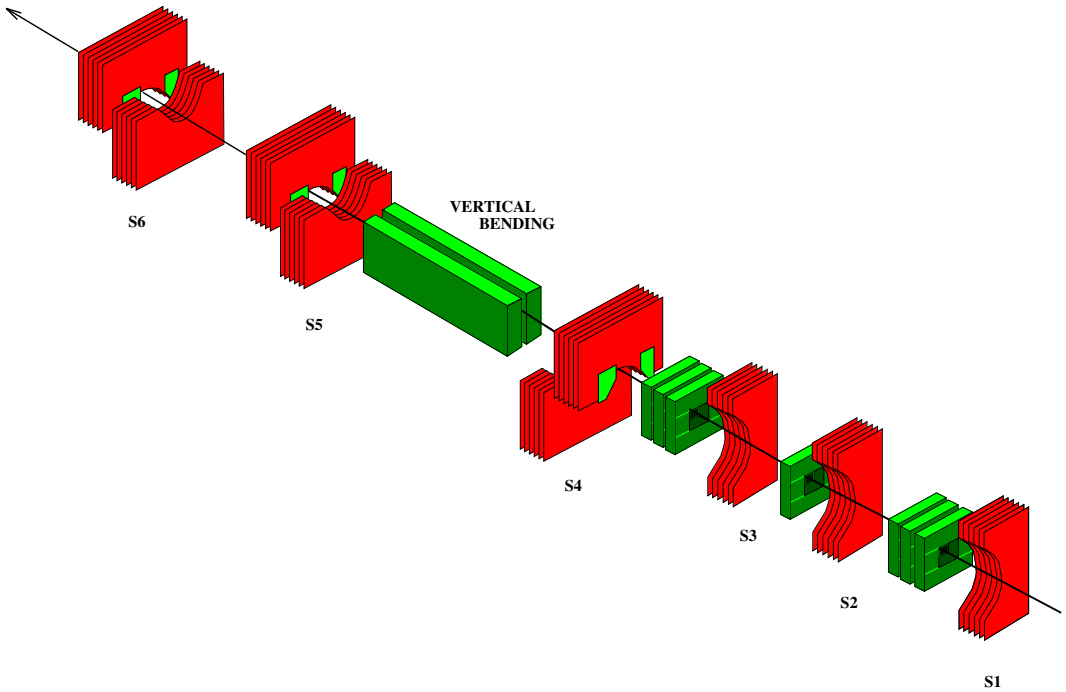

Figure 4.1: Layout of the LPS along the outgoing proton direction with some of the beam optic elements crucial for the LPS operation. The trapezoidal detectors on the upper pot on S4, S5, and S6 are trigger planes. The distances between the single stations are not drawn to scale.

magnet in front of S1 (not shown in figure 4.2), while S4 to S6 use a long, vertical proton bend over about 15 m between S4 and S5. Located between S1 and S2, S2 and S3, and S3 and S4 are various quadrupole magnets, which add more fields and act as lenses. They focus in X while defocus in Y (or vice versa). Nominally, S1 to S3 were designed to measure protons with low momentum, while S4 to S6 handle the high momentum particles, but in practice also the first three stations contribute to the high momentum acceptance.

The first part of the spectrometer with the stations S1, S2, and S3 is located at $Z \simeq 24$ m, 41 m, and 44 m, respectively. These three stations are single pot stations which move horizontally (in the direction of positive X) to the beam. The stations S4, S5, S6 positioned at about 63 m, 82 m, and 90 m, respectively, form the second part. These stations have two pots each moving towards the beam from above (*up pot*) and below (*down pot*) the beam line. Each pot consists of six planes of silicon-microstrip detectors with orientations of the strips (2 planes each) of 0° (x view) and $\pm 45°$ (u and v view) to the direction of motion.

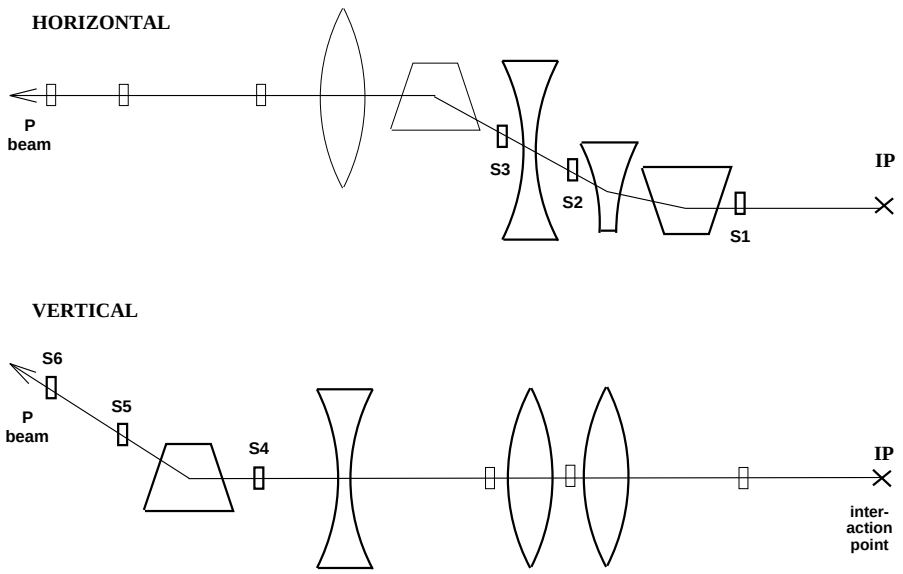

Figure 4.2: Sketch of the HERA proton beam optics providing the necessary magnetic fields for the LPS. The magnets operate analogously to optical elements and are drawn accordingly. The beam line advances from the top half (with S1, S2, and S3) to the bottom half (with S4, S5, and S6).

4.1.2 The Silicon-Microstrip Detectors

The Silicon-Microstrip Detectors for the LPS are made out of 300 μm thick, lightly doped n type silicon. Implanted in this material are p type strips with a pitch of 115 μm ($115/\sqrt{2}$ μm) for the 0° ($\pm$ 45°) planes ranging from 448 to 1024 in number, depending on the plane. The n type bulk and the p type strips form a diode junction. Just on top of the p implant, aluminum strips carry the signal and the leakage current to the front-end electronics, while a bias voltage (nominal 70 V) is applied to the backplane of the diode.

Figure 4.3 explains the functional principle of the silicon-microstrip detector. The bias voltage, which is applied to the backplane of the LPS detectors, removes all free charge carriers of the semiconductor material creating a *depleted* area in the detector starting at the *pn* junction on the strips (*reverse biasing* of the detector). If the depletion region reaches all the way to the backplane, the detector is fully depleted and the necessary bias voltage is called the *depletion voltage*. For highest efficiencies (fraction of charged particles passing through the detector for which a signal is recorded), the detector needs to be operated at or above the depletion voltage. However, even at lower bias voltages, the detector can still be operated satisfactory. Figure 4.3 shows a detector which is almost fully depleted leaving just

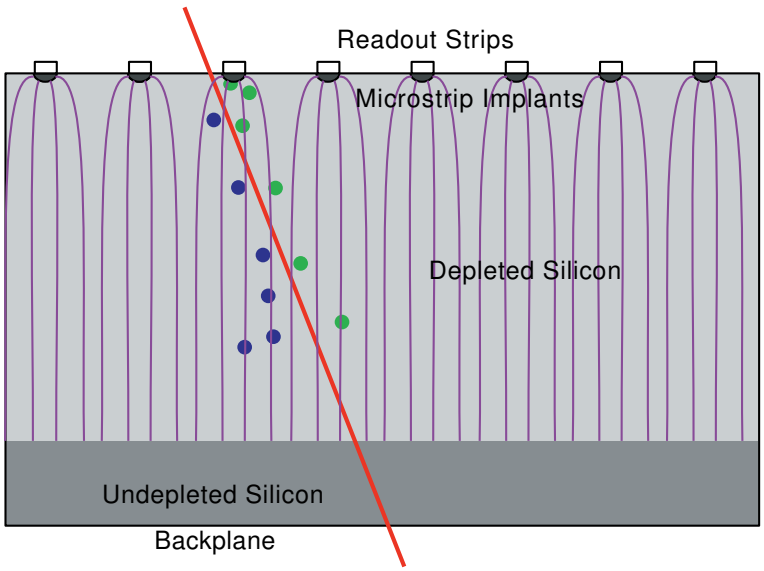

Figure 4.3: Functional principle of a silicon microstrip detector. A charged particle (solid line) passes through the depleted bulk material creating electron-hole pairs. These are separated by the electric field in the detector (indicated by the lines between implants and backplane) and travel to the implants and backplane, respectively. The signal is then recorded in the readout strip.

a small region at the backplane undepleted.

If a charged particle (solid line in Figure 4.3) is passing through the depleted material, it creates electron-hole pairs (dots around the line). These charge carriers are separated; the electrons travel to the backplane and the holes to the implants, respectively, along the electric field lines due to the bias voltage. The change in the electric field introduced by the traveling charges (holes) creates a signal in the readout strips which is carried to the input stages of the amplifiers. One ionizing particle produces typically 25000 electron-hole pairs of signal in a 300 μm detector.

In order to maximize the acceptance for proton tracks, the detectors had to be positioned as close to the proton beam in HERA as possible. To achieve this, the detectors were designed with elliptical cutouts with dimensions customized for each station to fit around a 10σ envelope around the proton beam.

A single pot was chosen to have six planes, two with $0°$, $+45°$ and $-45°$, to

- measure XY coordinates with a single pot,
- resolve ambiguities in the reconstructions of charged particles due to detector and electronic noise and photon hits,

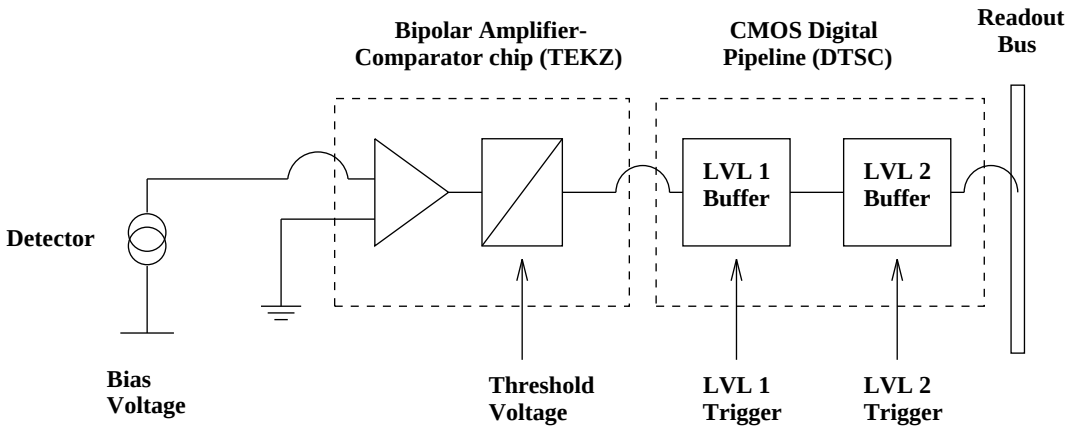

Figure 4.4: Schematic illustration of the binary readout system used by the LPS. The front-end electronics is composed of two custom designed chips: an analog amplifier-comparator chip (TEKZ), and a digital pipeline chip (DTSC).

- have redundancy in the measurement of XY coordinates within a single pot to prevent data loss in case of plane failures,
- improve resolution.

4.1.3 The Front-End Electronics

The LPS employs the binary readout scheme, which is schematically shown in Figure 4.4. In this scheme, the only information kept from the recorded signal on an individual strip of a detector is one bit, showing whether the strip was hit or not. This simplifies the analysis and reduces the cost for the readout system.

The front-end electronics consists of an analog chip with an amplifier and comparator (TEKZ chip) [68] and a digital storage chip (DTSC chip) [69]. The TEKZ amplifies the signal recorded on the readout chip, compares it to a threshold, and sends out the 1-bit information per channel to the DTSC. The DTSC stores the bits in a pipeline and makes it available to the ZEUS trigger system (see Section 3.6). Both chips were designed and produced with the high-radiation environment for operation in mind, which is given by the proximity to the proton beam, and a high flux of synchrotron radiation from the electron beam.

Silicon detectors, TEKZ, and DTSC are assembled on a custom hybrid printed circuit board with surface mount components, filters, temperature sensors, and cooling pipes to form one plane of a pot. Depending on the geometry, a plane can have between 7 and 16 pairs of TEKZ and DTSC chips, corresponding to 448 and 1024

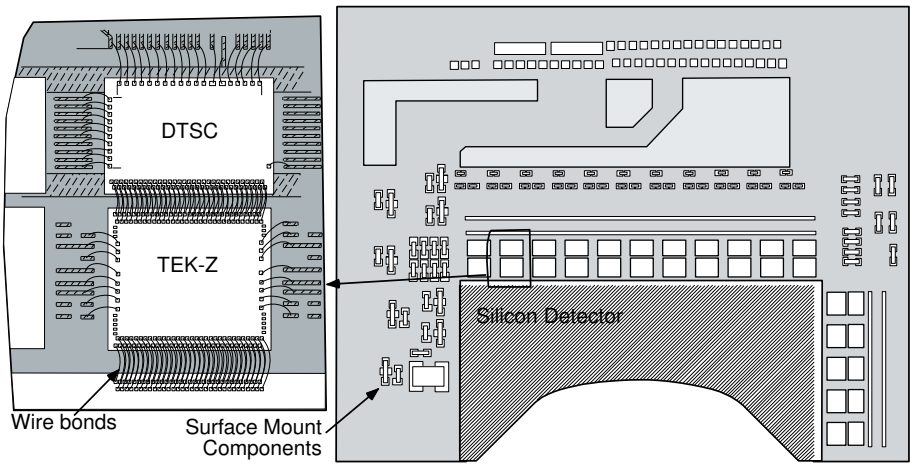

Figure 4.5: Layout of an LPS hybrid for Station S4. Magnified on the left-hand side is a pair of TEKZ and DTSC connected by wire bonds. The detector has 45° strips and an elliptical cutout to accommodate the proton beam profile.

channels, respectively. An example for such a plane is shown in Figure 4.5 for a S4 detector with 45° strips and the elliptical cutout for the beam profile.

TEKZ Amplifier-Comparator Chip The TEKZ chip [68] combines 64 channels consisting of a three-stage amplifier followed by a 1-bit analog to digital converter, the comparator. Figure 4.6 shows a simplified schematic of one TEKZ channel. A small input capacitor of $\simeq$ 14 fF is connected to the input stage of the amplifier to allow testing and calibration of the amplifier and readout system. The comparator uses an external threshold signal common to all channels of the TEKZ to decide whether a signal is considered a hit or not and send the appropriate bit to its output stage.

Fast response in comparison to the bunch crossing time of HERA, low electronic noise, and power consumption were required for the amplifier chip of the LPS. The shaping time of the TEKZ is 30 ns with a noise level below 1000 e^- and a power consumption of less than 2 mW/channel. Since the LPS detectors are DC coupled devices (see Section 4.1.2), the front end electronics needs to be able to sink the leakage current from the detector. The TEKZ chip is able to sink up to 1 μA per channel and still detect a signal.

The Digital Time Slice Chip (DTSC) The Digital Time Slice Chip (DTSC) [69] stores the information received from the output stage of the TEKZ in its 64 channels. Figure 4.7 shows a rough schematic of the chip.

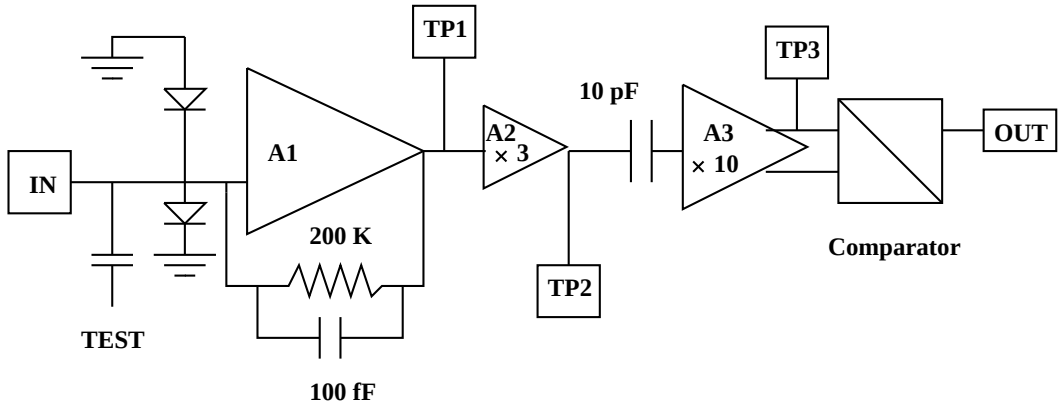

Figure 4.6: Simplified schematic of one channel of the TEKZ chip. Shown is the test input capacitor, the three-stage amplifier and the comparator.

At each bunch crossing, the comparator outputs are shifted into the level 1 buffer register. This buffer has 64 registers per channel and stores the information for 6 μs at a HERA clock rate of 10 MHz to wait for the trigger signal. The first level trigger causes the DTSC to copy the memory of the level 1 buffer to the level 2 buffer, which allows the data to be read out sequentially.

The Readout System The signals from the LPS front-end electronics have to be interfaced to the ZEUS data acquisition system outlined in Section 3.6. This is done via a VME bus using an OS/9 system. The schematics of the LPS readout system can be seen in Figure 4.8. The main components of the LPS readout chain are the Readout Controllers (ROC), the Fast Fan Outs (FFO), and the Serial Readout Controllers (SRC).

The ROC [70] interfaces between the ZEUS GFLT, the VME bus readout process, and the front-end electronics of the LPS. To achieve this task, the ROC contains a section of memory, which is organized in the same way as the front-end digital chips (DTSC) to incorporate flags and trigger information with the data from the detector.

The control signals from the ROC are transferred to the different LPS stations by the Fast Fan Out (FFO) [71]. One FFO can manage all six planes in one pot. However, it is equipped with two independent channels, so that two sets of three planes can be controlled separately. For redundancy, the three planes for one channel are chosen to have different strip orientation.

Finally, the SRC [72] transfers the data between the front-end electronics and the VME system. The ROC triggers the SRC, when an event can be read out and the SRC operates autonomously until the entire event is transferred. The total transfer

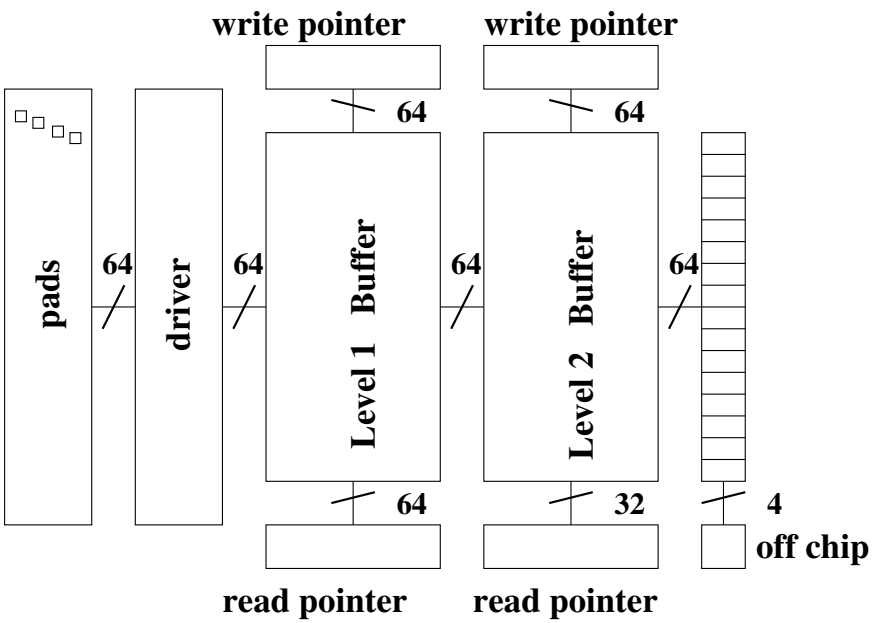

Figure 4.7: Simplified schematic of the DTSC. Shown are input stage with drivers and the two buffers.

time is about 300 μs for the full spectrometer, compared to up to 700 μs needed by the ZEUS GFLT. The SRC is equipped with a zero suppression, so that a group of four strips is readout only if at least one strip in this group has recorded a hit. For redundancy, each SRC has two dual port RAMs where the zero-suppressed data are stored, each dedicated to three detector planes. The data are stored in these RAMs until the SLT decision is made. Each pot is served by one SRC.

4.2 LPS operation

During the refilling and acceleration of protons in the HERA ring at the beginning of a fill and when the beams are dumped at the end of a fill, the LPS detectors would suffer extremely high radiation doses, which would damage the silicon strip detectors and the front-end electronics. In addition, to obtain good efficiencies for the refilling of the machine, tight restrictions were necessary for the operation of the LPS detectors and the resulting apertures. As a consequence, the LPS pots have to be retracted to a safe parking position far outside the beam when a luminosity run is about to be finished, and put back in the beam, after luminosity running is declared. These constraints on the operation can be satisfied with Roman pots

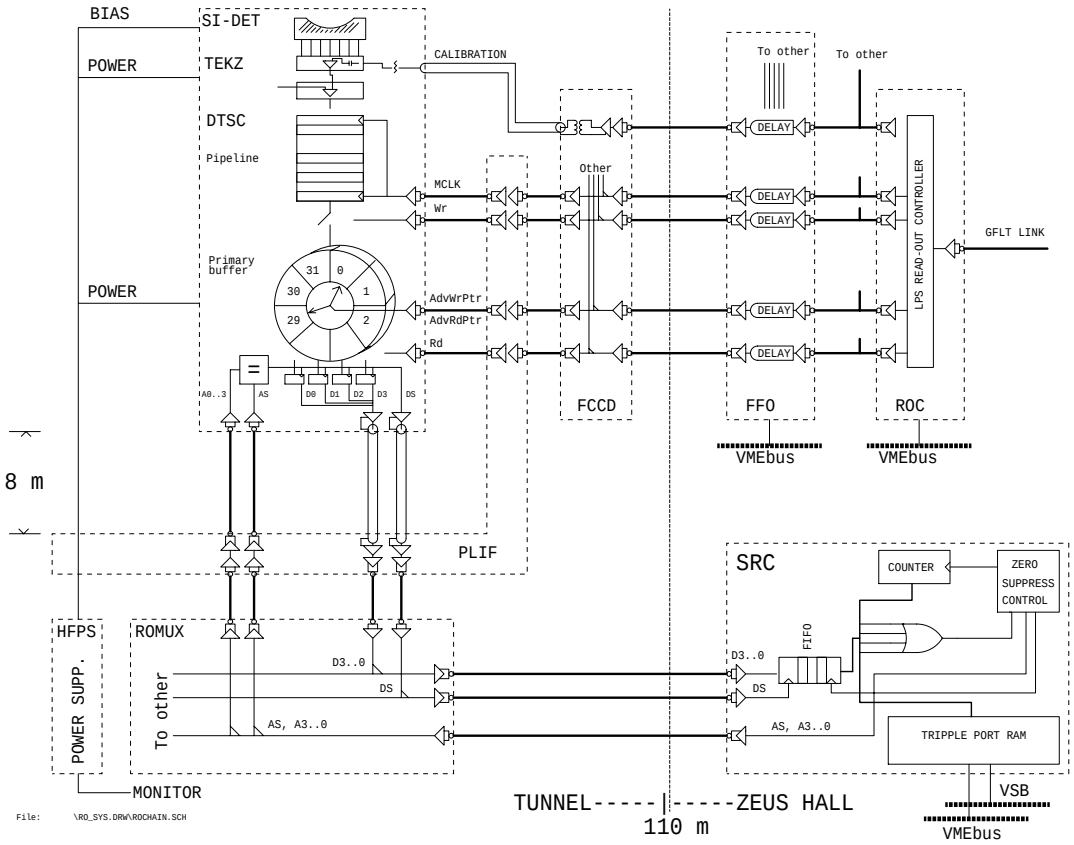

Figure 4.8: Schematic of the LPS readout system.

used for the LPS positioning mechanics. Figure 4.9 illustrates the functionality and insertion procedure for the Station S4.

From its safe parking position far outside the beam (about 0.5 m from the proton beam axis), a detector packet is moved into a stainless steel vacuum barrier (Figure 4.9A). This barrier is connected to the beam pipe using compressible bellows, so that the LPS detectors are actually operated under air pressure and not the vacuum of the beam pipe. As the detectors move into the beam (Figures 4.9A and B), the bellows are compressed. The right-hand side of the figure shows the aperture in the beam pipe at the three stages of insertion. For the Stations S4 to S6, which have pots above and below the beam pipe, the detectors surround the proton beam and have an overlap once fully inserted.

The requirements on the movement mechanics had to be very high precision, since the movement should be approximately as precise as the position resolution of the silicon detectors themselves, about 20 μm.

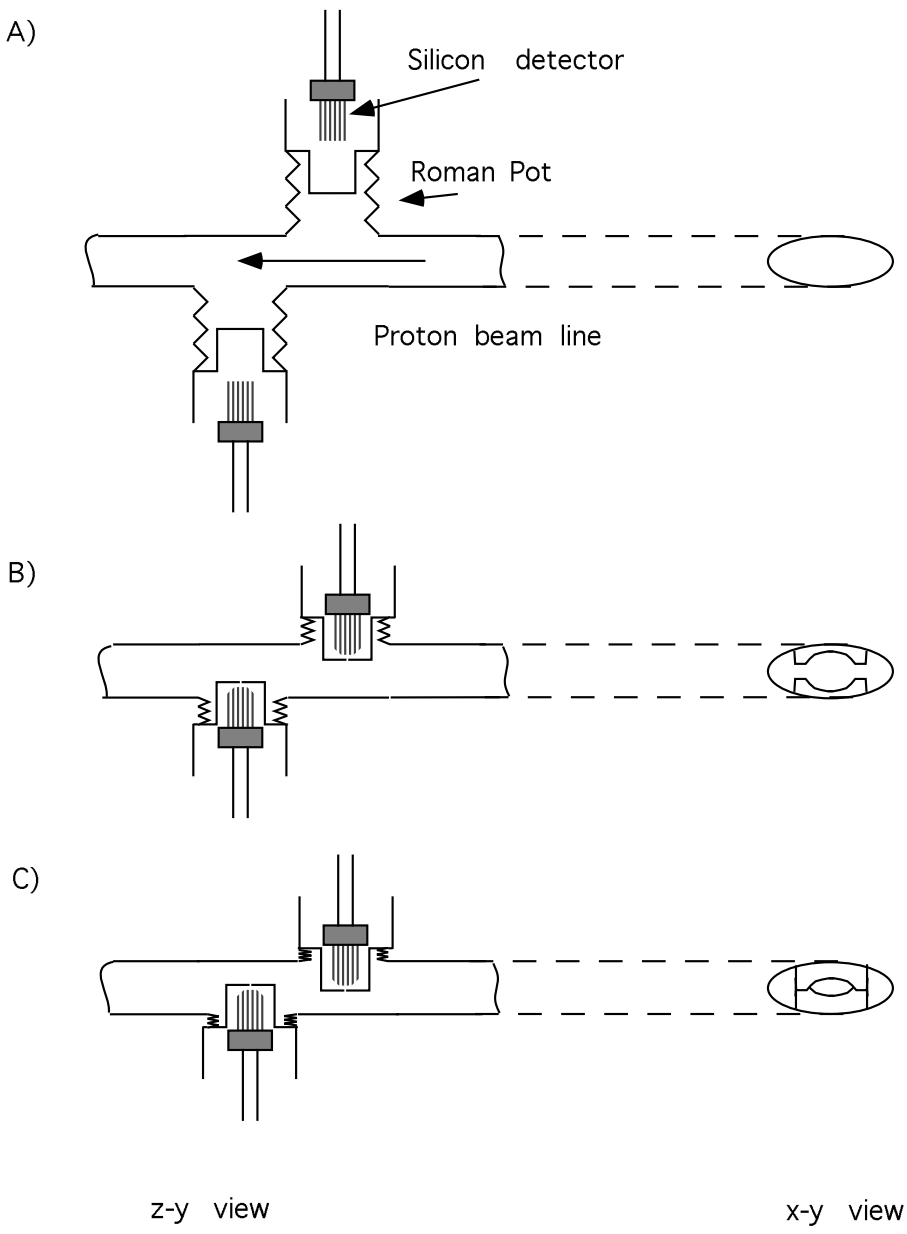

Figure 4.9: Illustration of the LPS insertion procedure using the Roman Pot technology (zy view). S4 is shown as an example. The right-hand side shows the beam pipe aperture at the corresponding stages of insertion (xy view).

4.3 LPS Reconstruction

The reconstruction software for the LPS (called *LP2RECON*) translates the raw data containing the hits in the silicon detectors, motor positions, and magnet currents into five charged particle track variables. These variables are the position X, Y of the track at $Z = 0$, and the momentum of the track in X, Y, and Z direction. If three stations in the LPS recorded hits of a track, the X and Y coordinate in each station are measured and constrain the five charged track variables unambiguously. If only two stations recorded a hit, the vertex position in X and Y is used as an additional constraint. The track reconstruction can only give accurate measurements of the track momentum if the positions of the whole detector are known precisely (with an accuracy given by the internal resolution of the LPS of about 20 μm). The procedure of determining these positions is known as *alignment* (Section 4.5).

4.3.1 Coordinate Reconstruction

The information for an LPS event is stored in terms of a list of strip hits in the detector. From this list, all strips which are known to be faulty (dead or very noisy, connected to a bad section of the front-end electronics) are removed from the list. Assuming that neighboring strip hits are due to the same particle, the list of strips is searched for adjacent strips, which are combined to form a *cluster*. The center of the strips which form the cluster is defined as the cluster position. The average cluster width in the LPS is 1.5 strips.

In a next step, clusters on planes with the same strip orientation in one pot, which have a difference of less than 2 strips, are combined into a *match*. Photons from synchrotron radiation, which are the dominant background in the LPS, can be completely absorbed within the silicon of one plane. As a consequence, synchrotron photon hits are mostly uncorrelated between different planes. Therefore, a match has a high probability of belonging to a real track.

Finally, local track segments are found by combining clusters and matches of all possible combinations of the u, v, and x views in one pot to find appropriate coordinates. If a local track segment passes through the up and down pot in the stations S456, the coordinates are combined into one. Using the strip equations (relation between strips and x, y coordinates in a plane) from the alignment (Section 4.5), the track segments are fit to obtain coordinates in the nominal beam reference frame. To distinguish these particle coordinates from noise hits, a set of quality codes was developed, which are listed in Table 4.1.

Using pattern recognition, the longitudinal momentum fraction, x_L, can be determined. In the presence of the dipole and quadrupole fields of the beam optic magnets, the propagation of a particle from position x_1 to x_2 is given by

Match and Cluster Pattern	Number of Hit Detectors	Quality Code
M M M	6	1
M M C	5	2
M M	4	3
M C C	4	4
M C	3	5
C C C	3	6
C C	2	7

Table 4.1: Quality codes for LPS coordinates. "M" stands for a match, "C" for a cluster.

$$x_2 = \mathbf{M_{1\to 2}}(x_L)x_1 + \mathbf{b_{1\to 2}}(x_L). \tag{4.1}$$

Here, $\mathbf{M_{1\to 2}}$ is a 2×2 matrix and $\mathbf{b_{1\to 2}}$ is a vector determined by the magnet strength and geometry between z_1 and z_2. The pattern recognition part computes $\mathbf{M_{1\to 2}}$ and $\mathbf{b_{1\to 2}}$ for a fixed number of x_L values. Figure 4.10 shows the relation between x_L and the hit position in two stations based on Equation 4.1. Each line represents the location of a coordinate pair, which will be observed at fixed x_L for a given vertex position with the acceptance of the LPS. By using the reconstructed coordinate x of two stations, x_L is extracted by taking the value corresponding to the closest line of Figure 4.10. x_L is determined in this way independently for the x and y coordinates. The two values of x_L are combined appropriately and their difference is used to estimate the error on x_L. With x_L known, the transverse momentum p_T can be extracted.

If more than two stations are hit, a solution of any two stations should yield nearly the same x_L and p_T. Subsequently, the solutions for x_L and p_T are combined accordingly.

4.4 Track Fitting

The pattern recognition determines the fit parameters x_L and p_T independently for a pair of pots and the vertex position. To get a better track fitting and include correlations between the fit parameters, all constraints of a track (all detector hits and the vertex) should be included. If more than two stations were hit, the vertex constraint to one point can be dropped and a track vertex can be used to determine the track parameters best satisfying all constraints. This is done with a global χ^2 minimization using the method of Levenberg-Marquardt [73]. The global χ^2 contains

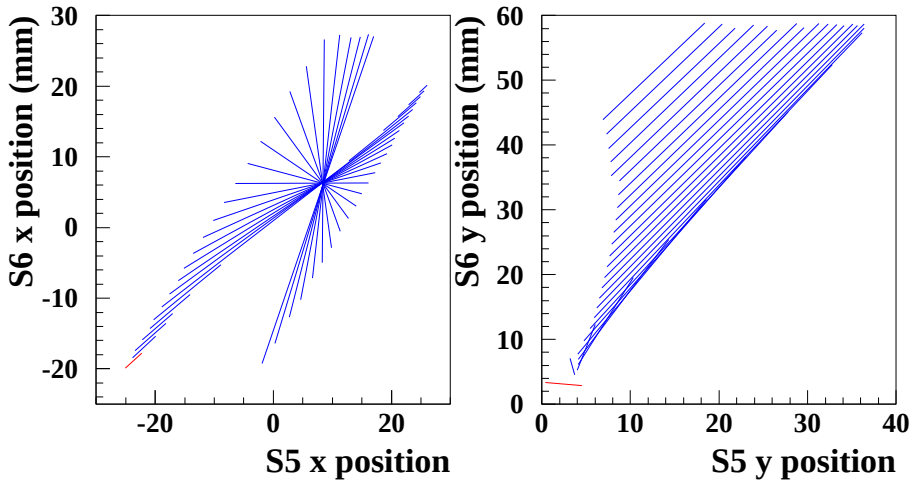

Figure 4.10: Correlation lines between x and y coordinates in stations S5 and S6 for x_L between 0.6 and 1.0. Each line represents the location of a coordinate pair, which will be observed at fixed x_L for a given vertex position with the acceptance of the LPS.

all the track parameters:

$$\chi^2 = \sum_{clusters} \frac{(x_i - X_i(\vec{v}, p_T, x_L))^2}{\sigma_i^2} + \frac{(v_x - x_0)}{\sigma_x^2} + \frac{(v_y - y_0)}{\sigma_y^2} \tag{4.2}$$

with X_i being the extrapolated position of the track to the silicon detector from the pattern recognition, $\vec{v} = (v_x, v_y, v_z)$ is the vertex position, and σ_x and σ_y its nominal width.

In addition to the optimized track parameters determined from the χ^2 minimization, the procedure returns parameters, which can be used to determine the best track if more than one track is found or to reject tracks which might be due to noise from the silicon detectors.

Each plane on or before the last pot of a track is checked if a hit was recorded on that plane. If no hit was recorded, the track is extrapolated to the plane. If this expected hit lies within at least 1 mm of the active detector area, the ten closest strips to this point are checked for clusters or noisy and dead channels. If this test is negative, then the plane is considered missing. The number of missing planes is recorded in the variable N_{miss}. Since most of the detector planes are more then 99% efficient, missing planes suggest a track, which is not real.

The LPS reconstruction code contains a complete description and simulation of all beam elements between the LPS stations and the interaction point. After a track was fitted, it is swum back through the beam pipe and the distance between the

track and the beam pipe aperture is calculated. The distance to the closest aperture is called the *distance of closest approach* and is stored in the variable *docap*. If the distance of closest approach is negative, the track passed through at least one beam element. Most of the protons, which originate from the interaction point and are tracked by the LPS, travel almost parallel to the beam line. If such a proton hits any beam aperture, it is most likely to be lost. Therefore, physical tracks should fulfill a minimum *docap* requirement.

If there is more than one track in a single event, tracks with a very bad $\chi^2/ndof > 20$, a negative *docap* ($docap < -0.05\ cm$), too many missed planes ($N_{miss} > 4$), or with an unphysical x_L ($x_L > 1.1$) are discarded. From the remaining tracks, the one with the highest number of silicon planes hit is considered the best track. The best χ^2 is used to select if two equal candidates are found.

4.5 Alignment - A brief overview

4.5.1 Alignment Procedure

Before tracks can be reconstructed with the LPS, it has to be determined where the detectors are with respect to each other, to the ZEUS main detector, the beam line, and the magnets of the beam optics during the whole data taking period. Once this information is known, input parameters for the reconstruction code can be extracted and stored in the condition GAF (*General Adamo File*), which is read by the LPS reconstruction code LP2RECON. Only after the location of the LPS is precisely known tracks can be reconstructed. The procedure to determine the location of the LPS is known as *alignment*. Since the operating conditions usually change with the running period (removing and reinstalling detectors for repair, the mechanics are disassembled for maintainance, charge of the colliding beams is changed, beam energy is changed), a separate alignment is necessary for each data taking period.

The steps necessary to align the LPS will be briefly reviewed. A more detailed description can be found elsewhere [74, 75, 76]. The main alignment steps are the following (here for the S456 telescope, the analogue is done for S123):

- Align the planes within one pot.
- Relative alignment of the up and down pots in S456.
- Relative alignment of S456 with respect to each other.
- Locate S456 in the ZEUS coordinate system.
- Find beam tilt and vertex position.

- Determine beam pipe apertures.
- Correct for run-by-run dependencies.

These steps have to be repeated to obtain a stable result. The alignment can be precisely done with physics events, mainly elastic ρ^0 events from the process $ep \to \rho^\circ ep$. Photoproduction events of ρ° have two important properties:

1. x_{IP} is very small, and therefore $x_L \simeq 1$:

$$\frac{M_\rho^2 + Q^2 - t}{ys} \simeq 1 - x_L \ll 0.001 \tag{4.3}$$

2. the proton p_T balances exactly the transverse momentum of the ρ°.

If low momentum tracks are needed, a DIS sample is selected.

Alignment of a Single Pot In the first step, the position of the silicon planes in one pot with respect to each other is determined. The basis for this is the *strip equation*

$$x = y \cdot \tan\phi_i - O_i - A_i \cdot N \tag{4.4}$$

which relates the coordinates x, y to the strip number N. The other parameters of the strip equation are the orientation of the strip ϕ_i relative to the beam axis and an offset O_i. The parameter A_i depends on the orientation of the strip and the pitch. The index i indicates the plane number. To determine the parameters for Equation 4.4, the residuals, obtained by subtracting the right-hand side of Equation 4.4 from the left-hand side, are centered at 0 (offset O_i) and their width is minimized (ϕ_i).

Alignment of Up and Down Pots To locate the up and down pots with respect to each other, residuals in x and y coordinates for particles, which pass through both the up and the down pot, are minimized and centered at 0. The degrees of freedom for this step are an offset between up and down pots and a rolling angle between them. Due to the beam optics, there is a small tilt in x, which results in a shift of the x coordinate over the approximately 10 cm spacing in z between the up and down pot. This tilt is corrected for when calculating the residuals. In y the tilt is negligible.

Since the up and down pot positions are uncorrelated, the residual distributions between them can be used to determine the resolution of the position reconstruction. By tracking the difference in the up and down pot coordinates over the running period, the stability of the mechanical structure of the LPS can be monitored.

Relative Location of the S456 Telescope Between S4 and S6 a strong dipole bending magnet is situated in y, which deflects the proton beam by 5.7 mrad and allows to use S456 as a spectrometer. Therefore, these three stations can be precisely aligned relative to each other, without knowing the absolute x and y coordinate. The relative alignment of S456 has a total of 4 degrees of freedom, since the position of one station is arbitrarily fixed, while the remaining two are aligned using translations in x and y. In the nominal beam reference frame, which follows the bend due to the magnet for $x_L = 1$ tracks (important only for the y coordinate), the coordinates in the three stations are collinear. Therefore, the coordinate in one station, for example, S5, can be extrapolated from the coordinates in S4 and S6:

$$x_{5,extra.} = \frac{x_4(z_6 - z_5) + x_6(z5 - z4)}{z_6 - z_4}, \tag{4.5}$$

and analogue equation for y.

The residual of the measured and extrapolated coordinates has to be centered at 0 and will be very sharply peaked. A correlation between the residual in x and y is an indication of a roll of the S456 spectrometer.

Location of S456 with Respect to ZEUS To find the location of the full S456 spectrometer, three station tracks are fitted with the vertex being a free parameter. These tracks are then swum back to the interaction point at $Z = 0$. The spectrometer is translated in x and y and rotated with respect to the beam axis (to pitch and yaw) until the reconstructed vertex from the LPS is identical to the average CTD vertex for the same run. The vertex position has to be independent of x_L.

This procedure requires two assumptions:

1. the CTD is well aligned with the axis of the beam line quadrupole axis,

2. the position of the quadrupoles is fixed relative to each other as designed by HERA.

Since the quadrupole field strength is proportional to the distance from the axis, it is important, that the location of the quadrupoles is precisely known in the reconstruction program.

Find Vertex Position and Beam Tilts So far, the position of the LPS was determined in the nominal beam reference frame, which follows the beam optics. The location of the beam in this reference frame needs to be known, since the vertex and the angle of the proton beam at the vertex is used in the LPS reconstruction code. The vertex is needed to constrain the track fitting procedure for events, which have hits in only two stations. The angle of the proton beam at the vertex is used

to calculate the track momentum by comparing it to the angle of the track at the vertex.

To determine the average vertex (as a function of run or fill number), elastic ρ^0 events with $x_L = 1$ of the proton are used, which hit three LPS stations. The track can be fitted without a vertex constraint from the CTD. The track is then swum back to $z = 0$ to determine the x and y vertex position. The extracted average vertex position of the run or fill is stored in the calibration GAF and is used for the track reconstruction. Using the CTD vertex would degrade the resolution in the track reconstruction.

For elastic ρ^0 events, the transverse momentum of the scattered proton should be exactly balanced by the transverse momentum of the ρ^0 measured using the CTD, since the momentum transfer at the electron vertex is 0 in photoproduction. The average of $p_x + p_x(\rho)$ and $p_y + p_y(\rho)$ is therefore a measure of the beam tilt at the vertex, which can be measured as a function of run or fill number.

Beam Pipe Apertures The beam pipe apertures need to be known for the Monte Carlo implementation of the LPS alignment in MOZART (see Section 5.2), because it strongly affects the acceptance of the spectrometer. In order to have the same track acceptance in data and Monte Carlo, the location of the apertures as seen by the LPS must be correctly reproduced by the Monte Carlo.

To check the aperture positions, tracks of all momenta (DIS sample) are extrapolated to the appropriate Z location of the aperture and the position of the track in x and y is plotted over the contour of the beam pipe element. All tracks should lie within the beam pipe aperture.

4.5.2 Status of the Alignment for 1997 Data

The 1997 alignment is of the same quality as the ones performed for the 1994 and 1995 data taking period. Figure 4.11 gives a comparison of important LPS variables between 1995 and 1997.

So far, this alignment has not been implemented in MOZART. The Monte Carlo simulation of the LPS is done outside MOZART with the MOLPS program (see Section 5.3). MOLPS is a standalone LPS simulation which uses the generated proton momentum as input and which can be linked to the analysis job.

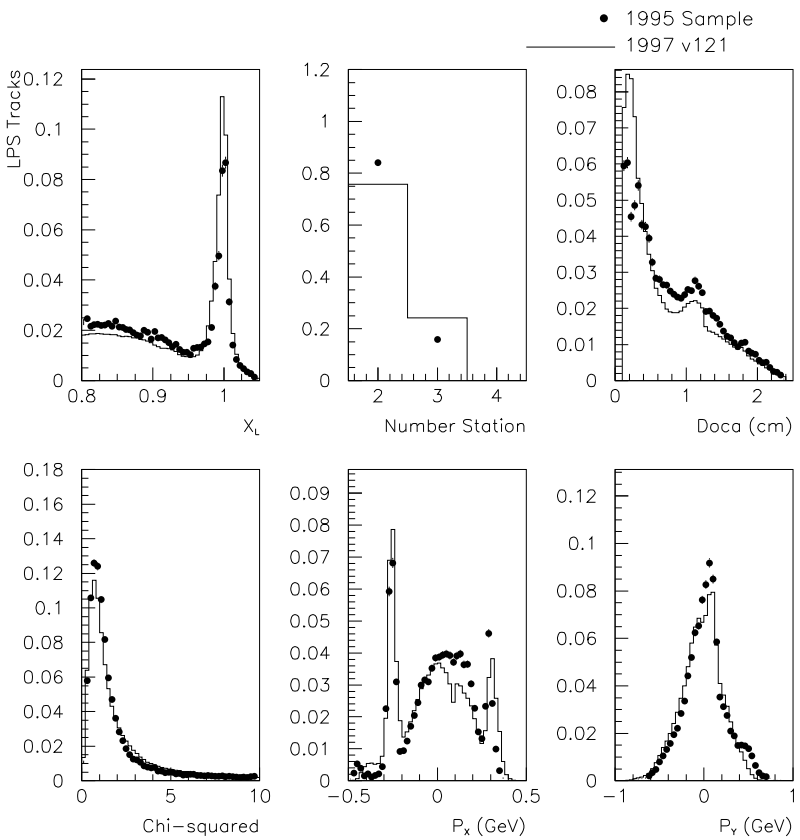

Figure 4.11: Comparison of important LPS variables for the 1995 (dots) and 1997 alignment (solid line). The quality of both alignments is comparable and suitable for physics analysis.

Chapter 5

Monte Carlo Simulation

Today's complex high-energy experiments rely heavily on detailed knowledge of physics processes, trigger efficiencies, and detector responses. Most of these quantities cannot be calculated analytically, but need to be simulated using well established Monte Carlo (MC) techniques. An accurate simulation of the physics and the response of the experiment is vital in any physics analysis to:

1. *determine the resolution of measured variables* by comparing the reconstructed value with the generated one;
2. *understand the acceptance* of the detector and the trigger by comparing the number of detected events with the number of originally generated events;
3. *test physics models* by comparing their generated distributions with the ones seen in the data;
4. *extract model and detector independent results* to compare with other measurements or theoretical calculations;
5. *check a measurement for systematic uncertainties* by adjusting the input distributions to the detector simulation.

The Monte Carlo simulation for the ZEUS experiment (and in general for any experiment) consists of two main parts: first, the *ep* scattering process is simulated with an MC event generator describing the cross section dependence on the event kinematics and the production of the hadronic final state topology; second, the response of the experiment (detector plus trigger) to these final state particles is simulated.

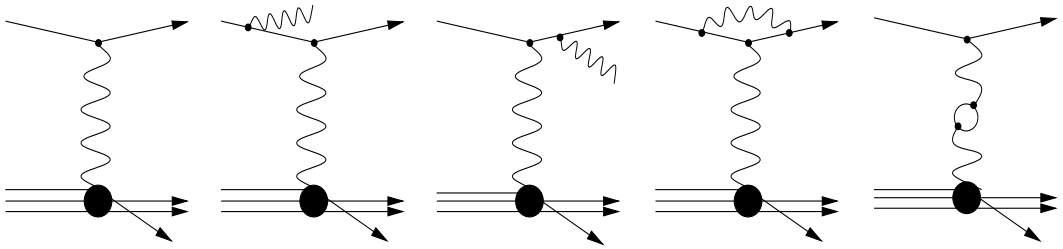

Figure 5.1: Feynman graphs of the processes contributing to the ep scattering process. The Born level process (a) is shown together with initial (b) and final (c) state radiation, lepton vertex correction (d) and the self-energy correction (e).

5.1 Monte Carlo Generators

5.1.1 Introduction

In general, the event generation with a MC generator starts with the differential cross section. To lowest order in perturbation theory, the neutral current (NC) ep scattering cross section can be described by summing the contributions from the exchange of a single photon between the electron and a quasi-free quark in the proton. This lowest order process is shown in Figure 5.1a and the corresponding cross section for an individual constituent is given by

$$\frac{d^2\sigma(eq \to eq)}{dydQ^2} = \frac{2\pi\alpha^2 e_q^2}{yQ^4}(1 + (1-y)^2), \tag{5.1}$$

where e_q is the charge of the quark.

When producing events for ep deep-inelastic scattering, the structure of the proton in terms of partons (quarks and gluons) enters by introducing the structure functions F_2 and F_L:

$$\frac{d^2\sigma(ep \to eX)}{dydQ^2} = \frac{4\pi\alpha^2}{yQ^4}\left((1 - y + \frac{y^2}{2})F_2^p(x,Q^2) - \frac{y^2}{2}F_L^p(x,Q^2)\right). \tag{5.2}$$

The distribution of the events in the kinematic phase space is determined by the dependence of the structure functions on the kinematic variables. In diffractive DIS, the differential cross section can be written in terms of the diffractive structure functions F_2^D and F_L^D:

$$\frac{d^2\sigma(ep \to eXp)}{dydQ^2dx_{IP}dt} = \frac{4\pi\alpha^2}{yQ^4}\left((1-y+\frac{y^2}{2})F_2^{D(4)}(x,Q^2;x_{IP},t) - \frac{y^2}{2}F_L^{D(4)}(x,Q^2;x_{IP},t)\right). \quad (5.3)$$

However, the interpretation of this diffractive structure function in terms of parton densities (unlike the proton structure functions) is not clear.

Higher order contributions to the Born level cross section of Equation 5.1 have to be taken into account, since they can result in substantial corrections to the observed variables y and Q^2. These corrections originate from the emission of additional real or virtual photons (and Z°, or $W^\pm$ in charged current events) from the lepton or quark lines. Since these corrections are proportional to the square of the charge, the corrections associated with quarks are smaller than the leptonic ones and are usually absorbed in the parton distributions which enter in the structure function. The QED corrections to the Born level process are shown in Figure 5.1 b) to e). Divergences, which arise from initial (Fig. 5.1b) and final (Fig. 5.1c) state radiation at small energies of the radiated photon are canceled by the ones introduced from the vertex correction (Fig. 5.1d). In the self-energy correction (Fig. 5.1e) term, all charged fermions with $m^2 \leq Q^2$ have to be considered.

These QED contributions can not only change the observed cross section (and therefore the structure function), but can also affect the measurement of the kinematic variables x, y, and Q^2. Therefore, it is important that these contributions are accounted for in the MC generators. The generators (except RIDI) discussed in the following sections were interfaced to the HERACLES MC generator [77] to simulate the radiative corrections. Because HERACLES operates on the parton level, an event is fully described by the flavor of the struck quark and the four-momentum of the electron and the quark.

In an experiment, only hadrons (along with the electron) can be observed in the final state. Since the strong coupling constant α_S becomes large at scales comparable to the hadron masses and perturbation theory is not applicable anymore, the hadronization of the partons needs to be described by a phenomenological procedure. The MC generators used in this analysis use the JETSET package [78] to simulate the production of the final state hadrons from partons. JETSET uses the LUND string fragmentation model [79]. The partons are connected by color strings. As they move away from each other, these color strings stretch and fragment into smaller pieces. If these pieces have not enough energy left to break further, hadrons are formed in the hadronic final state.

5.1.2 RAPGAP with H1 fit

The RAPGAP [80, 81] generator was used to simulate events with a resolved Pomeron $\mathbb{P}$, i.e. a $\mathbb{P}$ with a structure in terms of quarks and gluons, following the Ingelman and Schlein approach [46]. The diffractive scattering process is described by the exchange of a $\mathbb{P}$ with the cross section given in terms of a diffractive structure function (see Equation 5.3). The structure function F_2^D factorizes into a $\mathbb{P}$ flux factor $f_{p,\mathbb{P}}$ (probability of finding a $\mathbb{P}$ within the proton) and a $\mathbb{P}$ structure function $F_2^{\mathbb{P}}$:

$$F_2^{D(4)}(\beta, Q^2; x_{_{IP}}, t) = f_{p,\mathbb{P}}(x_{_{IP}}, t) F_2^{\mathbb{P}}(\beta, Q^2). \tag{5.4}$$

The $\mathbb{P}$ structure function can be interpreted in terms of quark and gluon densities.

The H1 collaboration used their 1994 measurement of the diffractive structure function $F_2^{D(3)}(x_{_{IP}}, \beta, Q^2)$ to perform fits to a QCD-motivated model to extract parton distributions for the $\mathbb{P}$ [82]. This parameterization will be referred to as *H1fit* in the remainder of this thesis.

To obtain a good description of the data, a subleading Reggeon $\mathbb{R}$ exchange in addition to the leading $\mathbb{P}$ exchange had to be assumed, so that the structure function $F_2^{D(3)}$ takes the form:

$$F_2^{D(3)}(x_{_{IP}}, \beta, Q^2) = f_{p,\mathbb{P}}(x_{_{IP}}) F_2^{\mathbb{P}}(\beta, Q^2) + f_{p,\mathbb{R}}(x_{_{IP}}) F_2^{\mathbb{R}}(\beta, Q^2) \tag{5.5}$$

with $\mathbb{P}$ flux factor given by:

$$f_{p,\mathbb{P}} = \int_{t_{cut}}^{t_{min}} \frac{e^{B_{\mathbb{P}} t}}{{x_{_{IP}}}^{2\alpha_{\mathbb{P}}(t)-1}} dt \tag{5.6}$$

and equivalently for the $\mathbb{R}$. An interference term between the $\mathbb{P}$ and $\mathbb{R}$ contribution is neglected and the corresponding trajectories were fitted to be:

$$\alpha_{\mathbb{P}}(0) = 1.200 \pm 0.017(stat.) \pm 0.011(sys)^{+0.029}_{-0.034}(model) \tag{5.7}$$

$$\alpha_{\mathbb{R}}(0) = 0.57 \pm 0.14(stat.) \pm 0.11(sys)^{+0.03}_{-0.07}(model). \tag{5.8}$$

The reggeons, which are combined to give the effective $\mathbb{R}$ trajectory, carry the quantum numbers of the ρ, ω, a or f meson.

The structure function $F_2^{\mathbb{P}}$ is parameterized in terms of parton dynamics adopting simple non-perturbative input parton distributions at a low scale $Q_0^2 = 3$ GeV^2. The DGLAP equation is then used to evolve the parton distribution to higher values of Q^2. The structure function of $\mathbb{R}$ is taken from a parameterization of the pion [83].

Fits were performed in the Q^2 regime of $4.5 < Q^2 < 75$ GeV^2 using three different parton distributions for the Pomeron:

1. $\mathbb{P}$ composed entirely out of quarks (*H1fit1*),

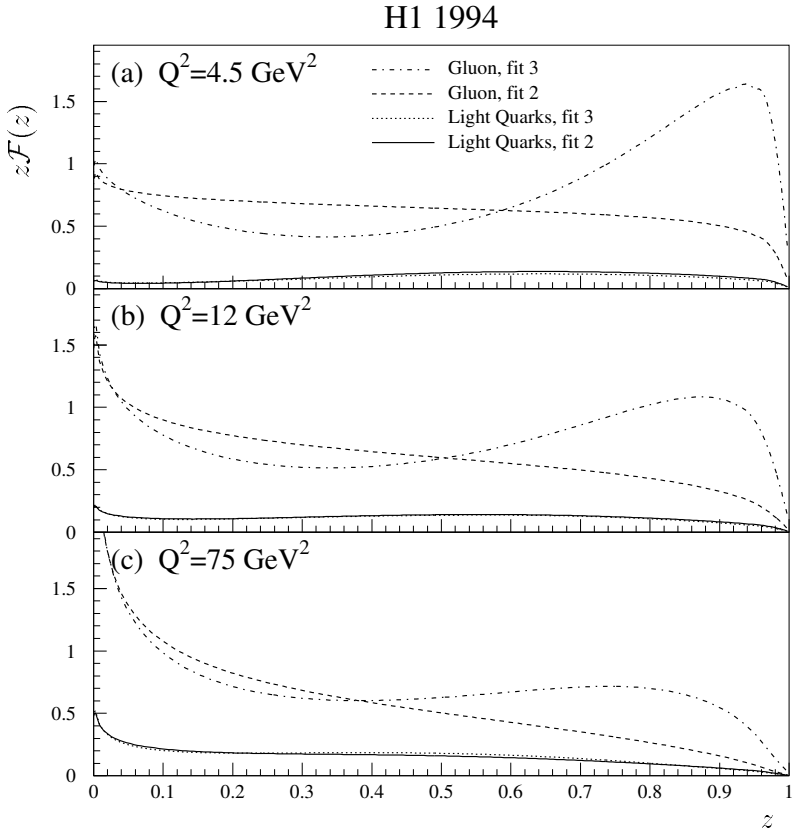

Figure 5.2: Sum of the light quark and gluon distributions of the H1fit 2 and 3 in three bins of Q^2 as a function of z, the fractional momentum of the IP carried by the gluon. H1fit 3 is characterized by the peak in the gluon distribution in the low Q^2 region when $z \to 1$.

2. IP composed out of quarks and gluons (*H1fit2*),

3. IP composed out of quarks and gluons and the gluon distribution peaked at fractional momentum $z \to 1$ (*H1fit3*).

Figure 5.2 shows the gluon distribution as a function of the fractional momentum z of the IP carried by the gluon.

In this analysis, RAPGAP with the *H1fit 2* was used to generate the main Monte Carlo sample.

Depending on whether the IP generated by RAPGAP contains quarks only or an appropriate mixture of partons and gluons, the implications for the produced hadronic final state are very different (Figure 5.3). If the virtual photon is scat-

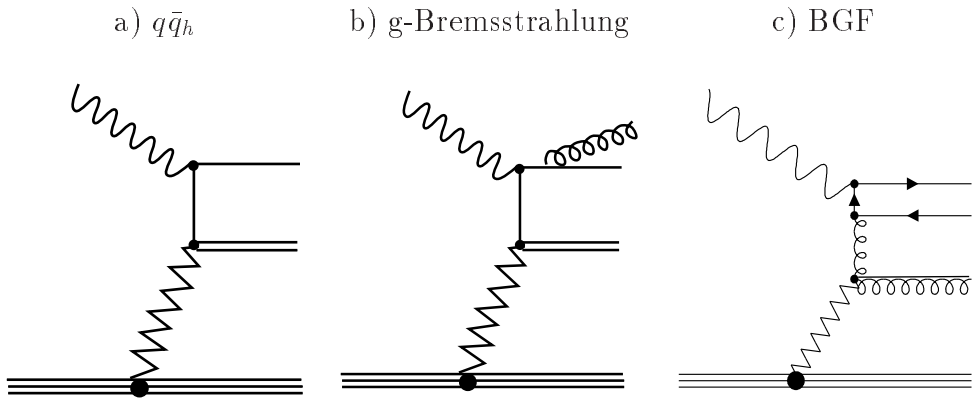

Figure 5.3: Feynman diagram of the three dominant processes contributing on parton level: a) the $\mathbb{P}$ is a $q\bar{q}$ state; b) in addition a gluon is radiated off the quark line; c) boson gluon fusion (BGF) occurs at lowest order for a gluon dominated $\mathbb{P}$. The double lines indicate a extended object ($\mathbb{P}$ remnant) as implemented in RAPGAP.

tered off a $\mathbb{P}$ which is made out of $q\bar{q}$ pairs (Figure 5.3a), the resulting final state will have a very collimated two-jet structure. Broadening of the final state can be expected from $O(\alpha_s)$ gluon radiation of the quark line. In the sample used for this analysis, this gluon radiation is treated according to the color dipole model (CDM) as implemented in the ARIADNE MC generator [84]. The struck quark and the $\mathbb{P}$ remnant (indicated by the double quark like in Figure 5.3a) form a color dipole. This dipole can radiate additional gluons (Figure 5.3b). Since RAPGAP treats the parton, which was not struck by the photon, as an extended color object, gluon radiation is suppressed for the $\mathbb{P}$ remnant.

A $\mathbb{P}$, which contains quarks and gluons, produces gluons already at lowest order in the final state via the Boson Gluon Fusion (BGF) diagram (Figure 5.3c). The final state is therefore expected to be broader than the one resulting from a quarkonic $\mathbb{P}$ due to three-jet events. In this case, one gluon forms the Pomeron remnant, which together with the $q\bar{q}$ pair from the hard scattering process (BGF) form the color-singlet state. The BGF contribution is calculated using full $O(\alpha_s)$ matrix elements and the fragmentation is done with leading log parton showers. To avoid divergences in the matrix element calculation for massless quarks in the BGF contribution, a cutoff p_T^2 has to be specified. The cutoff was chosen to be $p_T^2 \geq 3\,\mathrm{GeV}^2$ in order for the cross section due to the BGF diagram not to exceed the total cross section.

The main switches used to generate this sample are (see [81] for the details on these flags): `IFPS = 10, IPRO = 1200, IDIR = 0, IDISDIF = 0, IFULL = 1, NG = -11, NPOM = -12` and Λ_{QCD} = `0.200 GeV` in NLO. Charm production from BGF was not included in this MC sample (`NFLAV = 3`).

The phase space defined for the generated sample is $Q^2 > 3$ GeV^2, $x_L > 0.9$, and no explicit limit on x or y, corresponding to a total cross section of 59.2 nb. The exchange of the $\mathbb{P}$ contributes 28.0 nb to the total generated cross section, while the $\mathbb{R}$ contribution amounts to 31.2 nb; more than 50%.

5.1.3 RAPGAP with Bartels-Lotter-Wüsthoff $q\bar{q}$

Recent results from HERA [86] show, that the $\mathbb{P}$ trajectory is larger than the one obtained for a soft $\mathbb{P}$, which describes the high-energy behavior of hadron-hadron scattering, indicating that a hard, perturbative $\mathbb{P}$ component might be necessary. New insight into this hard $\mathbb{P}$ can be gained by selecting an event type where the hard component is expected to be enhanced. A class of this final state is the production of two-jet events with large transverse momenta from the diffractive dissociation of photons.

The simplest configuration to produce two-jet events is the production of $q\bar{q}$ pairs [87] (Figure 5.4a). At higher masses, additional production of gluon jets is expected to become dominant, but not included in this sample. Both the longitudinal and transverse cross sections are calculated in a restricted kinematic range, where the hard $\mathbb{P}$ is expected to dominate. The virtuality Q of the photon and the mass $M^2 = (q + x_{IP}p)^2$ (i.e., $x_{IP} \ll 1$, β near 1) are assumed to be much smaller than the total energy. Since the cross section peaks at $t = 0$, the momentum transfer at the proton vertex is set to zero for the calculation with a t dependence added on by hand later.

The fixed transverse momentum $\mathbf{k}$ of the (anti-)quarks enters as a second hard scale allowing the $\mathbb{P}$ to be treated perturbatively. In the considered kinematic range ($x_{IP} \ll 1$), the amplitude of the process is dominated by two-gluon exchange (see Figure 5.4a). Both gluons have to couple to the outgoing quarks in all possible configurations. It was found that the cross section is dominated by small $\mathbf{k}$, so that the two jets appear most frequently at small angles. In this model, the $\mathbb{P}$ can be identified with the gluon structure function of the proton and the energy dependence of the cross section is given by the square of the structure function:

$$d\sigma \sim [\frac{1}{k_T^2} x_{IP} g(x_{IP}, \frac{k_T^2}{1-\beta})]^2. \tag{5.9}$$

One feature of the hard $q\bar{q}$ production is that the two jets lie perpendicular to the scattering plane in the photon-Pomeron center-of-mass frame [88]. The scattering plane is defined by the photon-Pomeron direction and the momentum of the outgoing electron. This is in contrast to the photon-gluon fusion mechanism in DIS included in the H1fits implemented in RAPGAP (see Section 5.1.2). The two quarks originating from the photon-gluon fusion process prefer to lie inside the scattering plane.

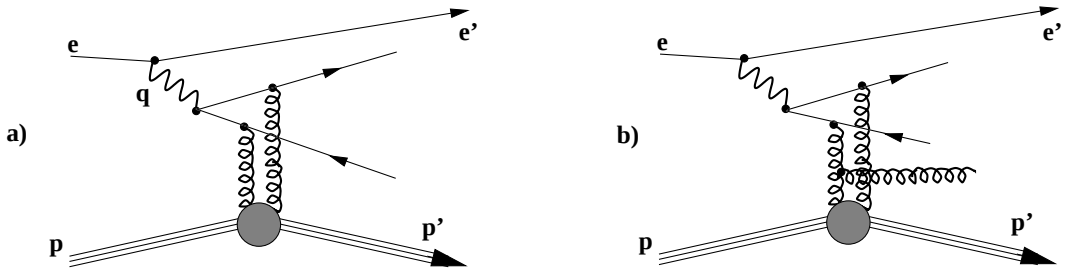

Figure 5.4: Diagrams for photon diffractive dissociation into a) $q\bar{q}$ and b) $q\bar{q}g$ states. The $\mathbb{P}$ exchange is modeled by a two-gluon exchange.

The relevant settings in the RAPGAP generator are: `IPRO = 21` with a p_T^2 cut of 1 GeV^2; only final state parton showers are included (`IFPS = 2`). The total cross section for the process was generated to be 6.2 nb with the same phase space as defined for the H1fit2 sample.

5.1.4 RAPGAP with Bartels-Wüsthoff $q\bar{q}g$

For diffractive masses larger than the ones considered in Section 5.1.3 ($\beta \ll 1$), the production of extra gluons becomes important. The simplest of such configurations consists of a $q\bar{q}$ pair and a gluon (Figure 5.4 b). A model of $q\bar{q}g$ production in diffractive DIS was developed in [89] and is available through the RAPGAP MC generator. In this model, the virtual photon splits into a $q\bar{q}$ pair and interacts with the proton via a two-gluon exchange plus an additionally radiated gluon. The exchanged gluons couple to the quarks in all possible ways. The result is the production of three-jet events.

The model is restricted to large diffractive masses M (small β) and the calculations were carried out in the forward direction, $t = 0$, and the region of $Q^2 \ll M^2 \ll W^2$. The $q\bar{q}$ system and the gluon are expected to be separated in rapidity. In the $\gamma^*\mathbb{P}$ center-of-mass-system the gluon is emitted in the direction of the $\mathbb{P}$. The opening angle Δ between the two quarks is of the order of m^2/M^2, with m being the mass of the $q\bar{q}$ system. For small opening angles, the gluon and the $q\bar{q}$ pair will come out back-to-back in the $\gamma^*\mathbb{P}$ center-of-mass system. For higher masses m, the $q\bar{q}$ pair will produce a broader jet, which eventually can be resolved into two separate jets, giving rise to a three-jet event together with the gluon jet. A large fraction (the amount depends heavily on the selected kinematic range and ranges from 40 to 80 %) of the $q\bar{q}g$ jets substantially contribute to the two-jet cross section. If both quarks of the $q\bar{q}$ pair carry similar longitudinal momentum (intermediate opening angles), three-jet events occur with a star-like structure. Events of this type are

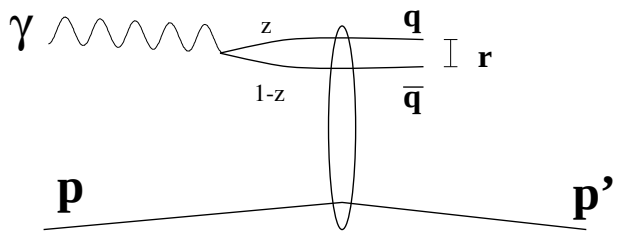

Figure 5.5: Diagram of the basic saturation model process.

more likely to appear at large transverse momenta of the gluon. For large opening angles, one of the quarks moves with maximum momentum forming one jet, while the second quark and the gluon form the second jet.

The relevant setting in the RAPGAP generator is: `IPRO = 20`; only final state parton showers are included (`IFPS = 2`). The total cross section generated amounts to 343.5 nb with the same phase space as defined for the H1fit2 sample.

5.1.5 The Saturation Model - SATRAP

The experimental data for the total and diffractive $\gamma^* p$ cross sections show as a function of the center-of-mass energy (W) a strong and similar rise [37] which is much faster than observed in hadron-hadron scattering. It was suggested, that the similarity of the rise for the total and the diffractive cross section is an indication for saturation of the parton density of the photon [56]. Based on this idea, the low and higher Q^2 behavior of the total cross section could be connected with the inclusive process in a quantitative way [57].

If the photon and the proton are collinear, the longitudinal and transverse part of the total cross section can be written in terms of the longitudinal and transverse wave function of the polarized photons ψ [49] [50]:

$$\sigma_{T,L} = \int d^2\mathbf{r} \int dz |\psi_{T,L}(z,\mathbf{r})|^2 \hat{\sigma}(x,r^2) \tag{5.10}$$

where $\hat{\sigma}$ is the dipole cross section for $q\bar{q}$ scattering on the proton, z the fractional momentum carried by the quarks and r the transverse separation of the quarks (figure 5.5). The wave functions are determined by the coupling of the quarks and the photon and can be calculated in QCD [50]. Similarly, the diffractive cross section is given by:

$$\left.\frac{d\sigma_{T,L}^{diff}}{dt}\right|_{t=0} = \frac{1}{16\pi} \int d^2\mathbf{r} \int dz |\psi_{T,L}(z,\mathbf{r})|^2 |\hat{\sigma}(x,r^2)|^2. \tag{5.11}$$

$\hat{\sigma}$ is assumed to be a function of the $q\bar{q}$ separation r and the saturation radius R_0:

$$\hat{\sigma}(x, r^2) = \sigma_0(1 - e^{-\frac{r^2}{4R_0^2}}). \tag{5.12}$$

For $r \ll 2R_0$, the dipole cross section grows quadratically with r, while for $r \gg 2R_0$, the cross section saturates at $\hat{\sigma} = \sigma_0$. In the asymptotic limit of small transverse separation, $Q \gg 1/R_0$, the cross section behaves as $\sigma_T \sim \sigma_0/(Q^2R_0^2)$ showing a scaling behavior, while for low $Q^2, Q \ll 1/R_0$ the scaling breaks down and $\sigma_T \sim \sigma_0$. The saturation radius R_0 is taken to be x dependent in order to describe the W (equivalently x) dependence of the total DIS cross section as measured at HERA:

$$R_0^2(x) = \frac{1}{Q_0^2}\left(\frac{x}{x_0}\right)^{\lambda} \tag{5.13}$$

with $Q_0 = 1$ GeV^2. All parameters of the model are determined from the HERA total cross section measurement between $Q^2 = 0.1$ GeV^2 and $Q^2 = 100$ GeV^2 to be $\sigma_0 = 23$ mb, $\lambda = 0.29$, and $x_0 = 0.0003$. In particular, no tuning of the model was performed with respect to the hadronic final state.

The saturation model is interfaced to the RAPGAP program and referred to as SATRAP [58].

The SATRAP model describes the HERA data with a similar quality as the BEKW model [52] where the structure function is written in a more intuitive way as a sum of the production of $q\bar{q}$ from longitudinal and transverse photons and of $q\bar{q}g$ from transverse photons:

$$x_{IP}F_2^{D(3)}(\beta, x_{IP}, Q^2) = c_T \cdot F_{q\bar{q}}^T + c_L \cdot F_{q\bar{q}}^T + c_g \cdot F_{q\bar{q}g}^T \tag{5.14}$$

where the single process structure functions are parameterized in terms of x_{IP}, Q^2, and with a β dependence as given in Section 2.5. The model has a total of 7 parameters which were extracted from the ZEUS measurement of the diffractive cross section [37]. The relative contributions of $q\bar{q}$ and $q\bar{q}g$ are given in Figure 5.6 for the BEKW model, but should correspond to the ones expected from the SATRAP model.

SATRAP is selected within the RAPGAP program with IPRO=3000 and produces a total cross section of 45.5 nb with the same phase space as defined for the H1fit2 sample [1].

[1] A word of caution: the implementation of the SATRAP model is in an early stage and not fully tested yet. However, as far as the reproduction of the final state is concerned, the model was stable over its last few iterations. Nevertheless, one should keep in mind when SATRAP is compared to the results of this analysis, that the displayed curves were not yet generated with a production version.

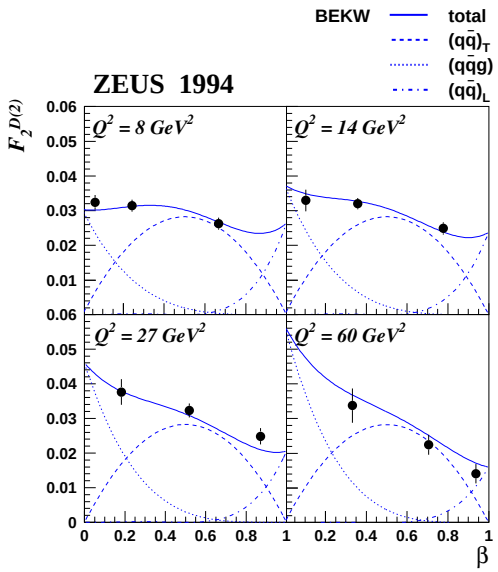

Figure 5.6: Comparison of the results from the BEKW fit and $F_2^{D(2)}$ data. The plot also shows the relative contributions of the production of $q\bar{q}$ and $q\bar{q}g$ from transverse photons and $q\bar{q}$ from longitudinal photons.

5.1.6 RIDI

In DIS, the presence of a deeply virtual photon as a probe may allow for a description of the diffractive scattering amplitude by means of perturbative QCD. For a pQCD $\mathbb{P}$, the intercept is higher than for a so-called soft $\mathbb{P}$ [90, 91] observed in the high-energy behavior of hadron-hadron scattering. The increase of the intercept can be related to the rise in the gluon structure function as observed by HERA, which can be interpreted in terms of a hard, i.e., perturbative, contribution.

The diagrams, which contribute to lowest order in a pQCD approach, are shown in Figure 5.7. For small masses ($M_X^2 \lesssim Q^2$), the simplest configuration is the production of a $q\bar{q}$ pair (Figure 5.7 a). For higher masses ($M_X^2 \gg Q^2$), the $q\bar{q}g$ contribution (Figure 5.7 b) dominates.

These two diagrams are implemented in the RIDI (RIDI2.0) MC generator [92] which simulates the diffractive dissociation of virtual photons in ep interactions following the approach of Ryskin [93]. Diffractive dissociation is studied in the framework of the leading log approximation (LLA) of perturbative QCD [94], in which the cross section is proportional to the square of the gluon structure function of the proton. The contribution of both transversely and longitudinally polarized photons is taken into account.

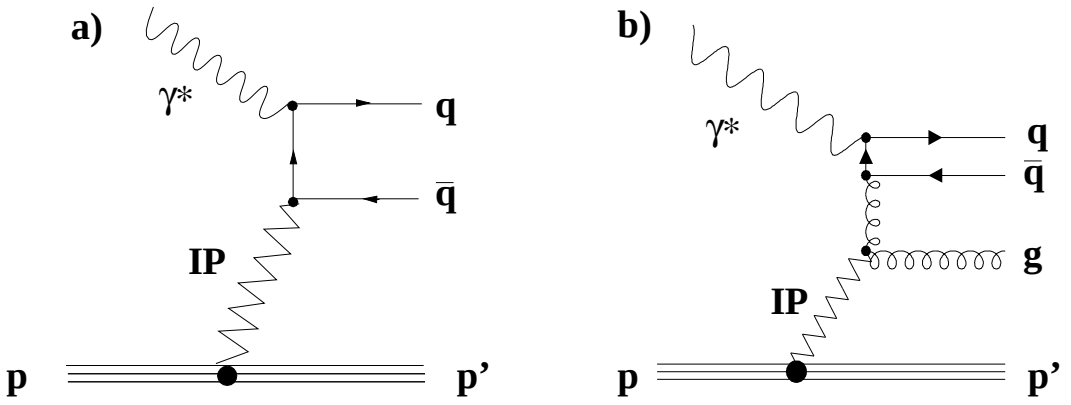

Figure 5.7: Diagrams for photon diffractive dissociation into a) $q\bar{q}$ and b) $q\bar{q}g$ states as implemented in the RIDI MC generator.

The differential cross section for photon dissociation [92] into $q\bar{q}$ pairs can be written as

$$\frac{d\sigma_T(ep \to e'p' + q\bar{q})}{dx dQ^2 dt} = K_2 \frac{\alpha_{em}}{\pi x Q^2}\left(1 - y + \frac{y^2}{2}\right)\frac{[F^{2G}(t) x_{I\!P} G(x_{I\!P}, q^2)]^2}{\sqrt{1 - 4\frac{(k_t'^2 + m_q^2)}{Q^2}\frac{z}{1-z}}}$$
$$\times \alpha_s^2(q^2) \sum_f e_f^2 \frac{4\pi^2 \alpha_{em}}{3Q^2}(1-z)^2 \left[\left(1 - 2\frac{(k_t'^2 + m_q^2)}{Q^2}\frac{z}{1-z}\right)\left[z k_t'^2 + m_q^2\right]^2 k_t'^2 \right.$$
$$\left. + \frac{m_q^2}{4}\left[k_t'^2(2z-1) + m_q^2\right]^2\right] \frac{dk_t'^2}{(k_t'^2 + m_q^2)^5}\left(\frac{k_t'^2}{k_t'^2 + a}\right)^2 dz \quad (5.15)$$

for transversely polarized photons and as

$$\frac{d\sigma_L(ep \to e'p' + q\bar{q})}{dx dQ^2 dt} = K_2 \frac{\alpha_{em}}{\pi x Q^2}(1-y)\frac{[F^{2G}(t) x_{I\!P} G(x_{I\!P}, q^2)]^2}{\sqrt{1 - 4\frac{(k_t'^2 + m_q^2)}{Q^2}\frac{z}{1-z}}}$$
$$\times \alpha_s^2(q^2) \sum_f e_f^2 \frac{4\pi^2 \alpha_{em}}{3Q^2}\frac{(k_t'^2 + m_q^2)}{Q^2} z^2 [k_t'^2(2z-1) + m_q^2]^2$$
$$\times \frac{dk_t'^2}{(k_t'^2 + m_q^2)^4}\left(\frac{k_t'^2}{k_t'^2 + a}\right)^2 dz \quad (5.16)$$

for longitudinally polarized photons.

Here, k_t' is the transverse momentum of the parton closest in rapidity to the scattered proton and defines a second hard scale in addition to Q^2 and $z \equiv \beta$, the momentum fraction of the struck quark with respect to the $\mathbb{P}$ momentum. The argument q^2 of the running coupling constant α_s and of the gluon structure function $G(x_{IP}, q^2)$ is $q^2 = (k_t'^2 + m_q^2)/(1-z)$. The contribution of longitudinal photons is small except for $z \to 1$. The two gluon form factor $F^{2G}(t)$ is unknown and should be measured. In RIDI, it is assumed to have an exponential behavior with a slope of $7\,\mathrm{GeV}^{-2}$.

The differential cross section for production of $q\bar{q}g$ from transversely polarized photons is given by:

$$\begin{aligned}\frac{d\sigma_T(ep \to e'p' + q\bar{q}g)}{dx dQ^2 dt} &= K_3 \frac{\alpha_{em}}{\pi x Q^2}\left(1 - y + \frac{y^2}{2}\right)[F^{2G}(t) x_{\mathbb{P}} G(x_{\mathbb{P}}, q'^2)]^2 \\ &\times \left[\frac{9}{16}\alpha_s^2(q'^2)\frac{dk_t'^2}{(k_t'^2 + m_g^2)^2}\right] 2\sum_f e_f^2 \frac{4\pi^2\alpha_{em}}{Q^2} \\ &\times \frac{\alpha_s(q'^2)}{4\pi}[z"^2 + (1-z")^2]dz" \frac{dq"^2}{q"^2}\left(\frac{k_t'^2}{k_t'^2 + a}\right)^2 w_g \frac{dx_{\mathbb{P}}}{x_{\mathbb{P}}} \quad , \end{aligned} \tag{5.17}$$

where z'' is the argument of the gluon to quark splitting kernel, q'' the momentum transferred through the t-channel quark line, and $w_g = (1-x_g)^3(2x_g+1)^2$ with $x_g = x/(x_{IP} z'')$. The contribution from longitudinal photons to the $q\bar{q}g$ cross section becomes relevant only at next to leading order and is computed via the relation $R = \sigma_L/\sigma_T$ from the photon-gluon fusion cross section (see [95]).

The topology of the hadronic final state depends strongly on the ratio of $q\bar{q}$ to $q\bar{q}g$ final states. Their relative contribution is determined by the K-factors K_2 and K_3 in the cross sections of Equations 5.15 and 5.16 and Equation 5.17 for $q\bar{q}$ and $q\bar{q}g$, respectively. These K-factors take into account the corrections due to one loop (virtual gluon) contributions.

Parton shower and fragmentation are done using JETSET [78].

The RIDI sample was generated in the kinematic range defined by Q^2 between 2 and 2000 GeV^2, M_X^2 between 3 and 10000 GeV^2, and $x_{BJ} < 0.1$, corresponding to a total cross section of 169 nb.

5.1.7 Beam Halo Background

The major background contribution to a diffractive event sample selected with the LPS is given by non-diffractive DIS events at x_L near 1. The proton tracked in the LPS does not originate from the ep collision, but comes from the halo of the proton beam. Since the halo is assumed to be approximately constant over the running period, its contribution should be uniform over all runs.

The quantity of $E + p_z$ summed over all final state particles (including the electron) is conserved and amounts to twice the initial proton energy, 1640 GeV. If a scattered proton with $x_L > 0.95$ is observed in the LPS, its contribution to the total $E + p_z$ is $2 \cdot x_L \cdot 820\,\text{GeV} > 1558\,\text{GeV}$. Therefore, only a maximum of 82 GeV can be seen in the central detector.

To estimate the contribution of this kind of background, data events with $E + p_z > 130$ GeV and a track in the LPS were combined with DIS events from the DJANGO MC generator [96]. The sample was normalized using the total $E + p_z$ distribution of Figure 5.9d, so that the sum (solid line) of RAPGAP (dashed-dotted) and the beam-halo distribution (hashed histogram) describes the data in the high $E - p_z$ tail.

5.2 ZEUS Monte Carlo Simulation

Events generated with Monte Carlo generators are passed through the ZEUS detector and trigger simulation, off-line reconstruction, and the physics analysis chain.

The ZEUS detector simulation is based on the GEANT [97] package, taking into account the geometry, position, and material of various detector components and incorporates the present understanding of the detector from test beam results and physics analysis. Hadronic and electromagnetic particles are tracked through the detector volumes simulating the response of the detector materials to electromagnetic and hadronic interactions. The trigger decision, which is based on the detector component signals, is simulated with the software package Zeus Geant Analysis (ZGANA) [98]. The detector simulation together with the trigger software package is called Monte Carlo for ZEUS Analysis, Reconstruction and Trigger (MOZART).

The input to the ZEUS detector simulation is a list of particles which includes their type, momentum four-vector, and production vertex from the ep event generator. The simulated detector response of the various components is stored in the same ADAMO tables as real data and can then be processed with the same reconstruction and analysis code. In addition, the true MC event information is available.

The MC samples for the analysis were processed with the MOZART version 97t1.3.

5.3 LPS Standalone Simulation with MOLPS

When the version 97t1.3 of the MOZART software package was released, the alignment (see Section 4.5) was not ready and was therefore not included in the release. As a result, the proton track reconstruction in the MC simulation was not

useful. Instead, the program library MOLPS was used to simulate the LPS tracking.

MOLPS is based on the MOZART LPS routines [99, 100], but is linked with the physics analysis job. The advantage of the method is that new calibration constants for the LPS can be easily included in the GAFs and the LPS simulation can be rerun, needing just the generated proton from the event generator as input. It is therefore not necessary to wait for a new MOZART release and to reprocess all simulated events. This procedure, however, is very time consuming on the analysis job. Processing one LPS event takes about 2 sec when invoking MOLPS.

Many systematics checks on the acceptance and resolution of the LPS are possible by changing parameters of the simulation with MOLPS. In practice, due to the large amount of computing time needed, this is not a feasible method.

The LPS simulation, like the rest of the ZEUS detector simulation, uses the GEANT software to model the response, acceptance, and efficiency of the detectors. However, not only the detector volumes of the silicon planes need to be included, but also about 90 m of the HERA beam line with its magnets and aperture, and the beam itself.

LPS Detector: Since the LPS detectors use the binary readout system, an LPS channel responds if it is hit by a charged particle. On top of this simple procedure, inefficiencies, noise, and dead channels need to be included. Inefficiencies in the planes were determined from physics data and randomly applied to each LPS track. Noise is simulated assuming 0.2 hits per event per plane randomly generated following a Poisson distribution. These noise hits are randomly positioned on the detector and added to the raw data. Dead and noisy channels are suppressed at the reconstruction level using dead and noisy channel lists in the Monte Carlo database, which were determined from the LPS data quality monitoring during the data taking period.

Only one position of the LPS is included in the simulation. Changes in the resolution and acceptance of the LPS detectors due to changing beam conditions during the data taking period and detector movements during LPS operations were not taken into account at this stage. Their average effect was included by smearing the MC distributions to match the data, when necessary (Section 5.4).

HERA Magnets and Apertures: Since the beam pipe apertures have a strong influence on the acceptance of the LPS detectors, the exact shape of the beam pipe matching the blue print specifications is included in the LPS simulation whenever possible. The position of these apertures can be checked using physics tracks during the alignment procedure (Section 4.5). If they are found to be inconsistent with the pot positions and the track fitting, they can be relocated.

The accurate position and field strength of the dipole and quadrupole magnets

inside the beam pipe necessary for the track reconstruction is simulated in GEANT. These parameters are also reviewed during the alignment procedure and can be adjusted accordingly. However, since they are surveyed by the HERA personnel and the survey results are used in the GEANT simulation, changes of these parameters need to be taken very seriously.

Beam Simulation: The beam parameters are essential for the accurate momentum reconstruction of the scattered proton: the vertex position is needed for vertex constraint tracks of events recorded in only two stations; the angle of the beam at the IP determines the measurement of the transverse momentum; the beam emittance dominates the momentum resolution. The beam tilt parameters are determined from the alignment and can be set externally for MOLPS by control cards. The vertex information is taken from MOZART. The values of these parameters for the beam simulation in 1997 are:

- vertex position: $x = -0.21$ mm and $y = -0.38$ cm,
- vertex Gaussian width: $\sigma_x = 0.33$ mm and $\sigma_y = 0.90$ mm,
- proton beam tilts: $p_x = 33$ MeV and $p_y = -68$ MeV,
- beam emittance of Gaussian width: $\sigma_{p_x} = 40$ MeV and $\sigma_{p_y} = 90$ MeV.

5.4 Comparison Data with Monte Carlo

Many variables were compared to ensure a reasonable description of the data by the MC models. The RAPGAP sample (with the background contribution of DIS overlay events as described in Section 5.1.7 added) was used to correct the data for acceptance and detector effects. Great care was taken that this sample reproduces the reconstructed data as good as possible.

In Figure 5.8 the momenta p_x and p_y reconstructed with the LPS (open circles) are compared with the generated values (histogram). A systematic shift of $+0.03$ GeV in p_x and -0.05 GeV in p_y can be observed and attributed to the alignment. Figure 5.9 compares a few kinematic variables which are effected by reconstruction problems. The x_L distribution (Figure 5.9a) shows a shift between data and MC. Also the width around $x_L = 1$ is not properly reproduced. This is due to a slight misalignment (shift) and the fact that the MC x_L is only reconstructed for one set of LPS and beam positions, while the data show the average over the full running period. In addition, the shape of the x_L spectrum is not well described, which can be attributed to the fact that the MC sample contains $\mathbb{R}$ exchange in addition to $\mathbb{P}$ exchange.

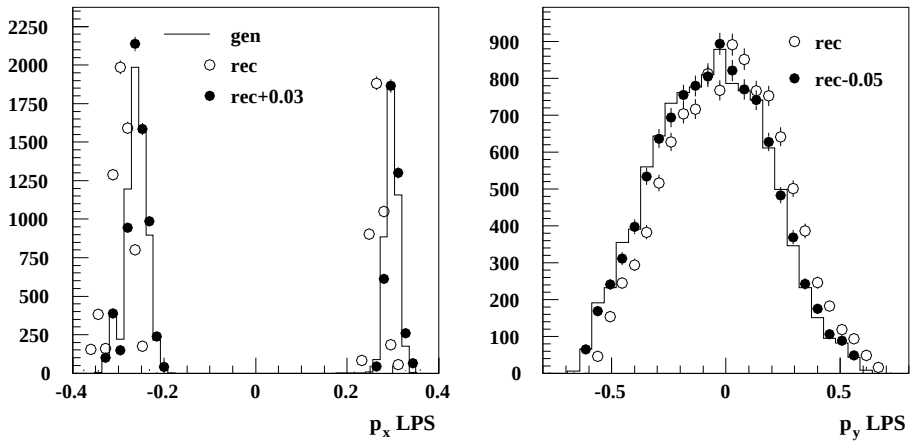

Figure 5.8: Comparison of the p_x and p_y (open circles) reconstructed with the LPS with the generated values (histogram). A systematic shift of $+0.03$ GeV and -0.05 GeV, respectively, is observed and can be corrected (dots).

The electron energy spectrum (Figure 5.9b) shows a shift by about 2.5 % between data and MC. This shift is expected, since a correction factor to the energy measured in the RCAL needs to be applied. However, electron finding with SINISTRA is advised to be done with the uncorrected RCAL cells. This correction factor should be applied only to data, but not MC and can therefore explain the observed shift.

As a result of these mismatches between data and MC x_L and electron energy distributions, the resulting $E-p_z$ (Figure 5.9c) and $E+p_z$ (Figure 5.9d) distributions are poorly described as well. Since they play an important role in the data selection, a fix of these reconstruction problems is necessary. To ensure good agreement between data and MC, the following corrections were applied to the reconstructed values:

- shift p_x reconstructed by the LPS: $p_x \rightarrow p_x + 0.03$ GeV,
- shift p_y reconstructed by the LPS: $p_y \rightarrow p_y - 0.05$ GeV,
- shift the data x_L according to $x_L = (x_L^{-1} + 0.0014)^{-1}$ to accommodate for the misalignment,
- smear the MC x_L according to $x_L = x_L + (x_L - x_L^{true}) * 0.8$ to account for the average effect of changing data taking conditions,
- scale in the data the energy E_e of the scattered electron by $E_e \rightarrow 1.025 \cdot E_e$ to include the RCAL correction.

Figure 5.10 shows the same distributions as Figure 5.9 with the above changes applied. The x_L and E_e distributions are in reasonable agreement now. The effect

on the $E - p_z$ and $E + p_z$ distributions is quite dramatic and the data are now well reproduced by the MC.

5.4.1 RAPGAP Reweighting

IR Contribution Looking at the x_{IP} distribution (Figure 5.10e) suggests that the generated distribution is not in agreement with the data. A large excess at high values of x_{IP} can be seen, which is due to a large fraction of events mediated by IR exchange. After normalizing the distributions to the luminosity, an additional normalization scale of 0.68 had to be applied to the MC sample. The generated total cross section for the phase space defined in Section 5.1.2 of 59.2 nb contains a contribution of 31.0 nb from the IR exchange alone, more than 50%. Since this large IR contribution clearly fails to describe the data, the sample was reweighted to remove the IR part. The reweighting function uses the routines of the RAPGAP generator to calculate the structure functions F_2 for both, IR and IP exchange as included in the available MC sample, and for the IR exchange alone. The weight is then given by the ratio of these two structure function.

The result of this reweighting is shown in Figure 5.11. The x_{IP} distribution is in much better agreement now. In fact, the MC has now a little less events in the high x_{IP} region than the data, suggesting that a small contribution from IR exchange would be desired. The same conclusion can of course be drawn from the x_L spectrum, where the MC shows an excess at $x_L = 1$ pointing to a normalization problem. Reweighting the MC to obtain a IR free sample also fixed the normalization problem of the original sample. No additional scale factor was applied to the distributions in Figure 5.11.

In summary, the measured distributions of kinematic variables show no evidence of a strong IR contribution. The contribution of IR exchange in the RAPGAP sample amounts to about 50% of the total diffractive cross section defined in the phase space given in Section 5.1.2. The sample reweighted to obtain a MC sample, which only contains contributions from IP exchange alone, gives an accurate description of the kinematic variables.

Figures 5.12 to 5.15 show a comparison of data and the sum of the reweighted RAPGAP Monte Carlo and DIS background for a number of DIS and LPS variables. The variables will be defined later (Section 6.3). The sample now gives a reasonable description of the data. The solid vertical lines, where shown, illustrate the cuts applied for the event selection. The cuts will be discussed in detail in Section 6.5. For these plots, all event selection cuts were applied, except for the ones on the variable displayed.

The results for the RIDI generator are also shown in the Figures 5.9 to 5.11. After normalizing to the luminosity, an additional scale of 0.3 had to be applied.

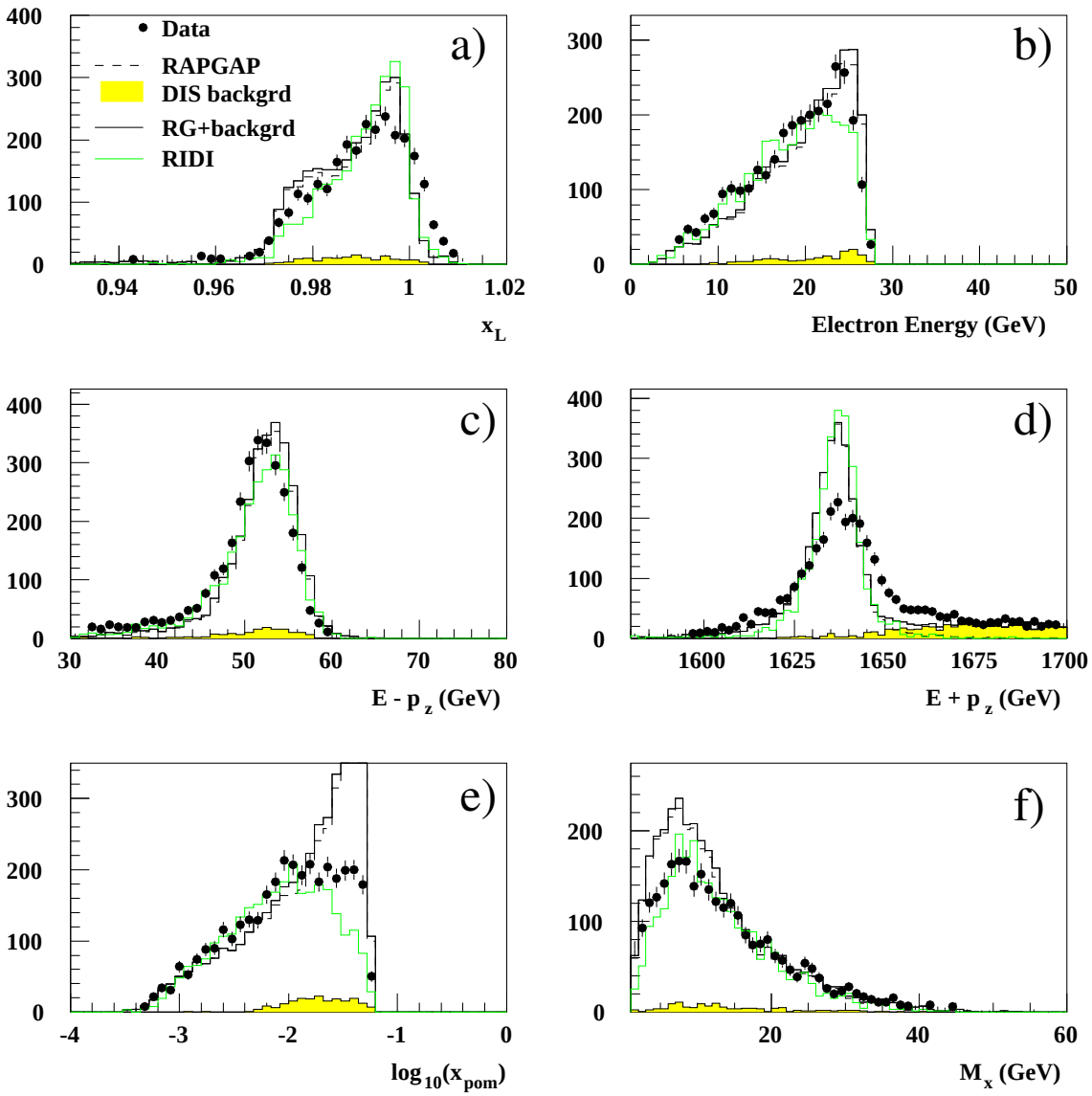

Figure 5.9: Comparison of some distributions of kinematic variables between 1997 data, RAPGAP Monte Carlo (dashed-dotted), DIS background (hashed), RAPGAP+background (solid) and RIDI Monte Carlo (grey). The RAPGAP sample, which is the primary MC, does not describe the data well. There are differences in the reconstruction of data versus MC (x_L, electron energy), but also in the shape of some distributions ($x_{I\!P}, M_X$).

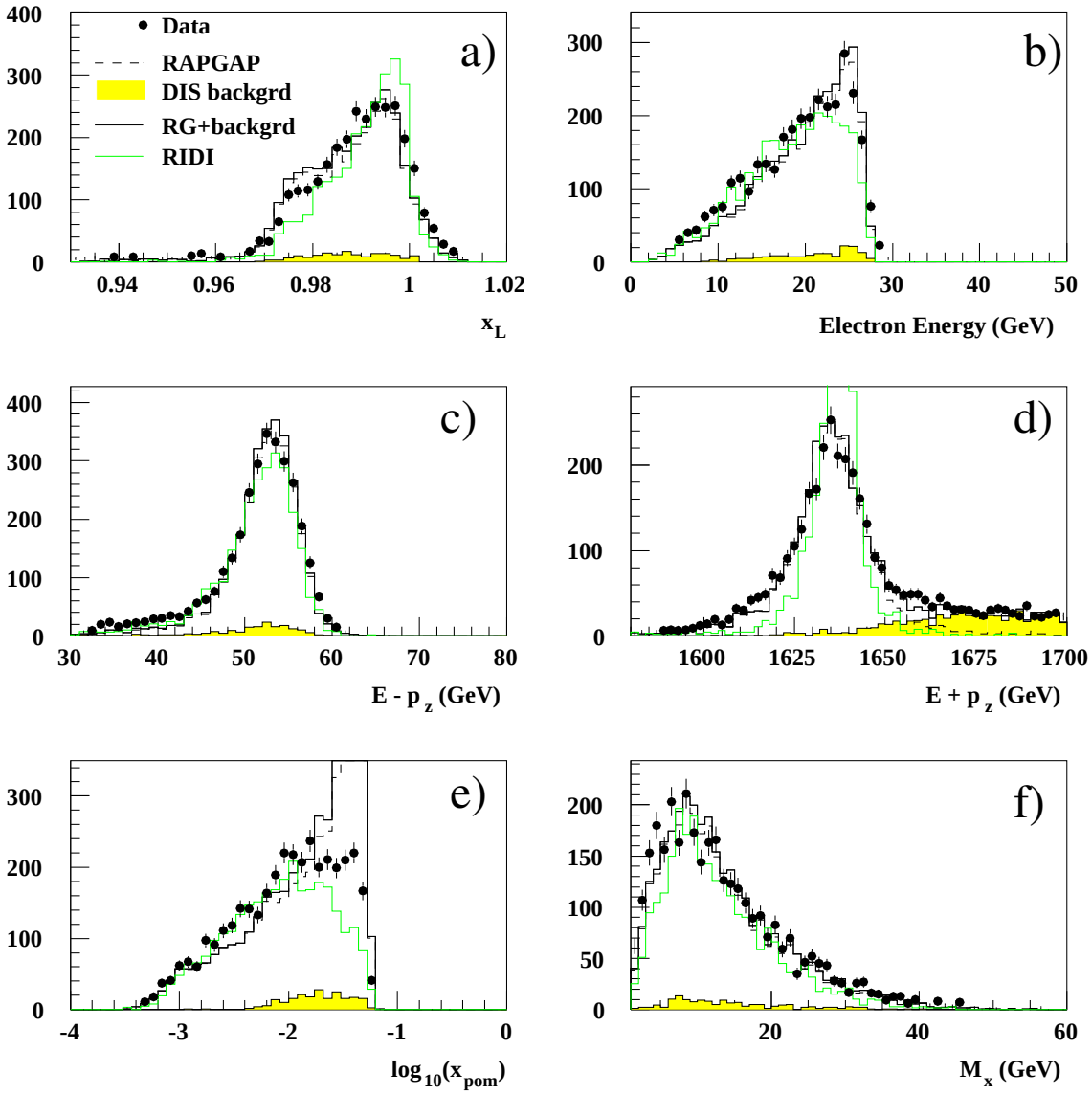

Figure 5.10: Comparison of some distributions of kinematic variables between 1997 data, RAPGAP Monte Carlo (dashed-dotted), DIS background (hashed), RAPGAP+background (solid), and RIDI Monte Carlo (grey) after the reconstruction problems in x_L and the electron energy were fixed.

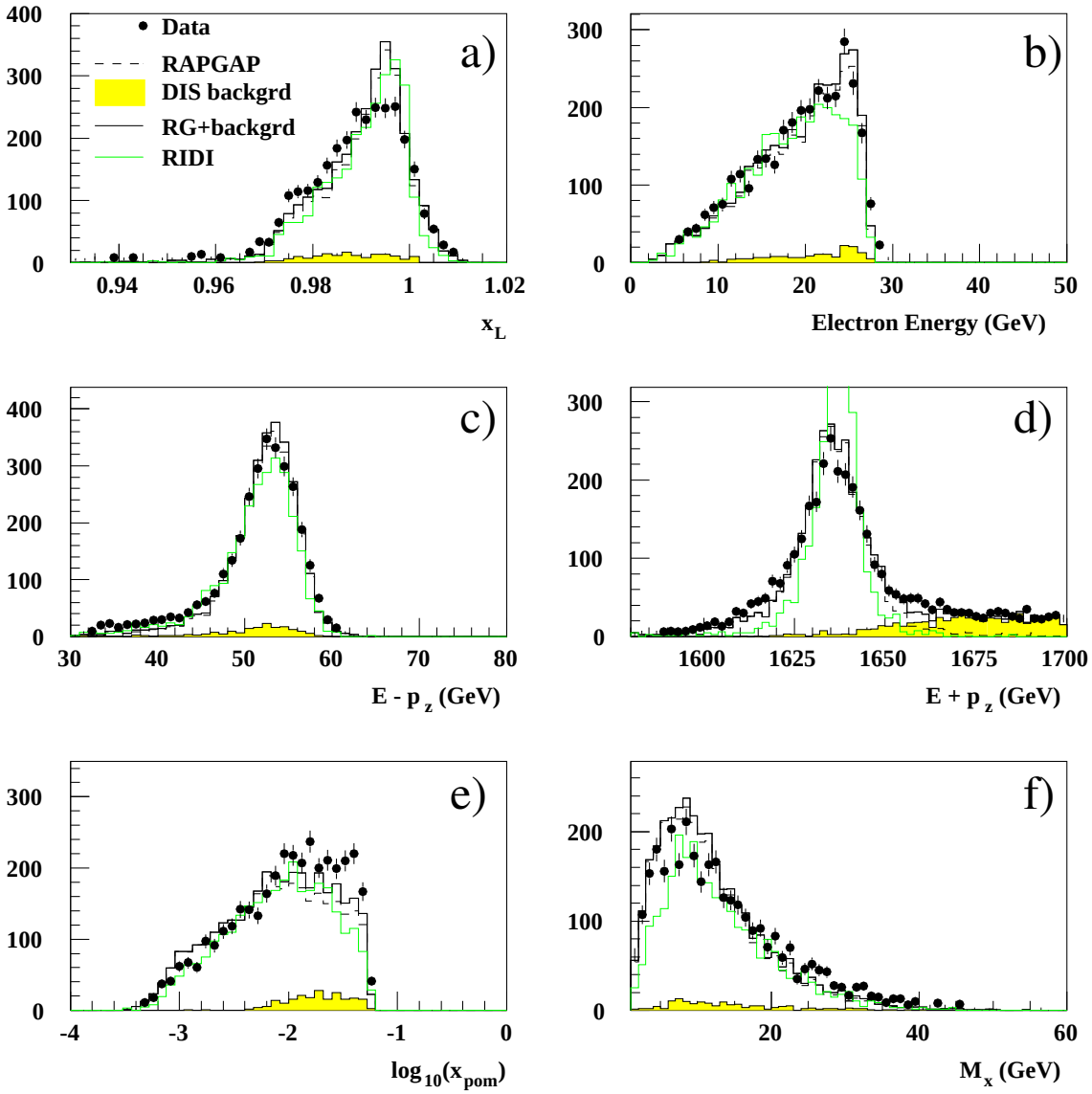

Figure 5.11: Comparison of some distributions of kinematic variables between 1997 data, RAPGAP Monte Carlo (dashed-dotted), DIS background (hashed), RAPGAP+background (solid), and RIDI Monte Carlo (grey). The RAPGAP sample was reweighted to take out the contribution from IR exchange. The x_{IP} distribution is now in reasonable agreement with that data.

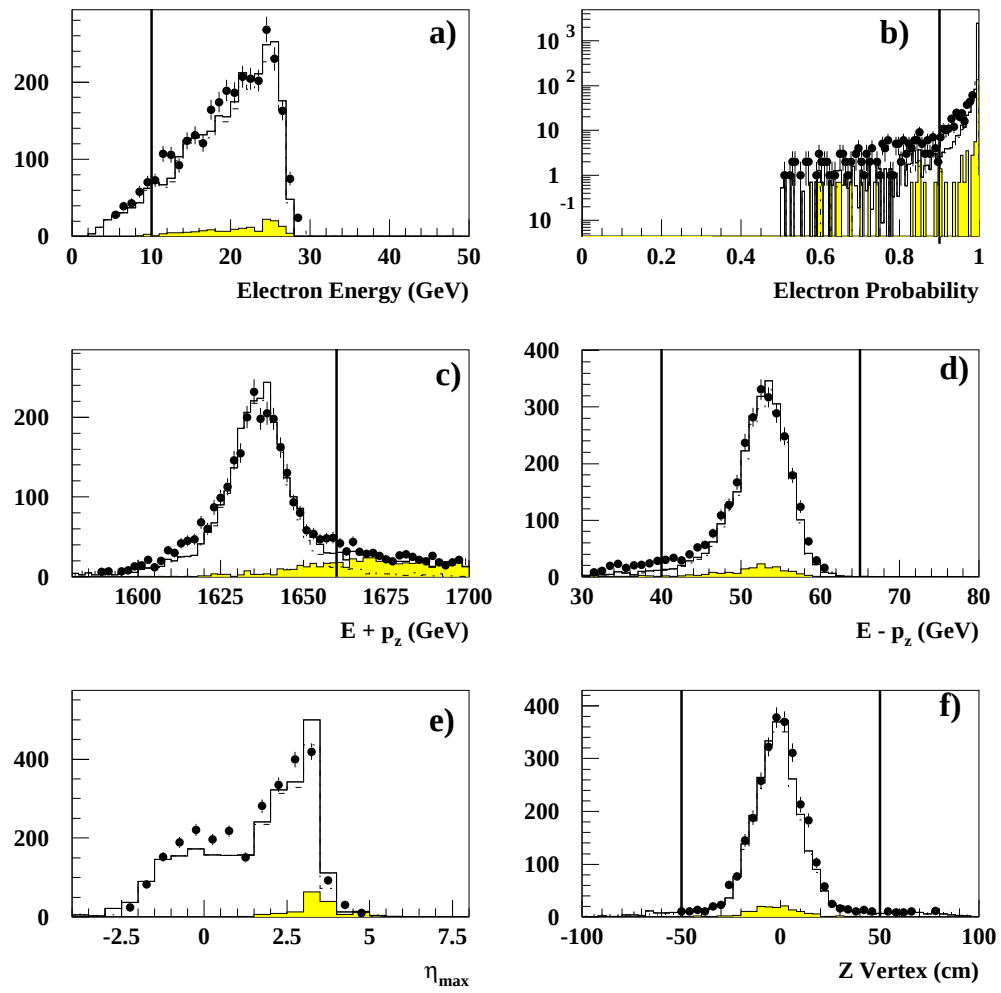

Figure 5.12: Comparison between data and RAPGAP with DIS background for various kinematic distributions. The corrections and weights described in this section are applied. The vertical solid lines (where shown) illustrate event selections cuts (Section 6.5).

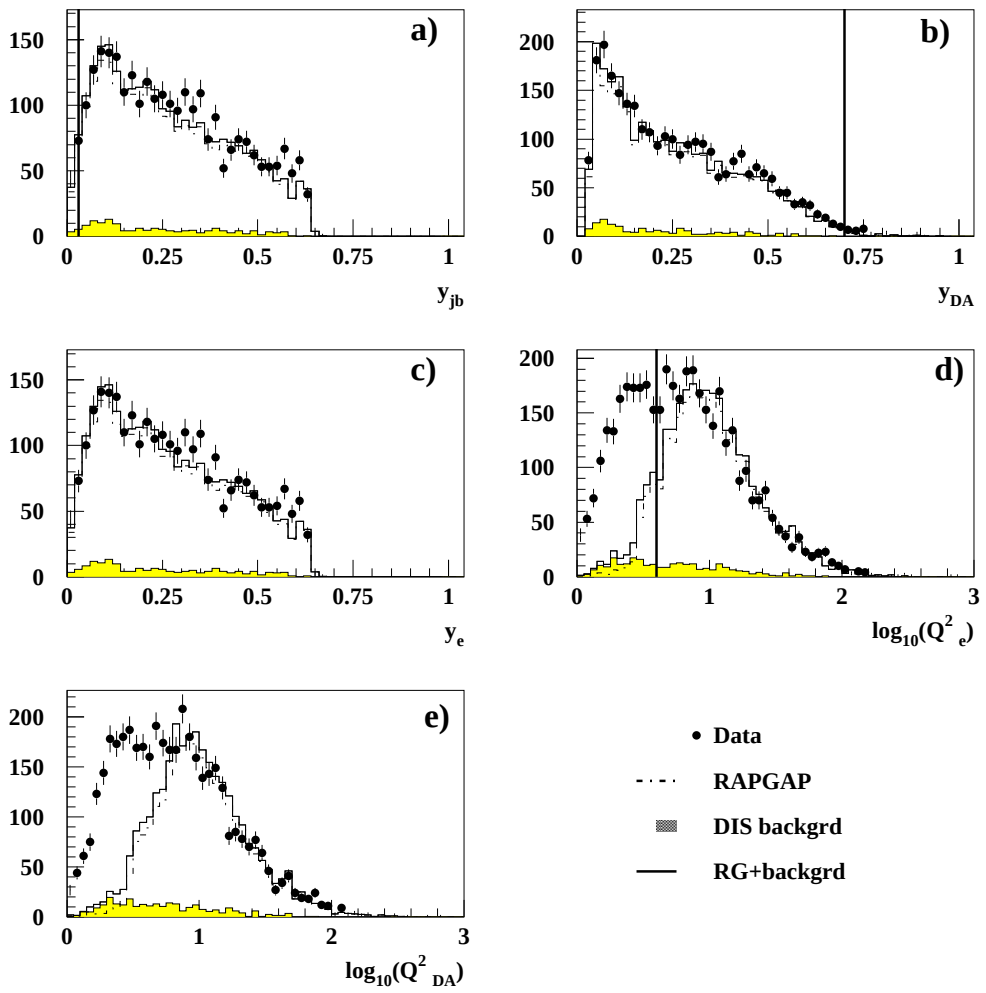

Figure 5.13: Comparison between data and RAPGAP with DIS background for various kinematic distributions. The corrections and weights described in this section are applied. The vertical solid lines (where shown) illustrate event selections cuts (Section 6.5).

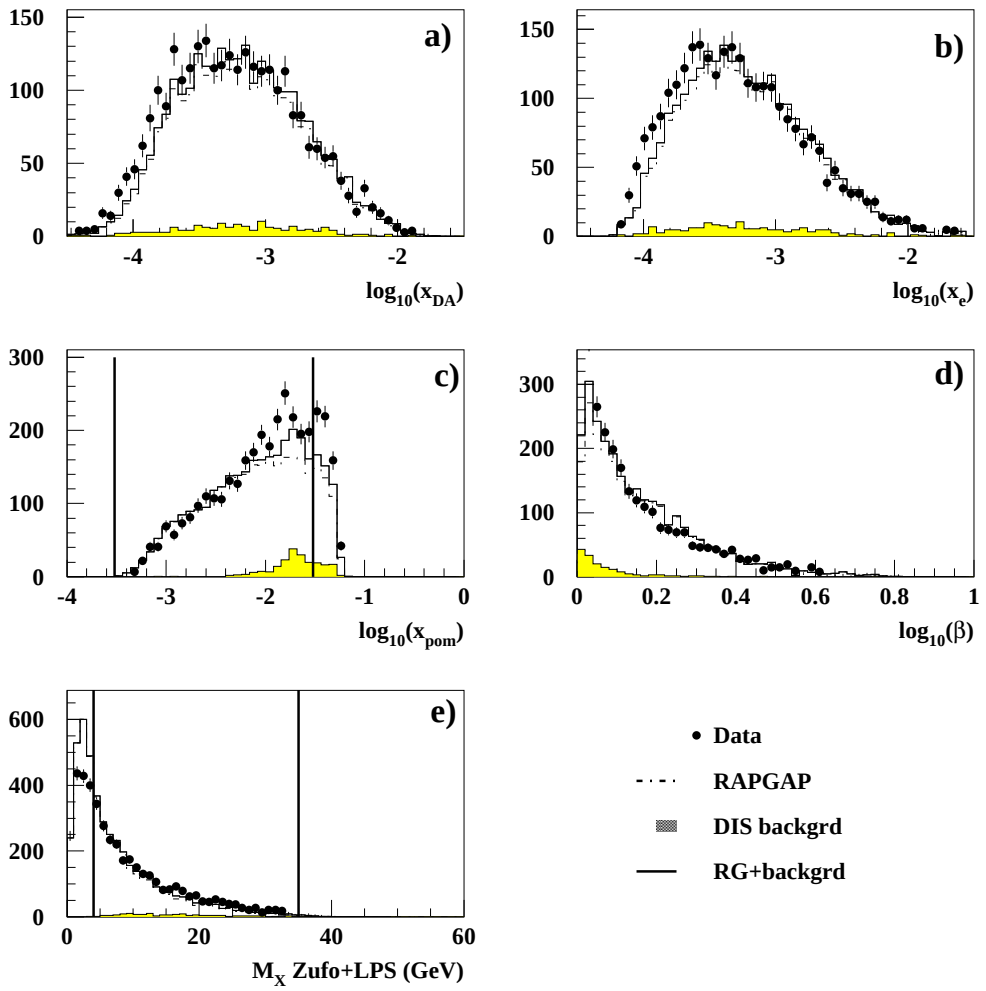

Figure 5.14: Comparison between data and RAPGAP with DIS background for various kinematic distributions. The corrections and weights described in this section are applied. The vertical solid lines (where shown) illustrate event selections cuts (Section 6.5).

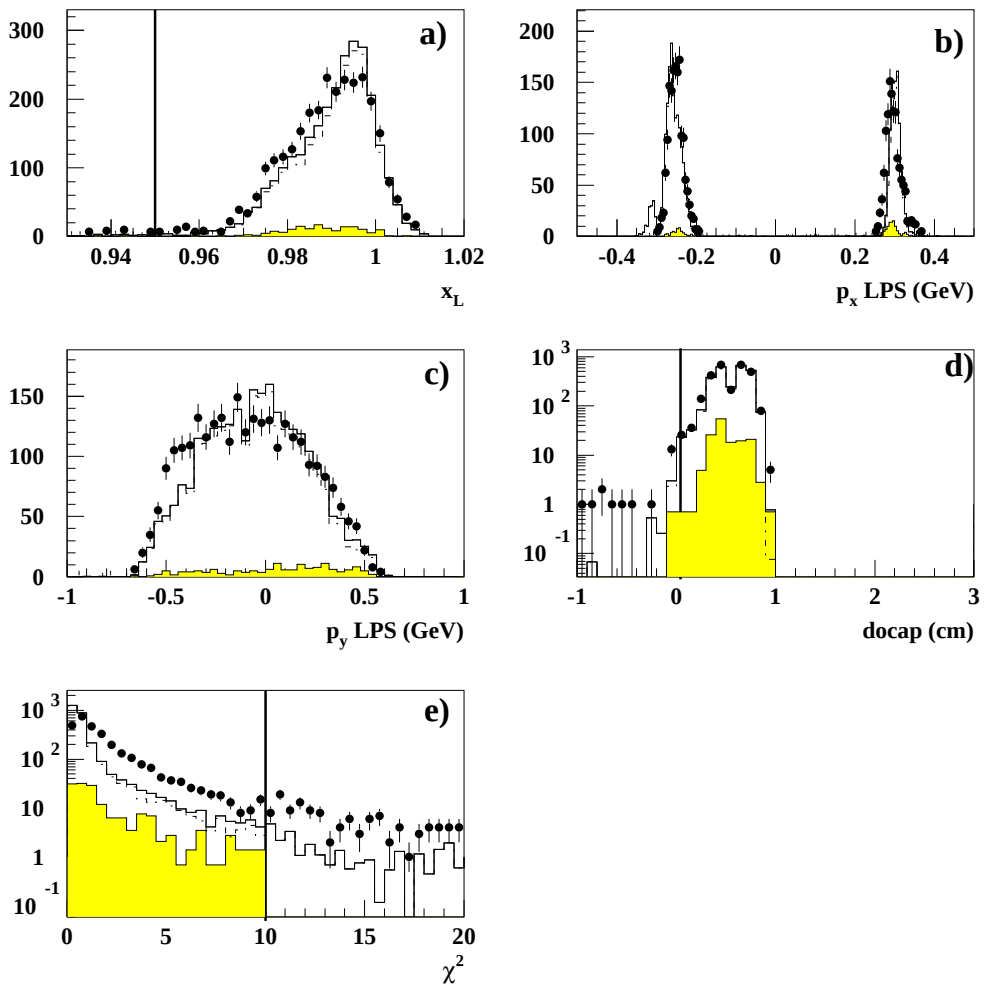

Figure 5.15: Comparison between data and RAPGAP with DIS background for important LPS distributions. The corrections and weights described in this section are applied. The vertical solid lines (where shown) illustrate event selections cuts (Section 6.5).

Reweighting of the Final State Another shortcoming of the RAPGAP sample is visible when looking at the hadronic final state, which is produced in the scattering of the virtual photon and the Pomeron. The top plot of Figure 5.16 shows a measurement of the reconstructed hadronic final state in terms of the event shape variable thrust T (see Section 7.2.1 for the definition of T). RAPGAP (open circles) clearly fails to describe the $<T>$ as a function of hadronic mass M_X over the full M_X range. This can be attributed to the necessity to run the generator with a cut on the minimum $p_T^2 > 3$ GeV^2 of the partons for the production of a BGF type event. This cut suppresses the production of partons (and subsequently hadrons) from the boson-gluon fusion process. The lines in the top plot of Figure 5.16 show the contribution of QPM (solid) and BGF (dashed) type processes. The suppression of BGF events causes the hadronic final state to be more collimated, which results in higher thrust values.

By remixing the contributions of QPM to BGF type events, one can tune the MC to describe the data. The needed fraction $x_{BGF} = N_{BGF}/N_{total}$ of BGF type events can be extracted according to:

$$\bar{T}_{data} = x_{BGF} \cdot \bar{T}_{BGF} + (1 - x_{BGF}) \cdot \bar{T}_{QPM} \tag{5.18}$$

with $\bar{T}_{BGF}$ and $\bar{T}_{QPM}$ being the average T values for the BGF and QPM type events, respectively, and $\bar{T}_{data}$ the value measured in the data. If R gives the current ratio of the number of BGF events to all events, the required weights can be calculated to:

$$weight_{BGF} = \frac{x_{BGF}}{R} \tag{5.19}$$

$$weight_{QPM} = \frac{1 - x_{BGF}}{1 - R}. \tag{5.20}$$

The result of this procedure is summarized in Table 5.1 as a function of the generated hadronic mass. The large variation in the needed weights is a result of the fluctuations observed in the reconstructed average values of thrust seen in Figure 5.16. However, assuming that the weights are a smooth function of the mass M_X (for example, a polynomial fit), and applying it to the RAPGAP sample gives an accurate reproduction of the final state in terms of thrust. Large or negative weights should be avoided. The result gives a nice description not only of the final state in terms of $<T>$ (Figure 5.16 middle), but also improves the description of single particle distributions like the energy flow (bottom plot), substantially.

However, these weights cannot be used as a "general" weight to tune the MC sample. The reason becomes apparent when looking at the M_X distribution shown in Figure 5.17. In the left half, we see that RAPGAP (solid line) does describe the

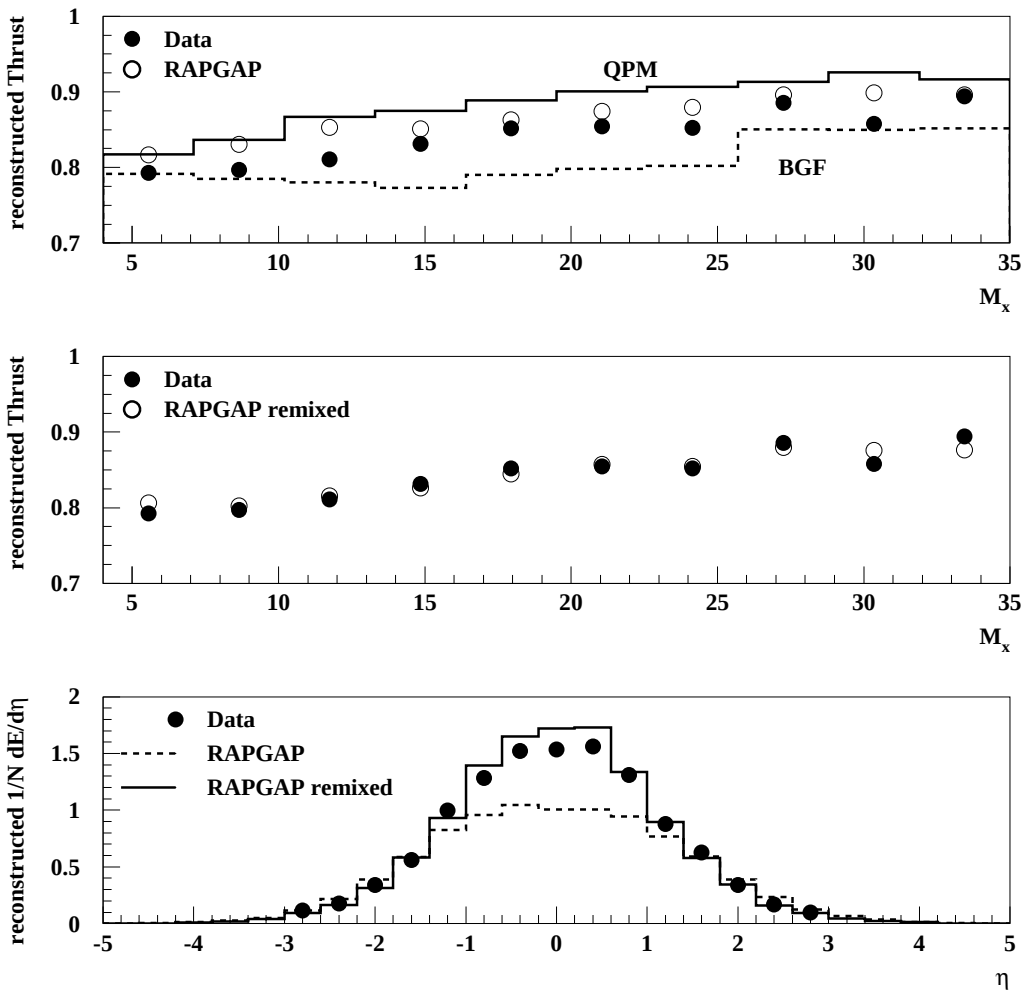

Figure 5.16: Comparison of the reconstructed hadronic final state in terms of thrust T between data (dots) and RAPGAP (open circles). The top plot shows that RAPGAP fails to describe the final state correctly. Remixing the contributions of QPM (solid line) and BGF (dashed) can be used to describe the data (middle plot). It also gives an improved description of single particle distributions like energy flow (bottom plot).

M_x^{gen}/GeV	R	x_{BGF} needed	$weight_{BGF}$	$weight_{QPM}$
5.43314	0.03137	1.23735	39.44515	-0.24504
8.52171	0.10178	0.85422	8.39250	0.16230
11.57566	0.15244	0.65654	4.30681	0.40523
14.70123	0.22545	0.39423	1.74864	0.78209
17.78918	0.26525	0.35314	1.33136	0.88038
20.96036	0.25102	0.42531	1.69435	0.76729
24.11794	0.26083	0.54336	2.08319	0.61778
27.20082	0.28954	0.46452	1.60435	0.75370
30.24105	0.35876	0.89612	2.49781	0.16200
32.91783	0.30902	0.47234	1.52851	0.76364

Table 5.1: Fraction of BGF type events in the RAPGAP sample with H1fit2, desired fraction to describe the measured thrust, and the necessary weights for BGF and QPM type events as a function of generated mass M_X. The fluctuations of the weights reflect the fluctuations of the reconstructed $<T>$ values used to obtain them. Taking the weights as a smooth function of M_X is consistent with the values display in the table.

M_X distribution of the data (dots) well. The M_X distributions of QPM (dashed) and BGF (dotted) type of processes are also plotted. Their M_X distributions are quite different and remixing them will distort the M_X distribution of the MC (right, solid line). The large discrepancies in the low mass region can be again attributed to the large p_T^2 cut imposed on the BGF diagram, which suppresses this kind of events. In addition, the overall normalization will be changed, since the cross section is affected by these weights as well.

The weights of Equations 5.19 and 5.20 were therefore not applied to the RAPGAP MC, since they introduce large model dependencies. Since the remixed RAPGAP sample does not represent a real physics model, these model dependencies do not reflect an accurate estimation of the uncertainty due to the MC model, which is used for the unfolding procedure. However, the numbers quoted in Table 5.1 give an indication in which way the MC needs to be tuned in order to describe the diffractive final state.

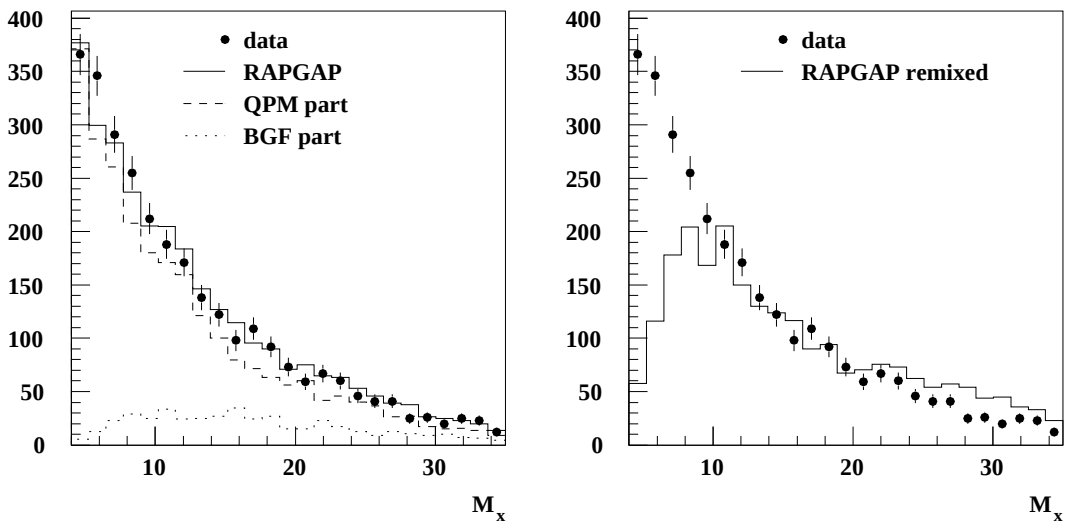

Figure 5.17: Comparison of the M_X distribution between data (dots) and RAPGAP MC (solid) in the left plot. Also shown are the contributions from QPM (dashed) and BGF (dotted) type of processes. Since their M_X distributions are very different, reweighting the sample with the weights calculated in Equations 5.20 and 5.19 does not describe the data M_X distribution anymore (right). M_X was calculated from the hadronic final state particles.

Chapter 6

Reconstruction of Diffractive Kinematic Variables

6.1 Electron Identification

Neutral current, deep-inelastic scattering events are identified by the presence of the scattered electron in the final state. Therefore, the correct and efficient reconstruction of the energy and position of the scattered electron is of great importance to any DIS analysis. Momentum conservation forces the transverse momentum of the electron and of the current jet to be balanced. Due to the back-to-back topology in the azimuthal angle, the electron is isolated from any hadronic activity and can easily be identified. This is true for a large part of the (x, Q^2) plane. However, in the high y, low x region the scattered electron transfers a large part of its initial energy to the struck quark. As a result, the energy of the scattered electron is low and the current jet from the struck quark goes backwards. In this case, hadronic and electromagnetic energy deposits in the calorimeter overlap and the separation of the electron becomes difficult. Inactive material in the inner detector (cables, CTD end plate, etc.) cause low-energy electrons to shower before reaching the calorimeter, giving rise to energy deposits similar to hadronic ones, which again makes it difficult to identify them as electrons. In addition, a low energy electron can be "faked" by electromagnetic showers from $\pi^\circ \rightarrow \gamma\gamma$ decays or by low energy hadronic activity from photoproduction events, where the scattered electron escapes down the beam pipe.

6.1.1 Electron Finding with SINISTRA

Electron identification was performed using the SINISTRA [101, 102] electron finder. SINISTRA is a neural network algorithm based on islands of calorimeter

cells. Cells of energy deposits, which are likely to belong to the shower of a single particle, are merged to form a cluster, i.e., a bump in the energy deposit surrounded by lower energy deposits. The energy of each tower in the calorimeter is compared to the energy of its neighbors. A calorimeter tower (see Section 3.4) is called a *seed* for an island if all neighboring towers have lower energy. All towers with lower energy are linked to the neighboring tower with the highest total energy. A seed together with its linked neighbors forms an *island*. The largest possible island is a 3×3 array of towers, which is sufficient to contain the shower of any single electromagnetic particle.

The neural network of SINISTRA takes as input a multidimensional space consisting of 55 variables: 54 energy deposits from the EMC and HAC section of the 3×3 tower array and the cosine of the angle of coincidence. The output is a projection onto one variable, which can be interpreted as the probability P that an island corresponds to the scattered electron ($P \simeq 1$) or is of hadronic origin ($P \simeq 0$).

In order for a candidate to be accepted as an electron, a probability cut of

$$P > 0.9$$

was required. In addition, a track in the CTD was required for a candidate to be accepted as the DIS electron, if the candidate was within the acceptance region of the CTD. If more than one candidate was found with equal probability, the candidate with the highest energy was selected.

The top row of Figure 5.12 shows the energy (a) and probability (b) of the SINISTRA electron.

6.1.2 Electron Position Reconstruction

If the impact position of the electron is known, the electron scattering angle can be reconstructed using the event vertex as a second space point. If the electron was recorded in the SRTD (see Section 3.5), the electron position was taken from the SRTD reconstruction, which falls in the ranges $-34.0 < X < 32.0$ cm and $-33.3 < Y < 32.7$ cm. The SRTD information was also used to correct the electron energy returned from SINISTRA.

For non-SRTD hits, the position of the scattered electron was determined from the energy sharing between the two sides (left and right) of a calorimeter cell using the imbalance

$$imbalance = \frac{E_{left} - E_{right}}{E_{left} + E_{right}}$$

which is strongly correlated with the impact point.

However, after all event selection cuts (Section 6.5) all electrons were recorded also in the SRTD. The electron position reconstruction is illustrated in Figure 6.1.

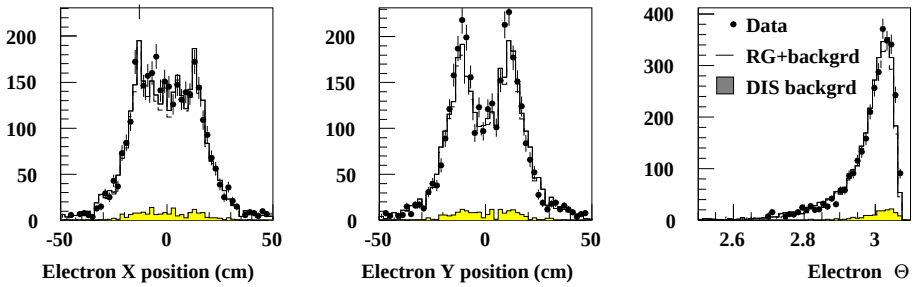

Figure 6.1: Comparison between data and RAPGAP with DIS background for the position reconstruction of the scattered electron. Shown are the X (left), Y (middle) position, and the scattering angle θ (right).

6.2 Final State Particle Reconstruction with ZUFOs

After the electron has been found and the corresponding energy cells are removed from the event, hadronic objects need to be identified to fully reconstruct the event. To do so accurately, not only should the sum of calorimeter cells be used, but the tracking information from the CTD, which can provide an improved resolution on the four-momenta of hadronic particles, should be used as well.

The *hadronic energy flow algorithm* provides the means to use the tracking information instead of calorimeter energy clusters whenever the CTD gives a better momentum resolution than the calorimeter cluster. Figure 6.2 shows a schematic view of the energy flow algorithm. After the electron calorimeter clusters and CTD track have been removed, the energy deposits in the calorimeter cells are clustered into cone islands. CTD tracks from charged particles are then extrapolated to the face of the calorimeter and associated with clusters. The result of this procedure are groups of topologically connected tracks and clusters. Next, a decision has to be made for each group about which information should be used: the one from the CAL or the one from the CTD. In three cases, the decision is simple.

1. Good tracks, which are not associated with any cluster, are counted as charged energy with an invariant mass equal to the π meson mass and a momentum given by the momentum of the track.

2. Clusters, not associated with any track, are counted as neutral energy in such a way that $E^2 = p^2$.

3. Clusters associated with more than three tracks (so-called *jet clusters*) are counted as one jet using the calorimeter information with $E^2 = p^2$.

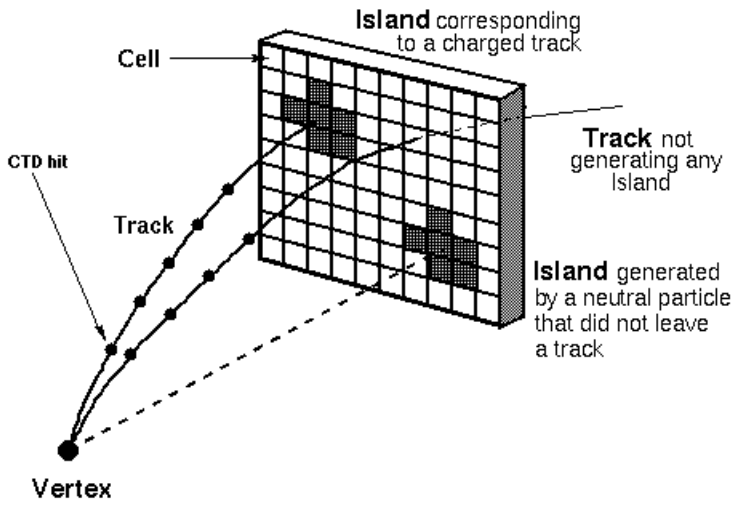

Figure 6.2: Schematic representation of the clustering of calorimeter and CTD information to form energy flow objects (ZUFOs).

For all other track-cluster combinations, the decision, whether the CTD information is used instead of the calorimeter, is based on two requirements, which have to be fulfilled simultaneously.

1. The energy deposit in the calorimeter is due to the associated track alone.

2. The momentum resolution of the track is better than the energy resolution of the calorimeter.

The details of how to ensure that these requirements are met can be found in [103]. The output of this energy flow algorithm is most commonly referred to as ZEUS Unidentified Flow Object (ZUFO).

In this analysis, version 6.2 of the ZUFO code was used. In addition to the extraction of ZUFOs, the recent versions of the ZUFO code allow a so-called *backsplash* correction. In the region of very low y ($y < 0.05$), the hadronic energy is concentrated in the forward direction and the value of hadronic $E - p_z$ is very low. If energy, which does not belong to the real event, gets deposited in the rear part of the detector, the value of the hadronic $E - p_z$ and therefore the hadronic angle γ (see Section 6.3 for definition and use of γ) can be strongly biased. These energy deposits can be due to backsplash from the calorimeter and can be tagged in the following way:

1. γ is calculated from all ZUFOs and a $\gamma_{max} = \gamma + \mathit{offset}$ is determined.

Backsplash Code	Offset Angle	Use
1	38.6	systematic
2	50.0	nominal
3	61.4	systematic

Table 6.1: Codes used for the backsplash correction and the corresponding offset angles to calculate $\gamma_{max} = \gamma + \mathit{offset}$.

2. Islands with energy less than 3 GeV, no good timing, and polar angle bigger than γ_{max} are removed.

3. Iterate the procedure, until the difference in γ_{max} between two successive steps is less than 1 % and the number of iteration is at least four.

The optimal value for the offset of 50° was determined from MC studies; for systematic checks on this background rejection, the offset value can be varied. Table 6.1 gives the correspondence between the *backsplash code* and the value of the offset.

ZUFOs with all backsplash type 2 objects removed, were used throughout this analysis for the determination of all hadronic variables and for the measurement of the hadronic final state. Figure 6.3 shows some summary plots of the distributions of individual ZUFOs.

6.3 DIS Kinematic Variables

The accurate knowledge of the Lorentz-invariant kinematic variables x, y, and Q^2 described in Section 2.2.1 is of utmost importance for every DIS analysis. Several methods to reconstruct these variables are available and three of them, which are used in this analysis, will be described in the following sections.

Figure 6.4 shows a sketch of a DIS ep scattering process. The initial four-momentum of the electron is denoted by

$$\mathbf{k} = (E_e;\ 0,\ 0,\ -E_e)$$

and the four-momentum of the scattered electron by

$$\mathbf{k'} = (E';\ E'\cos\phi\sin\theta,\ E'\sin\phi\sin\theta,\ E'\cos\theta)$$

where E_e and E' is the energy of the incoming and outgoing electron, respectively, and θ and ϕ the polar and azimuthal angle. The initial state proton has four-momentum

$$\mathbf{p} = (E_p;\ 0,\ 0,\ E_p).$$

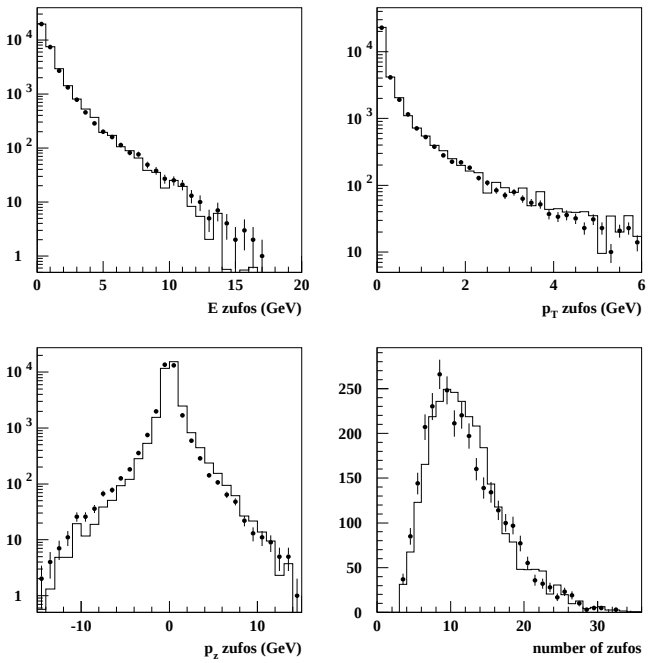

Figure 6.3: Distributions of energy, transverse (p_T), longitudinal (p_z) momentum, and number of ZUFOs. Shown are data (dots) and RAPGAP MC (solid line).

The hadronic final state X (which includes the proton or its remnant, if the proton does not survive the collision) is identified by

$$\mathbf{p}' = (E_h; \mathbf{p}_h)$$

where E_h and $\mathbf{p}_h$ are summed over all hadronic final state particles.

6.3.1 Electron Method

The electron method is the most straight forward procedure to calculate the kinematic variables. As the name indicates, it only uses measured quantities associated with the scattered electron, namely the energy E' and scattering angle θ:

$$y_e = 1 - \frac{E'}{2E_e}(1 - \cos\theta) \tag{6.1}$$

$$Q^2_e = 2E_e E'(1 + \cos\theta) \tag{6.2}$$

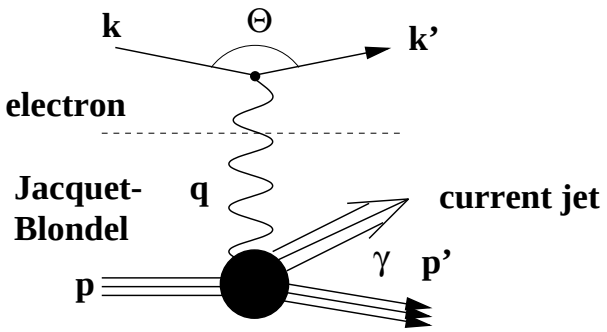

Figure 6.4: Schematic of a general ep deep inelastic scattering process.

$$x_e = \frac{E_e}{E_p}\frac{E'(1+\cos\theta)}{2E_p - E'(1-\cos\theta)} \tag{6.3}$$

Small electron energies E' give rise to high values of y. In the high y region, the y resolution is therefore good. At low y, E' is close to the initial electron energy and y depends on the difference $E_e - E'$, so that small mismeasurements in the energy affects the y measurement by a large amount. The Q^2 resolution is generally good as long as the electromagnetic shower associated with the scattered electron is fully contained in the calorimeter. In general, the resolution obtained with the electron reconstruction depends on the resolution of the measurement of the electron angle θ and energy E'. This method is by definition most sensitive to radiative effects.

6.3.2 Jacquet-Blondel Method

The method developed by Jacquet and Blondel [104], on the other hand, uses the hadronic information only to reconstruct x, y, and Q^2. Ideally, the method would be applied to the energy F and angle γ of the struck quark in the ep scattering process.

$$y_{JB} = \frac{F(1-\cos\gamma)}{2E_e} \tag{6.4}$$

$$Q^2_{JB} = \frac{F^2\sin^2\gamma}{1-y_{JB}} \tag{6.5}$$

However, due to the fragmentation process a measurement of the struck quark is not directly available, but can in good approximation be replaced by the quantities measured from the hadron flow of the current jet:

$$\cos\gamma \simeq \frac{p_{z,h}}{E_h} \tag{6.6}$$

$$\begin{aligned} F\sin\gamma &= p_T \\ &\simeq p_{T,h}. \end{aligned} \tag{6.7}$$

The Jacquet-Blondel variables then can be calculated easily from the hadronic energy flow:

$$y_{JB} = \frac{E_h - p_{z,h}}{2E_e} \tag{6.8}$$

$$Q^2_{JB} = \frac{p^2_{T,h}}{1 - y_{JB}}. \tag{6.9}$$

With these variables and the center-of-mass energy s, x_{JB} can be calculated according to:

$$x_{JB} = \frac{Q^2_{JB}}{s \cdot y_{JB}}. \tag{6.10}$$

The resolution of the Jacquet-Blondel variables is good at high x but deteriorates with decreasing x. The beam pipe holes in the FCAL and in the RCAL set limits on the applicability of this method to low y and very low x with high y, respectively. Since the calculation depends on the sum of all hadronic energy deposits, the presence of the uranium noise from the calorimeter distorts this measurement especially at low y.

6.3.3 Double Angle Method

The double angle method [105] uses information from both, the electron (scattering angle θ) and the hadronic system (hadronic angle γ, Equation 6.6). The physics variables can be calculated from these two angles according to:

$$y_{DA} = \frac{(1 - \cos\gamma) \cdot \sin\theta}{\sin\gamma + \sin\theta - \sin(\theta + \gamma)} \tag{6.11}$$

$$Q^2_{DA} = 4E^2_e \frac{(1 + \cos\theta) \cdot \sin\gamma}{\sin\gamma + \sin\theta - \sin(\theta + \gamma)}. \tag{6.12}$$

x_{DA} then can be extracted easily according to Equation 6.10. The advantage of the double angle method is that it uses angles, which are usually more accurately measured than energies. In particular, the double angle variables are to first order, independent of the calorimeter energy scale.

Figure 6.5 shows the reconstruction quality of all three methods in Q^2, y, and x after all selection cuts were applied. The solid line is a guide for the eye and corresponds to a perfect reconstruction. The correspondence between data and reconstructed MC in these variables can be seen in Figures 5.12 and 5.14.

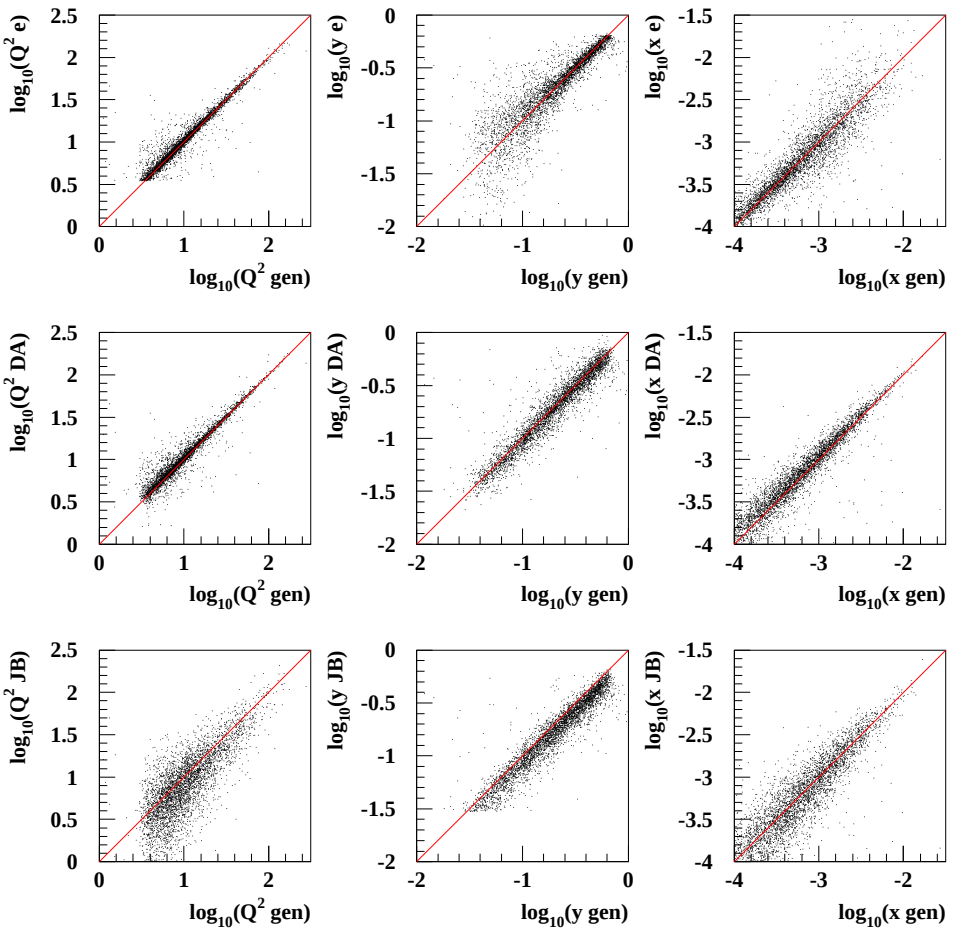

Figure 6.5: Reconstructed Q^2, y, and x with the electron (top), double angle (middle) and Jacquet-Blondel (bottom) method versus their generated values after all selection cuts. The line is a guide for the eye.

6.4 Reconstruction of the Invariant Mass M_X

The invariant mass M_X of the hadronic final state is the center-of-mass energy of the system under investigation. To reconstruct this mass accurately and with good resolution is therefore important, since the measurements of this analysis are performed in bins of M_X and the mass distribution is very steeply falling.

The most straightforward way to extract the mass of the hadronic final state makes use of the four-momenta of the measured hadrons. The particles of the measured final state are identified with the ZUFOs introduced in Section 6.2. With $(E_{zufo}, \mathbf{p}_{zufo})$ denoting the total four-momentum vector of all ZUFOs:

$$E_{zufo} = \sum_{i\,all\,zufo} E_i \tag{6.13}$$

$$\mathbf{p}_{zufo} = \sum_{i\,all\,zufo} \mathbf{p}_i, \tag{6.14}$$

the squared invariant mass M_X of the hadronic final state is given by the square of this four-momentum:

$$M^2_{X,ZUFO} = E^2_{zufo} - \mathbf{p}^2_{zufo}. \tag{6.15}$$

Dead material in the path of the hadronic objects, which are used to form the ZUFOs, result in a loss of energy. This energy loss can be compensated by scaling the invariant mass M_X by a factor of 1.30, which was determined from MC studies. The resolution in M_X is therefore directly correlated to the resolution of the calorimeter. However, due to the use of ZUFOs, which combine calorimeter and CTD information, the resolution is better than what would be expected from the calorimeter alone. Figure 6.6a shows the calibration factor and resolution of M_X based on ZUFOs alone using MC. In the low M_X region, the resolution amounts to about 25% and decreases to about 15% at the high mass end. The constancy of the correction factor over the full M_X range indicates that the hadronic final state is fully contained in the central detector.

An independent way of calculating M_X, which does not depend on the calorimeter energy scale, is available using the outgoing proton measured in the LPS, the electron angle θ and the hadronic angle γ. The invariant mass is then given by:

$$M_{X,LPS} = \sqrt{sy \cdot (1 - x - x_L)} \tag{6.16}$$

where s is the square of the center-of-mass energy of the colliding beams, $s = 4 \cdot E_p E_e = 90200$ GeV^2. The dependence on the electron and hadronic angle is introduced by using the DA method for x and y:

$$M_{X,LPS} = \sqrt{sy_{DA} \cdot (1 - x_{DA} - x_L)} \tag{6.17}$$

A small $M_{X,LPS}$ correction factor of 1.02 was applied. The resolution of $M_{X,LPS}$ is dominated by the resolution in x_L near $x_L = 1$ (low masses) of about 0.4 %. This values were determined from the 1994 and 1995 alignment [74, 75, 76] and is assumed to be the same in 1997. With x_L away from 1 (towards higher M_X), the resolution improves and is slightly better than the resolution of $M_{X,ZUFO}$ (Figure 6.6b).

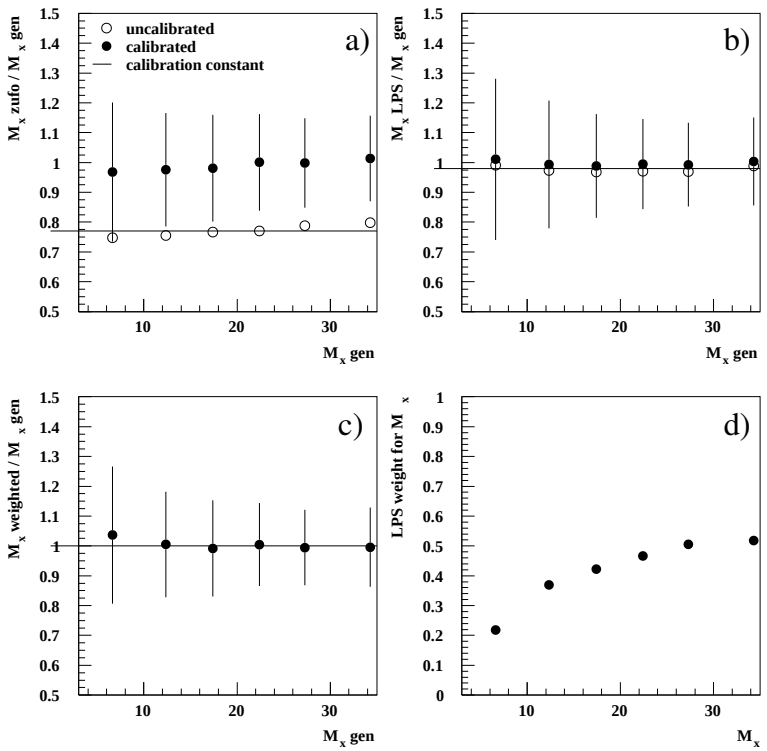

Figure 6.6: Resolution and calibration of M_X calculated with ZUFOs (a), LPS (b), and of the weighted average of $M_{X,ZUFO}$ and $M_{X,LPS}$ (c). The relative weight of the LPS measurement to M_x is shown in (d). The size of the error bars corresponds to the width of a Gaussian fit to the distributions.

To combine the two methods of the mass calculation in a way that emphasis is given to the one with the better resolution, a weighted average of $M_{X,ZUFO}$ and $M_{X,LPS}$ is used, where the weights are determined from the resolution of the two methods:

$$M_X = w_{ZUFO} \cdot M_{X,ZUFO} + w_{LPS} \cdot M_{X,LPS} \tag{6.18}$$

and the relative weights are calculated according to:

$$w_{LPS} = \frac{1/\sigma^2_{M_{X,LPS}}}{1/\sigma^2_{M_{X,LPS}} + 1/\sigma^2_{M_{X,ZUFO}}} \tag{6.19}$$

$$w_{ZUFO} = \frac{1/\sigma^2_{M_{X,ZUFO}}}{1/\sigma^2_{M_{X,LPS}} + 1/\sigma^2_{M_{X,ZUFO}}} \quad (6.20)$$

$$= 1 - w_{LPS} \quad (6.21)$$

where $\sigma_{M_{X,LPS}}$ and $\sigma_{M_{X,ZUFO}}$ are the resolutions of M_X using ZUFOs and the LPS, respectively. $\sigma_{M_{X,ZUFO}}$ was determined from MC and parameterized as a function of $M_{X,ZUFO}$. $\sigma_{M_{X,LPS}}$ is given by the resolution of x_L, y_{DA}, and x_{DA}:

$$\sigma^2_{M_{X,LPS}} = \left(\frac{\partial M_{X,LPS}}{\partial y_{DA}}\sigma_{y_{DA}}\right)^2 + \left(\frac{\partial M_{X,LPS}}{\partial x_{DA}}\sigma_{x_{DA}}\right)^2 + \left(\frac{\partial M_{X,LPS}}{\partial x_L}\sigma_{x_L}\right)^2 \quad (6.22)$$

where the resolution on y_{DA} and x_{DA} in turn is given by the resolution on the electron angle θ and hadronic angle γ:

$$\sigma^2_{y_{DA}} = \left(\frac{\partial y_{DA}}{\partial \theta}\sigma_\theta\right)^2 + \left(\frac{\partial y_{DA}}{\partial \gamma}\sigma_\gamma\right)^2 \quad (6.23)$$

and equivalently for x_{DA}. σ_θ and σ_γ were determined as a function of M_X from MC and parameterized. The result of this method is shown in the Figure 6.6c. The LPS contributes about 50 % of the total mass weight at high masses (Figure 6.6d).

6.5 Event Selection

The following cuts were applied to the data sample to select diffractive DIS events tagged with the LPS to measure the properties of the hadronic final state. All cuts are indicated in Figures 5.12 to 5.15 by solid vertical lines in the corresponding histograms. All selection cuts are applied to produce these plots except the one on the variable displayed.

- To select DIS events:

  $E'_e > 10$ GeV: For electron energies larger than 10 GeV, the electron finding efficiency of SINISTRA is well understood [27]. Also background from photoproduction is suppressed.

  $P_e > 0.9$: To ensure a reliable electron identification, the probability returned by SINISTRA has to be greater than 90 %.

  $40 < E - p_Z < 65$ GeV: If all backward moving particles would be contained in the central detector, the total $E - p_Z$ (including the scattered electron) peaks at twice the initial electron energy ($2 \cdot 27.5 = 55$ GeV). If particles are lost down the rear beam pipe as might be the case for initial radiation and photoproduction, $E - p_z$ decreases by twice the energy of the lost particles. A cut around twice the initial electron energy therefore excludes these kind of events.

$y_{DA} < 0.7$: Photoproduction events are located at y near 1. A cut on high values of y therefore reduces photoproduction background. However, most of these events are already removed by selecting a diffractive sample with the LPS ($x_L > 0.95$) and by the $E - p_Z$ cut (see Figure 5.13b). This cut therefore defines a certain region of the phase space.

$y_{JB} > 0.03$: Ensures good electron reconstruction.

$|Z_{Vertex}| < 50$ cm: A well reconstructed vertex is important for an accurate determination of the momenta of both the hadronic final state particles and the electron. Accepting events too far away from the IP in the forward direction may result in particle losses down the forward beam pipe and therefore would bias the final state.

H1 shaped box cut: This box cut is defined by the requirement that the electron must fall outside of $|X| < 13$ cm and $|Y| < 7$ cm to ensure full containment of the electron in the RCAL, and $X < -7$ cm and $X > -13$ cm or $X < 13$ cm and $X > 4$ cm if $|Y| < 11$ cm to accommodate the beam pipe cooling pipes, which are not modeled properly in the MC [106]. An illustration of this box cut can be found in Figure 6.7.

- To select diffractive events via a good LPS track:

  $x_L > 0.95$: Diffractive events are characterized by a colorless exchange at the proton vertex, after which the proton stays intact and keeps a large fraction of its initial energy. This selection criteria accepts protons with more than 95% of its initial momentum.

  $\chi^2 < 10$: Ensures a reasonable quality of the track fit.

  docap > 0.04 cm: To reject protons, which might be due to scattering off the beam pipe, all events with the track approaching the inner edge of the any beam pipe aperture closer than 0.04 cm are rejected.

  $E + p_Z < 1660$ GeV: Rejects background from DIS overlay events with a proton from the beam halo (see Section 5.1.7). After applying the $E + p_Z$ cut about 7% of the events may be due to DIS background. They are statistically subtracted in all final results.

- To define the kinematic phase space:

  $4 < Q^2_e < 150$ GeV^2: The lower cut is motivated by the fact that the MC sample starts to deviate from the Q^2 distribution measured in the data around $Q^2 = 4$ GeV^2 (Figure 5.13d). The high limit cuts away the tail in the Q^2 distribution and defines the phase space.

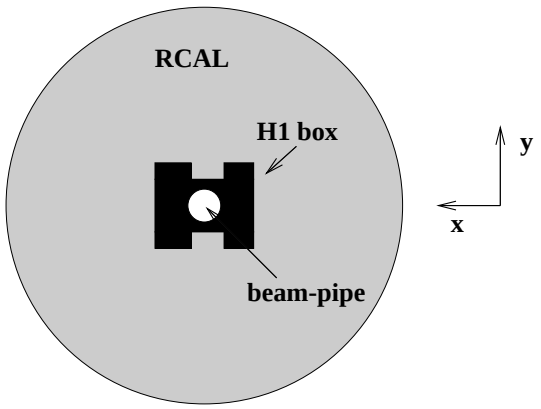

Figure 6.7: Sketch of the H1-shaped box cut (black) around the rear beam pipe (white) in RCAL (hashed); not drawn to scale. It ensures that the electron is well contained within the RCAL. The "ears" cut away regions, where the beam pipe cooling pipes are located, and are not well modeled in the MC.

$4 < M_X < 35$ GeV: The mass range was selected in a way to stay off the resonance region and vector meson production (low M_X) and to ensure full containment of the hadronic final state (high M_X).

$0.0003 < x_{IP} < 0.03$: This cut defines the phase space in x_{IP}. The x_{IP} distribution is cut off at high values due to the selection criteria on the scattered proton momentum ($x_L > 0.95$). The high cut was chosen to stay clear of the x_L cut-off. The lower limit in the M_X range also limits the available low x_{IP} range. The low cut again, defines the phase space and cuts away the tails of low statistics in the distribution.

6.6 Kinematic Phase Space of the Analysis

With the selection cuts imposed on the data sample as described in Section 6.5, an appropriate phase space had to be defined on the generator level, in order to not correct over a large part of the phase space, which is cut out by the selection cuts. The cuts used on the generator level, which ultimately define the kinematic range in which the results of this analysis are valid, are:

- $4.0 < M_X < 35.0$ GeV
- $0.03 < y < 0.7$
- $4.0 < Q^2 < 150.0$ GeV^2

- $0.0003 < x_{IP} < 0.03$.

6.7 Systematic Checks

The correction of the final state to the hadron level depends heavily on the MC simulation and the understanding of the detector and its accurate modeling in MOZART. If the implementation of the detector is inaccurate, then the correction factors, which are extracted from comparing measured MC distributions with their generated true distributions, will not correct to the true values when applied to the measured data distributions. The systematic error analysis should therefore estimate by how much the corrected data distributions would change within the uncertainty of the MC implementation of the ZEUS detector. In addition, results may vary if the distributions measured in the data are not well reproduced by the MC model. Uncertainties due to a model dependence of the results are therefore also included.

All systematic uncertainties were applied to the MC samples only. All measured variables were recalculated properly and the MC data reanalyzed to include the effect of the particular systematic check on the measurement. New correction factors for each check were extracted and applied to the data. The difference between the nominal value and the value resulting from the systematic check then gives the contribution to the total systematic error, which is given by the quadratic sum of all checks. The amount of variation was chosen to follow the current understanding of the detector or until the reconstructed MC events failed to reproduce the data properly.

The data were taken "as is," which means no variation on the data variables or cuts was performed.

In general, the systematic checks can be characterized by the part of the measurement they will affect: adjustments on the hadron reconstruction, the electron reconstruction, tracking of the final state proton, and uncertainties on the MC models. In the following a list of all systematic checks applied to the MC sample is given. The index assigned to each check can be used later to study its effect when systematic uncertainties are discussed with the measurement (Section 7.2.3). A total of 28 systematic checks were performed.

6.7.1 Hadronic Systematic Checks

The energy scale uncertainty of the hadronic section of the calorimeter is 3%[27]. Since the calorimeter consists of the RCAL, FCAL, and BCAL, this uncertainty should be applied to each part independently.

1. RCAL hadronic energy scaled by +3%

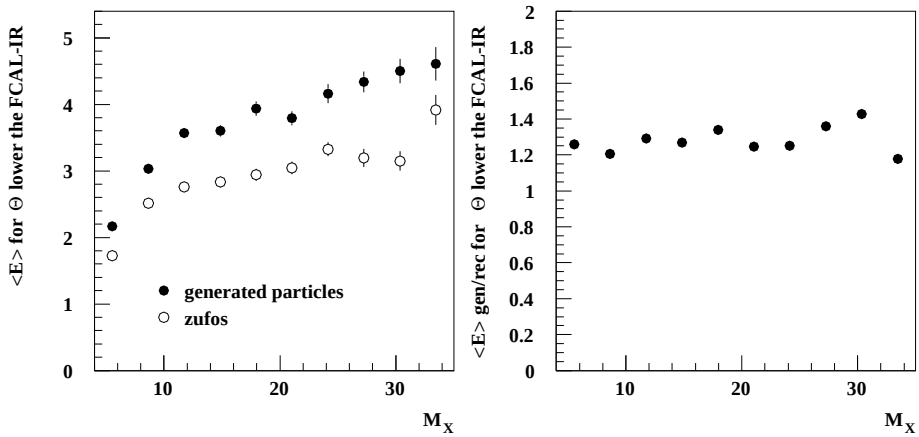

Figure 6.8: On the left, the average energy deposit of reconstructed ZUFOs (circles) in the FCAL inner ring is compared with the average energy generated within and below the angular acceptance of the inner ring (dots). About 25 % more energy is generated than reconstructed in the inner ring of the FCAL (right).

2. RCAL hadronic energy scaled by -3%
3. BCAL hadronic energy scaled by $+3\%$
4. BCAL hadronic energy scaled by -3%
5. FCAL hadronic energy scaled by $+3\%$
6. FCAL hadronic energy scaled by -3%

To check for the effect of possible particle losses down the forward beam pipe, the energy deposit in the inner ring of the FCAL is scaled. Figure 6.8 shows the average energy deposit in the inner ring of the FCAL (circles) compared to the average energy of the generated particles with polar angle θ within and below the polar angle covered by the FCAL inner ring (dots). The effect amounts to about 25% (right).

7. FCAL inner ring energy scaled by $+25\%$
8. FCAL inner ring energy scaled by -25%

Calorimeter islands which are considered to be associated with *backsplash* particles are located in the rear part of the calorimeter, while the rest of the event is concentrated in the forward direction. Therefore, keeping a backsplash particle in the final state can bias the determination of its center-of-mass frame and its topology,

in addition to influencing the calculation of the kinematic variables according to the double angle method. The offset value to calculate γ_{max}, which is used to reject backsplash particles (see Section 6.2), can be varied to study the effect of the backsplash correction (see Table 6.1 for the definition of the backsplash code).

9. Reject calorimeter islands tagged with backsplash code 1

10. Reject calorimeter islands tagged with backsplash code 3

6.7.2 Electron Systematic Checks

The accurate measurement of the electron energy and scattering angle is essential for the determination of the kinematic variables. Also, the four-momentum of the virtual photon emitted at the electron vertex is used in the boost of the hadronic final state and extracted from the four-momentum of the final state electron. A mismeasurement of the final state electron can therefore also bias the topology of the hadronic final state in the $\gamma^*\mathbb{P}$ center-of-mass system.

The comparison of data and MC in the previous section showed a missing RCAL correction of $\simeq 2.5\%$, which had to be applied to the data (Figures 5.9 and 5.10). The same correction is applied to the MC.

11. Scale electron energy by $+2.5\%$

12. Scale electron energy by -2.5%

The angle of the electron is determined by the position on the electron hit in the RCAL. The RCAL is known to have a misalignment of about 2 mm [27]. Shifting the RCAL by ± 2 mm has a visible effect on the electron position reconstruction in X and Y and therefore on the scattering angle θ.

13. Move RCAL by $+2$ mm

14. Move RCAL by -2 mm

6.7.3 Systematic Checks on the LPS

The LPS is not only used to tag diffractive events, but also to boost the hadronic final state to the $\gamma^*\mathbb{P}$ center-of-mass frame by taking part of the $\mathbb{P}$ four-momentum from the momentum of the final state proton. The alignment of the LPS is a lengthly and subtle procedure. Its implementation in MOZART has proven to be difficult, resulting in differences between the distributions observed in the data and the MC. The data-MC comparison discussed in Section 5.4 revealed that problems are also present for the 1997 data sample and the MC. The variations applied to the LPS

measured variables correspond to the shifts observed between the track reconstruction in data and MC (Figure 5.9).

15. Shift x_L by $+0.002$
16. Shift x_L by -0.002
17. Scale the error on x_L by 1.5
18. Add $+0.04$ mm to *docap* to remove more protons possibly scattered off the beam pipe
19. Add -0.04 mm to *docap* to remove less protons scattered off the beam pipe
20. Multiply the track χ^2 by 4 to account for the mismatch between data and MC χ^2 (Figure 5.15)
21. Shift p_x measured with the LPS by $+30$ MeV (Figure 5.8)
22. Shift p_x measured with the LPS by -30 MeV
23. Shift p_y measured with the LPS by $+50$ MeV (Figure 5.8)
24. Shift p_y measured with the LPS by -50 MeV

In addition to these checks which effect a specific component or part of the reconstruction, a shift in the Z-vertex was performed. A shift in the vertex influences the angle measurement and therefore the determination of the four-momentum of both the hadronic objects (ZUFOs) and the electron, respectively. A small shift in the position of the Z-vertex was observed between data and MC (Figure 5.12) and included in the systematic check.

25. Shift Z-vertex by $+5$ mm
26. Shift Z-vertex by -5 mm

6.7.4 Monte Carlo Systematic Checks

The sample of RAPGAP used to correct the data was generated with a leading $\mathbb{P}$ exchange and a subleading $\mathbb{R}$ exchange. The MC events had to be reweighted for the $\mathbb{R}$ contribution in order for the MC to reproduce the data (see Section 5.4.1). However, a small contribution from $\mathbb{R}$ exchange was found to be desired. To investigate the effect of this $\mathbb{R}$ contribution and of the reweighting procedure, the $\mathbb{R}$ weight was adjusted.

27. Subtract 15 % from the $\mathbb{R}$ weight
28. Add 15 % to the $\mathbb{R}$ weight

6.8 Correction

The final distributions were corrected for background from DIS beam halo overlay events, acceptance, migrations, and resolution. The beam halo background was determined in Section 5.1.7 and statistically subtracted from the raw data distributions to obtain uncorrected, normalized data distributions according to:

$$f^{uc} = \frac{f^{raw} - f^{bckgrd}}{N^{raw} - N^{bckgrd}} \tag{6.24}$$

with f^{uc}, f^{raw}, and f^{bckgrd} being the observable accumulated in a bin i for uncorrected data, raw data, and background events, respectively. N^{raw} and $N^{bckgrnd}$ are the corresponding effective number of events in that bin. After the uncorrected data distributions were extracted, they were corrected to the reported value f using a bin-by-bin unfolding method according to:

$$f = f^{uc} \times \frac{f^{gen}}{f^{mc}} \tag{6.25}$$

where f^{mc} is the value of the quantity obtained from reconstructed MC events after all event selection cuts and f^{gen} the generated value before event selection in the kinematic range defined in Section 6.6.

Chapter 7

The Diffractive Hadronic Final State

The study of elementary interactions is usually performed by measuring cross sections and differential cross sections to investigate the dependence of the process on various kinematic variables. The predictions for these cross section measurements from Monte Carlo models or theoretical calculations can then be used to interpret the results in terms of physics conclusions. However, a cross section measurement provides information about how the events are distributed in phase space, but nothing about the kinematic distributions of the hadrons in these events, which are in fact measured in the detector.

Depending on the nature of the process which mediates the interaction (for example, the structure of the exchanged particle), the topology of the hadrons in the final state will show certain features. For example, if we assume diffractive scattering to be mediated by a $\mathbb{P}$ with a partonic structure, the final state for a $\mathbb{P}$ dominated by quarks will look different from a $\mathbb{P}$ dominated by gluons. A $\mathbb{P}$ made out of a $q\bar{q}$ pair will produce two back-to-back jets in the center-of-mass frame of the hadronic system X at lowest order (see for example, Figure 5.3a). At higher order, gluon radiation off the quark line (Figure 5.3b) will cause the events to become broader. If the $\mathbb{P}$ has a dominant gluonic structure, gluons already appear at lower order via the boson-gluon fusion process (Figure 5.3c). This would result in a final state, which is broader than the one expected from $q\bar{q}$ production alone, and may result in distinctive three-jet events (see for example, Figure 5.16). A study of the properties of the hadronic final state can therefore give further insight into the structure of the diffractive scattering process. The hadronic interaction at short distance scale is clouded by the fragmentation during which quarks and gluons condense into hadronic objects. Due to the fragmentation, some information about the initial parton level state is lost. However, studying the properties of the produced hadronic final state can reveal some of the details of the parton level interaction.

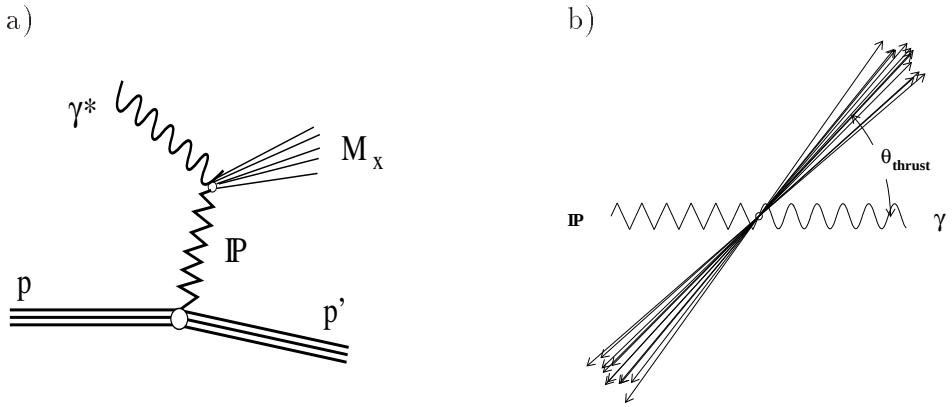

Figure 7.1: The hadronic final state produced in a diffractive DIS event (a) after boosting it to the $\gamma^*\mathbb{P}$ center-of-mass frame (b). The event is rotated so that the virtual photon γ^* is pointing in positive Z direction.

From the above, it appears that the measurement of jets would be the logical step. However, jet finding algorithms can be tuned with the parameters of the jet finder to always find a jet, even if none exists in the first place, for example, if the hadronic energy is distributed in a spherical way uniformly over the solid angle [14]. Since the hadronic mass in the diffractive hadronic final state is small, the fraction of events, which clearly contains jets, is small.

Instead, quantities which characterize the *shape* of an event, can be defined, for example, whether the hadrons are distributed pencil-like, spherical, etc. The diffractive hadronic final state will be studied in terms of these *global event shape* variables in Section 7.2.

The distribution of the transverse momenta within the final state can indicate the presence of gluons, since they are believed to give rise to additional transverse momentum compared to a $q\bar{q}$ pair. The transverse momenta will be studied in Section 7.3.

Finally, the study of the hadronic energy flow in the event can reveal whether the event is symmetric or asymmetric in its center-of-mass frame. An asymmetry of the final state could be interpreted as being due to a $\mathbb{P}$ remnant as expected in a resolved $\mathbb{P}$ approach of diffraction. The energy flow is measured in Section 7.4.

7.1 Reference Frame and Boost Method

The analysis of the hadronic final state is carried out in the center-of-mass frame of the $\gamma^*\mathbb{P}$ system. Since the momentum of the virtual photon and the $\mathbb{P}$ are the only

sources of energy in the diffractive scattering process, the $\gamma^*\mathbb{P}$ center-of-mass frame is equal to the center-of-mass frame of the hadronic system X (Figure 7.1). After the boost to the center-of-mass frame, an additional quantity θ_{thrust} is available, which measures the angle between the $\gamma^*\mathbb{P}$-axis and the symmetry axis of the event (thrust axis, Figure 7.1 b). The boost vector is given by

$$\beta_{\mathbf{b}} = \frac{\mathbf{p}_{\gamma^*} + \mathbf{p}_{\mathbb{P}}}{E_{\gamma^*} + E_{\mathbb{P}}} \tag{7.1}$$

with $(E_{\gamma^*}; \mathbf{p}_{\gamma^*})$ and $(E_{\mathbb{P}}; \mathbf{p}_{\mathbb{P}})$ being the four-momentum of the virtual photon and the $\mathbb{P}$, respectively. The hadronic final state is then boosted to the $\gamma^*\mathbb{P}$ center-of-mass frame by applying the following Lorentz transformation to each final state ZUFO four-momentum $(E; \mathbf{p})$:

$$\begin{pmatrix} E^* \\ p^*_{\parallel} \end{pmatrix} = \begin{pmatrix} \gamma & -\gamma\beta_b \\ -\gamma\beta_b & \gamma \end{pmatrix} \begin{pmatrix} E \\ p_{\parallel} \end{pmatrix}, \; p^*_T = p_T \tag{7.2}$$

where $\gamma = (1 - \beta_b)^{-1/2}$ and $p_{\parallel}$ and p_T are the components of $\mathbf{p}$ parallel and perpendicular to $\beta_{\mathbf{b}}$ [107].

To avoid biases of the quantities characterizing the final state, the four-momenta of the photon and of the $\mathbb{P}$ need to be measured accurately. The γ^* four-momentum is determined readily from the initial four-momentum of the electron k and of the scattered electron k' measured in the RCAL (Section 3.4) and SRTD (Section 3.5):

$$p_{\gamma^*} = k - k'. \tag{7.3}$$

The four-momentum of the $\mathbb{P}$ can be obtained in two ways: from the initial and final (measured with the LPS) momentum of the proton and from the total momentum of all ZUFOs minus the contribution from the virtual photon (Equation 7.3). Both methods are compared in Figure 7.2. The x and y component of the $\mathbb{P}$ momentum (dots show the momentum of the generated $\mathbb{P}$) are well reconstructed with the LPS (solid histograms), while the ZUFOs show a much broader distribution (dashed). The z component on the other hand suffers at small p_z from the limited resolution of the LPS at $x_L = 1$. Here, the ZUFOs are more suitable to reconstruct the $\mathbb{P}$ momentum. Therefore in this analysis, the boost of the final state to the $\gamma^*\mathbb{P}$ center-of-mass frame was performed with the γ^* calculated according to Equation 7.3 and the $\mathbb{P}$ momentum obtained according to:

$$\begin{aligned} p_{\mathbb{P},x} &= -p_x^{LPS} \\ p_{\mathbb{P},y} &= -p_y^{LPS} \\ p_{\mathbb{P},z} &= \sum p_{z,zufo}. \end{aligned} \tag{7.4}$$

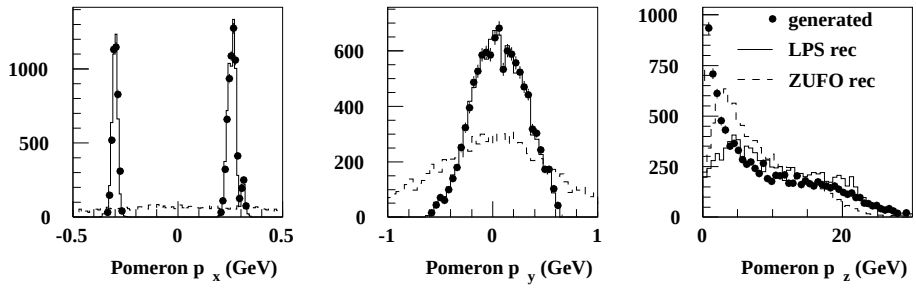

Figure 7.2: Reconstruction of the $\mathbb{P}$ momentum using the LPS (solid) and the ZUFOs (dashed) compared to the generated $\mathbb{P}$ momentum (dots). The LPS gives the best reconstruction in p_x, py, while the z-component suffers from the limited resolution near $x_L = 1$. Here the ZUFOs give a slightly better result.

The total energy $E_{\gamma^*} + E_{\mathbb{P}}$ of the $\gamma^*\mathbb{P}$ system was forced to be consistent with the invariant mass M_X of the hadronic final state X produced in the scattering process:

$$(E_{\gamma^*} + E_{\mathbb{P}})^2 \equiv (\mathbf{p}_{\gamma^*} + \mathbf{p}_{\mathbb{P}})^2 + M_X^2. \tag{7.5}$$

The effects of the boost method on the reconstructed event properties was studied for all methods introduced in this section. The method described by Equation 7.4 was found to give a better resolution for all event shape variables (see Figures 7.3 and 7.18).

7.2 Global Event Shape Variables

The hadronic final state produced in DIS events can have very complicated topologies. To describe these geometries, variables have been introduced, which provide a global view of a particular event by condensing the hadronic information into a small set of numbers. In the case of diffractive exchange with a partonic structure, the measurement of these global properties can therefore provide information related to the hadronic structure of the Pomeron. If diffraction is viewed in the context of photon dissociation, the parton structure of the produced system is reflected in the global properties.

In this analysis, the event shape variables *thrust* T and *sphericity* S are used. To extract the thrust and sphericity from the ZUFOs measured in this analysis, the routines supplied by JETSET [78] were used. It should be noted, that neither T nor S are Lorentz invariants. A comparison with other experiments is therefore only useful if they were performed in the same frame, usually the center-of-mass frame of the hadronic final state.

7.2.1 Definition of Thrust and Sphericity

The thrust T is defined by [78, 108, 109]

$$T = \max_{\vec{n}} \frac{\sum_i |\vec{n} \cdot \vec{p}_i|}{\sum_i |\vec{p}_i|}, \tag{7.6}$$

where $\vec{p}_i$ represents the momentum of the observed hadronic final state particle and the unit vector $\vec{n}$ gives the orientation of the thrust axis. By construction, T is essentially a measure of the longitudinal momentum. The allowed values for T are $1/2 \leq T \leq 1$, with very collimated, pencil-like events corresponding to $T \simeq 1$, while isotropic events yield $T \simeq 1/2$. It should be noted that other definitions of T can be found in the literature [110]. The results will agree as long as the event is studied in the center-of-mass frame and all particles are detected.

Since T is linear in the particle momenta, it is unchanged if one particle splits up in two collinear ones. Being infrared safe allows the thrust to be computed in perturbative QCD, which was successfully done for e^+e^- annihilation. The tail of the thrust distribution away from 1 is dominated by multijet final states. Through the shape of the distribution in this region a direct test of the QCD matrix elements is possible. A measurement of the strong coupling constant α_S is possible through the normalization to high precision, since the NLO corrections are known [111].

The sphericity S of the event is defined as

$$S = \frac{3}{2}(\lambda_2 + \lambda_3), \tag{7.7}$$

where λ_2 and λ_3 are the smallest eigenvalues of the sphericity tensor [78, 112]

$$S^{\alpha\beta} = \frac{\sum_i p_i^\alpha p_i^\beta}{\sum_i |\vec{p}_i|^2} \tag{7.8}$$

with $\alpha, \beta = x, y, z$. The allowed range of the sphericity is $0 \leq S \leq 1$. For isotropic events, the sphericity S approaches 1, while for very collimated two-jet events S is about 0. S is a measure of the summed p_T^2 with respect to the event axis. The eigenvectors $\mathbf{v}_i$ associated with the eigenvalues λ_i of the sphericity tensor $S^{\alpha\beta}$ can be used to define an event plane. The vectors $\mathbf{v}_1$, called the sphericity axis, and $\mathbf{v}_2$ define this plane, while $\mathbf{v}_3$ is perpendicular to the event plane.

Table 7.1 illustrates for different event geometries the values of the event shape variables T and S.

Figure 7.3 shows the reconstruction quality (left) of T and S in plots of reconstructed versus generated MC events after all selection cuts. The pull of T and S is shown in the right part of the plot. The error bars given are obtained from the widths of Gaussian fits and give resolutions of about 3 % for T and about 30% for S.

Particle Trajectories	Thrust	Sphericity
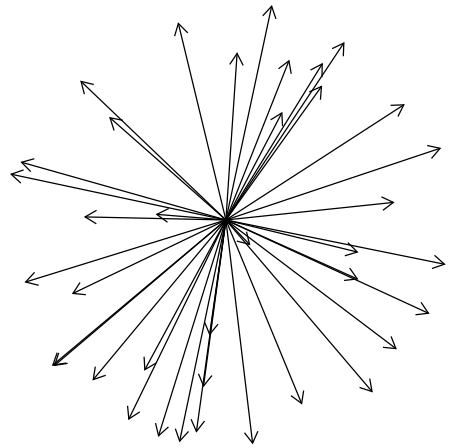	$\to \frac{1}{2}$	$\to 1$
	$\to 1$	$\to 0$
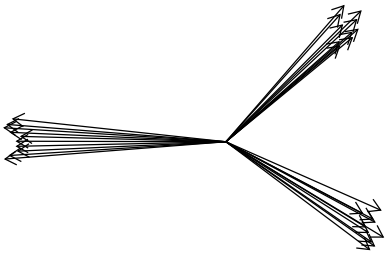	$\simeq \frac{3}{4}$	$\simeq \frac{1}{2}$

Table 7.1: Illustration of the event geometry and the resulting values of thrust T and sphericity S.

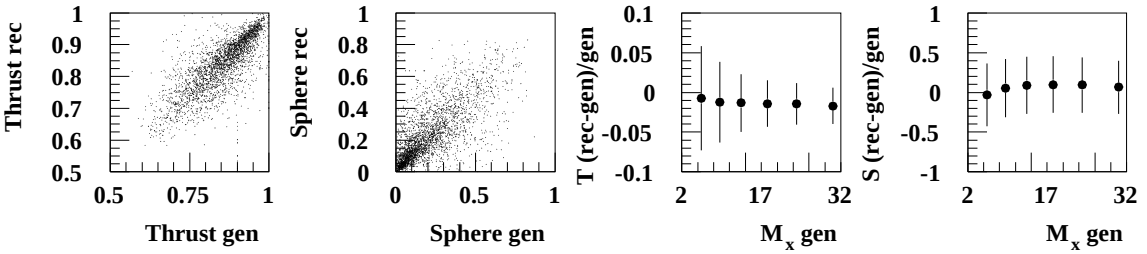

Figure 7.3: Resolution of the reconstruction of thrust T and sphericity S after all selection cuts have been applied. On the left, a scatter plot of reconstructed versus generated T and S is shown. On the right, two plots show the resolution as a function of the mass M_X.

Figure 7.4 shows how well the distributions measured in this analysis are reproduced by the reconstruction. Reconstructed (circles) thrust and sphericity distributions are compared with their generated (solid histograms) counterparts. The correction factors for the distributions are mostly on the order of 10 % to 20 % except in the region of the pencil-like limit ($T = 1$, $S = 0$). Here, hadronization corrections are assumed to be large [14] and can introduce large uncertainties. The correction factors for the average values $< T >$ and $< S >$ are around 1.5% and $10 - 20\%$, respectively, constant with M_X and comparable to the resolution.

Figure 7.5 shows how well the MC reproduces the distributions measured in the data. RAPGAP (solid histograms) does not do a particularly good job in reproducing the data (dots). However, since the correction factors are approximately independent of the mass M_X, the model dependence introduced by using the RAPGAP MC for correction purposes is expected to be small.

Figure 7.6 shows the effect of the systematic error analysis (section 6.7) on the average values of T (top) and S (bottom) in bins of the invariant mass as a function of the index of the systematic check. The variations are typically below 0.5 % and 5.0 % for $<T>$ and $<S>$, respectively. The largest contributions originate from the shift in x_L (check index 15 and 16) and from scaling of the energy deposit in the inner ring of the FCAL (index 7 and 8).

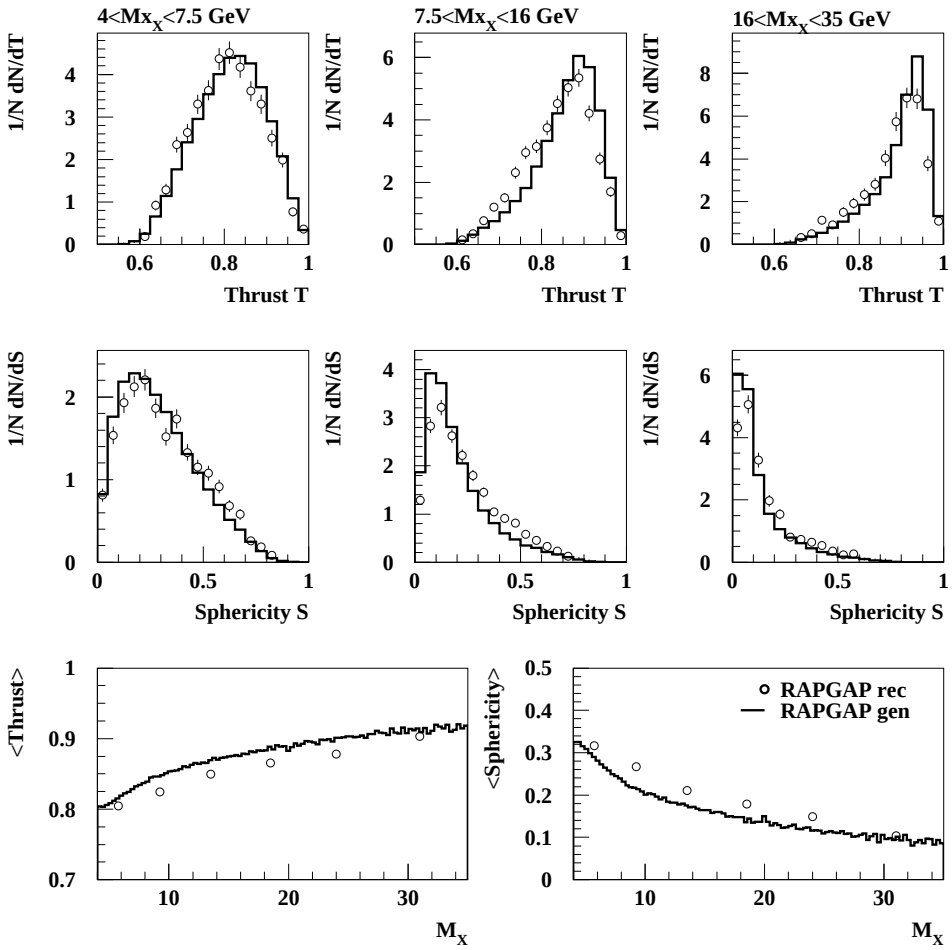

Figure 7.4: Reconstruction quality of the distributions of thrust and sphericity and their average values as a function of M_X by comparing generated (solid histogram) and reconstructed (circles) distributions.

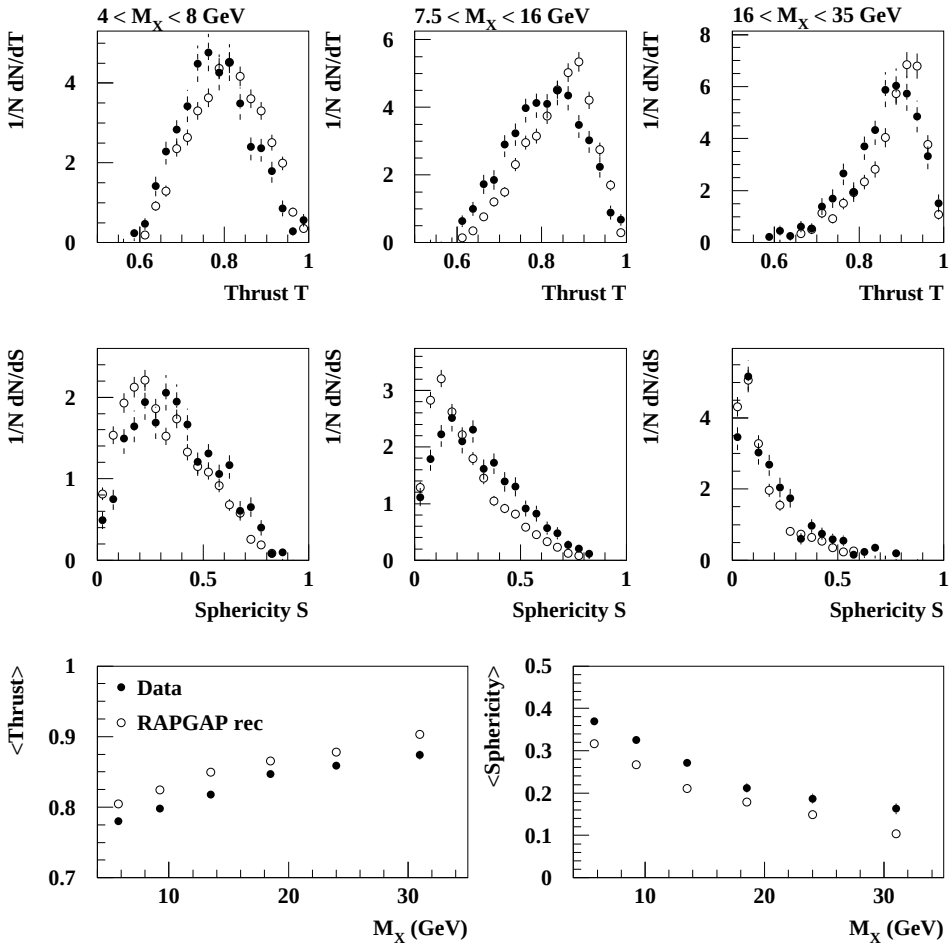

Figure 7.5: Quality of the reproduction of the measured event shape variables thrust and sphericity in the data (dots) by the RAPGAP MC (open circles). All event selection cuts are applied.

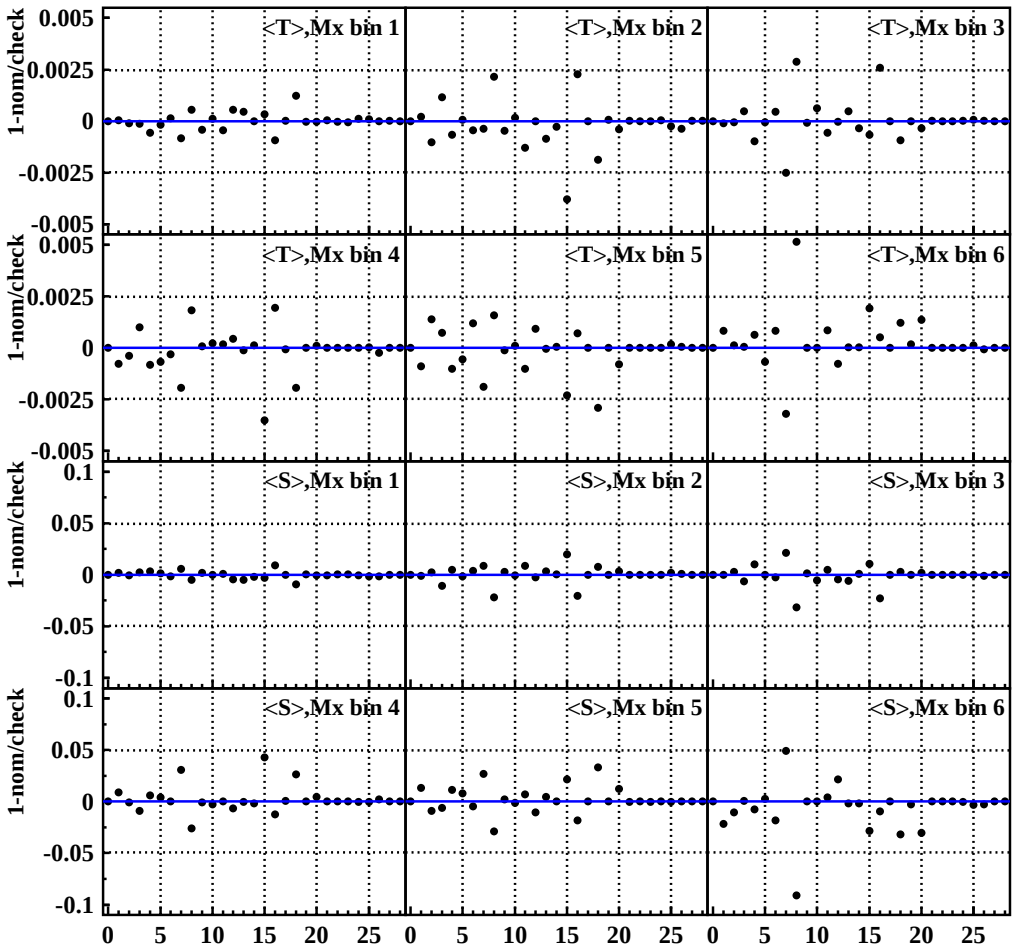

Figure 7.6: Effect of the systematic studies on the average values of T and S in bins of M_X. The horizontal axis corresponds to the index given in Section 6.7 with bin 0 indicating the nominal value. The top six plots show the result for $<T>$, the bottom plots the same for $<S>$.

7.2.2 Thrust and Sphericity Distributions

The distributions of thrust T and sphericity S corrected to the hadron level are shown in Figures 7.7 to 7.9 and Figures 7.10 to 7.12, respectively, in comparison with results expected from e^+e^- annihilation (JETSET in Figures 7.7 and 7.10) and various MC models described in Section 5.1. The entire sample was subdivided into three bins of the invariant mass M_X with bin edges 4.5, 7.0, 16.0, and 35.0 GeV corresponding to an average M_X of 5.6, 11.0, and 22.5 GeV, respectively. The distributions are corrected for detector and acceptance effects and normalized to the number of events in each M_X bin. The inner error bars show the statistical errors only, while the outer error bars correspond to the statistical error and the systematic uncertainty added in quadrature.

Figure 7.7 shows the comparison of the T distribution in these three M_X bins with results from e^+e^- annihilation (dashed) and the RAPGAP MC generator using the *H1fit2* (solid). In order to have a good agreement between the average mass M_X of the diffractive data and the average center-of-mass energies $\sqrt{s}$ for the e^+e^- results, the JETSET MC generator was used to produce events distributed in $\sqrt{s}$ according to the M_X distribution of the data. The JETSET results show in general a good agreement with the diffractive final state measurement. A slight shift of the distribution towards lower values of T for lower masses can be observed. The RAPGAP MC, assuming a partonic $\mathbb{P}$ containing quarks and gluons, produces a hadronic final state with the distribution of the thrust shifted towards larger T values in the low M_X region, therefore predicting a final state more collimated than what is observed in the data. The same observation holds for the sphericity distributions of Figure 7.10. Here, the distributions are slightly shifted towards higher values for JETSET and lower values for RAPGAP in the low mass regime, respectively, following the same trend as the T distributions.

Figures 7.8 for thrust and 7.11 for sphericity compare the distributions with predictions from MC generators based on diffractive models using perturbative QCD. The RIDI (Section 5.1.6) generator (solid) produces a hadronic final state which is a little less collimated at low and medium M_X (lower T and higher S) than what is observed in the data. The RIDI generator produces both, $q\bar{q}$ and $q\bar{q}g$ final states. A diffractive hadronic final state based on the production of a $q\bar{q}$ pair (dashed) (Section 5.1.3) shows a T (S) distribution shifted towards higher (lower) values with narrower distributions, especially for high M_X. The $q\bar{q}g$ final state (dotted) (Section 5.1.4) is comparable with the predictions from RIDI. This is not surprising, since with the default setting of RIDI, which were used to produce this sample, the final state is almost entirely due to $q\bar{q}g$ events (more than 99 % $q\bar{q}g$ for $M_X \gtrsim$ 10 GeV).

Finally, Figures 7.9 and 7.12 compare the measured distributions to predictions from the SATRAP model (solid) and with the *H1fit1* (dashed), which only assumes

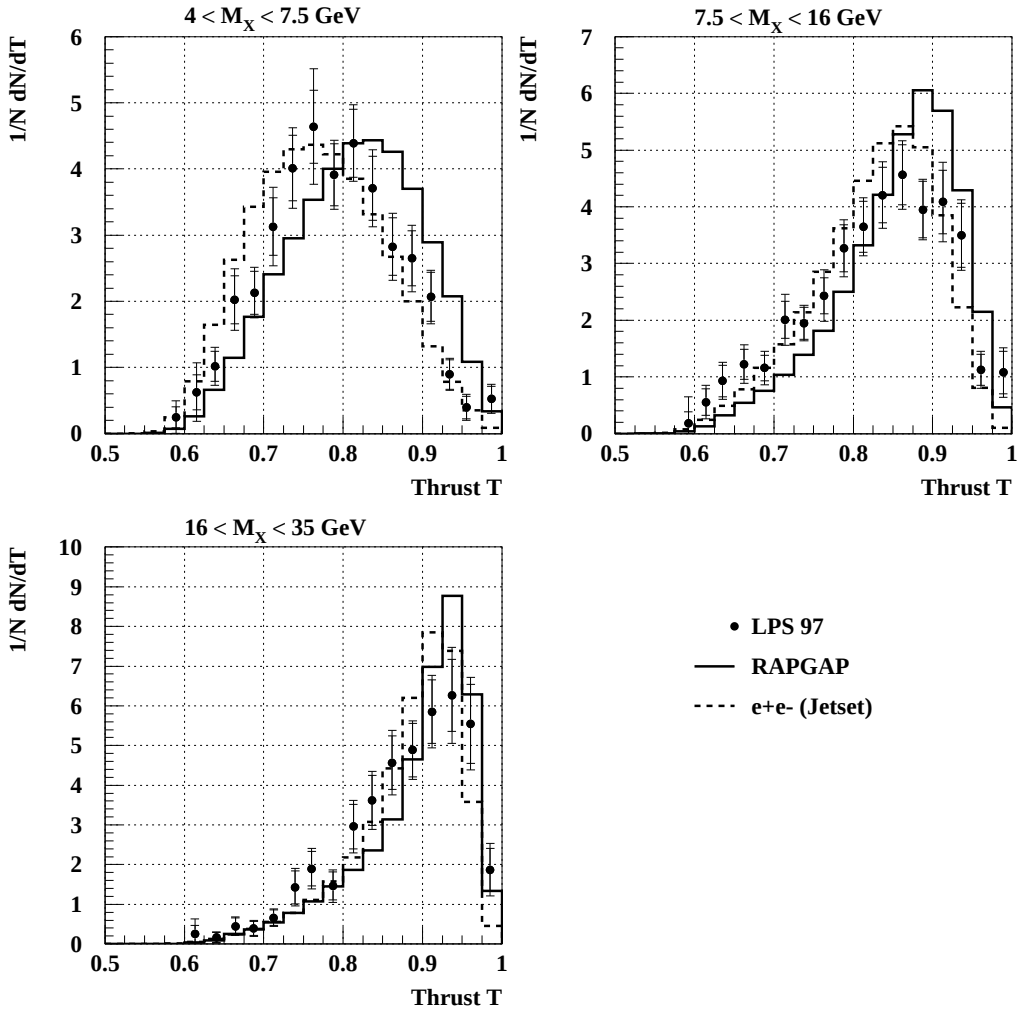

Figure 7.7: Comparison of the hadron level corrected, normalized T distribution of the diffractive hadronic final state (dots) with results from e^+e^- annihilation (represented by JETSET - dashed) and the RAPGAP MC (solid) in three bins of the invariant mass M_X (4 to 7.5, 7.5 to 16, and 16 to 35 GeV).

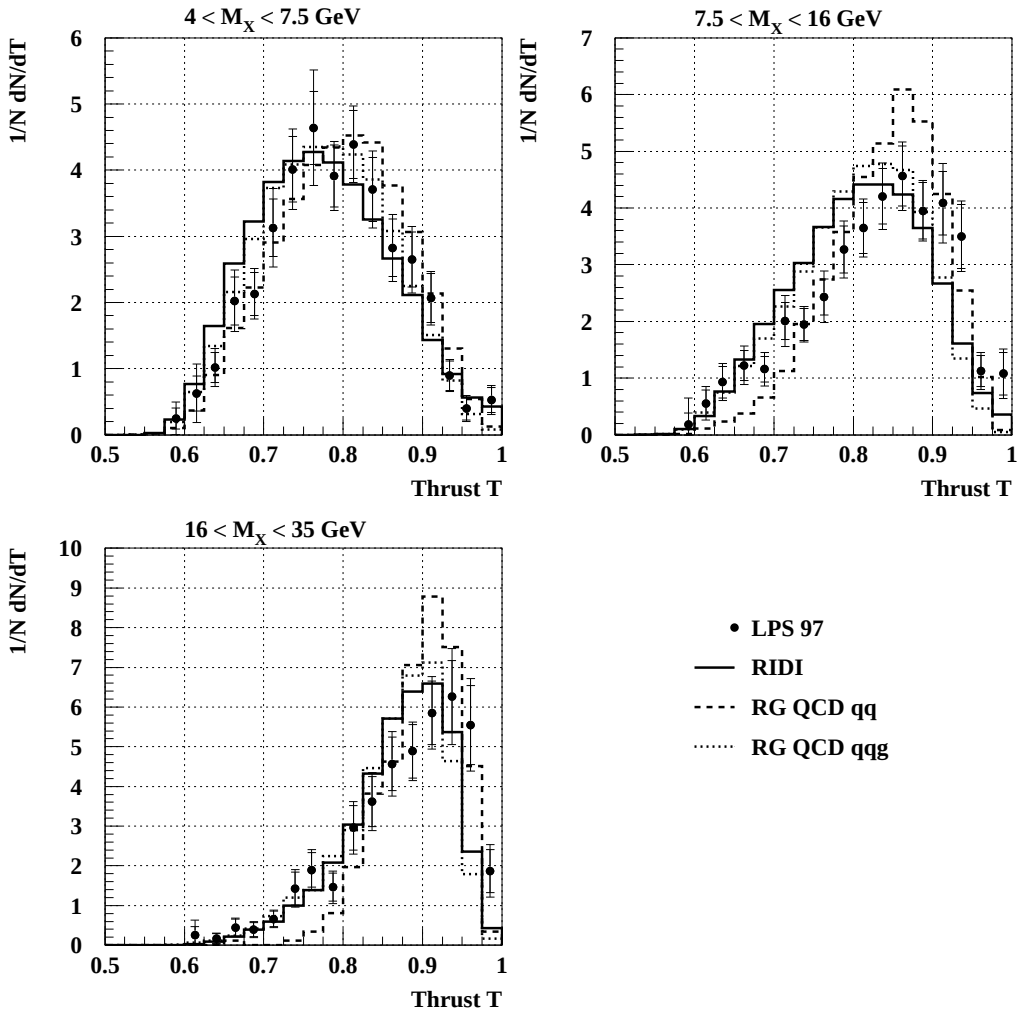

Figure 7.8: Comparison of the corrected T distribution with the RIDI (solid) MC and models based on the assumption that the $\mathbb{P}$ consists of $q\bar{q}$ (dashed) or $q\bar{q}g$ (dotted) only.

quarks in the $\mathbb{P}$. The SATRAP model reproduces the observed distributions very well, maybe with too steep a fall off when T approaches 1 at higher M_X. The SATRAP model contains both a $q\bar{q}$ and a $q\bar{q}g$ final state where the gluons dominate at small β corresponding to high M_X. Using a partonic $\mathbb{P}$ which consists entirely of quarks as implemented in the *H1fit1* clearly fails to describe the data for higher masses, where the produced distributions are too narrow and too peaked at high values of T.

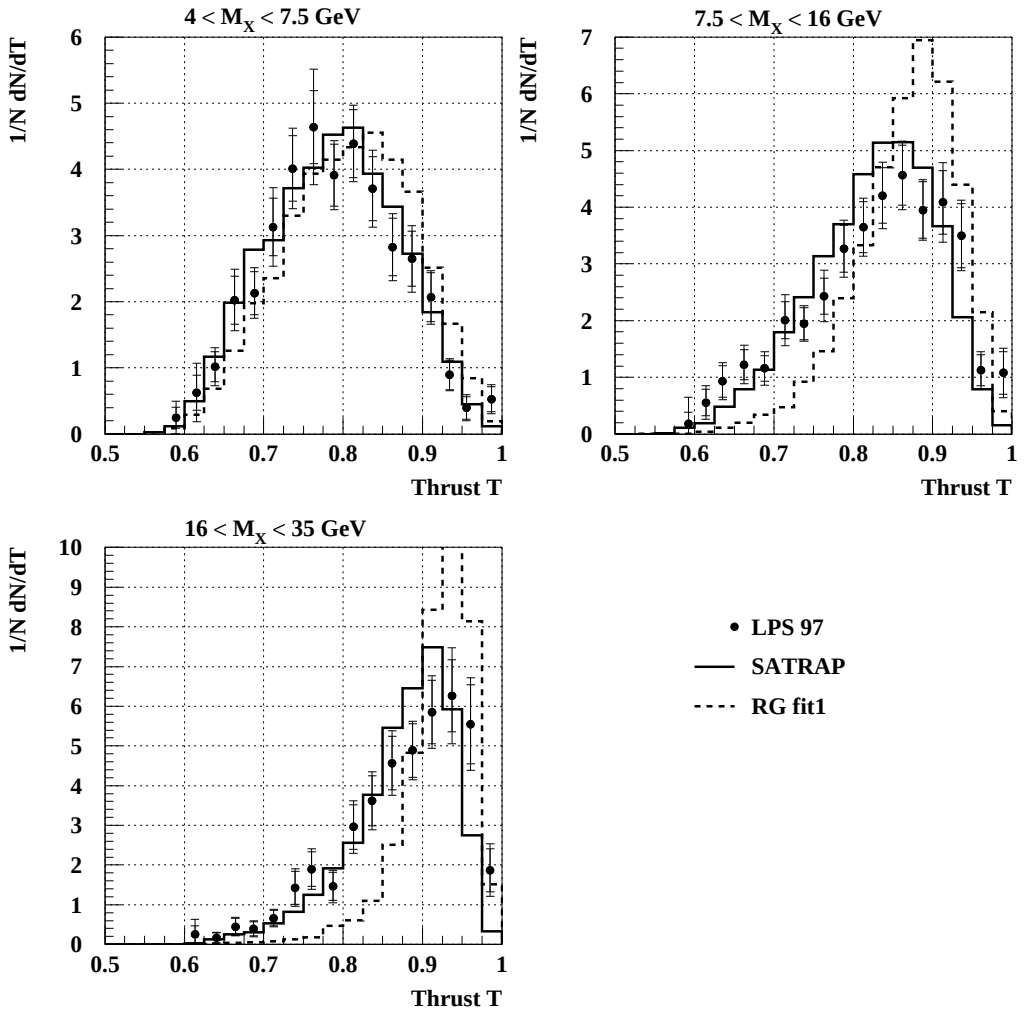

Figure 7.9: Comparison of the corrected T distribution with the SATRAP (solid) model and the RAPGAP with *H1fit1* (dashed) containing a $q\bar{q}$ $\mathbb{P}$.

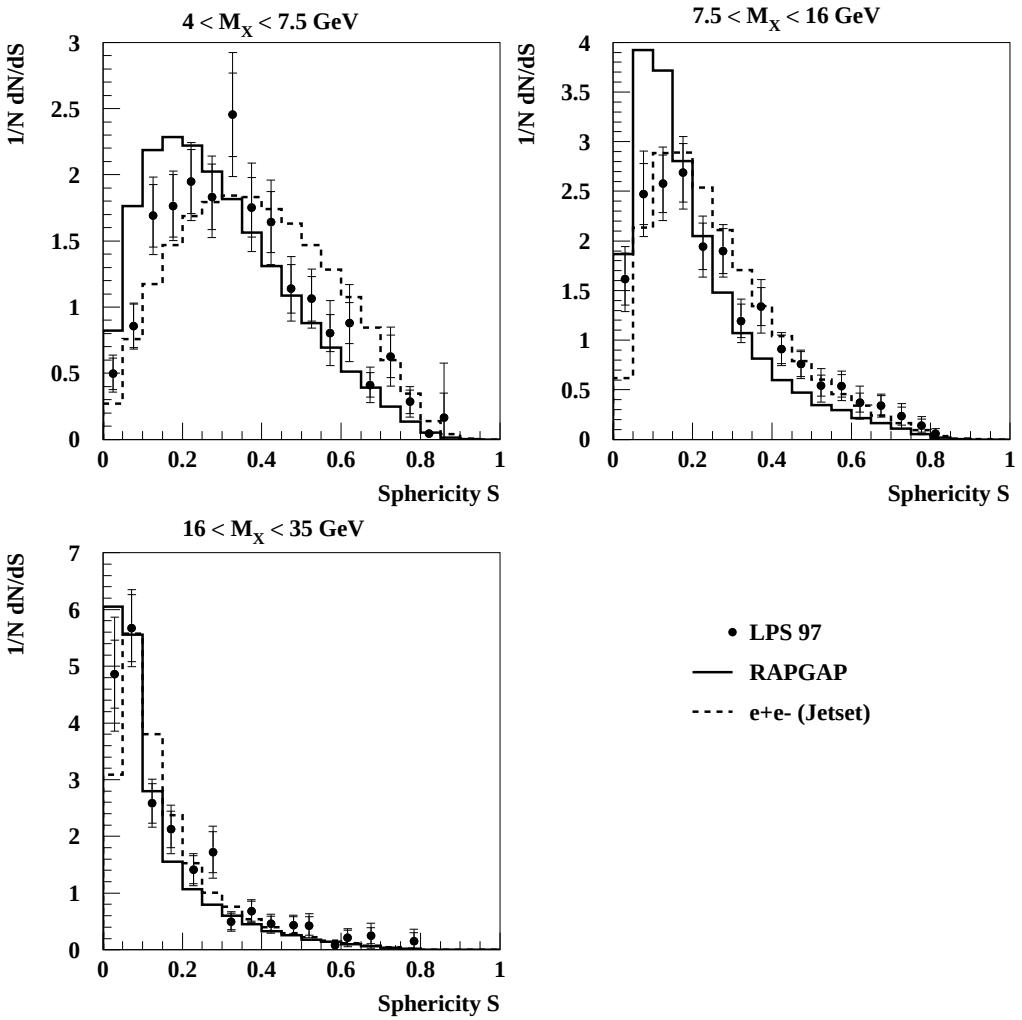

Figure 7.10: Comparison of the hadron level corrected, normalized S distribution of the diffractive hadronic final state (dots) with results from e^+e^- annihilation (represented by JETSET - dashed), and the RAPGAP MC (solid), which was used for correction, in three bins of the invariant mass M_X (4 to 7.5, 7.5 to 16, and 16 to 35 GeV).

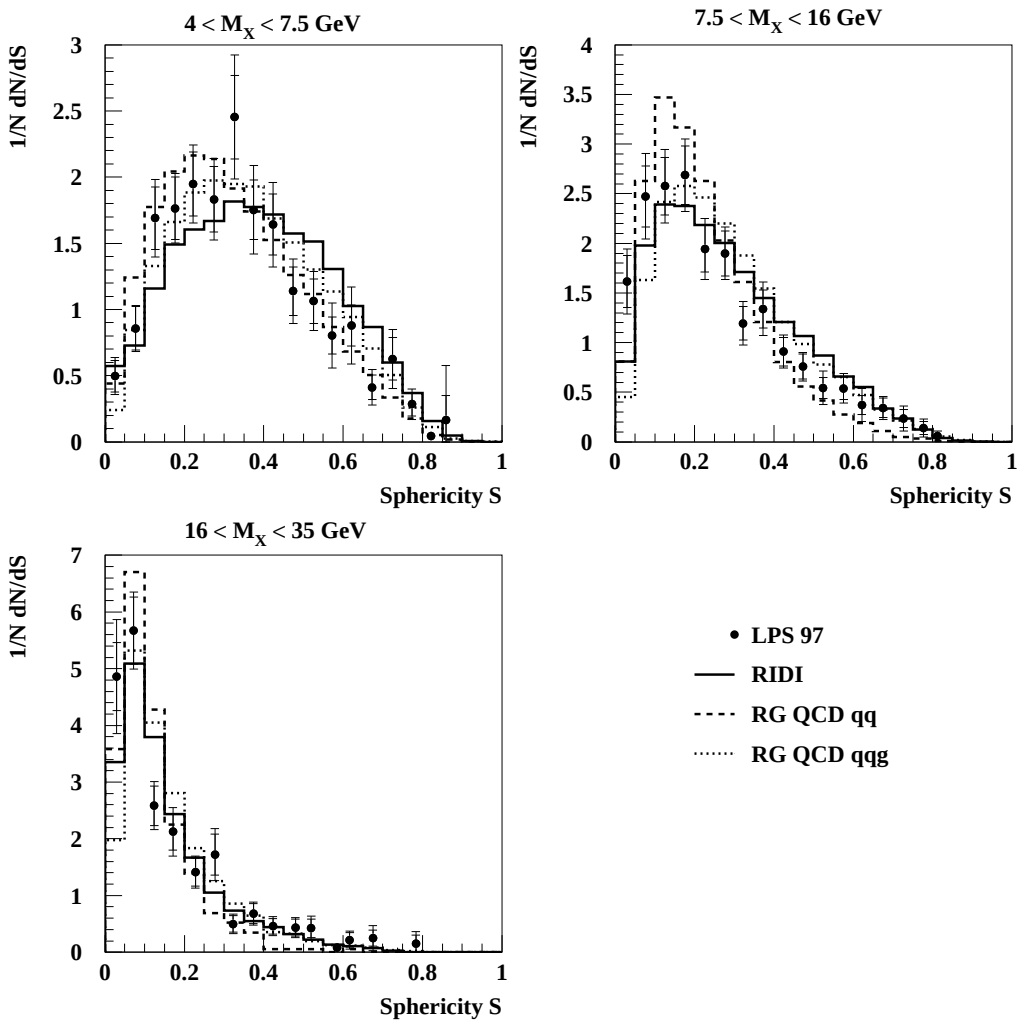

Figure 7.11: Comparison of the corrected S distribution with the RIDI (solid) MC and models based on the assumption that the $\mathbb{P}$ consists of $q\bar{q}$ (dashed) or $q\bar{q}g$ (dotted) only.

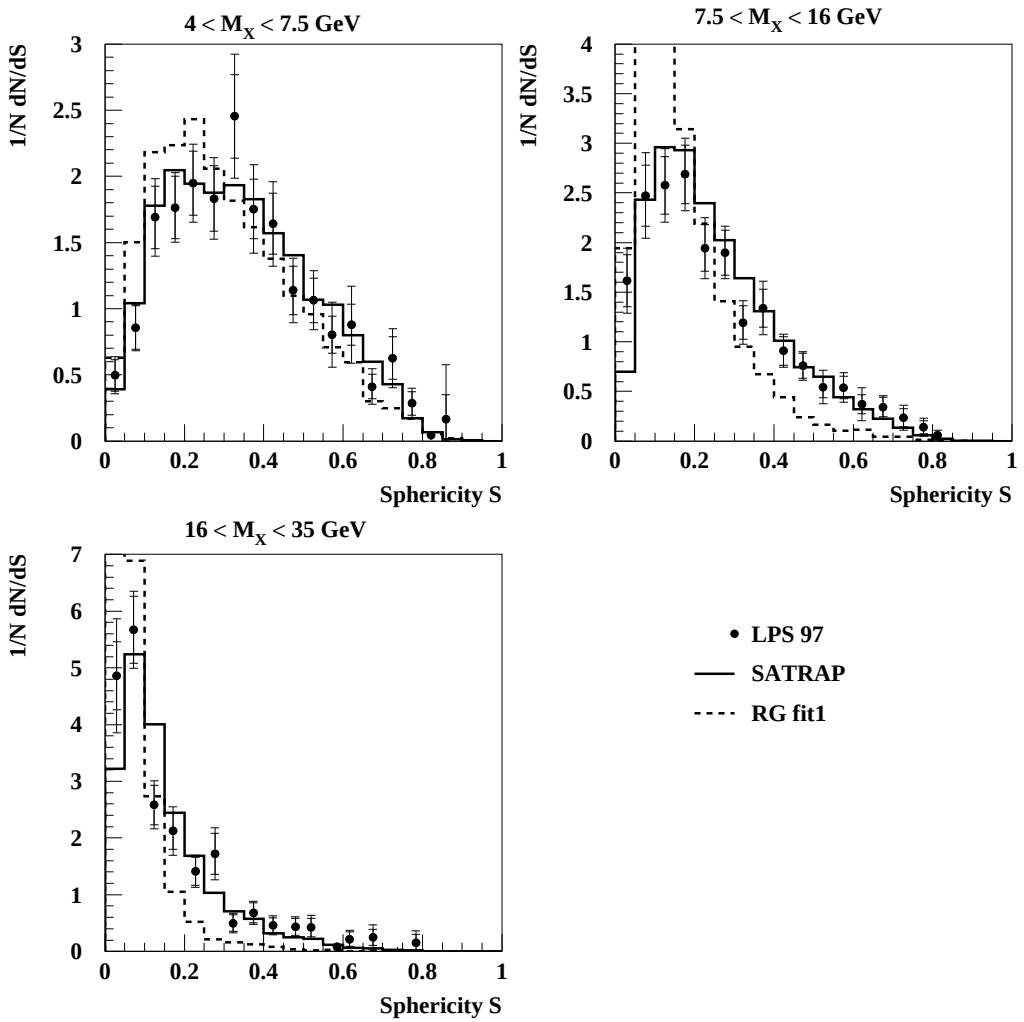

Figure 7.12: Comparison of the corrected T distribution with the SATRAP (solid) model and the RAPGAP with *H1fit1* (dashed) containing a $q\bar{q}$ $\mathbb{P}$.

7.2.3 Average Thrust and Sphericity

A global picture of the hadronic final state can be obtained by looking at the average values of thrust, $<T>$, and sphericity, $<S>$, and their variations with the center-of-mass energy M_X instead of studying the distributions. The bins were chosen so that the bin width corresponds to about $1.5 \cdot \sigma_{M_X}$, where σ_{M_X} is the resolution of the mass reconstruction obtained from MC studies. The bin edges are located at 4.0, 7.5, 11.0, 16.0, 21.0, 27.0, and 35.0 GeV.

Figures 7.13 and 7.14 show the measurement of the average event shape variables (dots) in comparison with results from other experiments and with MC predictions. The increase of $<T>$ and the decrease of $<S>$ with M_X indicates that the topology of the final state becomes more collimated if the center-of-mass energy of the $\gamma^*\mathbb{P}$ system increases. The H1 Collaboration measured $<T>$ as a function of M_X using large rapidity gap events (LRG) with a cut on $\eta_{max} < 3.2$ to select a diffractive sample [114] (Figure 7.13). The diffractive final state selected with the LPS lies systematically above the H1 results (circles) in the thrust measurement, even though for most of the points the total errors overlap. In addition to using different methods to select diffractive events, the kinematic range defined for the H1 analysis differs slightly from the phase space defined in this analysis. The phase space quoted for the H1 analysis is [114]: $M_Y < 1.6$ GeV, $x_{_{IP}} < 0.05$, $|t| < 1$ GeV^2, $10 < Q^2 < 100$ GeV^2, and $y < 0.5$, with M_Y being the mass of the hadronic system separated from the system X in rapidity. The difference in phase space plus the fact that the H1 Collaboration corrected back over a part of the phase space which is cut out by the η_{max} cut can probably explain the differences.

Results obtained in e^+e^- annihilation by the TASSO [115], PLUTO [116], and MARK II [117] collaborations (together with the predictions from JETSET) are shown as open triangles in Figure 7.13. The $<T>$ and $<S>$ measurement tagged with the LPS shows a close resemblance to the e^+e^- results, in particular for the sphericity measurement.

Figure 7.13 also shows the predictions of $<T>$ and $<S>$ versus M_X for RAPGAP with the *H1fit1* (dotted) and *H1fit2* (solid) and for the SATRAP model (dashed). The $q\bar{q}$ $\mathbb{P}$ as implemented in the *H1fit1* gives rise to a final state, which is more collimated than the LPS data (larger thrust, smaller sphericity). Note that one of the quarks from the $\mathbb{P}$ is treated as a remnant for which gluon radiation is suppressed. This is the reason for the difference compared to the e^+e^- results, where also a $q\bar{q}$ final state is produced with gluons only from QCD Compton radiation off (both) quark lines. The suppression of the gluon radiation off one of the quarks in the H1fit can be compensated by adding extra gluons to the final state via the boson-gluon fusion (BGF) process if the gluons are already part of the $\mathbb{P}$ structure. This is included in the *H1fit2* (solid). The current version of RAPGAP with the *H1fit2* does not produce enough gluons in the final state to describe the data.

M_x^{gen}/GeV	current fraction of $q\bar{q}g$	desired fraction
5.5	92.4 %	66.3 %
8.6	98.1 %	54.6 %
11.7	99.4 %	55.8 %
14.8	99.4 %	65.3 %
17.9	99.6 %	99.7 %
20.9	99.7 %	78.0 %
24.1	99.8 %	85.8 %
27.0	99.4 %	90.5 %
30.1	99.5 %	98.6 %
33.4	100.0%	99.8 %

Table 7.2: Fraction of $q\bar{q}g$-type events in RIDI as a function of M_X. The middle column gives the currently produced fraction, the left column the fraction desired to reproduce the measurement of $<T>$. The fluctuations of the weights reflect the fluctuations of the reconstructed $<T>$ values used to obtain them. Taking the weights as a smooth function of M_X is consistent with the values display in the table.

SATRAP (dashed), which produces quarks and gluons in the final state from the dissociation of the virtual photon, gives an excellent description of the average event shape variables thrust and sphericity over the full mass range.

Figure 7.14 compares $<T>$ and $<S>$ with the model predictions from RIDI (solid), $q\bar{q}$ (dashed), and $q\bar{q}g$ production (dotted). RIDI underestimates the thrust (overestimates S) in the low mass region. RIDI was tuned to the hadronic final state data of the H1 Collaboration and reproduces the H1 measurement in [114] very well. However, RIDI could easily be tuned to the LPS measurement as well, by finding the right K-factors (see Equations 5.15, 5.16, and 5.17), which are not predicted by the theory. These K-factors determine dominantly the relative contribution of $q\bar{q}$ and $q\bar{q}g$ production. The necessary mixture of $q\bar{q}$ and $q\bar{q}g$ in RIDI to reproduce the LPS event shapes can be obtained using the method described with Equation 5.18. Table 7.2 gives the current and the desired contribution of the $q\bar{q}g$ final state. However, since the sample available for this analysis did have almost only $q\bar{q}g$ events, a remixing of the two processes was not practical.

The predictions from $q\bar{q}g$ production (dotted line in Figure 7.14) are consistent with the RIDI sample, as one would have expected already from Figures 7.8 and 7.11. The final state emerging for the $q\bar{q}$ state is too collimated and shows thrust values even higher than the e^+e^- results, which might be attributed to the fact, that a QCD Compton radiation process was not explicitly included, so that gluons only emerge from the fragmentation algorithm. Combining the $q\bar{q}$ and the $q\bar{q}g$ final state properly should give a nice description. The $q\bar{q}$ curve ends at M_X near 27 GeV since

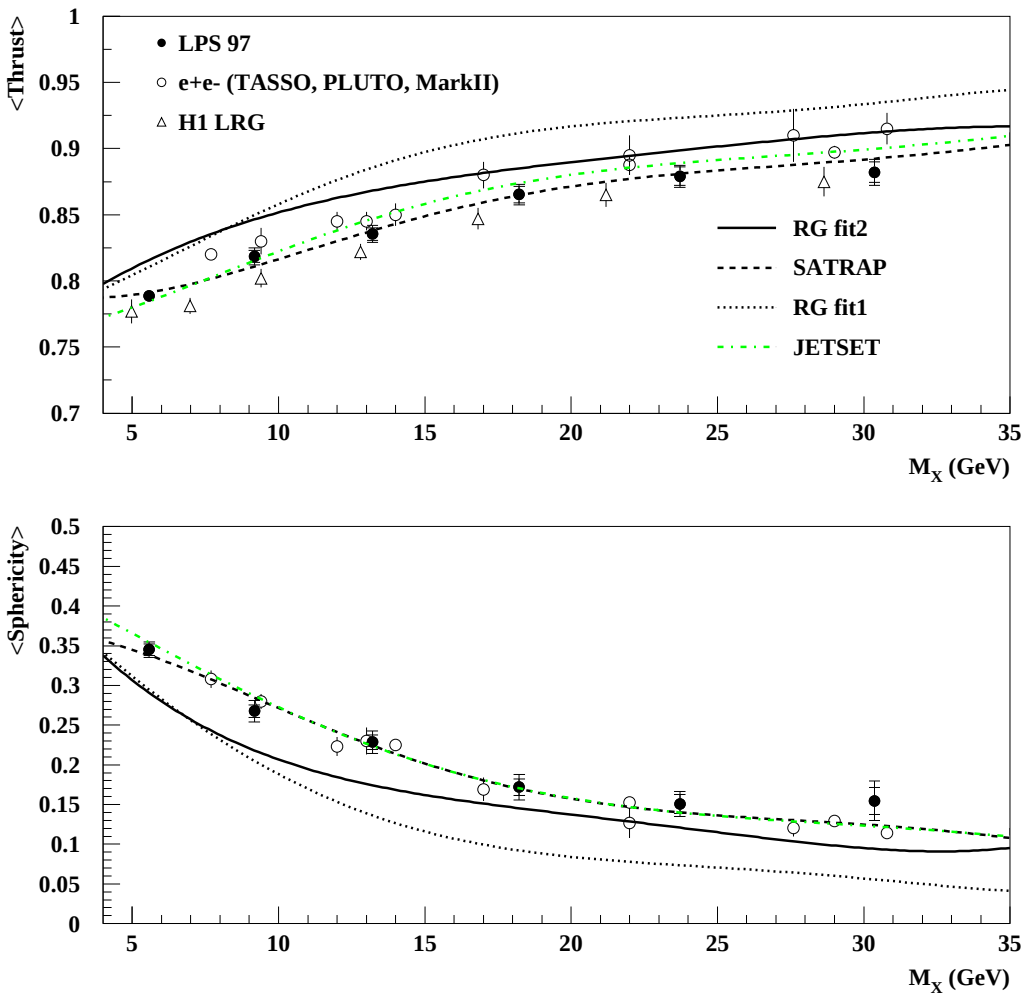

Figure 7.13: Comparison of the average values of thrust $<T>$ and sphericity $<S>$ (dots) as a function of the invariant mass M_X with results from e^+e^- annihilation (circles) with the JETSET prediction, H1 (LRG) analysis (open triangles), and predictions from the RAPGAP MC generator using *H1fit2* (solid) and *H1fit1* (dotted) and with the SATRAP model (dashed). Inner error bars show statistical error only; outer error bars statistical error and systematic uncertainty added in quadrature.

the number of events for higher masses was not sufficient enough to make a reliable extrapolation.

The measurement of $<T>$ and $<S>$ was also checked for a possible dependence on Q^2 (Figure 7.15) and x_{IP}(Figure 7.16). The sample was subdivided in two bins of Q^2: $Q^2 < 10$ GeV^2 corresponding to an average Q^2 of 6.5 GeV^2, and $Q^2 > 10$ GeV^2 corresponding to an average Q^2 of 24.4 GeV^2. No dependence on Q^2 is visible. To check for possible contributions from subleading Reggeon exchanges, the data were also divided into two bins in x_{IP}: $x_{IP} < 0.01$ corresponding to an average value of $4.4 \cdot 10^{-3}$ and $x_{IP} > 0.01$ corresponding to an average value of $1.8 \cdot 10^{-2}$. Again, no dependence was visible.

7.2.4 Summary of the Thrust and Sphericity Measurement

The thrust and sphericity measurement in diffractive DIS tagged with the LPS was compared to e^+e^- results and predictions from MC generators assuming various mechanisms for hadron production. Since the annihilation of electrons and positrons yields a $q\bar{q}$ final state with gluons originating from QCD Compton radiation off the quark line only, the similarity with the LPS measurement might be an indication that the diffractive hadronic final state can also be attributed to a $q\bar{q}$ final state. On the other hand, diffractive models which contain only quarks (RAPGAP *H1fit1* and QCD $q\bar{q}$) fail to describe the final state in terms of T and S correctly. However, in the $q\bar{q}$ $\mathbb{P}$ used in the *H1fit1*, a $\mathbb{P}$ remnant is left, for which gluon radiation is suppressed, and the resulting final state is expected to be more pencil-like. One solution seems to be to add gluons to the partonic structure of the $\mathbb{P}$, which will create broader final states from BGF type events (RAPGAP *H1fit2*). The comparisons with models which do not assume a partonic structure of a $\mathbb{P}$ but produce quarks and gluons from the dissociation of the virtual photon (RIDI, QCD $q\bar{q}$ and $q\bar{q}g$) seem to indicate that an appropriate mixture of both $q\bar{q}$ and $q\bar{q}g$ final states is necessary to reproduce the diffractive global event shape measurement.

A model which includes a final state composition like that in a photon dissociative approach is the SATRAP model, which gives a very good description of the T and S measurement without the need of further tuning.

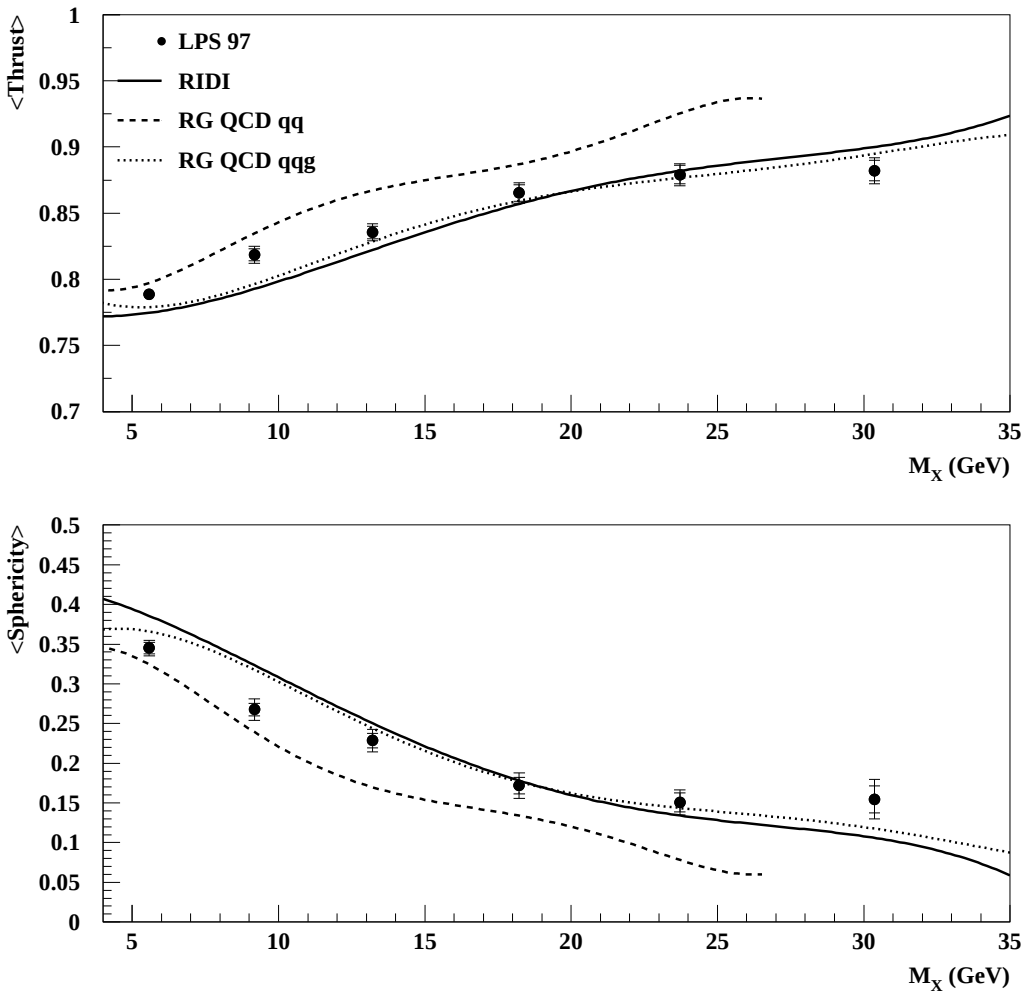

Figure 7.14: Comparison of the average values of thrust $<T>$ and sphericity $<S>$ (dots) as a function of the invariant mass M_X with predictions from the RIDI MC generator (solid) and QCD-based models of a $q\bar{q}$ (dashed) and a $q\bar{q}g$ (dotted) final state.

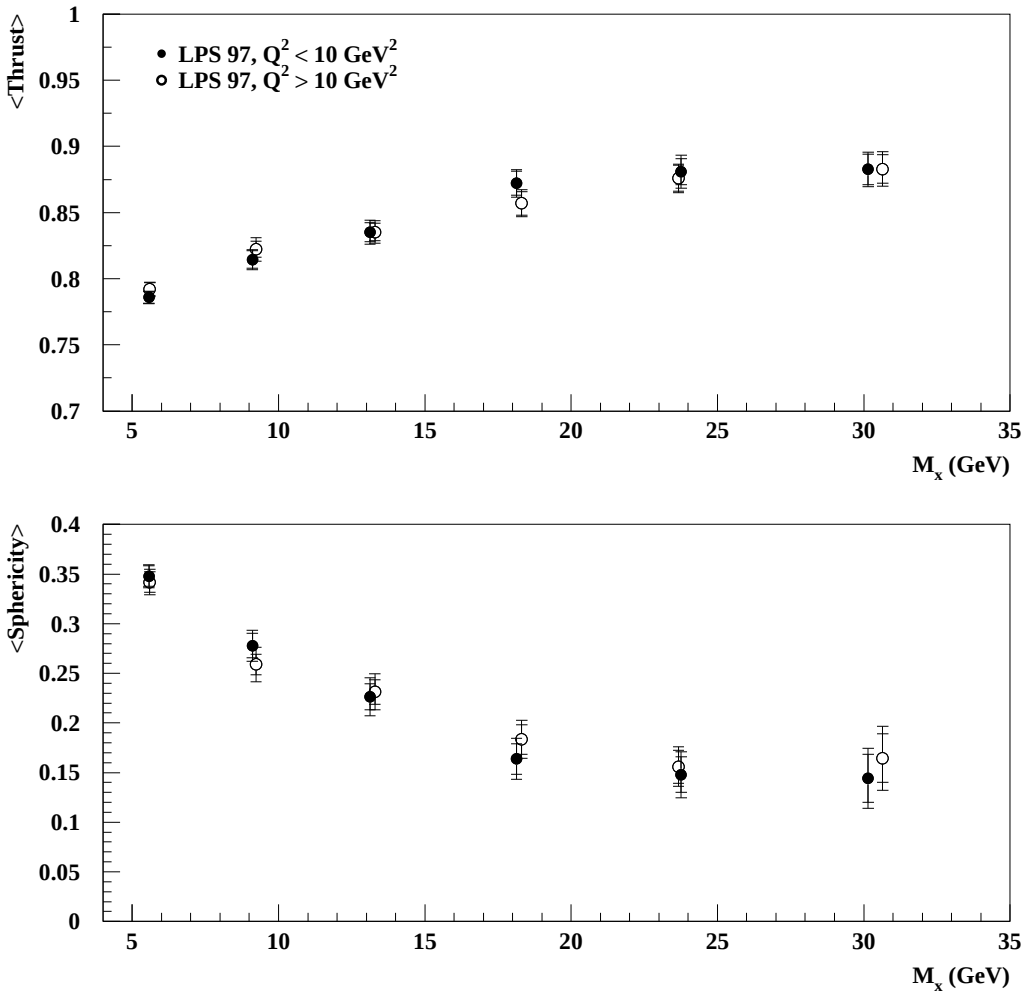

Figure 7.15: The average thrust and sphericity measurement in two bins of Q^2; $Q < 10$ GeV^2 and $Q > 10$ GeV^2. No dependence on Q^2 is visible in the data.

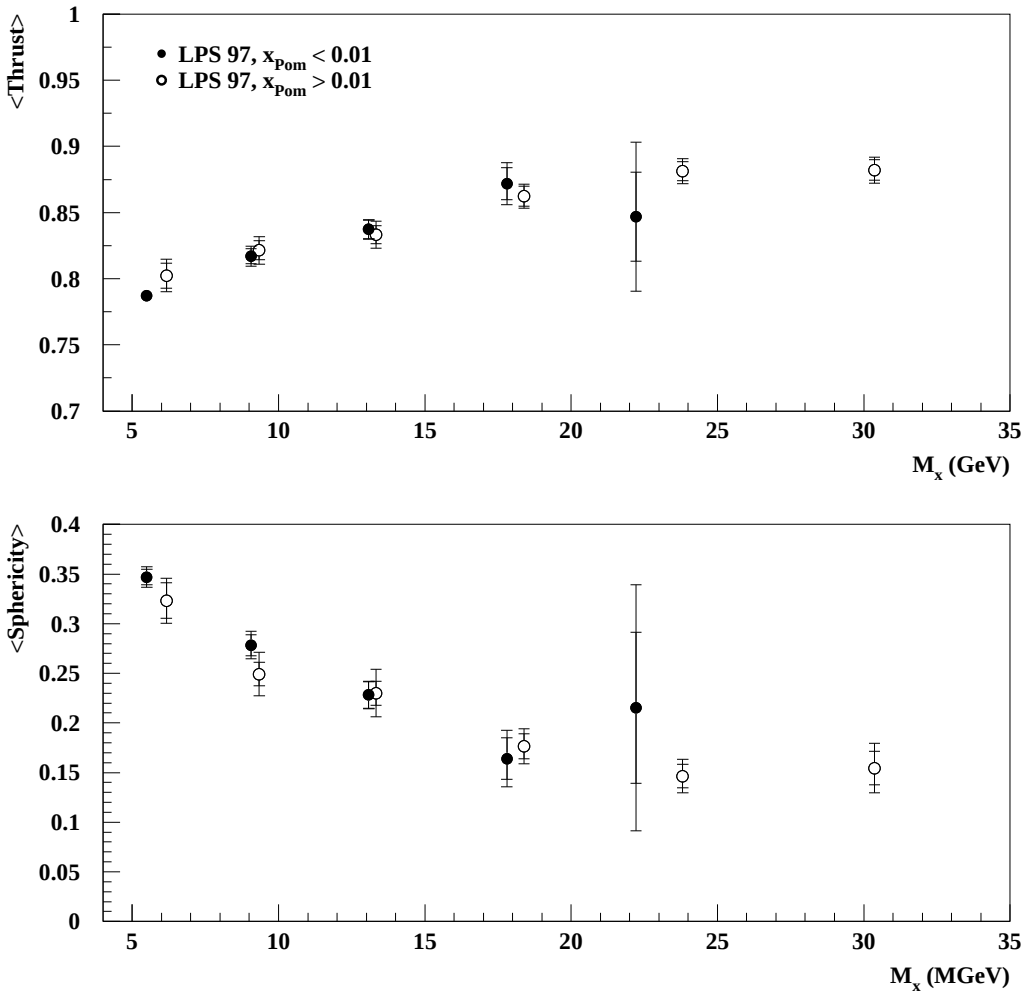

Figure 7.16: The average thrust and sphericity measurement in two bins of x_{IP}; $x_{IP} < 0.01$ and $x_{IP} > 0.01$. No dependence on x_{IP} is visible in the data.

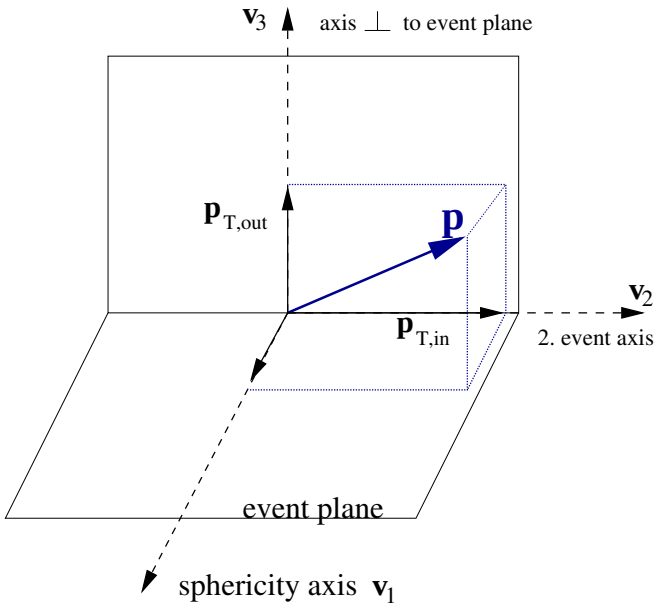

Figure 7.17: The event plane and the associated transverse momenta $p_{T,in}$ and $p_{T,out}$ of the event plane of a hadronic final state in the $\gamma^*\mathbb{P}$ center-of-mass system.

7.3 Transverse Momenta

7.3.1 Definition of $p^2_{t,in}$, $p^2_{t,out}$ and $p^2_{t,thrust}$

The eigenvectors of the sphericity tensor (Equation 7.8) can be used to define transverse momenta *in* and *out* of the event plane. The eigenvector $\mathbf{v}_1$ gives the direction of the sphericity axis, which is the symmetry axis of the event. Together with the eigenvector $\mathbf{v}_2$, which is associated with the second largest eigenvalue λ_2, the sphericity axis spans the event plane. The third eigenvector $\mathbf{v}_3$ belonging to the smallest eigenvalue λ_3 is normal to the event plane (Figure 7.17)

The average squared transverse momenta per event in and out of the event plane can then be defined as

$$<p^2_{T,in}> \;=\; \lambda_2 \cdot \frac{\sum p_i^2}{N_{final}} \tag{7.9}$$

$$<p^2_{T,out}> \;=\; \lambda_3 \cdot \frac{\sum p_i^2}{N_{final}} \tag{7.10}$$

where $\mathbf{p}_i$ are the momenta of the N_{final} hadronic final state particles. In e^+e^- annihilation, the measurement of $<p^2_{T,in}>$ and $<p^2_{T,out}>$ and their comparison was used to observe the appearance of gluons from QCD Comptons in the hadronic final

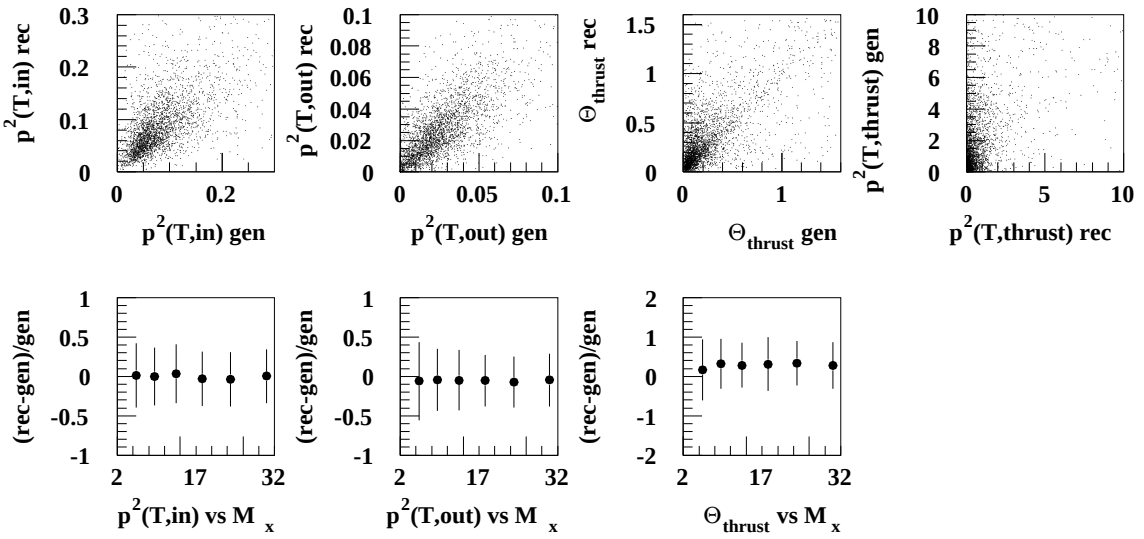

Figure 7.18: Resolution of $p^2_{T,in}$, $p^2_{T,out}$, θ_{thrust} and $p^2_{T,thrust}$. The top row shows scatter plots of reconstructed versus generated quantity; the bottom row, the resolution from Gaussian fits as a function of generated M_X. The resolution on $p^2_{T,thrust}$ is so poor that a Gaussian fit could not be performed and therefore this plot is not shown.

state as the center-of-mass energy $\sqrt{s}$ increased [20, 113]. While the average of $<p^2_{T,out}>$ stayed roughly constant as a function of $\sqrt{s}$, $<p^2_{T,in}>$ increased with $\sqrt{s}$. From QCD predictions of pure $q\bar{q}$ production in e^+e^- annihilation, this increase was not expected. Taking into account the radiation of gluons off the quark lines could account for this slope, ultimately resulting in planar three-jet events.

The left-hand side of Figure 7.18 shows the resolution of $<p^2_{T,in}>$ and $<p^2_{T,out}>$ as scatter plots (top) and as a function of the generated invariant mass M_X (bottom). The resolution was obtained from Gaussian fits and amounts to approximately 35% with little dependence on the mass.

As pointed out in Section 7.1 and illustrated in Figure 7.1, the boost (with the subsequent rotation) of the final state X to the $\gamma^*\mathbb{P}$ center-of-mass frame introduces another kinematical variable θ_{thrust}, which can be used to calculate the transverse momentum of the event with respect to the $\gamma^*\mathbb{P}$-axis via

$$p_{T,thrust} = \frac{1}{2} \cdot M_X \sin(\theta_{thrust}). \tag{7.11}$$

The determination of the thrust angle θ_{thrust} is a measurement of how far the event axis is rotated away from the axis of the $\gamma^*\mathbb{P}$ center-of-mass frame. The corresponding angle in e^+e^- collisions is dominated by the process $e^+e^- \to q\bar{q}$ which

follows a $(1 + \cos^2\theta)$ distribution for massless spin $\frac{1}{2}$ particles. A measurement of this angle could therefore reveal differences between the diffractive final state and the final state produced in e^+e^- annihilation if gluons from a BGF-type diagram, which are not present in e^+e^- annihilation, contribute in the final state.

However, the reconstruction of the thrust angle has very poor resolution as can be seen from the right-hand side of Figure 7.18. The mean of the Gaussian fits to $(\theta^{rec}_{thrust} - \theta^{gen}_{thrust})/\theta^{gen}_{thrust}$ indicates a resolution of only 60% and higher, not taking into account the large tails of the distributions. The generated thrust angle is very small (the distribution peaks around 2°), so that the measured value is dominated by the resolution of the measurement and not by the value itself.

The top half of Figure 7.19 demonstrates the reconstruction quality of the averages of the averaged squared transverse momenta by comparing the reconstructed values (circles) from the RAPGAP MC with the generated ones (solid line). $p^2_{T,in}$ and $p^2_{T,out}$ (Figure 7.19 a,b) are well reconstructed with correction factors of typically less the 5 %, while the thrust angle and the transverse momentum of the thrust (Figure 7.19 c,d) have very large corrections of more than 30 % depending on M_X. The bottom half Figure 7.19 shows how well the data are reproduced by the RAPGAP MC. The transverse momenta in and out of the event plane (Figure 7.19 e,f) show the same behavior in value and mass dependence in data and MC. The variables calculated using the thrust axis show large discrepancies of more than 25 %, again depending on the mass (Figure 7.19 g,h).

As a consequence of the bad resolution and large correction factors necessary to extract the hadron level values, and the poor reproduction of θ_{thrust} and $p^2_{T,thrust}$ by the RAPGAP MC, no attempt was made to measure their average values. However some qualitative studies on the thrust angle θ_{thrust} can be performed and are discussed in Section 7.3.2.

Figure 7.20 shows the effect of the systematic error analysis (section 6.7) on the values of $<p^2_{T,in}>$ (top) and $<p^2_{T,out}>$ (bottom) in bins of the invariant mass as a function of the index of the systematic check. The variations are typically below 5.0. The largest contributions originate from the shift in x_L (check index 15 and 16), and from scaling of the energy deposit in the inner ring of the FCAL (index 7 and 8).

7.3.2 Study of the Thrust Angle Θ_{thrust}

Two problems in the reconstruction of the angle Θ_{thrust} between the thrust axis and the $\gamma^*\mathbb{P}$ center-of-mass axis prevent an extraction of this angle and the related transverse momentum on the hadron level:

1. The angle produced in the RAPGAP MC does not describe the data (Figure 7.19 c).

2. The angle is very poorly reconstructed (Figure 7.19 g).

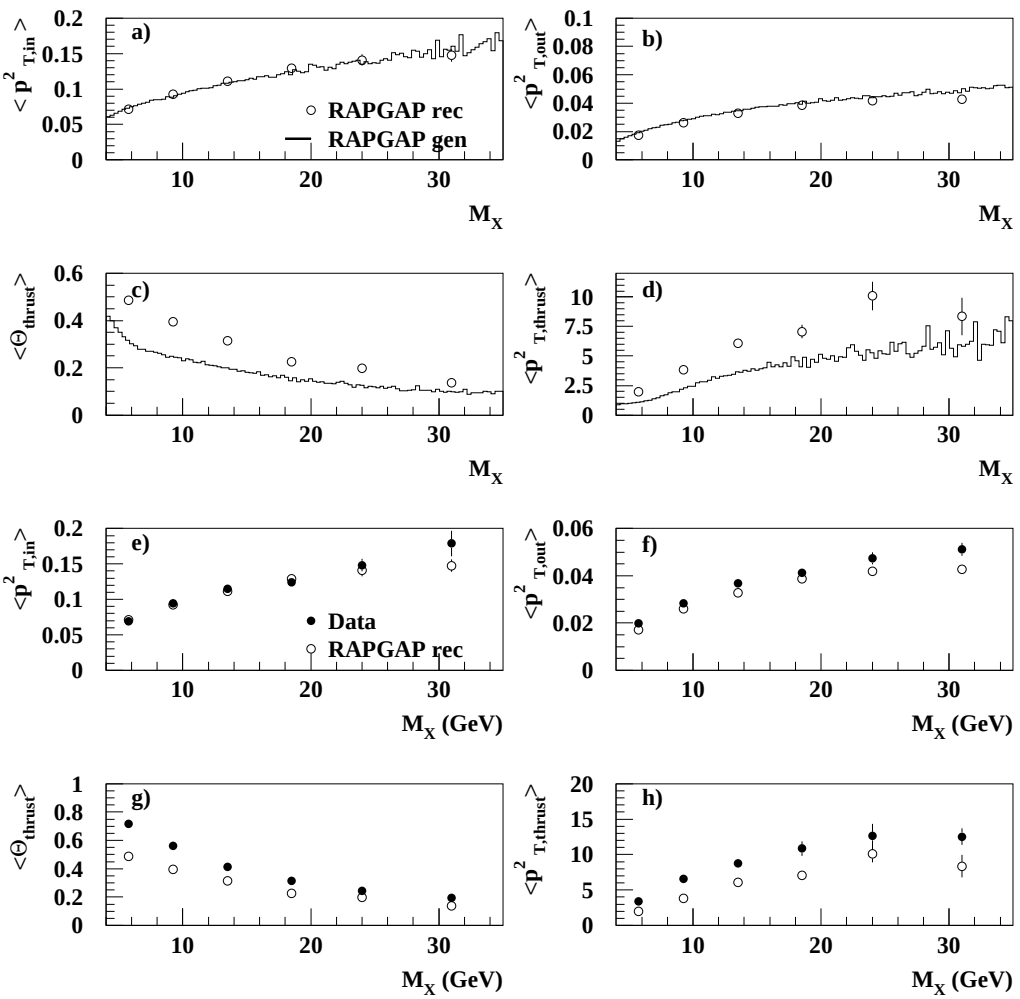

Figure 7.19: Top four plots: Comparison between the reconstructed (circles) and generated value (line) of the average values of the averaged squared transverse momenta using the RAPGAP MC. The correction factors for $p^2_{T,in}$ and $p^2_{T,out}$ (a,b) are typically below 5 %, for θ_{thrust} and $p^2_{T,thrust}$ (c,d) very large. Bottom four plots: Comparison between data (dots) and reconstructed RAPGAP MC. For $p^2_{T,in}$ and $p^2_{T,out}$ (e,f), the data are well reproduced by the MC, while the differences for θ_{thrust} and $p^2_{T,thrust}$ (g,h) are 25 % and higher depending on the M_X.

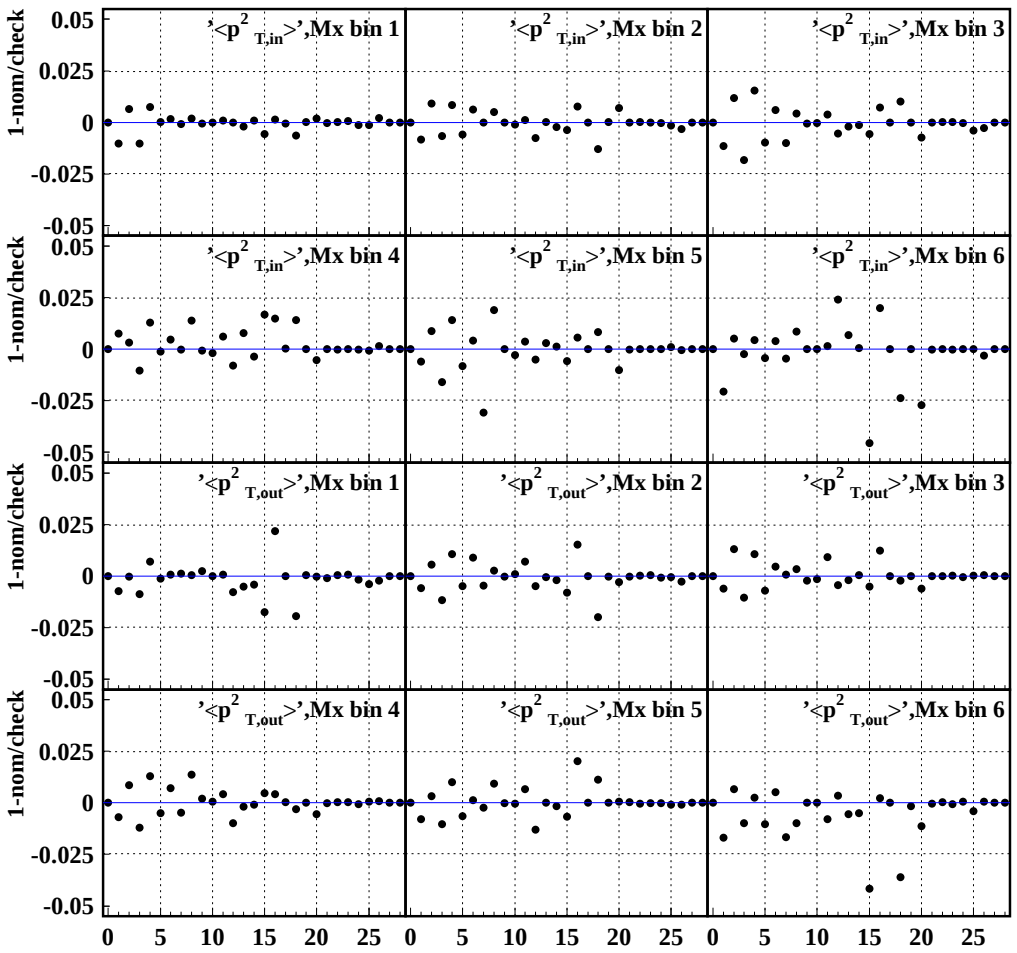

Figure 7.20: Effect of the systematic studies on the values of $<p^2_{T,in}>$ (top) and $<p^2_{T,out}>$ (bottom) in bins of M_X. The horizontal axis corresponds to the index given in Section 6.7 with bin 0 indicating the nominal value.

Since RAPGAP generates a very small Θ_{thrust}, a small mismeasurement of the thrust axis will have a large effect on the reconstruction quality of this angle. Figure 7.21 shows the distribution of Θ_{thrust} measured in the data (dots) for six bins of the invariant mass in comparison with the distributions reconstructed for RAPGAP *H1fit2* (solid histogram, has the DIS background contribution added in). The reconstructed distribution of Θ_{thrust} produced by RAPGAP is too narrow and too peaked around zero for all bins in M_X, and in particular fails to describe the tails of the distributions.

After applying a scale of 1.6 to the thrust angle produced by RAPGAP, the agreement between data and MC is satisfactory (Figure 7.22). Assuming, that the reconstruction of the thrust angle does not have any non-linear effects, the thrust angle can now be compared to the predictions of MC models, which are only available on the hadron level (SATRAP, RG $q\bar{q}$, RG $q\bar{q}g$, and *H1fit1*). The scale of 1.6 is applied to the generated values of Θ_{thrust} of the RAPGAP generator with *H1fit2* and is compared to the generated values of the other models.

In Figure 7.23 the scaled, generated thrust angle of RAPGAP with *H1fit2* (dots), which is now assumed to represent the corrected data distributions, is compared with the predictions of SATRAP (solid histogram), the QCD $q\bar{q}$ model (dashed), the QCD $q\bar{q}g$ model (dotted), and RIDI (open squares). As expected, the $q\bar{q}$ model generates an angle, which is much too small for higher values of M_X.. The $q\bar{q}g$ model produces a Θ_{thrust}, which is larger than the one in the $q\bar{q}$ model, and gives a very good description of the "data" in the medium M_X range. In the high M_X bins, the angle predicted by the $q\bar{q}g$ model seems to slightly smaller than the angle assumed for the "data". This could however be due to a smearing effect, which is not properly taken into account by the scaling procedure. SATRAP (solid) gives a very good description of the "data" over the full M_X range. It is interesting to note, that the angle produced by SATRAP can in general not be accounted for by an incoherent sum of the $q\bar{q}$ and $q\bar{q}g$ model, which produce the same kind of final state as SATRAP. Additional transverse momentum must enter into the SATRAP model. RIDI (open squares) gives a good description in the medium mass range, while the distribution is a bit too flat at low masses and falls too steeply for high masses.

Figure 7.24 shows the $q\bar{q}$ (dashed) and $q\bar{q}g$ (solid) contributions within the SATRAP model (dots) to the thrust angle. Both diagrams produce a finite angle, indicating that some intrinsic transverse momentum is present in both contributions. As expected, the angle associated with the $q\bar{q}g$ diagram is larger than the one present in the $q\bar{q}$ induced final state.

The thrust angle produced by the gluons from a BGF-type contribution as implemented in the RAPGAP model (*H1fit2*) (dots) is shown in Figure 7.25 as the solid histogram compared to the $q\bar{q}$ component (dashed), which corresponds to the

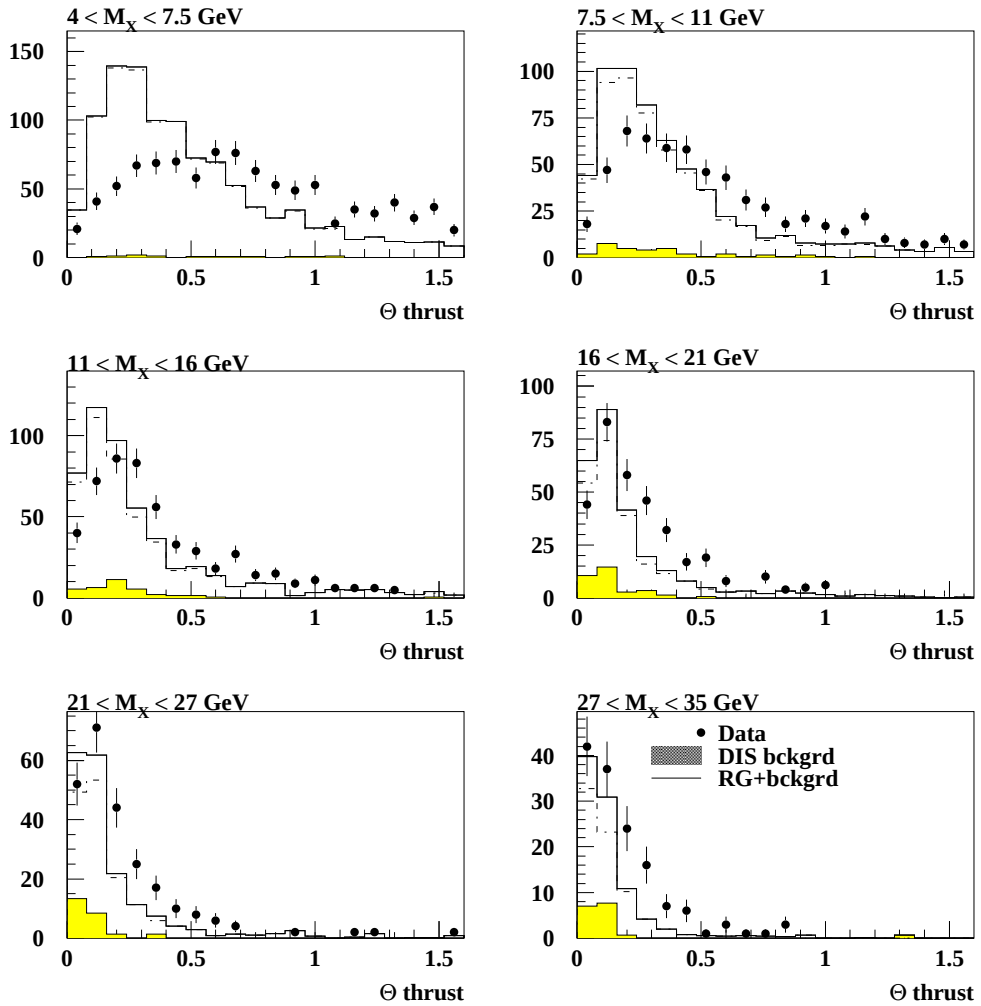

Figure 7.21: Reconstructed distributions of Θ_{thrust} in six bins of M_X to compare data (dots) with reconstructed MC (solid), and the contribution from DIS background (hashed histogram).

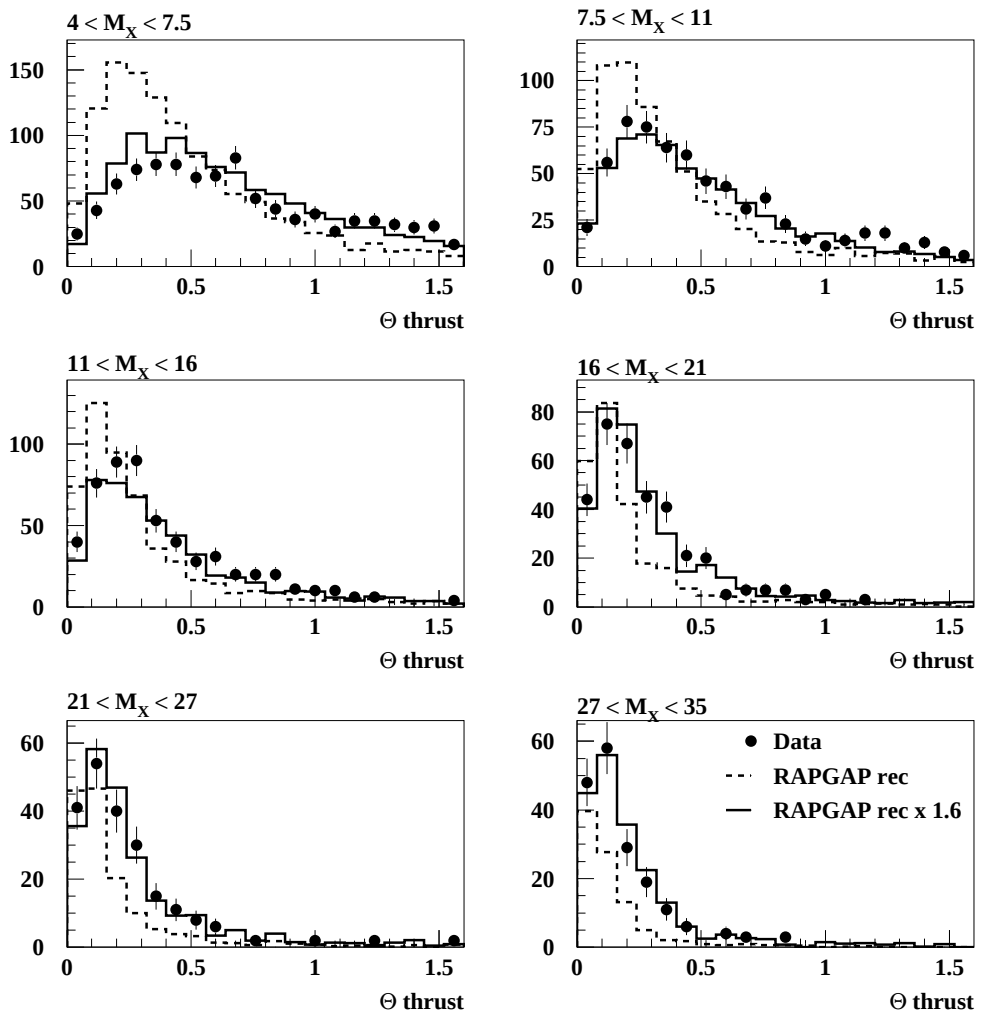

Figure 7.22: Reconstructed Θ_{thrust} of the data (dots) compared to the reconstructed values of the RAPGAP generator (dashed) and the RAPGAP values scaled by a factor 1.6 (solid). After applying this scale factor, the distributions are well described.

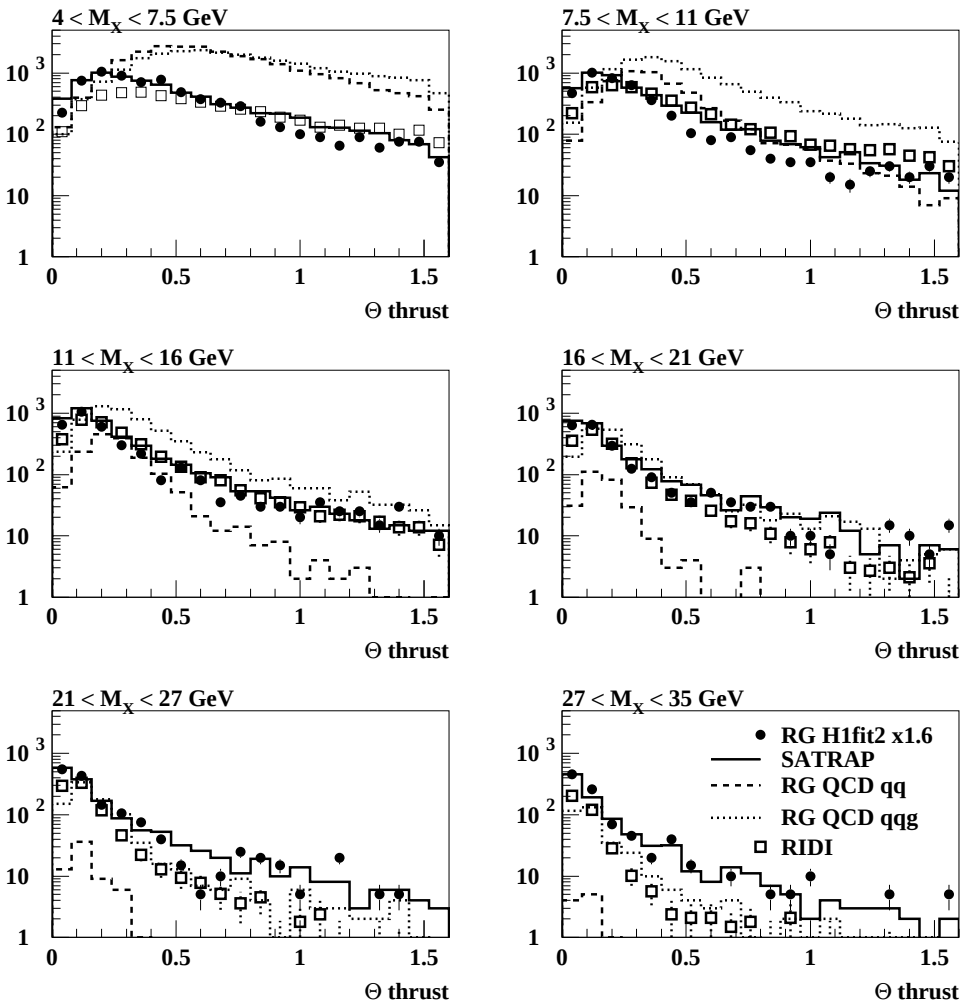

Figure 7.23: The scaled generated thrust angle of RAPGAP (dots) compared to the predictions of SATRAP (solid), $q\bar{q}$ (dashed), $q\bar{q}g$ (dotted), and RIDI (open squares).

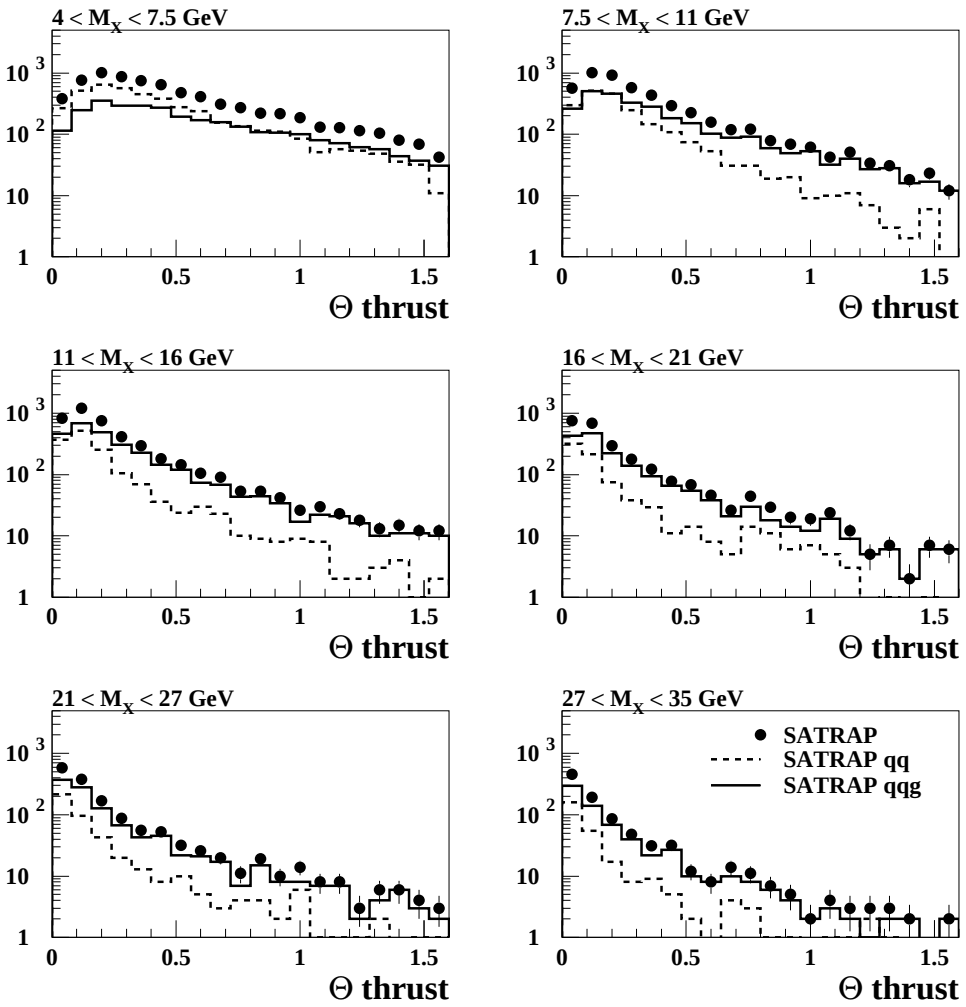

Figure 7.24: Relative contributions of the $q\bar{q}$ (dashed) and $q\bar{q}g$ (solid) components of the SATRAP (dots) model.

angle produced by RAPGAP with the *H1fit1*. The gluonic component of the thrust angle arising from a BGF-type process looks very different compared to the gluon component of a photon dissociative process as implemented in SATRAP. The BGF part contributes almost only to the tails of the distributions except for the highest masses. The peak at $\Theta_{thrust} = 0$ can be attributed exclusively to the $q\bar{q}$ component of the resolved $\mathbb{P}$.

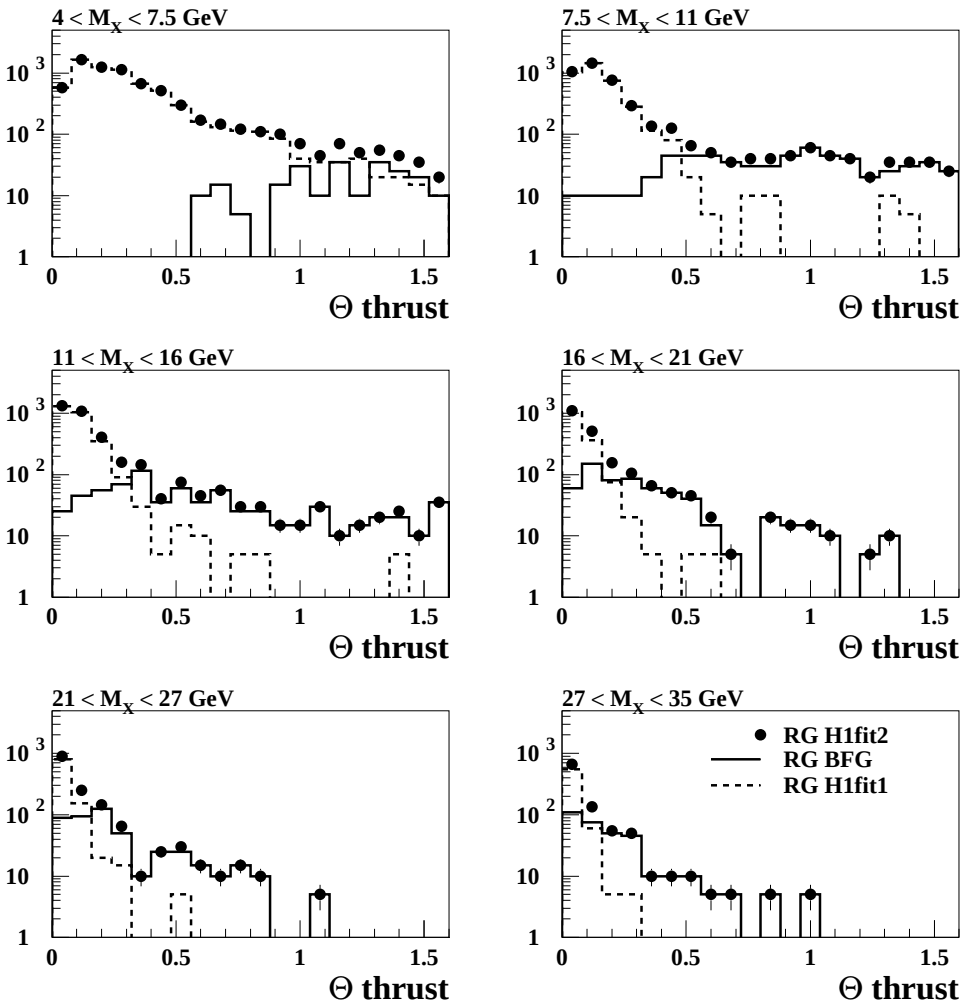

Figure 7.25: Relative contributions of the $q\bar{q}$ of the *H1fit1* (dashed) and BGF (solid) components of the RAPGAP model (dots) with *H1fit2*.

7.3.3 Average Transverse Momenta

Figure 7.26 shows the average of the averaged squared transverse momentum in (top) and out (bottom) of the event plane, $<p^2_{T,in}>$ and $<p^2_{T,out}>$, respectively, as a function of the invariant mass M_X in comparison with predictions of various MC generators.

Both $<p^2_{T,in}>$ and $<p^2_{T,out}>$ rise with increasing center-of-mass energy, but the rise in $<p^2_{T,in}>$ is steeper. Also, the average transverse momentum out of the event plane is smaller by about a factor of 3 than the average transverse momentum in the event plane, indicating that the events are planar. The RAPGAP MC with *H1fit2* (solid) gives a good description of $<p^2_{T,in}>$, but slightly underestimates $<p^2_{T,out}>$, while the *H1fit1* (dotted) underestimates both transverse momenta with the discrepancy in $<p^2_{T,in}>$ being larger. SATRAP (dashed) and JETSET (dashed-dotted) give almost the same result underestimating both $<p^2_{T,in}>$ and $<p^2_{T,out}>$ by about 25% in the medium M_X range. The increase of the average value of the averaged squared transverse momentum out of the event plane was attributed in e^+e^- annihilation to the larger spread of the sphericity axis due to gluon bremsstrahlung [113]. The behavior of the transverse momenta in the diffractive final state, which exhibit the same kind of behavior, may, therefore, be interpreted in a similar way. Even though the sphericity is correctly predicted by SATRAP, the transverse momenta are not. This could be explained, if the number of final state hadrons is different in the data and in SATRAP. This effect would be canceled out in the sphericity value, since it is a dimensionless number. The smaller value of $<p^2_{T,in}>$ for the *H1fit1* could be attributed to the $\mathbb{P}$ remnant treatment of one of the quarks, for which this gluon radiation is suppressed. On the other hand, looking at the behavior of the *H1fit2* with a gluonic $\mathbb{P}$, a similar trend can be observed from gluons, which originate from a BGF-type process. SATRAP, which did a very good job describing the thrust and sphericity measurement, does reproduce the slope correctly, but fails to generate the right amount of transverse momentum.

In Figure 7.27 the average squared transverse momenta in and out of the event plane are compared to predictions of the RIDI (solid), $q\bar{q}$ (dashed), and $q\bar{q}g$(dotted) MC models. RIDI overestimates $<p^2_{T,in}>$ by about 50 %, which is probably due to the large contribution from $q\bar{q}g$ events. However, this kind of final state seems to produce the right amount of $<p^2_{T,out}>$. The $q\bar{q}g$ model on the other hand, which produces a final state very similar to RIDI as can be seen in the thrust and sphericity measurement, predicts a lot less $<p^2_{T,in}>$ than RIDI and actually underestimates the amount compared to the data. This can be explained with a different kinematic distribution of the gluons relative to the quarks. Since the gluon and the $q\bar{q}$ pair in the $q\bar{q}g$ model move in opposite directions, with the gluon being collinear with the $\mathbb{P}$, transverse momentum would result from the opening angle of the two quarks. From the comparison with the $q\bar{q}$ model, which gives almost the same result, one

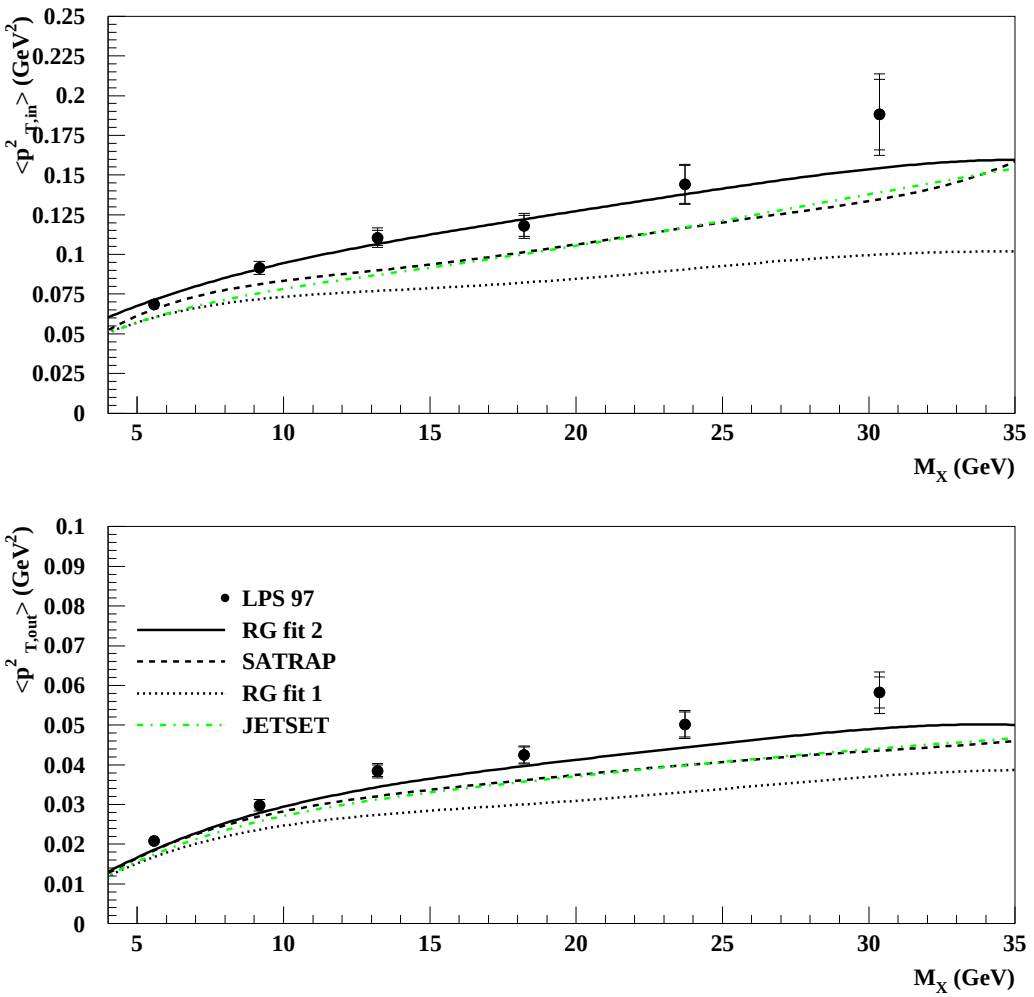

Figure 7.26: Average of the averaged squared transverse momentum in (top) and out (bottom) of the event plane. The LPS data (dots) are compared to predictions from JETSET (grey, dashed-dotted), RAGAP with *H1fit2* (solid), and *H1fit1* (dotted), and the SATRAP generator (dashed). Inner error bars show the statistical error only; the outer error bars, statistical error and systematic uncertainty added in quadrature.

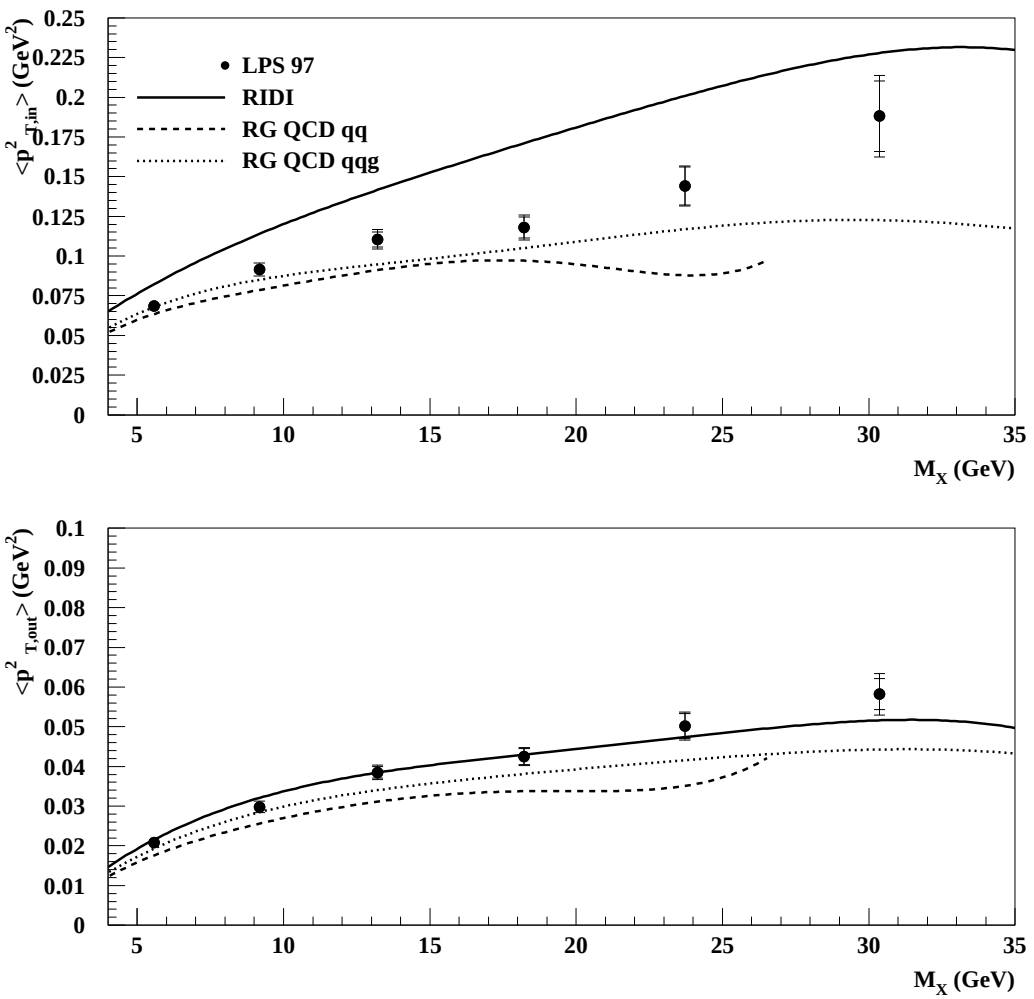

Figure 7.27: $<p^2_{T,in}>$ and $<p^2_{T,out}>$ (dots) as function of M_X compared to the predictions from the RIDI (solid) MC generator and from a pure $q\bar{q}$ (dashed) and $q\bar{q}g$ (dotted) final state.

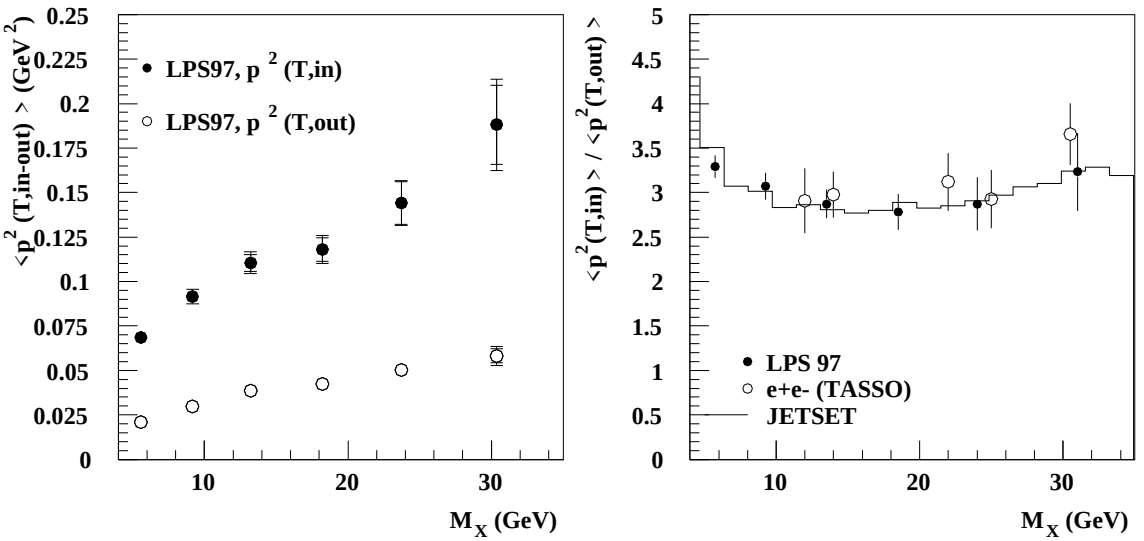

Figure 7.28: Comparison of $<p^2_{T,in}>$ (dots) with $<p^2_{T,out}>$ (circles) in the left plot. The rise in $<p^2_{T,in}>$ is stronger than the one observed in $<p^2_{T,out}>$. The right plot shows that the ratio of $<p^2_{T,in}>$ and $<p^2_{T,out}>$ is the same in the diffractive (dots) and e^+e^- (circles) final state (together with the predictions from JETSET). Only statistical errors are shown.

would conclude that the opening angle in this kinematic regime is very small and the two quarks travel almost collinear.

In Figure 7.28, the transverse momenta of the diffractive final state are compared directly with each other (left plot). The ratio of the two shows the same behavior as the transverse momenta observed in the e^+e^- experiments (right plot). For a pure $q\bar{q}$ state QCD predicts, that both transverse momenta are flat as a function of the center-of-mass energy [113], while the energy dependence comes almost exclusively from the radiation of gluons off the quark lines. A similar conclusion might be drawn for the diffractive scattering process, assuming that the dynamics are slightly different to account for the smaller amount of observed transverse momentum.

7.3.4 Summary of the Transverse Momenta Measurement

The fact that the transverse momentum in the event plane exceeds the momentum out of the event plane by roughly a factor of 3 shows that the events are mostly of planar topology. The observed ratio is in very good agreement with the ratio observed in e^+e^- collisions. Here, the difference and the increase of the momenta with increasing center-of-mass energy is explained with gluons in the final state radiated off the quark lines. This correspondence, supported by the comparisons with

the MC models, indicates that the observed values and energy dependence of the transverse momenta require also gluons in the diffractive final state. However, since the values are different from the ones expected in e^+e^- (JETSET), the production mechanism might be different. Transverse momenta different from those predicted by QCD Compton gluon radiation can be expected if the radiated gluon couples to one of the gluons exchanged with the proton, as implemented in the QCD-based diffractive models.

However, RAPGAP with the *H1fit2* (gluonic $\mathbb{P}$) describes the observed data best and the suppressed gluon radiation off the remnant can be compensated by gluons produced in the BGF process. But the global event shape analysis already disfavors this model.

Only qualitative statements can be made about the measurement of the thrust angle Θ_{thrust}, which suffers from poor resolution, and poor reproduction of the data by the MC. Scaling RAPGAP with *H1fit2* by a factor of 1.6 reproduces the data distributions well. After applying this scale to the generated values, the comparison with SATRAP shows, that it might give an accurate description of the data.

7.4 Inclusive Distributions

The fragmentation of the hadronic system in standard DIS occurs between the struck quark, which forms the current jet, and the remaining quarks in the proton, forming the proton remnant (see Section 2.2.2). The proton remnant is an extended hadronic object and therefore larger than the struck quark. As a result, the hadronic system is asymmetric in the $\gamma^* p$ center-of-mass frame. In particular, particle production is suppressed in the direction of the proton remnant.

If the $\mathbb{P}$ is an extended hadronic object and leaves behind a remnant after the scattering process, a similar situation is encountered in diffractive DIS and the hadronic final state in the $\gamma^*\mathbb{P}$ center-of-mass frame can be expected to show an asymmetric behavior. If, on the other hand, the diffractive scattering process is best described by the fluctuation of a γ^* in a $q\bar{q}$ pair, the final state should be symmetric. Therefore, looking at the particle production in bins of M_X might give extra information on whether the picture of an hadronic $\mathbb{P}$ holds. To study the final state with respect to symmetries in the particle production, the hadronic energy flow and transverse energy flow is measured in the $\gamma^*\mathbb{P}$ center-of-mass frame as a function of the pseudo-rapidity $\eta = -ln(tan\theta/2)$, where θ is the polar angle of a hadron with respect to the $\gamma^*\mathbb{P}$ axis. The virtual photon travels in the direction of positive η. The measurement is performed in three bins of the invariant mass M_X with bin edges chosen to be 4.0, 7.5, 16.0, and 35.0 GeV, which are the same as used in the measurement of the thrust and sphericity distributions.

Figure 7.29 demonstrates the reconstruction quality of the energy (left) and transverse energy (right) flow measurement by comparing the reconstructed (circles) and generated distributions (histograms) for the RAPGAP MC using *H1fit2* after all selection cuts. Unfortunately, the energy flow is not reconstructed well. The correction factors are of the order of 10 to 20 % in the central η region and larger outside. In addition, the shape of the distribution is severely distorted by the reconstruction, especially in the low mass region, introducing features which are not present at the hadron level. The situation looks slightly better for the transverse energy flow (right). Here, the correction factors are typically about half the size of the ones for the energy flow and extend further out of the central region. Also, the shape of the generated distribution is approximately preserved by the reconstruction.

Figure 7.30 shows how well the distributions of the data (dots) are reproduced by the RAPGAP MC (solid). On the left side, the result for the energy flow is shown, the result for the transverse energy flow is on the right. Again, the short-coming of this MC sample is obvious. The MC shows a clear two-peak structure for the energy flow in the lowest mass bin, while the data show only one peak centered at zero. The two-peak structure of RAPGAP can be entirely explained by the absence of BGF-type events in the low mass region due to the high p_T^2 cut of 3 GeV^2. As the mass increases, the agreement between data and MC improves. Also here,

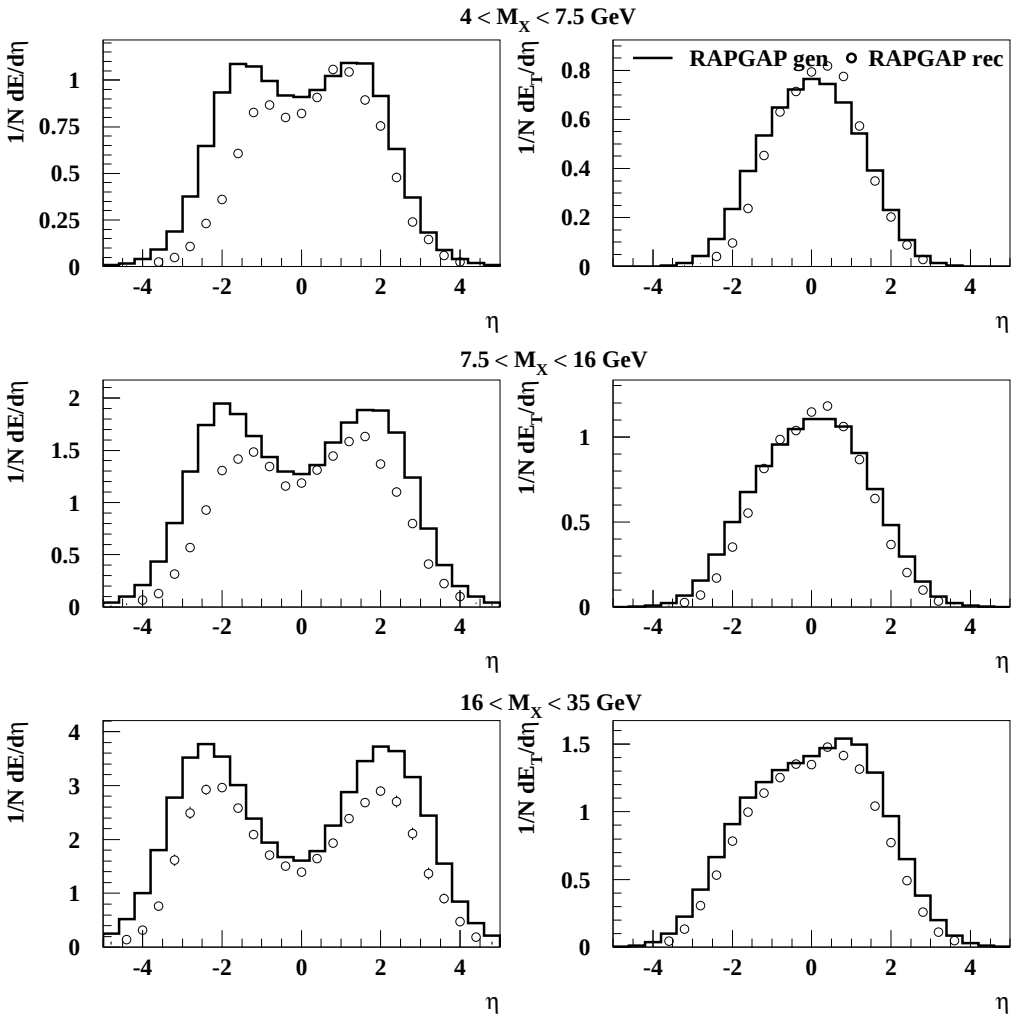

Figure 7.29: Reconstruction quality of the energy flow (left column) and transverse energy flow (right) comparing the reconstructed (circles) and generated (solid) distributions using the RAPGAP MC generator. All event selection cuts were applied.

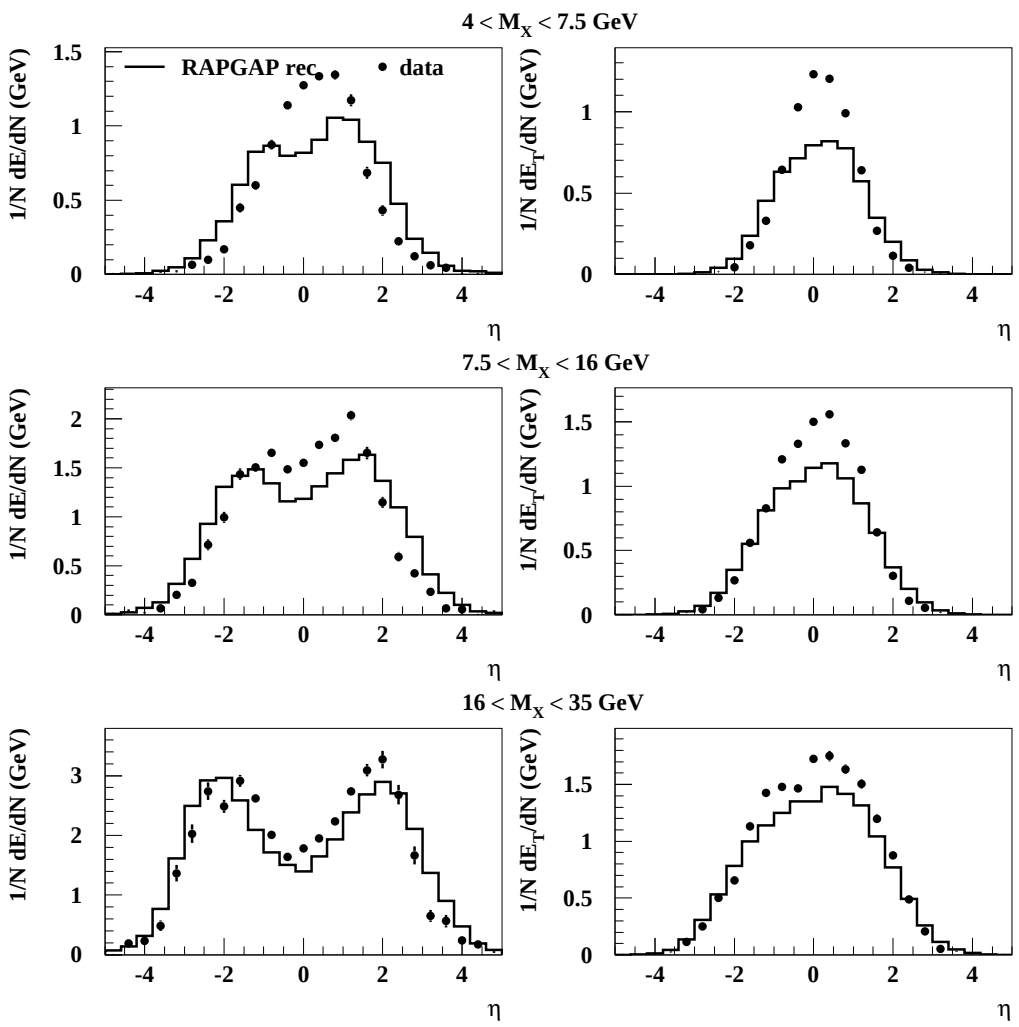

Figure 7.30: The RAPGAP MC with *H1fit2* does not describe the data well, especially in the low M_X region, as can be seen from the comparison of data (dots) and reconstructed (solid) MC energy flows. Most of these problems can be attributed to missing events from BGF-type processes in the low M_X region.

the transverse energy flow agrees slightly better, even though the MC deposits less energy in the central region than the data. However, the approximate shape of the data distributions is reproduced.

Keeping the large (and η dependent) corrections and the poor description of the data by the RAPGAP MC in mind, the following results should be taken with caution. Biases of the results can not be excluded and the dependence of the results on the model used for the corrections is unknown, since a second MC is not available at this moment.

7.4.1 Energy Flow

In Figure 7.31, the corrected energy flow $1/NdE/d\eta$ (dots) from this analysis is compared with results published by the H1 Collaboration [118] (asterisk) using LRG events to select the diffractive sample, and predictions from the JETSET MC generator (dashed) to represent results expected from e^+e^- annihilation, and predictions of the RAPGAP program using *H1fit2* (solid). The H1 results show a larger asymmetry in the second and third M_X bin than the results from the LPS measurement with more energy being deposited in the γ^* direction. This result would support the concept of the $\mathbb{P}$ remnant. The LPS results show a clear asymmetry in the uncorrected data (Figure 7.30), but the corrections have the opposite effect almost making the $\mathbb{P}$ and the γ^* side symmetric. The H1 results are also defined in a slightly different region of phase space: $M_Y < 1.6$ GeV, $x_{I\!P} < 0.025$, $|t| < 1$ GeV^2, $7.5 < Q^2 < 100$ GeV^2, and $0.005 < y < 0.6$, which is different than the phase space defined for the H1 thrust analysis [114]. Furthermore, the M_X bins chosen by the H1 Collaboration have bin edges at 3.0, 8.0, 16.0, and 30.0 GeV, slightly different from the ones used in the present analysis. The LPS results were checked in this region of phase space and no significant change in the distributions could be observed. The RAPGAP MC with *H1fit2* fails to describe the data in the low mass region as discussed earlier. A $q\bar{q}$ dominated final state as implemented in JETSET does not describe the energy flow in the low M_X region, where the clear double-peak structure is not visible in the data. For both, RAPGAP and JETSET, the distributions seem to be slightly too broad in all M_X bins compared to the data. In the highest mass bin, the two-peak structure is well reproduced by both models. It is interesting to note, that RAPGAP, even though it produces a $\mathbb{P}$ remnant, does not show a clear asymmetry in the energy flow between the $\mathbb{P}$ and the γ^* hemisphere.

Figure 7.32 compares the corrected energy flow distributions with the predictions from the RIDI (solid), $q\bar{q}$ (dashed), and $q\bar{q}g$ (dotted) model. The difference between these models are small. While all of them do not describe the peak in the lowest mass bin correctly, the situation improves as the mass increases. In the central M_X bin, the two-peak structure appears in all three models, with a light preference towards the $q\bar{q}$ model. In the highest M_X bin, RIDI and the model with the $q\bar{q}g$ final state

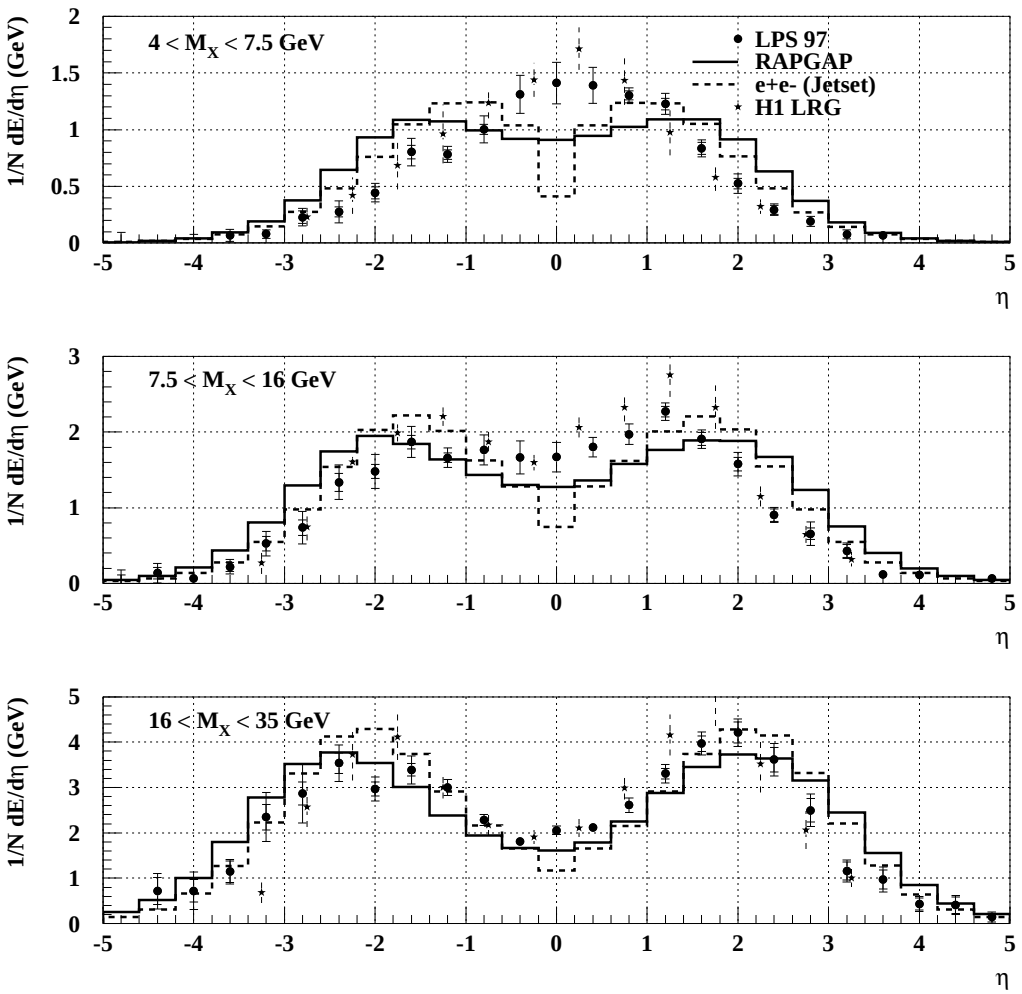

Figure 7.31: Comparison of the corrected energy flow (dots) with results from the H1 Collaboration (asterisk), the RAPGAP MC with *H1fit2* (solid) and predictions from JETSET (dashed). The measurement is performed in three bins of M_X with bin edges at 4.0, 7.5, 16.0, and 35.0 GeV. The inner error bars show statistical errors only; the outer error bars, the statistical error, and systematic uncertainty added in quadrature. The γ^* moves in the direction of positive η.

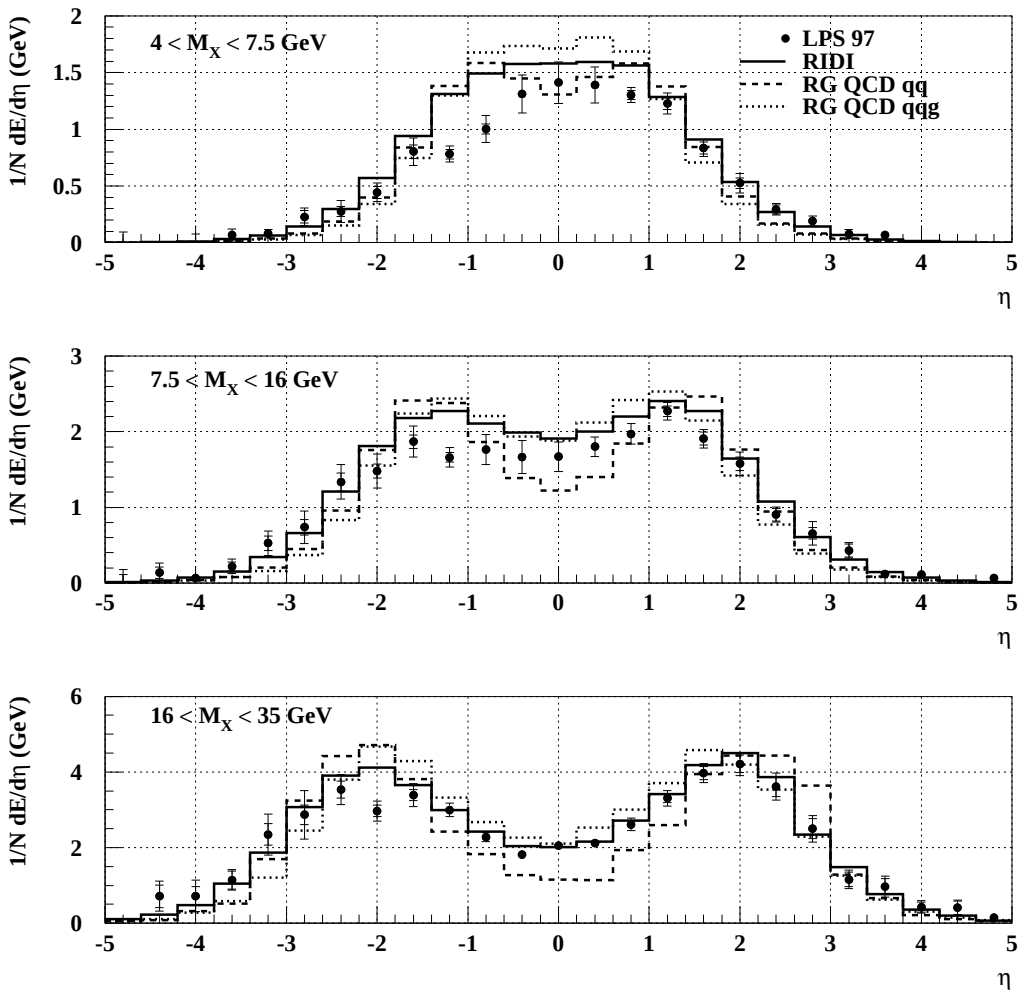

Figure 7.32: Comparison of the corrected energy flow (dots) with predictions from RIDI (solid), the $q\bar{q}$ model (dashed) and the $q\bar{q}g$ model (dotted). Positive η is in the direction of γ^*.

describe the data with approximately the same quality. Here, the $q\bar{q}$ model producing a two-jet final state shows a double-peak structure, which is more pronounced than what is observed in the data. The width of the distributions in all M_X bins is better described by these models than by the RAPGAP MC or by JETSET. The gluon in the final state of the $q\bar{q}g$ model seems to change the particle production only slightly compared to the $q\bar{q}$ system, which is in agreement with the finding of the $<p^2_{T,in}>$ and $<p^2_{T,out}>$ measurement. The final state is dominated by the fact that the gluon and the $q\bar{q}$ pair move in opposite directions and the quark and anti-quark are very close in rapidity.

Figure 7.33 compares the energy flow with the SATRAP model (solid) and with RAPGAP using the *H1fit1*. The $q\bar{q}$ $\mathbb{P}$ clearly fails to describe the data in all M_X bins. The two-peak structure already appears in the lowest mass bin and is too well separated in rapidity at higher masses. Again, no clear evidence of a $\mathbb{P}$ remnant is visible. The SATRAP model reproduces the data well in almost the entire M_X range with a few problems in the lowest mass bin, where the plateau of the distribution is too wide, maybe due to a too large gluon component.

7.4.2 Transverse Energy Flow

The corrected transverse energy flow $1/NdE_T/d\eta$ (dots) is compared to predictions from the RAPGAP MC with *H1fit2* (solid) and JETSET (dashed) in Figure 7.34 in the same three M_X bins as the energy flow measurement described previously. A slight asymmetry between the $\mathbb{P}$ side (negative η) and the γ^* hemisphere, with more energy going into the direction of positive η, seems to be visible with increasing mass. Both models fail to describe the central region of the transverse energy distribution in all M_X bins. JETSET shows a clear two-jet structure, which is symmetric in η and cannot be observed in the data. RAPGAP reproduces the slight asymmetry seen in the data, but not enough energy is deposited in the central region.

Figure 7.35 shows a comparison with RIDI (solid), the $q\bar{q}$ (dashed), and the $q\bar{q}g$ (dotted) model. The $q\bar{q}$ model gives a reasonable description of the data for the lowest mass bin, but shows a two-peak structure for higher masses, which is not observed in the data. The $q\bar{q}g$ model overestimates the energy deposit in the central region systematically for all masses. However, the general shape is reasonably well described showing a slight enhancement in the γ^* direction without the concept of a $\mathbb{P}$ remnant. The same is true for RIDI, with the difference that the amount of energy deposit comes closer to the values observed in the data and is in good agreement in the highest M_X bin. The slight enhancement of the transverse energy flow in the γ^* direction is probably due to the finite opening angle of the $q\bar{q}$ pair giving rise to some small amount of transverse momentum. A $\mathbb{P}$ remnant is not necessary for an asymmetry in the transverse energy flow.

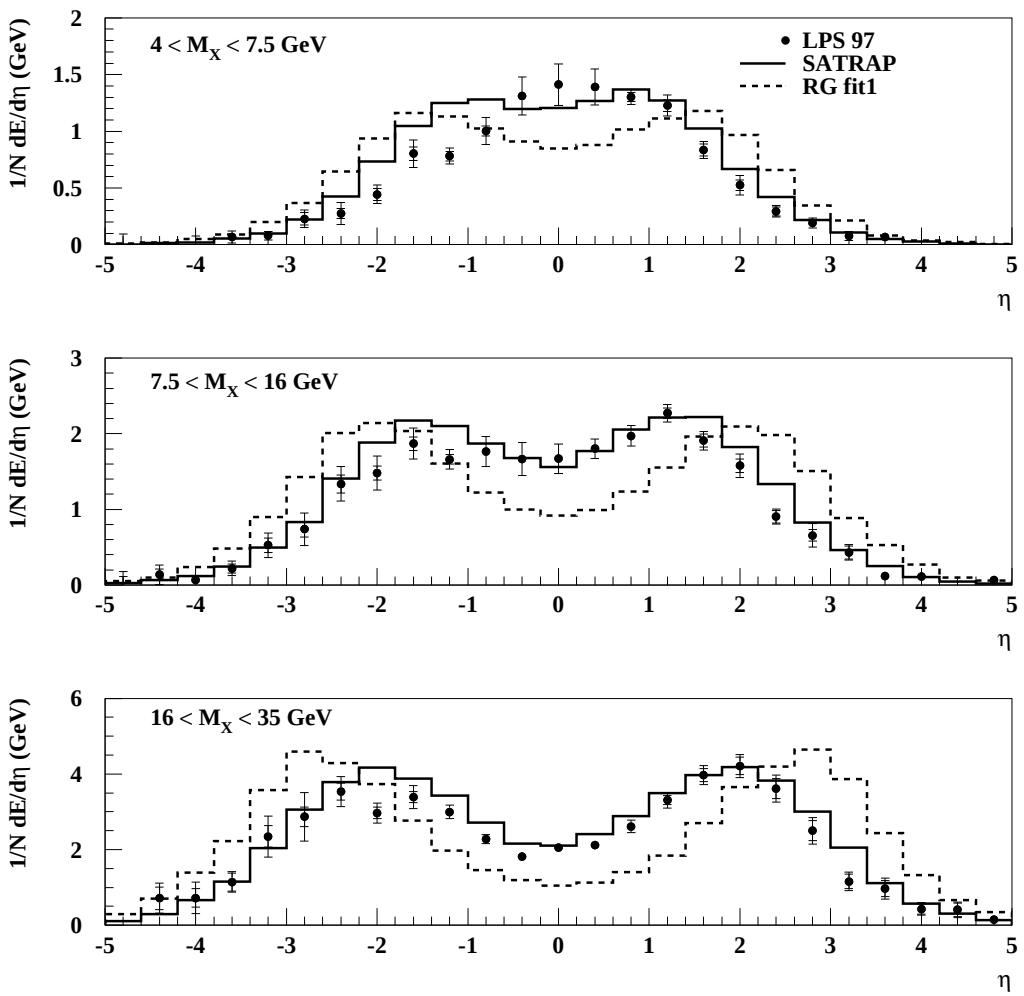

Figure 7.33: Comparison of the corrected energy flow (dots) with the predictions from SATRAP and the RAPGAP MC with *H1fit1*. The virtual photon moves in the direction of positive η.

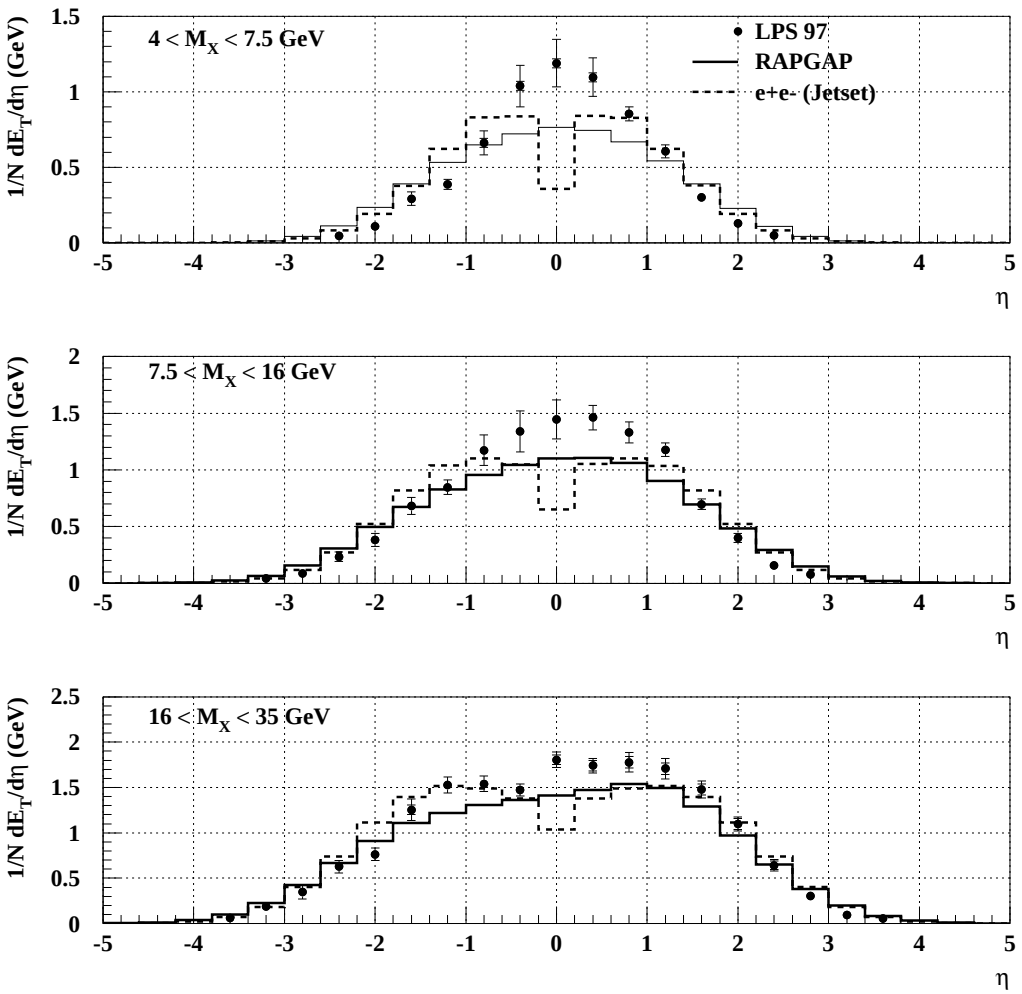

Figure 7.34: Comparison of the corrected transverse energy flow (dots) with results from the RAPGAP MC with *H1fit2* (solid) and predictions from JETSET (dashed). The measurement is performed in three bins of M_X with bin edges at 4.0, 7.5, 16.0, and 35.0 GeV. The inner error bars show statistical errors only; the outer errors bars, the statistical error, and systematic uncertainty added in quadrature. The γ^* moves in the direction of positive η.

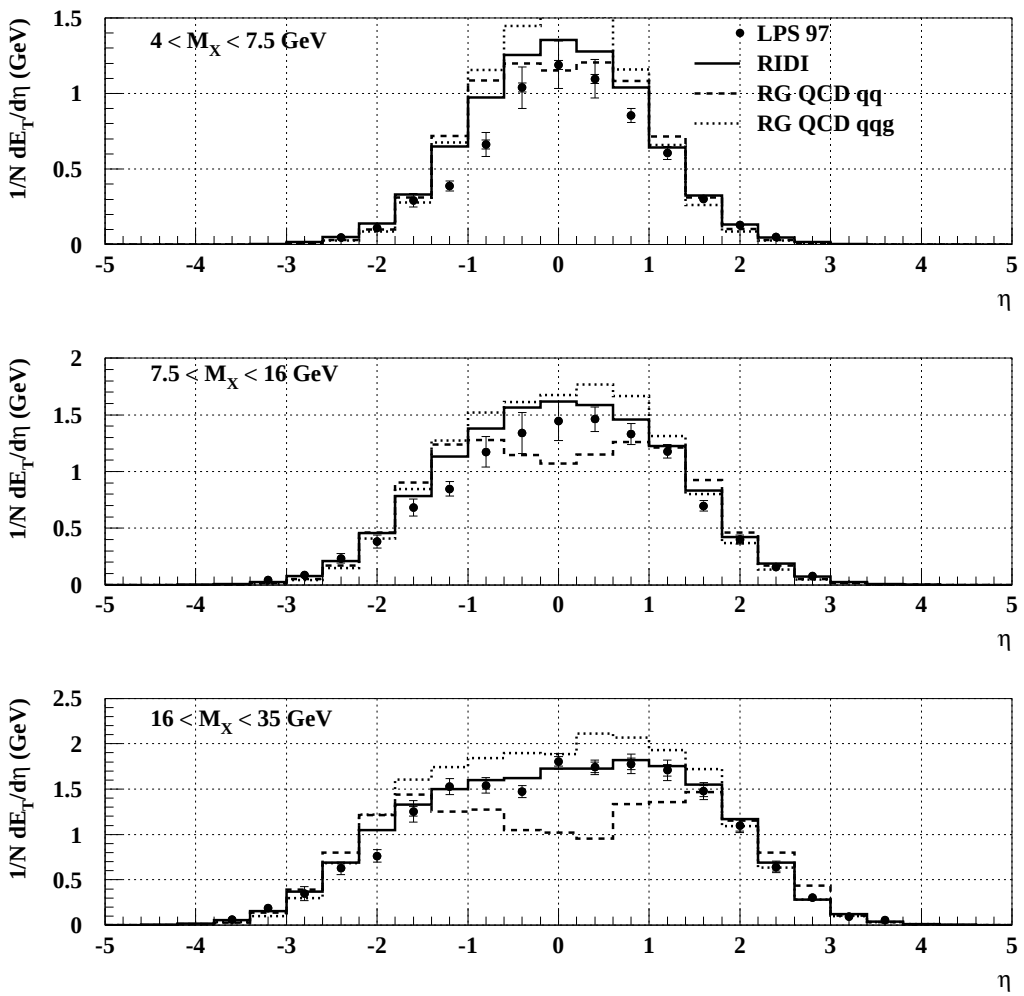

Figure 7.35: Comparison of the corrected transverse energy flow (dots) with predictions from RIDI (solid), the $q\bar{q}$ model (dashed), and the $q\bar{q}g$ model (dotted). The γ^* moves in the direction of positive η.

Finally, Figure 7.36 compares the data with the results from the SATRAP simulation (solid) and the prediction of RAPGAP with *H1fit1* (dashed). The quark-only $\mathbb{P}$ clearly fails to describe the data everywhere producing distributions too flat in the central region. Again, no asymmetry due to the $\mathbb{P}$ remnant is visible. SATRAP gives a generally good description of the data reproducing the correct asymmetry as observed in the data. The larger transverse energy flow in the direction of the γ^* is due to the finite opening angle of the $q\bar{q}$ pair, which moves in the direction of the virtual photon.

7.4.3 Summary of the Energy Flow Measurement

Due to the large correction factors involved and possible model dependencies arising from using RAPGAP for corrections - a model which fails to describe the data - conclusions need to be drawn with caution, especially those based on the energy flow alone and not also on the transverse energy flow. The conclusions here will be based on the transverse energy flow alone.

A $q\bar{q}$ final state similar to the one in e^+e^- as implemented in the JETSET generator fails to describe the energy flow. RAPGAP, leaving a $\mathbb{P}$ remnant behind, also does not give a proper description of the data. In particular, no clear asymmetry due to the $\mathbb{P}$ remnant cannot be observed. However, an asymmetry with a slight enhancement in the virtual photon direction is observed in the data and can be described by models, which assume a dissociation of the virtual photon producing also a $q\bar{q}g$ final state. This kind of final state is included in the RIDI and SATRAP models. A proper mixture of the $q\bar{q}$ and the $q\bar{q}g$ model would probably give a equally good description of the data.

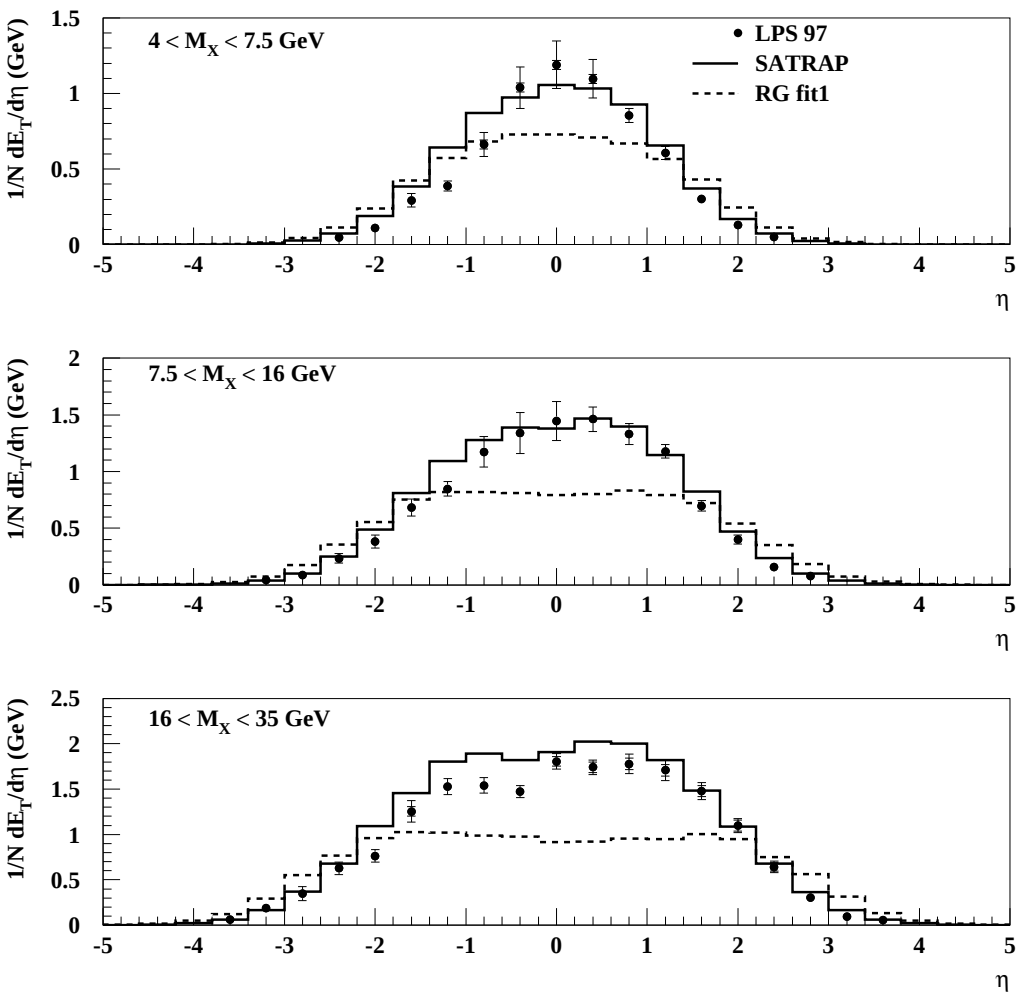

Figure 7.36: Comparison of the corrected transverses energy flow (dots) with the predictions from SATRAP and the RAPGAP MC with *H1fit1*. The γ^* moves in the direction of positive η.

Chapter 8

Summary and Conclusion

Diffractive ep scattering was studied with the ZEUS Leading Proton Spectrometer (LPS) to select a diffractive sample by tagging the leading proton. The hadronic final state X produced in the diffractive events was characterized in terms of the events global properties thrust T, sphericity S, squared average transverse momentum in ($p^2_{T,in}$) and out ($p^2_{T,out}$) of the event plane as a function of its invariant mass M_X as well as in terms of the inclusive distributions of energy flow $dE/Nd\eta$ and transverse energy flow $dE_T/Nd\eta$. The measurement is defined in the kinematic regime of:

$$\begin{array}{lcccl} 4.0 & < & M_X & < & 35.0 \text{ GeV} \\ 4.0 & < & Q^2 & < & 150.0 \text{ GeV}^2 \\ 0.03 & < & y & < & 0.7 \\ 0.0003 & < & x_{_{IP}} & < & 0.03 \end{array}$$

The results obtained in this measurement were compared with results from e^+e^- annihilation and with various MC models implementing a partonic Pomeron or QCD-based exchanges to model the diffractive process. A summary of the comparison between corrected data and all Monte Carlo models can be found in Table 8.1. The final state produced in e^+e^- annihilation is described in detail by QCD producing a $q\bar{q}$ pair with gluons originating from QCD Compton radiation only. The measurement of T and S is in good agreement with e^+e^- results indicating that the final state might have a significant contribution from $q\bar{q}$ production. This is further supported by the good agreement between the data and a MC model (SATRAP) which produces $q\bar{q}$ and $q\bar{q}g$ states from photon dissociation.

Differences between the diffractive final state and an e^+e^- type final state were observed when studying the average transverse momenta in and out of the event plane, where the diffractive final state produces slightly more transverse momentum. However, the ratio between $p^2_{T,in}$ and $p^2_{T,out}$ is the same as in e^+e^-. The final state produced by the $q\bar{q}$ pair should be the same in the hadronic center mass

Var./Model	RG H1fit2	SATRAP	RIDI	QCD $q\bar{q}$	QCD $q\bar{q}g$	RG H1fit1
gluon content	20 - 30 %	60 - 70 %	$>$ 99 %	0	100 %	0
gluon direction	$\mathbb{P}$ remnant	$\mathbb{P}$	$\mathbb{P}$?	-	$\mathbb{P}$	-
Thrust	+2+1+1 more BGF	0 0 0 like e^+e^-	−1 0 0 more $q\bar{q}$	+1+1+2	−1 0 0	+1+2+2
Sphericity	−2−1−1	0 0 0	+1 0 0	−1−2−2	+1 0 0	−1−2−2
$<p^2_{T,in}>$	0 0 0 overall best	0−1−1 like e^+e^-	+2+2+2	0−1−2	0−1−1	−1−2−2 too shallow
$<p^2_{T,out}>$ (fragmentation)	0 0−1	0−1−1	0 0 0	0−1−2	0−1−1	−1−2−2
Eflow (central)	−2−1−1	0 0 0	+1+1 0	+1−1−1	+2+1 0	−2−2−2
Eflow (wings)	+2+2+2	+1 0 0	0 0 0	0−1−1	0−1−1	+2+2+2
Trans. Eflow (c)	−2−2−2	0 0+1	+1+1 0	+1−1−2	0+1+1	−2−2−2
Trans. Eflow (w)	+1 0 0 $\mathbb{P}$ suppressed	0 0 0 $\mathbb{P}$ suppressed	0 0 0 $\mathbb{P}$ suppressed	0 0 0 symmetric	0 0 0 $\mathbb{P}$ suppressed	0 0 0 symmetric

Legend	too low	low	ok	high	too high
	−2	−1	0	+1	+2

Table 8.1: Summary of how the different Monte Carlo models considered in this analysis describe the measurement of the hadronic final state. An underestimation of the value of the variable is indicated by a negative number, an overestimate by a positive number. The numbers indicate the result of the comparison for the low (left), middle and high (right) mass bins.

frame for e^+e^- and photon dissociation. The observed difference is therefore due to the different geometry of the gluon relative to the $q\bar{q}$ pair. In e^+e^-, the gluon is dominantly collinear to the direction of one of the quarks, while in QCD-based diffractive models, the gluon balances the momentum of the $q\bar{q}$. The value of $p_{T,in}$ should therefore be related to the opening angle of the $q\bar{q}$ pair. This geometry still maintains a mainly two-jet structure.

The difference between e^+e^- and the diffractive final state is confirmed by the energy flow measurement, where the e^+e^- results (modeled by JETSET) show a final state with a clear symmetric two-jet structure up to the highest studied masses, which is less pronounced in the hadronic case. A slight asymmetry is observed in the transverse energy flow in the high mass region. This asymmetry is reproduced by the QCD-based diffractive models, which include gluons in the final state. If the gluon balances the momentum of the $q\bar{q}$-pair, an asymmetry can be produced in the transverse energy flow by the finite opening angle of the $q\bar{q}$ pair. The total energy flow would be less effected. The same asymmetry is reproduced by the SATRAP model, which overall gives the best description of the diffractive hadronic final state.

Models, based on a partonic Pomeron with a remnant remaining after the scattering process, overall fail to describe the presented data.

The hadronic final state is subject to contributions from final state gluons. However, a model which produces these gluons by boson-gluon fusion is disfavored. Instead, the hadronic final state can be described in terms of photon dissociation into $q\bar{q}$ pairs with subsequent gluon radiation calculated using methods of perturbative QCD. These gluons can couple to the proton via two-gluons exchanged.

Appendix A

A.1 Tables for $\frac{1}{N}\frac{dN}{dT}$

T Range	$\frac{1}{N}\frac{dN}{dT}$	Stat.	Sys.	Total
0.500 to 0.525	0.00	0.00	0.00	0.00
0.525 to 0.550	0.00	0.00	0.00	0.00
0.550 to 0.575	0.02	0.02	0.06	0.06
0.575 to 0.600	0.25	0.16	0.17	0.24
0.600 to 0.625	0.63	0.26	0.35	0.44
0.625 to 0.650	1.02	0.23	0.18	0.29
0.650 to 0.675	2.02	0.36	0.28	0.46
0.675 to 0.700	2.13	0.32	0.20	0.38
0.700 to 0.725	3.13	0.44	0.39	0.59
0.725 to 0.750	4.01	0.49	0.35	0.60
0.750 to 0.775	4.64	0.55	0.66	0.86
0.775 to 0.800	3.91	0.47	0.22	0.52
0.800 to 0.825	4.39	0.52	0.25	0.57
0.825 to 0.850	3.71	0.49	0.30	0.57
0.850 to 0.875	2.83	0.44	0.24	0.50
0.875 to 0.900	2.65	0.41	0.27	0.49
0.900 to 0.925	2.07	0.37	0.15	0.40
0.925 to 0.950	0.89	0.22	0.09	0.24
0.950 to 0.975	0.40	0.17	0.09	0.19
0.975 to 1.000	0.53	0.19	0.11	0.22

Table A.1: Tabulated values of $\frac{1}{N}\frac{dN}{dT}$ (where T = thrust) with statistical error (stat.), systematic uncertainty (sys.), and total error for $4.0 < M_X < 7.5$ GeV with $<M_X>$ = 5.62 GeV.

T Range	$\frac{1}{N}\frac{dN}{dT}$	Stat.	Sys.	Total
0.500 to 0.525	0.00	0.00	0.00	0.00
0.525 to 0.550	0.00	0.00	0.00	0.00
0.550 to 0.575	0.00	0.00	0.00	0.00
0.575 to 0.600	0.18	0.21	0.34	0.40
0.600 to 0.625	0.56	0.23	0.17	0.29
0.625 to 0.650	0.93	0.28	0.17	0.32
0.650 to 0.675	1.22	0.27	0.19	0.33
0.675 to 0.700	1.16	0.22	0.19	0.29
0.700 to 0.725	2.01	0.33	0.26	0.41
0.725 to 0.750	1.95	0.28	0.13	0.31
0.750 to 0.775	2.43	0.32	0.29	0.43
0.775 to 0.800	3.27	0.41	0.28	0.50
0.800 to 0.825	3.65	0.45	0.20	0.49
0.825 to 0.850	4.21	0.49	0.30	0.57
0.850 to 0.875	4.56	0.53	0.25	0.59
0.875 to 0.900	3.95	0.50	0.18	0.53
0.900 to 0.925	4.09	0.56	0.29	0.63
0.925 to 0.950	3.50	0.56	0.24	0.61
0.950 to 0.975	1.12	0.28	0.14	0.31
0.975 to 1.000	1.08	0.37	0.16	0.41

Table A.2: Tabulated values of $\frac{1}{N}\frac{dN}{dT}$ (where T = thrust) with statistical error (stat.), systematic uncertainty (sys.), and total error for $7.5 < M_X < 16.0$ GeV with $<M_X>$ = 11.1 GeV.

T Range	$\frac{1}{N}\frac{dN}{dT}$	Stat.	Sys.	Total
0.500 to 0.525	0.00	0.00	0.00	0.00
0.525 to 0.550	0.00	0.00	0.00	0.00
0.550 to 0.575	0.00	0.00	0.00	0.00
0.575 to 0.600	0.00	0.00	0.00	0.00
0.600 to 0.625	0.25	0.22	0.30	0.37
0.625 to 0.650	0.17	0.13	0.06	0.14
0.650 to 0.675	0.45	0.21	0.09	0.23
0.675 to 0.700	0.39	0.18	0.09	0.20
0.700 to 0.725	0.66	0.20	0.10	0.22
0.725 to 0.750	1.43	0.41	0.23	0.47
0.750 to 0.775	1.90	0.43	0.26	0.51
0.775 to 0.800	1.46	0.35	0.13	0.38
0.800 to 0.825	2.96	0.56	0.35	0.66
0.825 to 0.850	3.62	0.63	0.33	0.71
0.850 to 0.875	4.57	0.68	0.32	0.75
0.875 to 0.900	4.89	0.67	0.24	0.71
0.900 to 0.925	5.85	0.80	0.30	0.85
0.925 to 0.950	6.27	0.91	0.34	0.97
0.950 to 0.975	5.55	1.00	0.40	1.07
0.975 to 1.000	1.87	0.54	0.23	0.59

Table A.3: Tabulated values of $\frac{1}{N}\frac{dN}{dT}$ (where T = thrust) with statistical error (stat.), systematic uncertainty (sys.), and total error for $16.0 < M_X < 35.0$ GeV with $<M_X>$ = 22.5 GeV.

A.2 Tables for $\frac{1}{N}\frac{dN}{dS}$

S Range	$\frac{1}{N}\frac{dN}{dS}$	Stat.	Sys.	Total
0.000 to 0.050	0.50	0.12	0.07	0.14
0.050 to 0.100	0.86	0.16	0.05	0.17
0.100 to 0.150	1.69	0.24	0.17	0.29
0.150 to 0.200	1.76	0.24	0.11	0.26
0.200 to 0.250	1.95	0.24	0.17	0.30
0.250 to 0.300	1.83	0.25	0.18	0.30
0.300 to 0.350	2.45	0.31	0.34	0.46
0.350 to 0.400	1.75	0.23	0.23	0.32
0.400 to 0.450	1.64	0.23	0.20	0.31
0.450 to 0.500	1.14	0.18	0.16	0.24
0.500 to 0.550	1.06	0.17	0.14	0.22
0.550 to 0.600	0.80	0.14	0.20	0.24
0.600 to 0.650	0.88	0.16	0.24	0.29
0.650 to 0.700	0.41	0.09	0.10	0.13
0.700 to 0.750	0.63	0.16	0.15	0.22
0.750 to 0.800	0.28	0.09	0.07	0.11
0.800 to 0.850	0.04	0.03	0.01	0.03
0.850 to 0.900	0.16	0.19	0.37	0.41
0.900 to 0.950	0.00	0.00	0.00	0.00
0.950 to 1.000	0.00	0.00	0.00	0.00

Table A.4: Tabulated values of $\frac{1}{N}\frac{dN}{dS}$ (where S = sphericity) with statistical error (stat.), systematic uncertainty (sys.), and total error for $4.0 < M_X < 7.5$ GeV with $<M_X>$ = 5.62 GeV.

S Range	$\frac{1}{N}\frac{dN}{dS}$	Stat.	Sys.	Total
0.000 to 0.050	1.62	0.26	0.11	0.29
0.050 to 0.100	2.47	0.31	0.25	0.40
0.100 to 0.150	2.58	0.29	0.09	0.30
0.150 to 0.200	2.69	0.29	0.17	0.34
0.200 to 0.250	1.94	0.23	0.14	0.27
0.250 to 0.300	1.90	0.23	0.14	0.26
0.300 to 0.350	1.19	0.17	0.09	0.19
0.350 to 0.400	1.34	0.19	0.14	0.24
0.400 to 0.450	0.91	0.14	0.08	0.17
0.450 to 0.500	0.76	0.13	0.07	0.15
0.500 to 0.550	0.54	0.11	0.12	0.16
0.550 to 0.600	0.54	0.11	0.09	0.15
0.600 to 0.650	0.37	0.09	0.14	0.16
0.650 to 0.700	0.34	0.10	0.06	0.12
0.700 to 0.750	0.23	0.09	0.08	0.12
0.750 to 0.800	0.14	0.06	0.04	0.08
0.800 to 0.850	0.06	0.04	0.03	0.05
0.850 to 0.900	0.00	0.00	0.00	0.00
0.900 to 0.950	0.00	0.00	0.00	0.00
0.950 to 1.000	0.00	0.00	0.00	0.00

Table A.5: Tabulated values of $\frac{1}{N}\frac{dN}{dS}$ (where S = sphericity) with statistical error (stat.), systematic uncertainty (sys.), and total error for $7.5 < M_X < 16.0$ GeV with $<M_X>$ = 11.1 GeV.

S Range	$\frac{1}{N}\frac{dN}{dS}$	Stat.	Sys.	Total
0.000 to 0.050	4.86	0.60	0.32	0.68
0.050 to 0.100	5.67	0.59	0.27	0.65
0.100 to 0.150	2.58	0.35	0.10	0.36
0.150 to 0.200	2.12	0.32	0.19	0.38
0.200 to 0.250	1.41	0.25	0.11	0.27
0.250 to 0.300	1.72	0.36	0.28	0.46
0.300 to 0.350	0.50	0.15	0.07	0.16
0.350 to 0.400	0.68	0.18	0.09	0.20
0.400 to 0.450	0.46	0.13	0.08	0.16
0.450 to 0.500	0.43	0.15	0.09	0.17
0.500 to 0.550	0.42	0.16	0.13	0.21
0.550 to 0.600	0.08	0.05	0.02	0.05
0.600 to 0.650	0.22	0.13	0.09	0.15
0.650 to 0.700	0.25	0.14	0.17	0.22
0.700 to 0.750	0.04	0.03	0.03	0.04
0.750 to 0.800	0.15	0.15	0.14	0.21
0.800 to 0.850	0.00	0.00	0.00	0.00
0.850 to 0.900	0.00	0.00	0.00	0.00
0.900 to 0.950	0.00	0.00	0.00	0.00
0.950 to 1.000	0.00	0.00	0.00	0.00

Table A.6: Tabulated values of $\frac{1}{N}\frac{dN}{dS}$ (where S = sphericity) with statistical error (stat.), systematic uncertainty (sys.), and total error for $16.0 < M_X < 35.0$ GeV with $<M_X> = 22.5$ GeV.

A.3 Tables of $<T>$ and $<S>$

M_x/GeV Range	$<M_X>$ /GeV	$<T>$	Stat.	Sys.	Total
4.00 to 7.50	5.58	0.789	0.003	0.002	0.004
7.50 to 11.00	9.17	0.819	0.004	0.004	0.006
11.00 to 16.00	13.21	0.835	0.005	0.003	0.006
16.00 to 21.00	18.22	0.865	0.006	0.004	0.008
21.00 to 27.00	23.71	0.879	0.007	0.004	0.008
27.00 to 35.00	30.37	0.882	0.008	0.003	0.008

Table A.7: Tabulated values of average thrust $<T>$ as function of M_x with statistical error (stat.), systematic uncertainty (sys.), and total error.

M_x/GeV Range	$<M_X>$ /GeV	$<S>$	Stat.	Sys.	Total
4.00 to 7.50	5.58	0.345	0.007	0.006	0.009
7.50 to 11.00	9.17	0.268	0.008	0.009	0.012
11.00 to 16.00	13.21	0.228	0.009	0.007	0.011
16.00 to 21.00	18.22	0.172	0.011	0.010	0.014
21.00 to 27.00	23.71	0.151	0.012	0.008	0.014
27.00 to 35.00	30.37	0.154	0.017	0.010	0.020

Table A.8: Tabulated values of average sphericity $< S >$ as function of M_x with statistical error (stat.), systematic uncertainty (sys.), and total error.

A.4 Tables of $<p^2_{T,in}>$ and $<p^2_{T,out}>$

M_x/GeV Range	$<M_X>$ /GeV	$<p^2_{T,in}>$	Stat.	Sys.	Total
4.00 to 7.50	5.58	0.069	0.002	0.001	0.002
7.50 to 11.00	9.17	0.091	0.003	0.002	0.004
11.00 to 16.00	13.21	0.110	0.005	0.004	0.006
16.00 to 21.00	18.22	0.118	0.007	0.004	0.008
21.00 to 27.00	23.71	0.144	0.012	0.004	0.013
27.00 to 35.00	30.37	0.188	0.022	0.013	0.026

Table A.9: Tabulated values of $<p^2_{T,in}>$ as function of M_x with statistical error (stat.), systematic uncertainty (sys.), and total error.

M_x/GeV Range	$<M_X>$ /GeV	$<p^2_{T,out}>$	Stat.	Sys.	Total
4.00 to 7.50	5.58	0.021	0.001	0.001	0.001
7.50 to 11.00	9.17	0.030	0.001	0.001	0.001
11.00 to 16.00	13.21	0.038	0.001	0.001	0.002
16.00 to 21.00	18.22	0.042	0.002	0.001	0.002
21.00 to 27.00	23.71	0.050	0.003	0.002	0.004
27.00 to 35.00	30.37	0.058	0.004	0.004	0.005

Table A.10: Tabulated values of $<p^2_{T,out}>$ as function of M_x with statistical error (stat.), systematic uncertainty (sys.), and total error.

A.5 Tables of Energy Flow

η Range	$\frac{1}{N}\frac{dE}{d\eta}$	Stat.	Sys.	Total
-5.000 to -4.600	0.01	0.02	0.08	0.08
-4.600 to -4.200	0.00	0.00	0.00	0.00
-4.200 to -3.800	0.03	0.03	0.04	0.05
-3.800 to -3.400	0.07	0.03	0.04	0.05
-3.400 to -3.000	0.08	0.03	0.03	0.04
-3.000 to -2.600	0.23	0.05	0.05	0.08
-2.600 to -2.200	0.28	0.05	0.09	0.10
-2.200 to -1.800	0.44	0.05	0.06	0.08
-1.800 to -1.400	0.80	0.06	0.10	0.12
-1.400 to -1.000	0.78	0.04	0.06	0.07
-1.000 to -0.600	1.00	0.04	0.11	0.12
-0.600 to -0.200	1.31	0.04	0.16	0.17
-0.200 to 0.200	1.41	0.04	0.18	0.18
0.200 to 0.600	1.39	0.04	0.15	0.16
0.600 to 1.000	1.30	0.04	0.06	0.07
1.000 to 1.400	1.23	0.05	0.08	0.09
1.400 to 1.800	0.84	0.05	0.05	0.07
1.800 to 2.200	0.52	0.05	0.07	0.09
2.200 to 2.600	0.29	0.04	0.03	0.05
2.600 to 3.000	0.19	0.04	0.02	0.04
3.000 to 3.400	0.08	0.02	0.03	0.04
3.400 to 3.800	0.07	0.02	0.02	0.03
3.800 to 4.200	0.01	0.01	0.01	0.01
4.200 to 4.600	0.00	0.01	0.01	0.01
4.600 to 5.000	0.00	0.00	0.00	0.00

Table A.11: Tabulated values of energy flow $\frac{1}{N}\frac{dE}{d\eta}$ with statistical error (stat.), systematic uncertainty (sys.), and total error for $4.0 < M_X < 7.5$ GeV with $<M_X> = 5.62$ GeV.

η Range	$\frac{1}{N}\frac{dE}{d\eta}$	Stat.	Sys.	Total
-5.000 to -4.600	0.05	0.06	0.11	0.12
-4.600 to -4.200	0.13	0.08	0.10	0.12
-4.200 to -3.800	0.07	0.03	0.02	0.03
-3.800 to -3.400	0.22	0.06	0.07	0.09
-3.400 to -3.000	0.52	0.09	0.12	0.15
-3.000 to -2.600	0.74	0.10	0.18	0.21
-2.600 to -2.200	1.34	0.12	0.19	0.22
-2.200 to -1.800	1.48	0.09	0.20	0.22
-1.800 to -1.400	1.87	0.09	0.19	0.21
-1.400 to -1.000	1.66	0.06	0.11	0.13
-1.000 to -0.600	1.76	0.05	0.19	0.20
-0.600 to -0.200	1.67	0.04	0.22	0.22
-0.200 to 0.200	1.67	0.04	0.19	0.19
0.200 to 0.600	1.80	0.04	0.12	0.13
0.600 to 1.000	1.97	0.05	0.12	0.13
1.000 to 1.400	2.27	0.07	0.09	0.11
1.400 to 1.800	1.91	0.09	0.09	0.12
1.800 to 2.200	1.58	0.09	0.11	0.15
2.200 to 2.600	0.90	0.08	0.05	0.10
2.600 to 3.000	0.66	0.08	0.13	0.15
3.000 to 3.400	0.43	0.09	0.06	0.10
3.400 to 3.800	0.12	0.04	0.03	0.05
3.800 to 4.200	0.11	0.05	0.02	0.05
4.200 to 4.600	0.01	0.01	0.01	0.01
4.600 to 5.000	0.06	0.04	0.04	0.06

Table A.12: Tabulated values of energy flow $\frac{1}{N}\frac{dE}{d\eta}$ with statistical error (stat.), systematic uncertainty (sys.), and total error for $7.5 < M_X < 16.0$ GeV with $<M_X> = 11.1$ GeV.

η Range	$\frac{1}{N}\frac{dE}{d\eta}$	Stat.	Sys.	Total
-5.000 to -4.600	-0.02	0.02	0.01	0.02
-4.600 to -4.200	0.72	0.30	0.28	0.41
-4.200 to -3.800	0.72	0.25	0.30	0.39
-3.800 to -3.400	1.14	0.24	0.11	0.26
-3.400 to -3.000	2.35	0.28	0.31	0.42
-3.000 to -2.600	2.87	0.26	0.37	0.45
-2.600 to -2.200	3.54	0.23	0.28	0.36
-2.200 to -1.800	2.97	0.15	0.22	0.27
-1.800 to -1.400	3.39	0.14	0.25	0.29
-1.400 to -1.000	3.00	0.08	0.14	0.16
-1.000 to -0.600	2.28	0.06	0.10	0.11
-0.600 to -0.200	1.81	0.05	0.06	0.08
-0.200 to 0.200	2.05	0.06	0.07	0.09
0.200 to 0.600	2.12	0.07	0.07	0.09
0.600 to 1.000	2.61	0.09	0.13	0.16
1.000 to 1.400	3.30	0.12	0.17	0.20
1.400 to 1.800	3.97	0.17	0.18	0.25
1.800 to 2.200	4.21	0.23	0.19	0.30
2.200 to 2.600	3.61	0.27	0.22	0.35
2.600 to 3.000	2.50	0.26	0.15	0.30
3.000 to 3.400	1.16	0.20	0.12	0.23
3.400 to 3.800	0.97	0.21	0.15	0.26
3.800 to 4.200	0.43	0.13	0.08	0.15
4.200 to 4.600	0.41	0.18	0.10	0.21
4.600 to 5.000	0.15	0.09	0.07	0.11

Table A.13: Tabulated values of energy flow $\frac{1}{N}\frac{dE}{d\eta}$ with statistical error (stat.), systematic uncertainty (sys.), and total error for $16.0 < M_X < 35.0$ GeV with $<M_X> = 22.5$ GeV.

A.6 Tables of Transverse Energy Flow

η Range	$\frac{1}{N}\frac{dE_T}{d\eta}$	Stat.	Sys.	Total
-5.000 to -4.600	0.000	0.000	0.001	0.002
-4.600 to -4.200	0.000	0.000	0.000	0.000
-4.200 to -3.800	0.001	0.001	0.002	0.002
-3.800 to -3.400	0.003	0.001	0.002	0.002
-3.400 to -3.000	0.006	0.002	0.002	0.003
-3.000 to -2.600	0.028	0.007	0.007	0.010
-2.600 to -2.200	0.048	0.008	0.015	0.017
-2.200 to -1.800	0.109	0.013	0.016	0.020
-1.800 to -1.400	0.293	0.022	0.039	0.045
-1.400 to -1.000	0.388	0.021	0.026	0.034
-1.000 to -0.600	0.663	0.029	0.073	0.079
-0.600 to -0.200	1.039	0.030	0.133	0.137
-0.200 to 0.200	1.189	0.031	0.156	0.159
0.200 to 0.600	1.097	0.030	0.122	0.126
0.600 to 1.000	0.853	0.025	0.039	0.046
1.000 to 1.400	0.606	0.025	0.036	0.044
1.400 to 1.800	0.302	0.020	0.017	0.026
1.800 to 2.200	0.132	0.012	0.019	0.023
2.200 to 2.600	0.052	0.007	0.006	0.009
2.600 to 3.000	0.023	0.004	0.003	0.005
3.000 to 3.400	0.006	0.002	0.003	0.003
3.400 to 3.800	0.004	0.001	0.001	0.002
3.800 to 4.200	0.000	0.000	0.000	0.000
4.200 to 4.600	0.000	0.000	0.000	0.000
4.600 to 5.000	0.000	0.000	0.000	0.000

Table A.14: Tabulated values of transverse energy flow $\frac{1}{N}\frac{dE_T}{d\eta}$ with statistical error (stat.), systematic uncertainty (sys.), and total error for $4.0 < M_X < 7.5$ GeV with $<M_X> = 5.62$ GeV.

η Range	$\frac{1}{N}\frac{dE_T}{d\eta}$	Stat.	Sys.	Total
-5.000 to -4.600	0.001	0.001	0.002	0.002
-4.600 to -4.200	0.004	0.002	0.003	0.003
-4.200 to -3.800	0.002	0.001	0.001	0.001
-3.800 to -3.400	0.011	0.003	0.004	0.005
-3.400 to -3.000	0.042	0.008	0.010	0.012
-3.000 to -2.600	0.089	0.013	0.022	0.025
-2.600 to -2.200	0.235	0.021	0.034	0.040
-2.200 to -1.800	0.382	0.024	0.050	0.056
-1.800 to -1.400	0.681	0.032	0.068	0.075
-1.400 to -1.000	0.847	0.030	0.056	0.064
-1.000 to -0.600	1.174	0.032	0.129	0.133
-0.600 to -0.200	1.339	0.032	0.179	0.182
-0.200 to 0.200	1.446	0.034	0.168	0.172
0.200 to 0.600	1.462	0.036	0.099	0.105
0.600 to 1.000	1.332	0.036	0.085	0.092
1.000 to 1.400	1.177	0.036	0.044	0.057
1.400 to 1.800	0.698	0.031	0.033	0.046
1.800 to 2.200	0.400	0.023	0.027	0.036
2.200 to 2.600	0.157	0.014	0.009	0.017
2.600 to 3.000	0.079	0.009	0.015	0.018
3.000 to 3.400	0.034	0.007	0.004	0.008
3.400 to 3.800	0.007	0.002	0.001	0.003
3.800 to 4.200	0.004	0.002	0.001	0.002
4.200 to 4.600	0.000	0.000	0.000	0.000
4.600 to 5.000	0.001	0.001	0.001	0.001

Table A.15: Tabulated values of transverse energy flow $\frac{1}{N}\frac{dE_T}{d\eta}$ with statistical error (stat.), systematic uncertainty (sys.), and total error for $7.5 < M_X < 16.0$ GeV with $<M_X> = 11.1$ GeV.

η Range	$\frac{1}{N}\frac{dE_T}{d\eta}$	Stat.	Sys.	Total
-5.000 to -4.600	0.000	0.000	0.000	0.000
-4.600 to -4.200	0.016	0.007	0.006	0.009
-4.200 to -3.800	0.027	0.010	0.012	0.015
-3.800 to -3.400	0.064	0.014	0.007	0.016
-3.400 to -3.000	0.191	0.023	0.024	0.033
-3.000 to -2.600	0.347	0.032	0.044	0.054
-2.600 to -2.200	0.628	0.040	0.048	0.063
-2.200 to -1.800	0.762	0.038	0.057	0.069
-1.800 to -1.400	1.255	0.052	0.098	0.111
-1.400 to -1.000	1.527	0.042	0.073	0.084
-1.000 to -0.600	1.542	0.041	0.065	0.077
-0.600 to -0.200	1.473	0.042	0.048	0.064
-0.200 to 0.200	1.806	0.055	0.064	0.084
0.200 to 0.600	1.741	0.058	0.055	0.080
0.600 to 1.000	1.778	0.064	0.083	0.105
1.000 to 1.400	1.709	0.063	0.090	0.110
1.400 to 1.800	1.478	0.062	0.064	0.090
1.800 to 2.200	1.097	0.060	0.049	0.078
2.200 to 2.600	0.642	0.047	0.038	0.061
2.600 to 3.000	0.303	0.032	0.019	0.038
3.000 to 3.400	0.094	0.016	0.010	0.019
3.400 to 3.800	0.054	0.012	0.008	0.014
3.800 to 4.200	0.017	0.005	0.003	0.006
4.200 to 4.600	0.011	0.005	0.003	0.006
4.600 to 5.000	0.002	0.001	0.001	0.002

Table A.16: Tabulated values of transverse energy flow $\frac{1}{N}\frac{dE_T}{d\eta}$ with statistical error (stat.), systematic uncertainty (sys.), and total error for $16.0 < M_X < 35.0$ GeV with $<M_X> = 22.5$ GeV.

Bibliography

[1] E. Rutherford, *Phil. Mag.* **21** 669, (1911).

[2] N.F. Mott, *Proc. Roy. Soc.* **A124** 425 (1929);
N.F. Mott, *Proc. Roy. Soc.* **A135** 429 (1932).

[3] M.N. Rosenbluth, *Phys. Rev.* **79**, 615 (1950).

[4] R.W. McAllister, R. Hoftadter, *Phys. Rev.* **102**, 851 (1956);
R. Hofstadter, *Rev. Mod. Phys.* **28**, 214 (1956).

[5] J.J. Sakurai, "Theory od strong interactions", *Ann. Phys.* **11** 1 (1960).

[6] R.P. Feynman, "Very high energy collisions of hadrons", *Phys. Rev. Lett.* **23**, 1415 (1969).

[7] O.W. Greenberg, *Phys. Rev. Lett.* **13**, 598 (1964);
M.Y. Han, Y. Nambu, *Phys. Lett.* B **139**, 1006 (1965).

[8] H.D. Politzer, *Phys. Rev. Lett.* **30**, 1346 (1973);
D.J. Gross F. Wilczek, *Phys. Rev. Lett.* **30**, 1343 (1973).

[9] W.A. Caswell, *Phys. Rev. Lett.* **33**, 244 (1974).

[10] O.V. Tarasov, A.A. Vladimirov, A.Yu. Zharkov, *Phys. Lett.* B **93**, 429 (1980);
S.A. Larin, J.A.M. Vermaseren, *Phys. Lett.* B **303**, 334 (1993).

[11] K.G. Wilson, *Phys. Rev.* D **10**, 2445 (1974).

[12] A. Seiden, T.L. Shalk, J.F. Martin, *Phys. Rev.* D **18**, 3990 (1978);
A. Seiden, *Phys. Lett.* B **68**, 157 (1977).

[13] J.I. Friedman, H.W. Kendall, R.E. Taylor, *Rev. Mod. Phys.* **63**, 173 (1991).

[14] R.K. Ellis, W.J. Stirling, B.R. Webber, "QCD and Collider Physics", Cambridge University Press, 1996

[15] J.D. Bjorken, *Phys. Rev.* **179**, 1547 (1969).

[16] M. Gell-Mann, *Phys. Rev.* **125**, 214 (1962).

[17] G. Zweig, CERN-8192/TH 401 (1964);
G. Zweig, CERN-8419/TH 412 (1964);

[18] Deden et al., *Nucl. Phys.* B **85**, 269 (1975).

[19] T. Eichten et al,. *Phys. Lett.* B **46**, 274 (1973).

[20] M. Althoff, et al., *Phys. Lett.* B **86**, 243 (1979).

[21] V.N. Gribov, L.N. Lipatov, *Sov. J. Nucl. Phys.* **15**, 438 (1972);
L.N. Lipatov, *Sov. J. Nucl. Phys.* **20**, 96 (1975).
Y.L. Dokshitzer, *Sov. Phys. JETP* **46**, 641 (1977);

[22] G. Altarelli, G. Parisi, *Nucl. Phys.* B **126**, 298 (1977);
G. Altarelli, *Nucl. Phys.* B **1**, 1 (1981).

[23] M. Glück, E. Reya, A. Vogt, *Phys. Rev.* D **45**, 3986 (1992).

[24] A.D. Martin, W.J. Stirling, R.G Roberts, *Phys. Lett.* B **387**, 419 (1996);
A.D. Martin, W.J. Stirling, R.G Roberts, *Phys. Lett.* B **306**, 145 (1993) with Erratum-ibid. *Phys. Lett.* B **309**, 429 (1993).

[25] H.L. Lai, *Phys. Rev.* D **51**, 4763 (1995).

[26] ZEUS Collab., M.Derrick et al., *Phys. Lett.* B **303**, 183 (1993).

[27] ZEUS Collab., M.Derrick et al., *Z. Phys.* C **72**, 399 (1996).

[28] H1 Collab., T. Ahmed et al., *Nucl. Phys.* B **470**, 3 (1996).

[29] UA4 Collab., D. Bernard et al., *Phys. Lett.* B **166**, 459 (1986);
UA4 Collab., D. Bernard et al., *Phys. Lett.* B **186**, 227 (1987).

[30] UA5 Collab., R.E. Ansorge et al., *Z. Phys.* C **33**, 175 (1986).

[31] UA8 Collab., R. Bonino et al., *Phys. Lett.* B **211**, 239 (1988);
UA8 Collab., A. Brandt et al., *Phys. Lett.* B **297**, 417 (1992).

[32] E710 Collab., N.A, Amos et al., *Phys. Lett.* B **243**, 158 (1990);
E710 Collab., N.A, Amos et al., *Phys. Lett.* B **301**, 313 (1993).

[33] EHS/NA22 Collab., M. Begalli et al., *Z. Phys.* C **55**, 531 (1992).

[34] CDF Collab., F. Abe et al., *Phys. Rev.* D **50**, 5535 (1994).

[35] ZEUS Collab., M. Derrick et al., *Phys. Lett.* B **315**, 481 (1993).

[36] H1 Collab., T. Ahmed et al., *Nucl. Phys.* B **429**, 477 (1994).

[37] ZEUS Collab., M.Derrick et al., *Euro. Phys. J.* C **6**, 43 (1999).

[38] T. Regge, "Introduction to complex orbital momenta", *Nouvo Cim.* **14** 951 (1959).

[39] P.D.B. Collins, "An Introduction to Regge Theory and High Energy Physics", Cambridge University Press 1977.

[40] A. Donnachie, P.V. Landshoff, *Nucl. Phys.* B **244**, 322 (1984);
A. Donnachie, P.V. Landshoff, *Phys. Lett.* B **191**, 309 (1987);
A. Donnachie, P.V. Landshoff, *Nucl. Phys.* B **303**, 634 (1988);
A. Donnachie, P.V. Landshoff, *Phys. Lett.* B **296**, 227 (1992).

[41] I.Y. Pomeranchuk, *Sov. Phys. JETP* **7** 499 (1985).

[42] H. Abramowicz, E.M. Levin, A. Levy, U. Maor, *Phys. Lett.* B **269**, 465 (1991).

[43] Landolt-Börnstein, "Total Cross-Section for Reactions of High Energy Particles", New Series, Vol. 12b, H. Schopper, Ed. 1987.

[44] ZEUS Collab., M. Derrick et al., *Z. Phys.* C **63**, 391 (1994).

[45] H1 Collab., T. Ahmed et al., *Z. Phys.* C **69**, 27 (1995).

[46] G. Ingelman, P. Schlein, *Phys. Lett.* B **152**, 256 (1985).

[47] Riko Wichmann, "Measurement of the diffractive cross section and properties of the hadronic final state", PHOTON99, International Conference on Structure and Interaction of the Photon, Freiburg im Breisgau, May 23-27, 1999 and references therein.

[48] J. Bartels, H. Lotter, M. Wüsthoff, *Z. Phys.* C **68**, 121 (1995).

[49] N.N. Nikolaev, B.G. Zakharov, *Z. Phys.* C **49**, 607 (1990).

[50] J.R. Forshaw, D.A. Ross, "QCD and the Pomeron", Cambridge University Press, 1997.

[51] J.D. Bjorken, J. Kogul, *Phys. Rev.* D **8**, 1341 (1973).

[52] J. Bartels, J. Ellis, H. Kowalski, M. Wüsthoff, *Euro. Phys. J.* C **7**, 443 (1999).

[53] W. Buchmüller, A. Hebecker, *Nucl. Phys.* B **476**, 203 (1996);
W. Buchmüller, M.F. McDermott, A. Hebecker, *Nucl. Phys.* B **487**, 283 (1997);
W. Buchmüller, T. Gehrmann, A. Hebecker, *Nucl. Phys.* B **537**, 477 (1999).

[54] N.N. Nikolaev, B.G. Zakharov, *Z. Phys.* C **53**, 331 (1992);
M. Genovese, N.N. Nikolaev, B.G. Zakharov, *Sov. Phys. JETP* **81** 625 (1995);
M. Genovese, N.N. Nikolaev, A.V Pronyaev, B.G. Zakharov, *Phys. Lett.* B **422**, 238 (1998).

[55] M. Wüsthoff, PhD thesis, University of Hamburg, DESY-95-166.

[56] A.H. Mueller, 6th International Workshop on Deep Inelastic Scattering and QCD, DIS98, World Scientifc

[57] K. Golec-Biernat, M. Wüsthoff, *Phys. Rev.* D **59**, 014017 (1999);
K. Golec-Biernat, M. Wüsthoff, DTP-99-20, hep-ph/9903358.

[58] H. Kowalski, "Inclusive Diffraction at HERA", New trends in HERA Physics 1999, Ringberg Workshop, June 1999, DESY-99-141.

[59] G. Wolf, "HERA: physics, machine and exeriments", Lectures given at *Inst. on Techniques and Concepts of High Energy Physics*, St. Croix, Virgin Islands, June 19-30, 19986, DESY 86-089 (1986).

[60] HERA, "A proposal for a large Electron-Proton Colliding Beam Facility at DESY", DESY HERA 81-10.

[61] The ZEUS Detector, Status Report, DESY (1993).

[62] B. Foster, et al., *Nucl. Instrum. Methods* A **338**, 254 (1993).

[63] M. Derrick, et al., *Nucl. Instrum. Methods* A **309**, 77 (1991);
A. Bernstein, et al., *Nucl. Instrum. Methods* A **336**, 23 (1993).

[64] A. Andresen, et al., *Nucl. Instrum. Methods* A **309**, 101 (1991)

[65] ZEUS Collab., "Proposal for a Small Angle Rear Tracking Detector for ZEUS", ZEUS 93-016;
A. Bamberger, et al., "The Small Angle Rear Tracking Detector for ZEUS", ZEUS 95-095.

[66] C. Youngman, "The ZEUS Data Acquisition System", DESY 92-150A;
W.H. Smith, et al, "The ZEUS Trigger System", ZEUS 89-084.

[67] H. A.J.R. Uijterwaal, "The Global Second Level Trigger", Ph.D. Thesis, University of Amsterdam 1992.

[68] D.E. Dorfan, NIMA **342**, 143 (1994);
E. Barberis, et al., *Nucl. Phys. Proc. Suppl.* **B32** (1993).

[69] J. DeWitt, NIMA **288**, 209 (1990);
"The Digital Time Slice Ship", Senior Thesis 1989, UC Santa Cruz, SCIPP 89-24.

[70] H. Larsen, "The LPS Readout Controller", CERN-LAA (1994).

[71] H. Larsen, "The LPS Fast Fan Out", CERN-LAA (1994).

[72] H. Larsen, "The LPS Serial Readout Controller", CERN-LAA (1994).

[73] W. Press et al., *Numerical Recipes*, Cambridge University Press, 1989.

[74] J. Rahn, R. Wichmann, "Alignment of LPS for 1995 data", ZEUS 98-006.

[75] L. Iannotti, "LPS 1995 alignment and calibration", ZEUS 97-83.

[76] J. T. Rahn, "Studying Characteristics of Diffractive Deep Inelastic Scattering with the ZEUS Leading Proton Spectrometer", PhD Thesis, UC Santa Cruz, SCIPP 97-29.

[77] A. Kwiatkowski, H. Spiesberger, H.-J. Möhring, "HERACLES 4.6 - An event generator for *ep* interaction at HERA includinng radiative processes", *http://www.desy.de/~hspiesb/heracles.html*.

[78] T. Sjöstrand, *Comp. Phys. Comm.* **82** (1994) 74.

[79] B. Anderson et al., *Phys. Rev.* D **97**, 31 (1993).

[80] H. Jung, *Comp. Phys. Comm.* **86** (1995) 147.

[81] H. Jung, "The RAPGAP Monte Carlo for Deep Inelastic Scattering", version 2.08/01, *http://www-h1.desy.de/~jung/rapgap.html*.

[82] H1 Collab., C. Adloff et al., *Z. Phys.* C **76**, 613 (1997).

[83] J.F. Owens, *Phys. Rev.* D **30**, 943 (1984).

[84] ARIADNE 4.08, L. Lönnblad, *Comp. Phys. Comm.* **71** (1992) 74.

[85] G. Ingelman, A. Edin, and J. Rathsman, *Comp. Phys. Comm.* **101** (1997) 108.

[86] ZEUS Collab., M.Derrick et al., *Z. Phys.* C **70**, 391 (1996).

[87] J. Bartels, H. Lotter, M. Wüsthoff, *Phys. Lett.* B **379**, 239 (1996); *hep-ph/9602363.*

[88] J. Bartels, C. Ewerts, H. Lotter, M. Wüsthoff, *Phys. Lett.* B **386**, 389 (1996).

[89] J. Bartels, H. Jung, M. Wüsthoff, "Quark-Antiquark-Gluon Jets in DIS Diffractive Dissociation", *DESY 99-027, hep-ph/9903265.*

[90] A. Donnachie, P.V. Landshof, *Nucl. Phys.* B **244**, 322 (1984).

[91] A. Donnachie, P.V. Landshof, *Nucl. Phys.* B **303**, 634 (1988).

[92] M.G. Ryskin, A. Solano, "RIDI: a Monte Carlo generator for diffractive dissociation of virtual photons in ep scattering", Monte Carlo Generators for HERA Physics, DESY Workshop 1998/99, *http://www.desy.de/~heramc/proceedings/wg50/ryskin.ps.gz.*

[93] M.G. Ryskin, *Sov. J. Nucl. Phys.* **52** (1990) 529;
M.G. Ryskin, M. Besancon, Proceedings of the Workshop 'Physics at HERA', DESY, 29-30 October 1991, Edited by W. Buchmüller and G. Ingelman, p. 215;
M.G. Ryskin, S.Yu. Sivoklokov, A. Solano, Proceedings of the International Conference (5th "Blois" Workshop) on Elastic and Diffractive Scattering, Ed. H.M. Fried, K. Kang and C-I. Tan, World Scientific, Singapore (1993);
E.M. Levin *et al.*, hep-ph 9606443.

[94] See also: N.N. Nikolaev and B.G. Zakharov, *Z. Phys.* C **49**, 607 (1991);
E.M. Levin and M. Wüsthoff, *Phys. Rev.* D **50**, 4306 (1994);
J. Bartels, H. Lotter and M. Wüsthoff, *Z. Phys.* C **66**, 157 (1995).

[95] E. Witten, *Nucl. Phys.* B **104**, 445 (1976);
M.A. Shifman, A.I. Vainshtein, and V.I. Zakharov, *Nucl. Phys.* B **136**, 157 (178).

[96] H. Spiesberger, K. Charchula and G. A. Schuler, "DJANGO6 - An Monte Carlo Generator for Deep Inelastic Lepton Proton Scattering Including QED and QCD Radiative Effects", *http://www.desy.de/~hspiesb/django6.html.*

[97] R. Brun, et al., "GEANT3", *CERN DD/EE/11-1 (1989).*

[98] Els de Wolf (editor) et al., "ZGANA, ZEUS trigger simulation library".

[99] S. Maselli, A. Solano, "The LPS simulation in MOZART", ZEUS 91-112.

[100] S. Maselli, R. Sacchi, "LPS acceptance calculation and update of the LPS simulation", ZEUS 92-43.

[101] H. Abramowicz, A. Caldwell, R. Sinkus, "Neutral Network Based Electron Identification in the ZEUS Calorimeter", DESY 95-054.

[102] R. Sinkus, *Nucl. Instrum. Methods* A **361**, 290 (1995).

[103] N. Tuning, "ZUFOs", *http://www-zeus.desy.de/~ntuning/ZEUS_ONLY/zufo_new.html*

[104] F. Jacquet, A. Blondel, Proceedings of "The study of an *ep* facility for Europe", DESY 79-48, 391 (1979)

[105] S. Bentvelsen, J, Engelen, P. Koijman, "Reconstruction of (x, Q^2) and extraction of the structure function in neutral current scattering at HERA", Proceedings of the Workshop on Physics at HERA, vol. 1, (1992) 23.

[106] for reference see the SFEW tool web page: *http://www-zeus.desy.de/~sfew/ZEUS_ONLY/doc/documentation.html*

[107] Partcile Data Book (July 98), extracted from C. Caso, et al., EPJ **3**, 1 (1998).

[108] S. Brandt et al., *Phys. Lett.* **12**, 152 (1964).

[109] E. Fahri, *Phys. Rev. Lett.* **39**, 1587 (1977).

[110] S. Brandt et al., *Z. Phys.* C **1**, 61 (1979).

[111] Z. Kuntszt et al., "Z. Physics at LEP1", CERN Report 89-08 (1989), Vol. 1, 373

[112] J.D. Bjorken and S.J. Brodsky, *Phys. Rev.* D **1**, 1416 (1970)

[113] M. Althoff, et al., *Z. Phys.* C **22**, 307 (1984).

[114] H1 Collab., C. Adloff et al., *Euro. Phys. J.* C **1**, 495 (1998).

[115] TASSO Collab., W. Braunschweiger et al., *Z. Phys.* C **47**, 187 (1990).

[116] PLUTO Collab., C. Berger et al., *Z. Phys.* C **12**, 297 (198).

[117] MARK II Collab., A. Peterson et al., *Phys. Rev.* D **37**, 1 (1998).

[118] H1 Collab., C. Adloff et al., *Phys. Lett.* B **428**, 206 (1998).